



**HAL**  
open science

# Response of sandy beaches in West Africa, gulf of Guinea, to multi-scale forcing

Grégoire Abessolo Ondoa

► **To cite this version:**

Grégoire Abessolo Ondoa. Response of sandy beaches in West Africa, gulf of Guinea, to multi-scale forcing. Geomorphology. Université Paul Sabatier - Toulouse III, 2020. English. NNT : 2020TOU30029 . tel-02987804

**HAL Id: tel-02987804**

**<https://theses.hal.science/tel-02987804>**

Submitted on 4 Nov 2020

**HAL** is a multi-disciplinary open access archive for the deposit and dissemination of scientific research documents, whether they are published or not. The documents may come from teaching and research institutions in France or abroad, or from public or private research centers.

L'archive ouverte pluridisciplinaire **HAL**, est destinée au dépôt et à la diffusion de documents scientifiques de niveau recherche, publiés ou non, émanant des établissements d'enseignement et de recherche français ou étrangers, des laboratoires publics ou privés.



# THÈSE

## En vue de l'obtention du DOCTORAT DE L'UNIVERSITÉ DE TOULOUSE

Délivré par l'Université Toulouse 3 - Paul Sabatier

---

Présentée et soutenue par  
**Grégoire ABESSOLO ONDOA**

Le 11 juin 2020

**Réponse des plages sableuses d'Afrique de l'Ouest, Golfe de  
Guinée, face au forçage multi-échelle**

---

Ecole doctorale : **SDU2E - Sciences de l'Univers, de l'Environnement et de  
l'Espace**

Spécialité : **Océan, Atmosphère, Climat**

Unité de recherche :

**LEGOS - Laboratoire d'Etudes en Géophysique et Océanographie Spatiale**

Thèse dirigée par

**Rafaël ALMAR et Magnus LARSON**

Jury

M. Yann BALOUIN, Rapporteur  
M. Kwasi APPEANING ADDO, Rapporteur  
Mme Florence BIROL, Examinatrice  
M. Olusegun DADA, Examineur  
M. Edward ANTHONY, Examineur  
M. Bruno CASTELLE, Examineur  
M. Rafaël ALMAR, Directeur de thèse  
M. Magnus LARSON, Directeur de thèse





# THÈSE

En vue de l'obtention du

**DOCTORAT DE L'UNIVERSITÉ DE TOULOUSE**

Délivré par : *l'Université Toulouse 3 Paul Sabatier (UT3 Paul Sabatier)*

---

---

Présentée et soutenue le 11/06/2020 par :

**ABESSOLO ONDOA GRÉGOIRE**

Réponse des plages sableuses d'Afrique de l'Ouest, Golfe de Guinée,  
face au forçage multi-échelle

---

---

## JURY

BIROL FLORENCE	Physicienne	Présidente du Jury
BALOUIN YANN	HDR/Chargé de Recherche	Rapporteur
ADDO A. KWASI	Maître de Conférences	Rapporteur
ANTHONY EDWARD	Professeur	Examineur
CASTELLE BRUNO	Directeur de Recherche	Examineur
DADA OLUSEGUN	Chargé de Recherche	Examineur
ALMAR RAFAEL	HDR/Chargé de Recherche	Directeur de thèse
MAGNUS LARSON	Professeur	Co-directeur de thèse

---

**École doctorale et spécialité :**

*SDU2E : Océan, Atmosphère, Climat*

**Unité de Recherche :**

*Laboratoire d'Études en Géophysique et Océanographie Spatiales (UMR 5566)*

**Directeur(s) de Thèse :**

*ALMAR Rafael et LARSON Magnus*

**Rapporteurs :**

*BALOUIN Yann et APPEANING ADDO Kwasi*



*In memory of my mother*



# Acknowledgements

This thesis represents not only my work at the field and at the keyboard, it is a milestone in more than seven years of work and collaboration with IRD and specifically within the LEGOS Laboratory. My experience with IRD has been nothing short of amazing. Since my first trip at Cotonou on March 2014 for training on remote sensing devices in coastal areas, I have been given unique opportunities... and taken advantage of them. Therefore, I would like to express my sincere thanks to the IRD's ARTS Fellowship. But this thesis is also the result of many experiences that would not have been possible without the help of remarkable individuals whom I also wish to thank.

Foremost, I wish to thank my supervisor Dr Rafael Almar, for his patience, conscientious and enthusiasm. Throughout the four years of my PhD, he provided lots of good ideas, valuable guidance and great encouragement. He was my primary resource for getting my science questions answered and was instrumental in helping me crank out this thesis. He's an excellent example for me and an inspiration in many ways.

I am also very grateful to Prof. Magnus Larson whose simplicity and self-sacrifice is unmatched by any. I still remember his first trip at Douala where we discussed a lot about the post-thesis and possible collaborations. It's an honor to work with him.

I would also like to thank Dr. Bruno Castelle, for his active and rapid feedback to all my requests. I appreciate his scientific rigor which always leads to outstanding results. Thank you for keeping me motivated throughout the writing and editing of the articles bound in this thesis.

Special thanks should also be given to Prof. Tomedi Eyango Minette epe Tabi Abodo, Prof. du Penhoat Yves and Dr Onguéné Raphaël. Thank you for introducing me to the IRD's ARTS Fellowship four years ago, for your continuous support and guidance in the years that followed. Thank you for creating various opportunities for me, believing in me and giving me the necessary pep-talks whenever I started doubting myself.

My sincerest thanks to Zacharie Sohou, Frédéric Bonou, Hoan Le Xuan and Elodie Kestenare for their essential support in the acquisition, recording, processing and simulation of the data required for this thesis.

My thesis committee guided me through all these years. Thank you to Julien Jouanno, Le Cozannet Goneri, and Benoit Meyssignac for being my major advisors. They are a source of friendships as well as good advice and collaboration.

It would be very difficult to study away from home without the help of people in Toulouse. So I would like to thank LEGOS director (Alexandre Ganachaud), and secretaries (Brigitte Cournou, Martine Mena, Agathe Baritaud, Nadine Lacroux and Sabriya Oulad). Thanks also to those who provided me with assistance during my stays in Toulouse.

Finally, I would like to send my deepest thanks to my family who are always with me, encouraging me to complete this thesis. And above all, I want to thank my Wife and my son

because I know they are always my greatest supporters.

---

# Abstract

This thesis presents a multi-scale investigation of the role of waves, sea level and human settlements to understand long-term coastal evolution of the 400-km long sandy Bight of Benin coast (Gulf of Guinea, West Africa). Coastal morphology and its ocean drivers are monitored using local shore-based video camera and regional satellite remote sensing. New video developments show the potential of video camera in sensing daily beach profile, waves and sea level at the coast. The results reveal the dominant influence of waves on shoreline variability at the event (daily) and seasonal scales, whereas at the intraseasonal and interannual scales, the shoreline is dominantly modulated by sea level changes. Over longer periods (decades), anthropogenic influence, such as deep water harbours and the reduction of sediment river (such as Volta and Niger) discharge due to dams significantly alter sediment transport, creating several erosion zones. These observations over the long term are satisfactorily reproduced by the implemented shoreline model, specially in the vicinity of the harbors, and allows to estimate, for example, the amount of sediment nourishment necessary to limit erosion downstream of Lagos harbor. Beside their fundamental interest, these results put strong basis to improve regional coastal policies.

**Keywords:** Bight of Benin, waves, sea level, sediment transport, nearshore, shoreline, beach profile, long term shoreline modeling



# Résumé

Cette thèse présente une étude multi-échelle du rôle des vagues, du niveau de la mer et des infrastructures humaines pour comprendre l'évolution à long terme des 400 km de côte sableuse dans la Baie du Bénin (Golfe de Guinée, Afrique de l'Ouest). La morphologie côtière et les forçages océaniques sont mesurés au niveau local par un système d'observation vidéo et au niveau régional par télédétection satellite. De nouvelles améliorations des techniques vidéo montrent le potentiel des systèmes vidéo dans l'estimation journalière du profil de la plage, des vagues et du niveau de la mer à la côte. Les résultats révèlent l'influence dominante des vagues sur la variabilité côtière aux échelles événementielle (journalière) et saisonnière, tandis qu'aux échelles intrasaisonnière et interannuelle, le trait de côte est modulé de manière dominante par les changements du niveau de la mer. Sur des périodes plus longues (décennies), les influences anthropiques, telles que les ports en eau profonde et la réduction des flux sédimentaires fluviaux (à l'exemple de la Volta et le Niger) due aux barrages, modifient considérablement le transport sédimentaire, conduisant à l'apparition de plusieurs zones d'érosion. Ces observations à long terme sont reproduites de manière satisfaisante par le modèle de trait de côte mis en œuvre, en particulier à proximité des ports, et permettent d'estimer, par exemple, la quantité de sédiments nécessaire pour limiter l'érosion en aval du port de Lagos. Outre leur intérêt fondamental, ces résultats constituent un cadre solide pour l'amélioration des politiques côtières dans la région.

**Mots clés :** Baie du Bénin, vagues, niveau de la mer, transport sédimentaire, littoral, trait de côte, profil de plage, modélisation d'évolution long terme du trait de côte



# Contents

<b>Acknowledgements</b>	<b>iii</b>
<b>Abstract</b>	<b>v</b>
<b>Résumé</b>	<b>vii</b>
<b>List of Figures</b>	<b>xiii</b>
<b>List of Tables</b>	<b>xvii</b>
<b>Introduction</b>	<b>1</b>
<b>Introduction en Français</b>	<b>5</b>
<b>1 Background</b>	<b>9</b>
1.1 Introduction . . . . .	9
1.2 Contributors to beach changes . . . . .	10
1.2.1 Waves and beach morphology . . . . .	10
1.2.2 Storms . . . . .	13
1.2.3 Wave-induced currents and undertow . . . . .	15
1.2.4 Sediment budget . . . . .	16
1.2.5 Sea level variations at the coast . . . . .	17
1.3 Measuring beach changes and profile . . . . .	20
1.3.1 Several techniques for measuring beach morphology . . . . .	21
1.3.2 Altimetry and video for continuous coastal monitoring . . . . .	21
1.4 Shoreline model review . . . . .	22
1.4.1 Modeling shoreline changes driven by longshore transport . . . . .	22
1.4.2 Modeling shoreline changes driven by cross-shore transport . . . . .	24
1.4.3 Longshore and cross-shore integrated model . . . . .	27
1.5 Conclusion . . . . .	30
<b>2 Study area, methods and data</b>	<b>31</b>
2.1 Introduction . . . . .	31
2.2 The Bight of Benin, Gulf of Guinea . . . . .	32
2.2.1 Location and general overview . . . . .	32
2.2.2 Oceanic forcing . . . . .	32
2.2.3 Harbors and coastal infrastructure . . . . .	34
2.2.4 River discharges . . . . .	34

2.2.5	Grand Popo beach, Benin . . . . .	35
2.3	Data . . . . .	35
2.3.1	The Grand Popo 2014 field measurements . . . . .	35
2.3.2	Waves from Era-Interim global reanalysis . . . . .	36
2.3.3	Tide gauge and FES2014 model . . . . .	38
2.3.4	Satellite measurements . . . . .	38
2.3.5	Video-based station, images and processing . . . . .	39
2.4	Conclusion . . . . .	47
<b>3</b>	<b>Depth inversion and sea level from video</b>	<b>49</b>
3.1	Introduction . . . . .	49
3.2	New approach in the temporal method of estimating wave celerity . . . . .	50
3.2.1	Approach statement . . . . .	50
3.2.2	Validation of video-derived depths . . . . .	51
3.3	Error proxies in video-based depth inversion: temporal celerity estimation . . . . .	52
3.3.1	Background . . . . .	53
3.3.2	Depth Error Estimates . . . . .	54
3.3.3	Kalman filter . . . . .	54
3.3.4	Results . . . . .	55
3.3.5	Discussion . . . . .	57
3.3.6	Conslusion . . . . .	57
3.4	Sea level at the coast from video-sensed waves . . . . .	58
3.4.1	Background . . . . .	58
3.4.2	Water level estimation . . . . .	60
3.4.3	Results . . . . .	61
3.4.4	Discussion . . . . .	64
3.4.5	Conslusions . . . . .	67
3.5	Conclusion . . . . .	68
<b>4</b>	<b>Beach response to multi-scale wave forcing and sea level variations</b>	<b>69</b>
4.1	Introduction . . . . .	69
4.2	Beach response to wave forcing from event to inter-annual time scales . . . . .	70
4.2.1	Background . . . . .	70
4.2.2	Methods . . . . .	71
4.2.3	Results . . . . .	73
4.2.4	Discussion . . . . .	77
4.2.5	Conclusions . . . . .	78
4.3	Beach adaptation to intra-seasonal sea level changes . . . . .	79
4.3.1	Background . . . . .	80
4.3.2	Sea Level Data . . . . .	81
4.3.3	Intra-seasonal sea level forcing . . . . .	82
4.3.4	Detection algorithm for intraseasonal sea level event and Kelvin waves . . . . .	82
4.3.5	Intra-seasonal beach response . . . . .	83
4.3.6	Influence of intraseasonal sea level variations on beach morphology . . . . .	84
4.3.7	Conclusions . . . . .	86
4.4	Conclusion . . . . .	87

---

<b>5</b>	<b>The Bight of Benin coast evolution from 1990 to 2015</b>	<b>89</b>
5.1	Introduction . . . . .	89
5.2	Sedimentary cell dynamics in the Bight of Benin . . . . .	90
5.3	Trends in shoreline evolution . . . . .	91
5.4	Causes of shoreline mobility in the Bight of Benin . . . . .	92
5.4.1	EOF Analysis . . . . .	92
5.4.2	Longshore sediment transport, coastal infrastructures and rivers sand supply	94
5.4.3	Influence of South Atlantic climate dynamics . . . . .	96
5.4.4	Localized sand mining . . . . .	98
5.4.5	Outer shoreface/inner shelf sand supply . . . . .	98
5.4.6	Future management and climate change . . . . .	98
5.5	Conclusion . . . . .	100
<b>6</b>	<b>Modeling regional coastal evolution</b>	<b>101</b>
6.1	Introduction . . . . .	102
6.2	Data form employed . . . . .	103
6.3	Modeling regional coastal evolution . . . . .	103
6.3.1	Background and theoretical formulations . . . . .	103
6.3.2	Model set-up . . . . .	105
6.3.3	Model calibration . . . . .	105
6.3.4	Model validation . . . . .	106
6.4	Simulation results for selected scenarios . . . . .	108
6.4.1	Overview . . . . .	108
6.4.2	Transport pattern without harbor structures . . . . .	109
6.4.3	Nourishment to remedy downdrift erosion . . . . .	110
6.4.4	Influence of reduced boundary transport . . . . .	110
6.5	Discussion . . . . .	111
6.6	Conclusions . . . . .	114
	<b>Conclusions and Future Research</b>	<b>115</b>
	<b>Conclusions et perspectives</b>	<b>121</b>
	<b>Bibliography</b>	<b>127</b>
	<b>Appendix I : Potential of Video Cameras in Assessing Event and Seasonal Coast-</b> <b>line Behaviour: Grand Popo, Benin (Gulf of Guinea)</b>	<b>149</b>
	<b>Appendix II : Development of a West and Central Africa regional video camera</b> <b>network to monitor coastal response to multi-scale ocean forcing</b>	<b>155</b>
	<b>Appendix III : Réponse d'une plage à terrasse face aux variations intra-saisonniers</b> <b>régionales du niveau de la mer</b>	<b>167</b>
	<b>Appendix IV : Modeling regional coastal evolution in the Bight of Benin, Gulf</b> <b>of Guinea, West Africa</b>	<b>179</b>
	<b>Appendix V : A deep learning approach for estimation of the nearshore bathymetry</b>	<b>191</b>

<b>Appendix VI : Assessment of the Evolution of Cameroon Coastline: An Overview from 1986 to 2015</b>	<b>197</b>
---	------------

---

# List of Figures

1.1	Beaches classification . . . . .	12
1.2	Storm impact scale on barrier islands . . . . .	14
1.3	Sources and sinks for a littoral sediment budget . . . . .	16
1.4	Sketch of shoreline change due to longshore transport . . . . .	23
2.1	The Bight of Benin in the Gulf of Guinea, West Africa . . . . .	33
2.2	Grand Popo beach, Benin, Gulf of Guinea, West Africa . . . . .	35
2.3	Data collected during the Grand Popo 2014 field measurements . . . . .	36
2.4	Location of data sources in the Bight of Benin, next to Grand Popo town . . . . .	37
2.5	Grand Popo video system and stored video images . . . . .	40
2.6	Image rectification: (a) Grounds control points, (b) Averaged pixel footprint $\Delta X_0$ and cross-shore coordinate on the cross-shore stack and (c) rectified image . . . . .	41
2.7	Standard deviation of pixel intensity of a good and a bad timestack image . . . . .	42
2.8	Example of shoreline detection for a tidal cycle . . . . .	43
2.9	Wave period estimate using upward zero-crossing method applied to a filtered time series of pixel intensity . . . . .	45
2.10	Description of the main sources of error for the use of video-based depth inversion methods. . . . .	46
3.1	Spectral distribution. Time series spectra of (a) water height and (b) pixel intensity	50
3.2	Temporal approach for depth inversion scheme during the Grand Popo experiment from March 10 to 19, 2014: (a) Cross-correlation matrix, (b) Wave celerities and (c) depth estimates . . . . .	51
3.3	Forcing parameters and beach evolution at Grand Popo, Benin . . . . .	52
3.4	Errors proxies . . . . .	55
3.5	Daily bathymetry derived from video inversion: original and filtered . . . . .	56
3.6	Comparison between observed and reconstructed differences ( $\Delta h$ ) between original bathymetry and filtered bathymetry using $\Delta_{tide}$ proxy (a) and $\Delta_{WL}$ proxy (b) for the study period (February 2013 to June 2016) . . . . .	57
3.7	Data processing scheme for water levels estimation. . . . .	61
3.8	Evolution of the correlation coefficients between video and field/altimetry data . . . . .	62
3.9	Comparison of video-derived water levels with time series of tide derived from the ADCP, the Cotonou tide gauge, and the FES2014 model . . . . .	63
3.10	Comparison of video (black), SSALTO/DUACS (red), and CTOH X-TRACK (blue) monthly derived sea level anomalies . . . . .	63

3.11	Tidal constituents derived with the Python version of the Utide software from video (black), Cotonou tide gauge (red), and FES2014 (blue) data. . . . .	64
4.1	Monthly-averaged video estimates (black) and Wavewatch III data (red) . . . . .	73
4.2	Time series of $H_s$ , and along-shore-averaged location $\langle X_s \rangle$ from the tower of camera location . . . . .	75
4.3	Ensemble-averaged evolution during the wave event and post-event recovery period	75
4.4	Seasonal variability (monthly average) of: (a) $H_s$ , (b) $T_m$ , (c) wave direction (Dir), and (d) wave events intensity in $m^2.h$ (red) and the number of wave events $N_s$ (blue) . . . . .	76
4.5	Monthly average seasonal variability: (a) mean shoreline location $\langle X_s \rangle$ from video camera location, and (b) beach slope . . . . .	76
4.6	Ensemble-averaged shoreline variation $\langle \Delta X_j \rangle$ during and after wave events . .	77
4.7	Study site. (a) Bight of Benin, West Africa, Gulf of Guinea. (b) Video camera system deployed on a tower made available by the Beninese Navy at Grand Popo. (c) Average beach profile. . . . .	81
4.8	Intra-seasonal variations in sea level anomalies $SLA_i$ and wave height $H_{si}$ . . . . .	82
4.9	Ensemble-averaged evolution over intra-seasonal events and morphological changes	84
4.10	Ensemble-averaged evolution over intra-seasonal events and morphological changes	85
5.1	Shoreline change rates and net change in the Bight of Benin between 1990 and 2015	91
5.2	Maps of shoreline change in the Bight of Benin for the four individual intervals of analysis, and Hovmöller diagram of the spatio-temporal change pattern . . . . .	93
5.3	Shoreline change rates in the Bight of Benin over the intervals of analysis between 1990 and 2015 . . . . .	94
5.4	EOF modes of shoreline change in the Bight of Benin from 1990 to 2015 . . . . .	95
5.5	Schematic morphology and cell dynamics downdrift of the mouth of the Volta delta and and shoreline changes between 1990 and 2015 . . . . .	97
6.1	Grid reference (0, X, Y) used to model the shoreline evolution in the Bight of Benin together with the locations of wave input stations (1 to 8) with wave roses and of the main cities in the bight. . . . .	104
6.2	Calculated mean annual net longshore sediment transport rate along the study area in the Bight of Benin for the calibration period from 2000 to 2010. . . . .	106
6.3	The initial shoreline (black line) at year 2000 together with the modelled and observed shorelines at 2010 (grey lines, respectively), as well as the modelled and observed shoreline change represented with dots ( $\Delta Y_{mod}$ and $\Delta Y_{obs}$ , respectively). 107	107
6.4	Shoreline changes for the areas around the harbors of (a) Lome, (b) Cotonou, and (c) Lagos for the calibration period from 2000 to 2010. . . . .	107
6.5	Comparison of observed (x-axis) and modelled (left y-axis) shoreline changes for the calibration (2000-2010) and validation (2010-2015) periods. . . . .	108
6.6	Panel above: shoreline changes for the validation period from 2010 to 2015. Panel below: corresponding shoreline changes for the areas around the harbors of (a) Lome, (b) Cotonou, and (c) Lagos. . . . .	109

---

---

6.7	Mean annual net transport rate for the validation period (2010 – 2015) for the cases with (black) and without (red) the harbors at Lagos, Cotonou, and Lomé and inlets. . . . .	110
6.8	Nourishment simulation at Lagos Harbor for the period from 2010 to 2015. . . .	111
6.9	The effect of reduced boundary influx on the shoreline evolution through a multiplier $\alpha$ with different spatial influence determined by a coefficient $\kappa$ . . . . .	112

---



# List of Tables

- 3.1 Comparison of original (h) and filtered depth ( $h_{\Delta_{tide}}$  and  $h_{\Delta_{WL}}$ ) with measured field-depth measured during Grand Popo 2014 from March 11<sup>th</sup> to 19<sup>th</sup>, 2014 . . . 57
- 3.2 Correlations r and RMS differences in video-derived tide AT with the time series of tides derived from the ADCP, Cotonou tide gauge, and FES2014 model . . . . 62
- 3.3 Correlations r and RMS differences between monthly video-derived water-level anomalies with monthly CTOH X-TRACK and monthly SSALTO/DUACS sea level anomalies. . . . . 64
  
- 4.1 Comparison of daily hydrodynamic video data and WW3 model outputs . . . . . 74
- 4.2 Annual averaged values and anomalies ( $R_a$ ) for the study period . . . . . 77



# Acronyms

**ADCP** Acoustic Doppler Current Profiler. [36](#), [54](#), [68](#), [78](#), [115](#), [122](#)

**BoB** Bight of Benin. [2](#), [3](#), [8](#), [30–32](#), [34](#), [35](#), [47](#), [69](#), [78](#), [79](#), [87](#), [90](#), [96–103](#), [105](#), [108](#), [112](#), [114–116](#), [118](#)

**GPP** Grand Popo. [35](#), [47](#), [58](#), [68–70](#), [78](#), [87](#), [116](#), [122](#)



# Introduction

## Motivations

**Issues on West African coasts:** The economic and social pressure on the West African coasts is very marked. 80% of the economic activity of this African sub-region remains concentrated on the coasts ([West African Economic and Monetary Union, 2012](#)), with the three major harbors (Lomé, Cotonou and Lagos) covering much of the trade in the sub-region. More than one third of the population of the West African countries bordering the Gulf of Guinea (Côte d'Ivoire, Ghana, Togo, Benin and Nigeria) live in the coastal zone and is exposed to all coastal hazards, as its density is booming in the large coastal cities. Recent observations and studies ([Laibi et al., 2014](#); [Almar et al., 2015b](#); [Dada et al., 2016](#); [Ngom et al., 2018](#)) have pointed out several disturbances on forcing and shoreline stability in recent decades, increasing risks to properties and people. As the coast is particularly vulnerable to erosion and flooding due to wave climate, sea level rise and the high proportion of soft low-lying coastlines, its stability can be substantially affected by breakwaters in deep-water harbours and groynes ([Laibi et al., 2014](#); [Giardino et al., 2018](#)). To this must be added the action of dams on the main local rivers (Volta and Niger) and the reduction of rainfall, which reduce sediment supply at the coast. Unfortunately, very few local indicators ([Tano et al., 2016](#)) exist to enable decision-makers to consider sustainable solutions for the protection of properties and people of this region. The understanding of the coastline dynamics associated with these processes is still very limited, as they act on different time scales. Waves, storms, tides, currents, river flows and sea level anomalies play an important role in short-term (seasonal to multi-year) coastal morphological changes, while natural and anthropogenic sediment input, relative sea level change, wind transport, land use, gradients in sediment transport along the coasts and climatic variations are often responsible for long-term coastal changes ([Vitousek et al., 2017](#)). Although modelling could provide a better understanding of the dynamics of this region, all models, whether physics-based, process-based or empirical models, inevitably rely on more or less important approximations of complex and multi-scale systems. Thus, as models are by definition not perfect, more data and a better description of nearshore processes are needed for calibration and improvement. In addition, much remains to be done to fully integrate all small-scale processes into large-scale modelling ([Larson et al., 2016](#); [Robinet et al., 2018](#); [Vitousek et al., 2017](#)).

**Tropical sea level variations:** Tropical regions, particularly those in the Gulf of Guinea, are characterized by intra-seasonal and seasonal fluctuations ([Polo et al., 2008](#); [Ding et al., 2009](#)), to which the sea-level rise trend is superimposed. These fluctuations are the result of the combination of forcings and stresses due to global ocean warming and land ice mass transfer, land water storage, ocean circulation, global and regional variations in water density, local effects

of astronomical tides, atmospheric waves and wave transformations in the surf zone (Melet et al., 2016; Slangen et al., 2017). Several studies have explored the relationships between sea level rise and shoreline changes over the past few decades (Le Cozannet et al., 2014). But, the literature on the impact of sea level variations at shorter time scales (intra-seasonal and seasonal) on coastal morphology remains scarce. Measuring total sea level on the coast (Melet et al., 2016) is still difficult as the nearshore is an environment particularly complex and energetic. Satellite altimetry, optimised for the open sea, is not very effective within 25 km of the coast because the continental masses disturb the radar signal (Cipollini et al., 2017), although more can be expected with new approaches (Marti et al., 2019). Tide gauges are limited to deep waters or sheltered harbours and omit some of the total natural sea level variability on open coasts (Melet et al., 2016). The coastal research community therefore needs new and better adapted observational tools to provide accurate measurements of water level on complex and energetic coasts, including all contributions to total sea level.

**Beach morphology and bathymetric changes:** Bathymetry is probably one of the most critical parameters for understanding and modelling the dynamics of coastal processes (Holman et al., 2013). Traditionally, it has been measured in-situ by the time of flight of an acoustic signal reflected from the bottom and generated by echo sounder technology. More recently, new technologies, including video imaging and X-band radar, have made it possible to estimate depths and coastline position continuously and at daily or monthly frequency (Holman et al., 2013; Bergsma and Almar, 2018). However, most of the investigations on the daily and long-term variability of beach morphology remains limited to the shoreline. And more needs to be done to understand the variability of beach profiles in tropical environments characterized by low energy wave and wind conditions. In order to establish at a longer time scale the link between wave forcing, longshore drift and morphological evolution of beach profiles, in situ measurement campaigns (Almar et al., 2014) have been conducted and video cameras installed in West Africa. The oldest video acquisition system in this sub-region was installed in Grand Popo, Benin, in February 2013, as part of the LEFE-EC2CO INSU 2013-2014 project. Will the different data acquired allow analysis of the daily variability of a beach profile with a reasonable acquisition error? Is the understanding of the integrated effects of short-scale processes crucial for large-scale morphological processes?

## Research question and objectives

Waves and tide are classically the two natural forcing studied to understand beach dynamics. Sediment supply (from rivers, beach nourishment) or traps (dikes) have long been known and taken into account when addressing long-term shoreline changes. Several studies have been carried out and are underway to understand and predict the impact of sea-level rise on the coasts, while very little is known about the impact of short-term (daily to annual/inter-annual) changes in sea level. In this thesis, all these natural and anthropogenic factors are considered to understand the dynamics of the tropical beaches of the Gulf of Guinea at different time scales.

The present thesis therefore addresses an essential scientific question: What are the primary drivers of shoreline changes in the [Bight of Benin \(BoB\)](#), Gulf of Guinea ?

---

The main objective is to predict long-term shoreline position and beach state in the BoB, taking into account the long-shore and cross-shore processes simultaneously.

To answer this question, secondary objectives have been identified:

- Quantify the shoreline response to wave forcing at different time scales
- Measure the total sea level at the coast and its impact on shoreline variability
- Identify the main anthropogenic factors affecting shoreline evolution in the BoB
- Model long term shoreline change.

## Methodology

In order to achieve our goals, this thesis work was divided into four parts:

- Formatting and processing of long-term daily data of hydrodynamic and morphological (intertidal and bathymetric profile) parameters of the West African coastline.
- Analysis of the response of the West African coastline to tropical Atlantic multi-scale forcing
- Investigations on the role of coastal infrastructures to beach changes
- Construction of a model for the long-term evolution of the West African coastline

## Organization of the thesis

The organization of the thesis is as follows :

- Chapter 1 presents a review of common knowledge on the main natural oceanic forcing causing shoreline variability, on the techniques for monitoring beach changes and on existing shoreline models based on the longshore and cross-shore sediment transport.
  - Chapter 2 presents the hydrodynamic and morphological characteristics of the coast in the BoB, with particular emphasis on the different data and methods to be used for this thesis.
  - Chapter 3 details the improvements in temporal approach to celerity-based depth inversion method to derive depths and sea level variations at the coast from video imagery.
  - Chapter 4 investigates the behavior of the beach at the Grand Popo pilot site in response to wave forcing from event to interannual scales and to intra-seasonal sea level variations, that are characteristic of this region.
  - Chapter 5 analyses the shoreline mobility and the changes in coastal area in the BoB over the period 1990–2015 using 5 shorelines (1990, 2000, 2005, 2010 and 2015) derived from Landsat images. The dynamics of the different identified cells, the trends and the causes in shoreline mobility are discussed.
  - Chapter 6 presents the development and the implementation of a regional model for shoreline evolution in the Bight of Benin, Gulf of Guinea, taking into account the main factors of shoreline variability.
  - Chapter 7 gives a summary and a perspective of this thesis.
-



# Introduction en Français

## Motivations

**Enjeux sur les côtes de l’Afrique de l’Ouest** : La pression économique et sociale sur les côtes de l’Afrique de l’Ouest est très marquée. 80% de l’activité économique de cette sous-région africaine reste concentrée sur les côtes ([West African Economic and Monetary Union, 2012](#)), avec les trois grands ports (Lomé, Cotonou et Lagos) qui couvrent une grande partie des échanges de la sous-région. Plus d’un tiers de la population des pays d’Afrique de l’Ouest riverains du Golfe de Guinée (Côte d’Ivoire, Ghana, Togo, Bénin et Nigeria) vit dans la zone côtière et est confrontée à tous les aléas du littoral car la croissance démographique est en plein essor dans les grandes villes côtières. Des observations et études récentes ([Laibi et al., 2014](#); [Almar et al., 2015b](#); [Dada et al., 2016](#); [Ngom et al., 2018](#)) ont mis en évidence plusieurs perturbations du forçage et de la stabilité du littoral au cours des dernières décennies, augmentant les risques pour les biens et les personnes. Comme la côte est particulièrement sujette à l’érosion et aux inondations en raison du climat des vagues, de l’élévation du niveau de la mer et de la forte proportion de côtes meubles et basses, sa stabilité peut être grandement affectée par les brise-lames dans les ports et les épis de protection ([Laibi et al., 2014](#); [Giardino et al., 2018](#)). A cela, il faut ajouter l’action des barrages sur les principaux fleuves locaux (Volta et Niger) et la réduction des précipitations, qui réduisent les apports de sédiments à la côte. Malheureusement, très peu d’indicateurs locaux ([Tano et al., 2016](#)) existent pour permettre aux décideurs d’envisager des solutions durables pour la protection des biens et des personnes de cette région. La compréhension de la dynamique du trait de côte associée à ces processus est encore très limitée, car ils agissent à des échelles de temps différentes. Les vagues, les tempêtes, les marées, les courants, les débits fluviaux et les anomalies du niveau de la mer jouent un rôle important dans les changements morphologiques côtiers à court terme (saisonniers à pluriannuels), tandis que l’apport naturel et anthropique de sédiments, la variation relative du niveau de la mer, le transport éolien, l’utilisation des terres, les gradients de transport de sédiments le long des côtes et les variations climatiques sont souvent responsables des changements côtiers à long terme ([Vitousek et al., 2017](#)). Bien que la modélisation puisse permettre de mieux comprendre la dynamique de cette région, tous les modèles d’évolution du trait de côte, qu’ils soient basés sur la prise en compte de la physique, des processus ou des modèles empiriques, reposent inévitablement sur des approximations plus ou moins importantes de systèmes complexes à plusieurs échelles temporelles. Ainsi, comme les modèles ne sont par définition pas parfaits, il faut davantage de données et une meilleure description des processus littoraux pour les calibrer et les améliorer. En outre, il reste beaucoup à faire pour intégrer pleinement tous les processus à petite échelle dans la modélisation à grande échelle ([Larson et al., 2016](#); [Robinet et al., 2018](#); [Vitousek et al., 2017](#)).

**Variations tropicales du niveau de la mer :** Les régions tropicales, en particulier celles du Golfe de Guinée, sont caractérisées par des fluctuations intra-saisonniers et saisonniers (Polo et al., 2008; Ding et al., 2009), auxquelles se superpose la tendance à l'élévation du niveau de la mer. Ces fluctuations sont le résultat d'une combinaison de forçages et de contraintes dus au réchauffement global des océans et au transfert de masse de glace terrestre, au stockage des eaux terrestres, à la circulation océanique, aux variations globales et régionales de la densité de l'eau, aux effets locaux des marées astronomiques, aux vagues atmosphériques et aux transformations des vagues dans la zone de déferlement (Melet et al., 2016; Slangen et al., 2017). Plusieurs études ont exploré les liens entre la montée du niveau de la mer et les variations du trait de côte au cours des dernières décennies (Le Cozannet et al., 2014). Mais, la littérature sur l'impact des variations du niveau de la mer à des échelles de temps plus courtes (intra-saisonniers et saisonniers) sur la morphologie côtière reste limitée (Melet et al., 2016). La mesure du niveau total de la mer sur la côte est encore délicate, car le littoral est un environnement particulièrement complexe et énergétique. L'altimétrie satellitaire, optimisée pour la haute mer, n'est pas très efficace à moins de 25 km des côtes car les masses continentales perturbent le signal radar (Cipollini et al., 2017), bien que l'on puisse s'attendre à plus avec les nouvelles approches (Marti et al., 2019). Les marégraphes sont limités aux eaux profondes ou aux ports protégés par des digues et omettent une partie de la variabilité naturelle totale du niveau de la mer (Melet et al., 2016). La communauté scientifique littorale a donc besoin de nouveaux outils d'observation mieux adaptés pour fournir des mesures précises du niveau de l'eau sur des côtes complexes et énergétiques, y compris toutes les contributions au niveau total de la mer.

**Morphologie de la plage et variations bathymétriques :** La bathymétrie est probablement l'un des paramètres les plus critiques pour la compréhension et la modélisation de la dynamique des processus côtiers (Holman et al., 2013). Traditionnellement, elle a été mesurée in situ par le temps de propagation d'un signal acoustique réfléchi par le fond et généré par un échosondeur. Plus récemment, de nouvelles technologies, notamment l'imagerie vidéo et le radar en bande X, ont permis d'estimer les profondeurs et la position du trait de côte en continu et à une fréquence quotidienne ou mensuelle (Holman et al., 2013; Bergsma and Almar, 2018). Cependant, la plupart des études sur la variabilité quotidienne et à long terme de la morphologie des plages restent limitées au trait de côte. Et il faut faire davantage pour comprendre la variabilité des profils de plage dans les environnements tropicaux caractérisés par des conditions de vagues et de vents de faible énergie. Afin d'établir sur une plus longue échelle de temps le lien entre le forçage des vagues, la dérive littorale et l'évolution morphologique des profils de plage, des campagnes de mesures in situ (Almar et al., 2014) ont été menées et des caméras vidéo installées en Afrique de l'Ouest. Le plus ancien système d'acquisition vidéo de cette sous-région a été installé à Grand Popo, au Bénin, en février 2013, dans le cadre du projet LEFE-EC2CO INSU 2013-2014. Les différentes données acquises permettront-elles d'analyser la variabilité quotidienne d'un profil de plage avec une erreur d'acquisition raisonnable? La compréhension des effets intégrés des processus à courte échelle est-elle cruciale pour les processus morphologiques à grande échelle?

## Questions et objectifs de la recherche

Les vagues et la marée sont classiquement les deux forçages naturels étudiés pour comprendre la dynamique des plages. L'apport de sédiments (rivières, recharge des plages) ou les barrières (digues) sont connus depuis longtemps et pris en compte lors de l'étude des changements à long terme du littoral. Plusieurs études ont été réalisées et sont en cours pour comprendre et prévoir l'impact de l'élévation du niveau de la mer sur les côtes, bien que l'on sache très peu de choses sur l'impact des changements à court terme (journalier à annuel/interannuel) du niveau de la mer. Dans cette thèse, tous ces facteurs naturels et anthropiques sont pris en compte pour comprendre la dynamique des plages tropicales du Golfe de Guinée à différentes échelles de temps.

Cette thèse aborde donc une question scientifique clé : Quels sont les principaux facteurs contribuant à la variabilité du trait de côte dans la Baie du Bénin, Golfe de Guinée ?

L'objectif principal est de prédire à long terme la position du trait de côte et la morphologie des plages de la Baie du Bénin en Afrique de l'Ouest, en prenant en compte simultanément les processus "long-shore" et "cross-shore".

Pour répondre à cette question, des objectifs secondaires ont été identifiés :

- Quantifier la réponse littorale face au forçage des vagues à différentes échelles de temps
- Mesurer le niveau d'eau total à la côte et son impact sur la variabilité morphologique du littoral
- Identifier les principaux facteurs anthropiques affectant l'évolution du trait de côte dans la Baie du Bénin
- Modéliser à long terme l'évolution du trait de côte

## Méthodologie

Afin d'atteindre nos objectifs, ce travail de thèse a été découpé en trois parties :

- Mise en forme et traitement des données journalières long terme des paramètres hydrodynamiques et morphologiques (profil intertidal et bathymétrique) du littoral Ouest Africain
- Analyse de la réponse du littoral Ouest Africain face au forçage multi-échelle de l'Atlantique tropicale
- Investigations sur le rôle des infrastructures côtières dans les changements morphologiques de plage
- Construction d'un modèle d'évolution long terme du littoral Ouest Africain

## Organisation de la thèse

L'organisation de la thèse est la suivante :

- Le chapitre 1 est un résumé de l'état des connaissances sur les principaux forçages océaniques naturels à l'origine de la variabilité du littoral, sur les techniques d'observation des variations morphologiques des plages et sur les modèles de trait de côte existants basés sur le transport sédimentaire.
-

- Le chapitre 2 présente les caractéristiques hydrodynamiques et morphologiques de la côte dans le BoB, avec un accent particulier sur les différentes données et méthodes à utiliser dans cette thèse.
  - Le chapitre 3 détaille les améliorations apportées à l'approche temporelle de la méthode d'inversion basée sur la célérité pour estimer les profondeurs et les variations du niveau de la mer à la côte à partir de l'imagerie vidéo.
  - Le chapitre 4 étudie le comportement de la plage sur le site pilote de Grand Popo en réponse au forçage des vagues de l'échelle événementielle aux échelles interannuelles, et aux variations intra-saisonniers du niveau de la mer, qui sont caractéristiques de cette région.
  - Le chapitre 5 analyse la variabilité du trait de côte et les changements dans la zone littorale dans la Baie du Bénin sur la période 1990-2015 en utilisant 5 lignes de côte (1990, 2000, 2005, 2010 et 2015) estimées à l'aide d'images Landsat. La dynamique des différentes cellules identifiées, les tendances et les causes de la mobilité du littoral sont examinées.
  - Le chapitre 6 présente l'élaboration et la mise en œuvre d'un modèle d'évolution du trait de côte dans la Baie du Bénin, Golfe de Guinée, prenant en compte les principaux facteurs de variabilité du littoral.
  - Le chapitre 7 donne un résumé et une perspective de cette thèse.
-

# Chapter 1

## Background

### Contents

---

<b>1.1</b>	<b>Introduction</b>	<b>9</b>
<b>1.2</b>	<b>Contributors to beach changes</b>	<b>10</b>
1.2.1	Waves and beach morphology	10
1.2.2	Storms	13
1.2.3	Wave-induced currents and undertow	15
1.2.4	Sediment budget	16
1.2.5	Sea level variations at the coast	17
<b>1.3</b>	<b>Measuring beach changes and profile</b>	<b>20</b>
1.3.1	Several techniques for measuring beach morphology	21
1.3.2	Altimetry and video for continuous coastal monitoring	21
<b>1.4</b>	<b>Shoreline model review</b>	<b>22</b>
1.4.1	Modeling shoreline changes driven by longshore transport	22
1.4.2	Modeling shoreline changes driven by cross-shore transport	24
1.4.3	Longshore and cross-shore integrated model	27
<b>1.5</b>	<b>Conclusion</b>	<b>30</b>

---

### 1.1 Introduction

The coastal zone defined as the interface between the water and the land adapts its morphology to wave, sea level, sediment budget and anthropogenic conditions. This chapter gives a brief overview of common knowledge on the factors that control changes on wave-dominated beaches and on the tools used for monitoring and modeling beach morphology. First a literature review is done on the main contributors to beach changes, including sea level at the coast (section 1.2). Section 1.3 lists the various techniques used in the literature to monitor beach morphology. Particular emphasis is given to advances in the processing of video images for shoreline and bathymetry estimation. Finally, a state of the art in shoreline evolution models (section 1.4) for predicting beach conditions examines the characteristics of existing empirical and one-line coastline models.

## 1.2 Contributors to beach changes

### 1.2.1 Waves and beach morphology

#### Waves

Waves are generally described by wave height  $H$ , period  $T$  and direction, which depend on wind speed, duration, fetch and water depth in the wave generation area (Dean and Dalrymple, 2004). There are generally two types of waves depending on where they were generated. Wind waves are those generated near the shoreline by local winds. Wind waves are characterized by short periods, wide direction and frequency bands. Swells are waves that are generated remotely during storms and propagate towards the coast where they are observed, regardless of local wind conditions. As waves propagate, shorter wavelengths dissipate faster. Swell waves that reach the coast present longer periods than wind waves and narrow frequency bands.

As waves propagate towards the coast, they undergo several transformations mainly due to the decrease in depth: shoaling (Dean and Dalrymple, 2004; Holthuijsen, 2010), breaking (Komar, 1999; Masselink and Hughes, 2014; Holthuijsen, 2010), refraction (Dean and Dalrymple, 2004), reflection (Dean and Dalrymple, 2004; Holthuijsen, 2010) and diffraction (Holthuijsen, 2010; Masselink and Hughes, 2014). The wave celerity  $C$  is then given as a function of wavelength (or period) and water depth (Dingemans, 1997):

$$C = \sqrt{\frac{gL}{2\pi} \tanh\left(\frac{2\pi d}{L}\right)} \quad (1.1)$$

where  $g$  is the gravitational acceleration  $9.81 \text{ m/s}^2$ ,  $L$  is wavelength in meters and  $d$  is the water depth in meters.

An additional term must be added to equation 1.1, representing the mean current contribution, which depends on the direction of the mean current compared with that of the waves. This term is typically neglected on wave-dominated beaches for practical reasons, as suggested by Bergsma and Almar (2018).

In deep water, i.e.  $d/L \geq 1/2$ , the wave speed is approximated by (Lamb, 1994):

$$C_\infty \approx \frac{gT}{2\pi} \quad (1.2)$$

In shallow water, i.e.  $d/L \leq 1/25$ , the wave speed approximates to (Lamb, 1994):

$$C \approx \sqrt{g \cdot h} \quad (1.3)$$

In transitional water (depths between deep water and shallow water), i.e.  $1/25 < d/L < 1/2$ , the wave velocity is given by (Lamb, 1994):

$$C = C_\infty \cdot \tanh\left(\frac{2\pi d}{L}\right) \quad (1.4)$$

#### Beach morphology under wave conditions

Beaches are deposited accumulations of sediment located at the shoreline and their morphology depend on specific parameters: incident wave energy, wind, sediment type and input, sea bed morphology (Short, 2012). Under equilibrium conditions, these parameters are in balance

and although there is motion of the individual sand grains under even low wave activity, the profile remains more or less static. Cross-shore sediment transport occurs when hydrodynamic conditions within the nearshore zone change, thereby modifying one or more of the parameters resulting in an imbalance and thus causing transport gradients and profile change. Based on the assumption of beaches in "equilibrium" with wave climate, limited number of morphological classifications have been described in the literature. [Gourlay \(1968\)](#) presented a dimensionless environmental parameter  $\Omega$  which depends on site grain size and wave forcing, and led to the classification of sandy beaches into three states : reflective ( $\Omega < 1$ ), intermediate ( $1 < \Omega < 6$ ) and dissipative ( $\Omega > 6$ ).

$$\Omega = \frac{H_b}{T \cdot w_s} \quad (1.5)$$

with  $H_b$  the significant wave height at breakpoint,  $T$  wave's period and  $w_s$  sediment fall velocity.

Later, several studies ([Wright and Short, 1984](#); [Lippmann and Holman, 1990](#); [Short and Aagaard, 1993](#); [Hegge et al., 1996](#); [Short, 1999](#); [Tran, 2018](#)) have described the diversity of "intermediate" beaches in four sub-states (Fig. 1.1) :

- Longshore Bar and Trough (LBT):  $\Omega \approx 2$ ;
- Rhythmic Bar and Beach (RBB):  $\Omega \approx 3$ ;
- Transverse Bar Rip (TBR):  $\Omega \approx 4$ ;
- Low Tide Terrace (LTT):  $\Omega \approx 5$ .

These four sub-states depend mainly on the sand bar position, from the most offshore position for the most dissipative state to a bar connected to the beachface for the reflective state. All of these conceptual models of beach states are based on observations showing strong correlations between beach sedimentology and wave's processes.

Morphological variability on a single beach, investigated from time series of beach state, most of the times suggests that beach state is strongly reliant to varying waves ([Brander, 1999](#); [Costas et al., 2005](#); [Jimenez et al., 2008](#); [Senechal et al., 2008](#); [Pianca et al., 2015](#)). However, there is a fundamental difference between validation studies based on temporal data and those based on spatial data. In the latter case, investigations tend to highlight the importance of factors specific to the study area, such as geology ([Jackson et al., 2005](#)) and wave height variability ([Gomez-Pujol et al., 2005](#)). In addition, the concept of an equilibrium beach profile has been criticized because natural forces that affect equilibrium are constantly changing with varying tides, waves, currents and winds. And this concept may have limitations in certain geological contexts (e.g. close bedrock and perched beaches). Nevertheless, at a macroscale level, it has been demonstrated that an equilibrium profile can be approached, in which no significant systematic net sand transport occurs, although small perturbations still remain ([Larson and Kraus, 1989](#)). The concept of "equilibrium based response" is one of the most valuable tools for the coastal engineer to provide a framework to explain beach and shoreline response to changes in incident wave conditions on cross-shore transport dominated sites.

for taking into account imbalance and thus the transverse transport of sediments ([Splinter et al., 2014](#)). And, many useful and powerful conceptual and design relationships for cross-shore sand transport are based on equilibrium profiles ([Yates et al., 2009](#); [Davidson et al., 2013](#); [Castelle et al., 2014](#)).

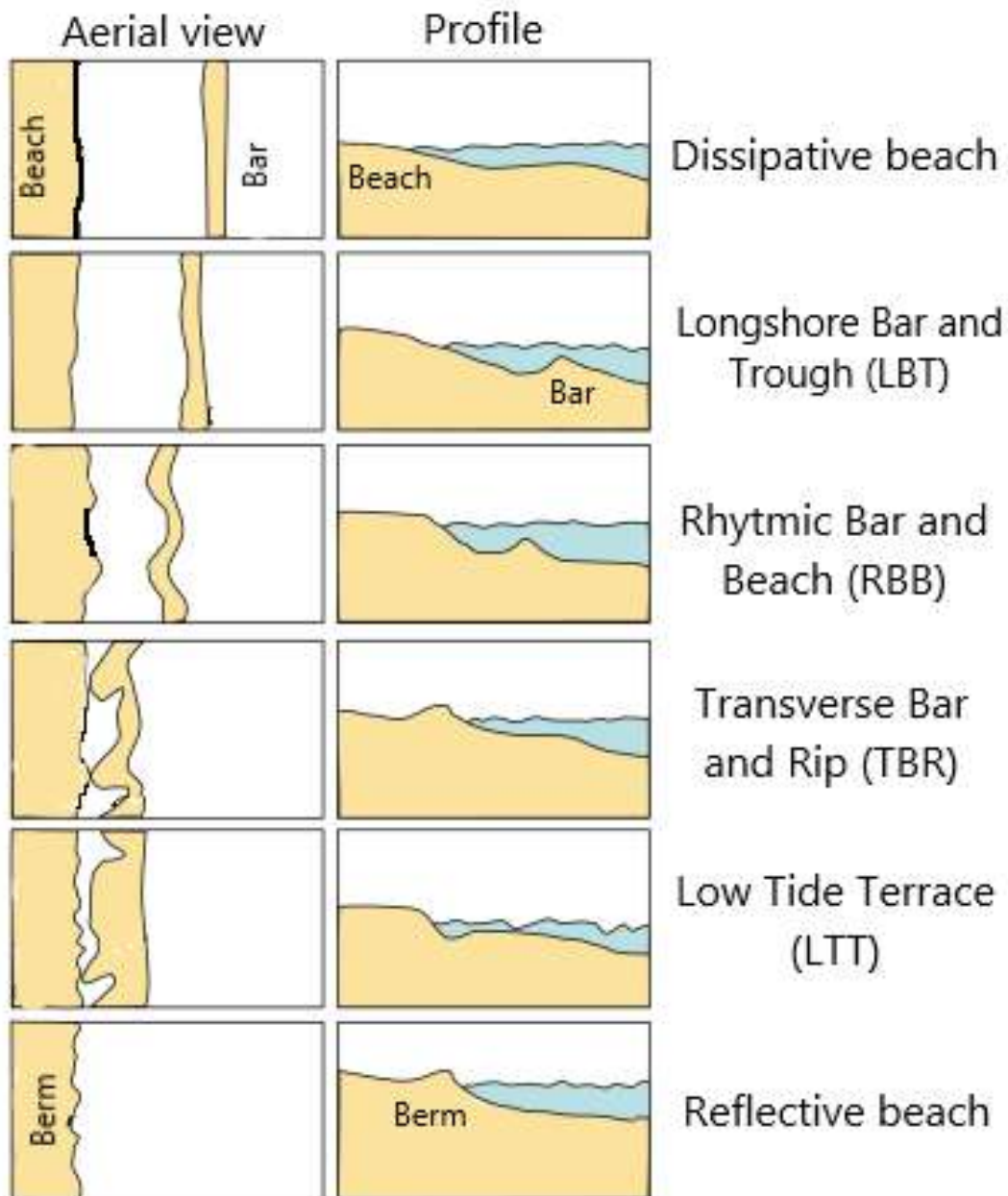


**Figure 1.1** – Beaches classification. Six states : Dissipative, intermediate (LBT, RBB, TBR and LTT), and reflective. Adapted from [Short and Aagaard \(1993\)](#) and [Short \(1999\)](#)

### 1.2.2 Storms

Harley (2017) defined a coastal storm as "a meteorologically-induced disturbance to the local maritime conditions (i.e. waves and/or water levels) that has the potential to significantly alter the underlying morphology and expose the backshore to waves, currents and/or inundation".

#### Coastal storm detection

Statistical approaches to identifying coastal storms on wave-dominated coasts involve the analysis of significant wave height (Hs) timeseries, through the application of the so-called peaks-over-threshold (POT) method (Angnuureng et al., 2017; Harley, 2017). The Hs storm threshold is defined as the critical value that separates storm waves from non-storm waves for a particular coastal site. The storm duration meanwhile is defined by the length of time between an upcrossing and subsequent down-crossing of the storm threshold and a minimum storm duration can be set to only include storm events of a significant duration. A common approach is to set the threshold based on the 95th percentile of the Hs dataset (Masselink and Hughes, 2014; Castelle et al., 2015).

#### Individual storm impact

During a storm event, the beach is observed to evolve dramatically, dominated by surf processes that can rapidly lead to an up-state transition through offshore sediment transport by the undertow and sandbar formation. The storm impacts may vary from minor erosion and overwash of beaches and dunes to widespread erosion and flooding events. The nature of coastal storm response is often based on the storm impact scale proposed by Sallenger (2000), which comprises four wave energy conditions or regimes of increasing hazard of swash, collision, overwash, and inundation; the impact of each depending on the tide + wave + run-up + storm setup heights R relative to the height of the dune toe and crest D (Fig. 1.2).

#### Post-storm recovery duration

After such extreme event, the beach slowly evolves through transient states while recovering under low or moderate energy wave forcing (Splinter et al., 2014; Coco et al., 2014a). There are several ways to define the recovery duration after a storm. It can be defined as the time taken by the beach morphology to evolve from a post-storm state to its modal state, i.e. the most frequently occurring beach state (Ranasinghe et al., 2012b). Another approach, often used, is to consider the time duration taken to reach the first maximum recovery value (of the along-shore-averaged shoreline location), at the end of which the beach is assumed stabilized (Angnuureng et al., 2017). But, this approach contrasts with some existing methods (e.g. using beach state as in Ranasinghe et al. 2012b), as it does not depend on any forcing parameter.

#### Storm clustering and beach response

Initially, two main approaches have been used in the literature to investigate storm impact on the beach : non-cumulative analyses (Coco et al., 2014b; Splinter et al., 2014) and cumulative storms analysis (Karunaratna et al., 2014; Ferreira, 2005a). In the latter case, the erosional response to clusters of storms is generally much larger than the sum impact of the individual storms in the former case. The term "cluster" is still nowadays not commonly used in the

---

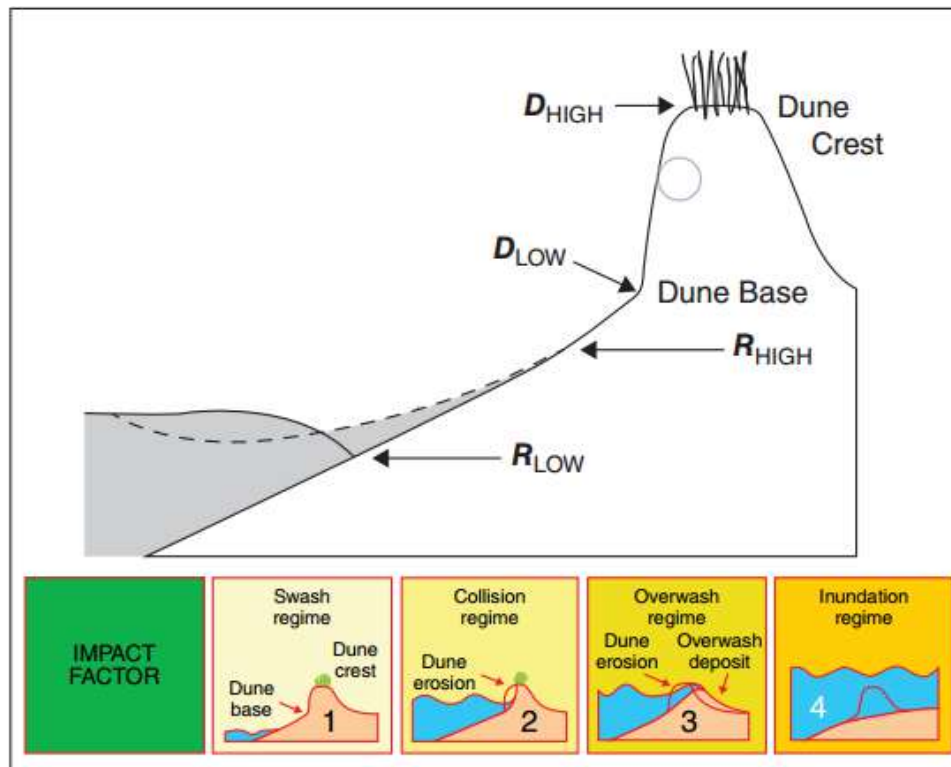


**Figure 1.2** – storm impact scale on barrier islands: (1) Swash regime: wave run-up confined to beach, temporary erosion, offshore sediment transport followed by non-storm return and no net change to the system. (2) Collision regime: wave run-up exceeds the elevation of the base of the dune, run-up collision causes erosion and net, or (semi-) permanent dune retreat. (3) Overwash regime: wave run-up exceeds the dune elevation or beach berm, overtopping transports sand landward to produce net change and landward barrier migration of the order of 100 m. (4) Inundation regime: combined wave run-up and storm surge exceeds elevation of low seaward dune to inundate entire beach; if barrier is also narrow, entire island may be inundated; results in net change and barrier migration landward of the order of 1,000 m (figure by Ciavola et al. 2015)

nearshore community, because of the lack of clear definition (Senechal et al., 2017; Karunarathna et al., 2014). In the literature, authors might sometimes use the terms storm groups (e.g. Ferreira 2005b) or sequence of storms (e.g. Coco et al. 2014b; Castelle et al. 2015). Senechal et al. (2017) noted that the term "cluster" may refer to a sequence of coastal storm events separated by a small time interval. A much-used approach (but not recommended) is to consider that this time interval should be less than the beach recovery duration for individual storms (Senechal et al., 2015).

Today's literature agrees that the rate of shoreline migration under a storm depends on the disequilibrium between the storm energy and previous beach state, and the beach constantly trying to reach a new equilibrium under varying waves (Angnuureng et al., 2017). This was evidenced by the emergence of equilibrium-based semi-empirical shoreline models (Yates et al., 2009; Davidson et al., 2013; Castelle et al., 2014). The equilibrium approach raises the importance of the so-called beach "memory effect" that suggests the present beach state is determined by the recent history of both the wave conditions and the beach morphology (Wright et al., 1985). Models based on this concept have been successfully used for a wide range of sites worldwide to hindcast shoreline erosion during a sequence of storms for cross-shore transport-dominated sandy coastlines (Splinter et al., 2014). Dodet et al. (2019) showed that these models work well

on cross-shore transport but non-surprisingly failed on beaches with other driving processes (*e.g.* longshore drift gradients, sediment sink). The models also reproduce the fact that sequences of storms are increasingly ineffective in eroding the beach over time as the beach reaches a new equilibrium with the prevailing high-energy wave conditions.

### 1.2.3 Wave-induced currents and undertow

Waves approaching the shoreline cause secondary fluid motions such as undertow and wave-induced currents, namely longshore and rips currents. All have the potential to contribute to sediment transport and lead to complex horizontal beach structures (Castelle, 2004).

#### Longshore currents

When the incidence of the swell is oblique, the waves induce a longshore current (Church and Thornton, 1993; Reniers and Battjes, 1997; Lippmann and Thornton, 1995; Kuriyama and Nakatsukasa, 2000) that can move large volumes of sediment from one location to another along the coastline. The amount of sediment transported by longshore currents is known as the littoral drift. Longshore current velocity depends primarily on the angle of the wave crest to the shoreline. But, the volume rate of flow of the current and transport rate depend on the breaker height (CERC, 1984). Longshore current velocity varies both across the surf zone and in the longshore direction (CERC, 1984). There are several formulations for the calculation of the longshore sediment transport associated with longshore current, *e.g.* of three of the most widely used: the Coastal Engineering Research Center CERC (CERC, 1984), Kamphuis (Kamphuis, 1991), Bayram (Bayram *et al.*, 2007).

#### Rip currents

In the review by Castelle *et al.* (2016), rips currents are defined as "narrow and concentrated seaward-directed flows that extend from close to the shoreline, through the surf zone, and varying distances beyond". Rip current flows are driven by alongshore variations in alongshore variations in breaking wave height that result from a number of different causes among which are the alongshore-variable surf-zone bathymetry, the wave energy focusing enforced by wave refraction over offshore bathymetric anomalies and the wave shadowing by a rigid boundary. Rip currents contribute to cross-cutting bars and thus to the instability of the bars along the coast, creating important sedimentary exchanges between surf zone and deep water. Rip currents can driven by swash processes, usually leading to small-scale rips (Castelle *et al.*, 2016). In the surf-zone, Castelle *et al.* (2016) described six fundamental surf-zone rip current types based on the dominant controlling forcing mechanism. Hydrodynamically-controlled rip currents (shear instability rips and flash rips) are spatially and temporally variable in occurrence and exist solely due to hydrodynamic forcing mechanisms. Bathymetrically-controlled rip currents (channel rips and focused rips) are, for a given wave regime and tidal elevation, relatively persistent in space and time. Boundary controlled rip currents (Shadow rips and Deflection rips) are dominated by the influence of rigid lateral boundaries, such as natural headlands or anthropogenic structures (groynes, jetties), on their hydrodynamic forcing.

---

## Undertow

The undertow is caused by shoreward movement of water and setup. The water that piles up at the shoreline is returned along the bottom (Davidson-Arnott, 2010a). The undertow can induce intense sediment transport offshore, especially during storms. This can expose the beach to erosion and cause significant movement of bars perpendicular to the shoreline.

### 1.2.4 Sediment budget

According to Davidson-Arnott (2010a) and Rosati (2005), the littoral sediment budget is a technique for estimating the amount of all inputs (called sources) and outputs (sinks) of sediment to a stretch of shoreline, in order to assess its long-term variability (interannual to decades).

#### Littoral cell

The coastal zone can be seen as a morphodynamic system composed of various sub-areas (cells), each with its own spatial and temporal scales. A sediment cell operates with alongshore wave energy gradients coupled with sediment availability (Davidson-Arnott, 2010a). The shoreline erodes under negative longshore sediment balance, and advances when the sediment balance is positive.

The concept seems to have been applied first to the California coast (Inman and Frautschy, 1966; Bowen and Inman, 1966). In the Bight of Benin, West Africa, this concept has been applied by Laibi et al. (2014) and Anthony et al. (2019) to understand the erosion trend affecting the entire coast of this region. Littoral cells may often be largely isolated from adjacent one with boundaries such as headlands that are easily demarcated and cells. However, there can be exchange of sediment between adjacent littoral cells as the boundaries between them may be quite fuzzy, unlike coastal compartments. Littoral cell boundaries can be convergent, divergent or interruptive and it is possible to recognise sub-cells within major littoral cell units.

Before collecting information on sediment inputs, the starting point for the determination of a littoral sediment budget might be the identification of the cells and direction of net longshore sediment transport (Davidson-Arnott, 2010a). This approach provides a systematic framework for research on coastal processes and coastal evolution, and for the establishment of coastal management plans (Davidson-Arnott, 2010a).

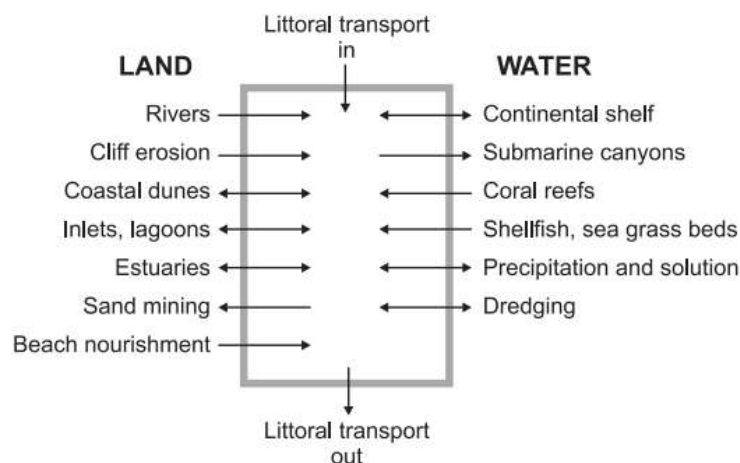


**Figure 1.3** – Sources and sinks for a littoral sediment budget (figure by Davidson-Arnott 2010a).

## Sediments sources and sinks

Inputs from rivers are probably the most important source, followed by cliff erosion, and in the tropics biogenic inputs from coral reefs may dominate. Many rivers around the world release large amounts of sediment at the coast. Although river bed transport is still difficult to measure, there are a number of good predictive equations for the total sediment discharges, e.g. [Logah et al. \(2017\)](#) for Volta river in the Bight of Benin. It is then easy to obtain an estimate of the order of magnitude of supply. However, this requires accurate measurements of sediment concentrations and river flows in the water column before the mouth. Other natural sources of sediment (dunes, inlets, lagoons, etc.) will be less important depending on the study site. In addition to the natural sources, human actions can have also contribute through activities such as jetty and seawall construction, and through dredging, beach mining and beach nourishment (Fig. 1.3).

### 1.2.5 Sea level variations at the coast

Understanding large-scale coastal evolution requires consideration of the sediment budget and sea-level changes as the dichotomy between their respective roles in coastal evolution becomes blurred when they are weak and act in tandem (see [Roy and Thom \(1994\)](#), p.169). This section details the latest advances in understanding sea level dynamics on the coast.

#### Global mean sea level

Since mid- and late 19th century, tide gauges have been used to measure mean sea level along continental and island coasts ([Cazenave and Le Cozannet, 2013](#)). Since the early 1990s, high-precision altimetry satellites have been providing regular measurements (orbital cycle of a few days to a few weeks) with almost global sea level coverage: Topex/Poseidon (1992-2006), Jason-1 (2001-2013), Envisat (2002-2011), Jason-2 (2008-), Cryosat-2 (2010-), HY-2A (2011-), SARAL/Altika (2013-), Sentinel-3A (2016-), Jason-3 (2016-), CFOSAT (2018-), Sentinel-3B (2018-). Tide gauges measure relative sea level variations with respect to the ground, while satellite altimetry measures "absolute" sea level variations in a geocentric reference frame ([Cazenave and Le Cozannet, 2013](#)).

Direct observations of sea level available from tide gauges and satellites show that sea level is rising ([Jevrejeva et al., 2008](#); [Nerem et al., 2010](#); [Mitchum et al., 2010](#); [Church et al., 2011](#)). And it has doubled in the last two decades compared to the average rise in the 20th century as observed by [Merrifield et al. \(2009\)](#). They suggested that this cannot be attributed to decadal variations but rather reflects a recent acceleration in the global average rise (since the early 1990s). The main factors behind this rise in global mean sea level are the thermal expansion of sea water due to ocean warming, land ice loss and fresh water mass exchange between oceans and land water reservoirs. These contributions vary according to natural climate variability and global climate change induced by anthropogenic green house gas emissions ([Cazenave and Le Cozannet, 2013](#)).

Satellite altimetry has also revealed that sea level is not rising uniformly ([Cazenave and Le Cozannet, 2013](#)). Observations show that the rate of rise displays strong regional variations ([Lombard et al., 2005](#); [Meysignac and Cazenave, 2012](#)). Observed spatial patterns in sea level trends mainly result from changes in the density structure of the oceans associated with temperature, wind stress and salinity variations ([Bindoff et al., 2007](#)). The largest contribution comes

---

from ocean temperature variations, except for the Arctic region. Salinity also plays a role (in particular in the Arctic) and, in many regions, partly offsets thermal expansion (Wunsch et al., 2007; Stammer et al., 2013). Tropical climate modes are often responsible of sea level variations at seasonal and interannual while coastally-trapped waves can be caused by wind stress variability, atmospheric disturbances and variations in the intensity of oceanic currents (Polo et al., 2008; Ding et al., 2009).

Future projections based on physical processes indicate that global average sea level will almost certainly accelerate during the 21st century (Church and al., 2013). However, the magnitude of this rise and its spatial variations remain uncertain due to uncertainties related to GHG emissions. In addition, the representation of climate change by more or less approximate models (due to the uncertainty inherent in the chaotic nature of climate variability) is still a scientific issue. Meyssignac et al. (2017) studied regional sea level variations between 1900 and 2015 using a set of 12 climate model simulations. Their results showed that coastal tide gauge records contain contributions from many coastal and local processes that are either absent from the climate models or not properly resolved by them. These processes include wind-trapped coastal waves, local flooding, the hydrological influence of nearby river flows, and others. This remains an important issue, as coastal communities need reliable projections to prepare adaptation plans for future sea-level rise (Slangen et al., 2017; Meyssignac et al., 2017).

### Local and short-term contributors to sea level at the coast

Variations in total water levels at the coast result from the superposition of variations in global mean sea level, regional sea level and local sea level (McInnes et al., 2016; Melet et al., 2016, 2018a; Slangen et al., 2017). As indicated in the previous section, changes in global mean sea level are driven by ocean global warming and the transfer of water mass from the cryosphere and land to the ocean. Regional-scale variations are mainly the result of changes in ocean circulation and associated ocean heat, variability in wind stress, atmospheric disturbances and variations in oceanic current intensity, salinity and regional mass distribution. Mass redistribution also leads to geoid changes that further impact regional sea-level variations (Tamisiea, 2011).

Other processes make additional substantial contributions to total water-level changes in the coastal ocean: astronomical tides, atmospheric surges, wind stress, oceanic currents and wave transformations in the surf zone (Melet et al., 2016, 2018a; Slangen et al., 2017). The atmospheric surges can be defined as changes due to surface atmospheric pressure and the displacement of surface waters by the wind, called wind set-up. Wave transformations in the surf zone include wave set-up, which is the time-mean sea-level elevation onshore the wave breaking point due to wave energy dissipation, and swash, which corresponds to the vertical fluctuation of the water line above the still water level induced by individual waves. Wave set-up and swash are particularly responsible for the overtopping or overflowing, occurring when individual waves pass over coastal defences or dunes because of swash, and when the mean water level is greater than the level of the land or defences, respectively, resulting in a continuous spillage of sea water on land (Melet et al., 2016, 2018a). And recent works showed that waves are dominant contributors to extreme sea levels at the coast (Serafin et al., 2017; Rueda and et al., 2017; Vitousek and et al., 2017) and can strongly modify the coastal effects of thermal expansion and land ice loss on coastal water-level changes at interannual-to-multidecadal timescales (Melet et al., 2016, 2018a).

Taking all of these contributions into account, it remains difficult to predict sea level variabil-

ity over shorter periods (season to decade) on the coast (Melet et al., 2016), as little attention has been focused on it. Only few locations in the western equatorial Pacific Ocean are available for statistically based operational prediction schemes of sea level anomalies at of interannual and seasonal scales (Chowdhury et al., 2007; Chowdhury and Guard, 2014). Nevertheless, some work (McIntosh et al., 2015) has shown the capability of physical-based models to address the challenge of providing skillful forecasts of seasonal sea level fluctuations for coastal communities over a broad area.

### Monitoring sea level at the coast

Observations from tide gauges, satellite altimetry and less developed methods such as new radars are essential for sea level monitoring. However, these devices are not adapted to the same environments and does not measure the same sea level components.

- **Altimetry:** Sea level variations are now well quantified by satellite altimeters, both in terms of global mean and geographical distribution. However, satellite altimetry, optimised for the open ocean, is poorly performing at less than 10 km from the coasts because land masses disturb the radar signal (Cipollini et al., 2017). New processing schemes (Marti et al., 2019), combining ALES retracked altimetry data (Passaro et al., 2018a,b) and geophysical corrections dedicated to coastal areas (Birol et al., 2017) allow to get a little closer to the coasts (up to 3 km). But, undergoing transformations of waves and sea level within depths of less than 10 m stil remain out of range.
- **Tide gauges:** There are several technologies used in tide gauges: pressure, acoustic and radar systems (Intergovernmental Oceanographic commission (IOC), 2006). Traditionally, tide gauges around the world have been mainly devoted to tide and mean sea level applications. This implies that any oscillation between wind waves and tides has not been considered a priority, and in fact has not been properly monitored, due to the standard sampling time of more than 5-6 minutes. And most tide gauges are limited to deep water or sheltered harbors and omit part of the natural total sea level variability at open coasts (Melet et al., 2016). The new radar gauges have capabilities to monitor wave contribution to sea level variations, but there is still a challenge in understanding wave effects on these sensors.
- **Field experiments:** One of the best solutions for monitoring water level variations along the continental shelf to the coast remains field experiments. However, intensive nearshore field experiments with high spatial and temporal sampling rates are limited and expensive. Bathymetric surveys with echo sounders are time consuming and often contain data gaps between the bathymetry and the topography, especially in the micro-to mesotidal regimes.

There is still an observational gap in our knowledge of total sea level propagation across the shelf to the shore (Cipollini et al., 2017). One of the objectives of this thesis is to make a contribution to this knowledge gap. This gap is in the region that represents the main interface between our society and the ocean, i.e. the coastal zone. It is therefore very important to be able to link altimetry observations from the open sea to measurements made on the coast (tide gauges, radar, etc.). This generally holds for most major recent studies dealing with sea level at the coast (Melet et al., 2016; Idzanovic et al., 2018a; Birol et al., 2017; Melet et al., 2018a; Marti et al., 2019).

---

## Multi-scale sea level impact at the coast

Sea level rise variations can have significant impacts on coastal zones. The most immediate impact of sea-level rise and local extreme sea level events is the increased risk of coastal flooding and submergence (Nicholls and Cazenave, 2010). Longer-term effects to sea level rise also occur as the coast adapts to new conditions, including increased erosion and saltwater intrusion into groundwater. In particular, sandy beaches are receiving particular attention, due to their potential sensitivity to sea level variations and at least 24% and up to 70% of the world's beaches are already chronically eroding, albeit with large regional and local differences (Le Cozannet et al., 2019). Coastal wetlands such as salt marshes and mangroves will also decline if the sediment supply remains insufficient to keep pace with sea-level rise (Nicholls and Cazenave, 2010). However, the response of coastal systems to sea level rise is highly dependent on local natural and human settings.

There are two main classes of models that can be used to study and predict the impact of sea level rise on the coast: the Bruun rule (and improvements) and the Probabilistic Coastline Recession (PCR). The Bruun rule and its variants are the most commonly used and historical approach to assess sea-level rise impacts on shorelines (Bruun, 1962b; Shand et al., 2013; Le Cozannet et al., 1962; Dean and Houston, 2016; Atkinson et al., 2018). It assumes a landward translation of the beach profile as sea level rises. The PCR model is a recently introduced approach that quantifies sediment losses at the dune toe during storms, as well as the nourishment of the dune by aeolian sediment transport processes between storms (Ranasinghe et al., 2012a). Over multi-decadal timescales, the superimposition of unchanged storms with rising mean sea levels results in more frequent and larger sediment losses in the PCR model. The Bruun rule and the PCR models are not only based on different assumptions regarding the physical processes guiding the response of sandy shorelines to sea-level rise, but they also provide different results (Ranasinghe et al., 2012a; Toimil et al., 2017). For instance, Le Cozannet et al. (2019) showed that for most of the world's beaches, structural uncertainties due to the choice of coastal impact model can be expected to have a significant impact on projections of shoreline change.

There are many studies in the literature on the response of coastlines and beaches to sea level rise (Nicholls and Cazenave, 2010; Cazenave and Le Cozannet, 2013; Le Cozannet et al., 2014; Le Cozannet et al., 2017; Leatherman et al., 2017). But, the literature on the impact of short-term sea level variations (10s-days to years) on coasts is scarce, as it is thought that at these time scales, waves, tides, sedimentary processes, and anthropogenic factors drive beach changes that surpass sea level impact (Stive, 2004; Ranasinghe, 2016). However, the coastal impact of short-term sea level variations may not be negligible and must be taken into account (Komar and Enfield, 1987). But, how they operate in the coastal zone is still a scientific issue (McInnes et al., 2016). There are only a few pioneering studies that showed the importance of short timescale variations in sea level on the coast, e.g. Segura et al. (2018) which studied the impact of seasonal sea level variations on a reef-fringed beach. Such studies are necessary and need to be intensified, especially since coastal environments are very different from one to another. That's part of what's going to be done in this thesis.

### 1.3 Measuring beach changes and profile

The evolution of a beach can be characterized at different time scales, i.e., interannual, seasonal or event scales (Quartel et al., 2008). The main difficulty in understanding and predicting

the response of sandy beaches to natural and anthropogenic forcing is that measuring beach profile at different timescales in an environment as dynamic and complex as the nearshore is difficult. Monitoring coastal morphology from the smallest to the largest scale is essential for a good understanding and prediction of its evolution.

### 1.3.1 Several techniques for measuring beach morphology

As the beach profile is considered to extend from the upper beach to beyond the surf zone, several traditional and new methods can be used to map parts of morphological changes, which include: aerial photographs (e.g., [Dolan et al. \(1983\)](#); [Paine and Kiser \(2012\)](#); [Segura et al. \(2018\)](#)), global positioning system (GPS) surveys (e.g., [Senechal et al. \(2014\)](#); [Castelle et al. \(2014, 2015\)](#)), satellite remote sensing data (e.g., [Teodoro \(2016\)](#); [Yeu et al. \(2018\)](#); [Almeida et al. \(2019\)](#)), Synthetic aperture radar SAR (e.g., [Demir et al. \(2017\)](#); [Wu et al. \(2019\)](#)), light detection and ranging LiDAR system (e.g., [White and Wang \(2003\)](#); [Almeida et al. \(2017\)](#); [Bergsma et al. \(2019a\)](#)), airborne hyperspectral remote sensing (e.g., [Deronde et al. \(2008\)](#); [Klemas \(2013\)](#)), unmanned aerial vehicle UAV system (e.g., [Mancini et al. \(2013\)](#); [Holman and Stanley \(2007\)](#); [Wilkowski et al. \(2017\)](#); [Laporte-Fauret et al. \(2019\)](#)), echo-sounding, sonar sensors (e.g., [Clarke et al. \(1996\)](#); [McIntyre et al. \(2006\)](#)), and video cameras (e.g., [Plant and Holman \(1997\)](#); [Holman and Stanley \(2007\)](#); [Holman et al. \(2013\)](#); [Bergsma and Almar \(2018\)](#)).

Most of these techniques imply that shoreface and bathymetry variations are captured separately or partially; failing to extract such variations simultaneously. In addition, most of these can only be used during measurement campaigns. Only a few allow regular and automatic monitoring of the evolution of the coastline.

### 1.3.2 Altimetry and video for continuous coastal monitoring

During the last decades, progress has been made and it is now possible to regularly monitor and estimate shoreface and bathymetry variations simultaneously, in addition to wave characteristics, from satellite remote sensing ([Almeida et al., 2019](#); [Almar et al., 2019](#)) and video cameras ([Bergsma and Almar, 2018](#)) at high temporal frequency (5-day and 1-day, respectively). Preliminary work that we carried out in Grand Popo already highlighted the possibilities of video cameras in assessing sandy beach dynamics ([Abessolo et al. 2016](#), see Appendix I). It has been shown that a video monitoring system can monitor the morphological and hydrodynamic parameters of the nearshore at high frequency (15 min).

[Boak and Turner \(2005\)](#) summarized the different definitions/techniques for shoreline delineation. Approaches for estimating bathymetry are recent methods of depth inversion with linear dispersion relationship ([Holman and Stanley, 2007](#); [Bergsma and Almar, 2018](#)), non-linear depth inversion ([Catalan and Haller, 2008](#)), extended Boussinesq equations ([Misra et al., 2003](#)) and coupling video models on wave energy dissipation by wave energy dispersion models ([Aarninkhof et al., 2005](#)). In the typical case of depth inversion methods with linear dispersion relationship (most popular), two main approaches exist: a temporal method and a spectral method ([Bergsma and Almar, 2018](#)).

- The spectral method correlates pixel intensity phases at different positions ([Stockdon and Holman, 2000](#); [Plant et al., 2008](#); [Holman et al., 2013](#)). The spectral method ([Plant et al., 2008](#); [Holman et al., 2013](#)) assesses the celerity by deploying a cross-spectral correlation to find the most coherent frequencies which are associated with a cross-shore spectral

phase ramp, hence a wavenumber  $k$  leading to celerity  $C$ . [Holman et al. \(2013\)](#) combined the earlier techniques used in [Stockdon and Holman \(2000\)](#) and [Plant et al. \(2008\)](#) and added a Kalman filter for robustness and error reduction.

- The temporal method correlates time-varying wave signals at different positions to find the best correlation, which is related to the celerity ([Catálan and Haller, 2008](#); [Bergsma and Almar, 2018](#)). No error estimator has yet been implemented for robustness and error reduction. However, recent work ([Bergsma and Almar, 2018](#); [Thuan et al., 2019](#)) has introduced two error proxies that could be used to implement a Kalman filter. The first error proxy ([Bergsma and Almar, 2018](#)) compares two celerity estimates with the cross correlation in the time domain while the second error proxy ([Thuan et al., 2019](#)) compared video-based estimate and direct measurement of tidal amplitudes to provide a quality criterion.

Although satellite images have a low ground resolution (10 m for Sentinel, 30 m for Landsat), they cover large spatial areas (10 to 100 km), while video images, which are limited to distances of less than 1 km, have errors of less than 1 meter. These new tools for measuring and estimating beach profiles will therefore make it possible to highlight sedimentary processes that are poorly known or not yet studied. The challenge of improving these techniques is still relevant and will be addressed in this thesis.

## 1.4 Shoreline model review

In order to understand the behaviour of a stretch of coast under the action of waves (and possibly sea level variations), with variable sedimentary inputs (from rivers or other sources), several models have been developed in the literature.

### 1.4.1 Modeling shoreline changes driven by longshore transport

Longshore shoreline evolution models are based on gradients of the longshore sediment transport rate that change the shape of the coastline, resulting in areas of erosion and accretion ([Larson et al., 2002b](#)). In one-line models, it is assumed that the sole longshore sediment transport is taken into account. One of the main assumptions here is that short-term variations due to storms or rip currents, which tend to act in the cross-coastal direction, are considered as temporary disturbances to the long-term trend of coastal change and can therefore be canceled. The beach profile is assumed to maintain a constant time-averaged form as the sand moves across the profile up to the closure depth, beyond which the beach is inactive, i.e. where no erosion and sedimentation occurs ([Tran, 2018](#)). Based on these assumptions, the beach responds to wave forcing by translating onshore and offshore either in an erosion or accretion sequence and the profile shape remains unchanged (Fig. 1.4). Therefore, the beach change can be only expressed by the shoreline position change, given by equation 1.6 if the nearshore sediment is conserved ([Ashton et al., 2006](#)) :

$$\frac{dS}{dt} = -\frac{1}{h_c} \frac{dQ_x}{dx} \quad (1.6)$$

where  $S(t)$  is the position of the shoreline,  $t$  is time,  $h_c$  the depth below which cross-shore fluxes are negligible compared to the gradients in alongshore fluxes above and  $Q_x$  the volumetric alongshore sediment transport. As previously stated,  $Q_x$  can be computed using [CERC \(1984\)](#);

Kamphuis (1991); Bayram et al. (2007).

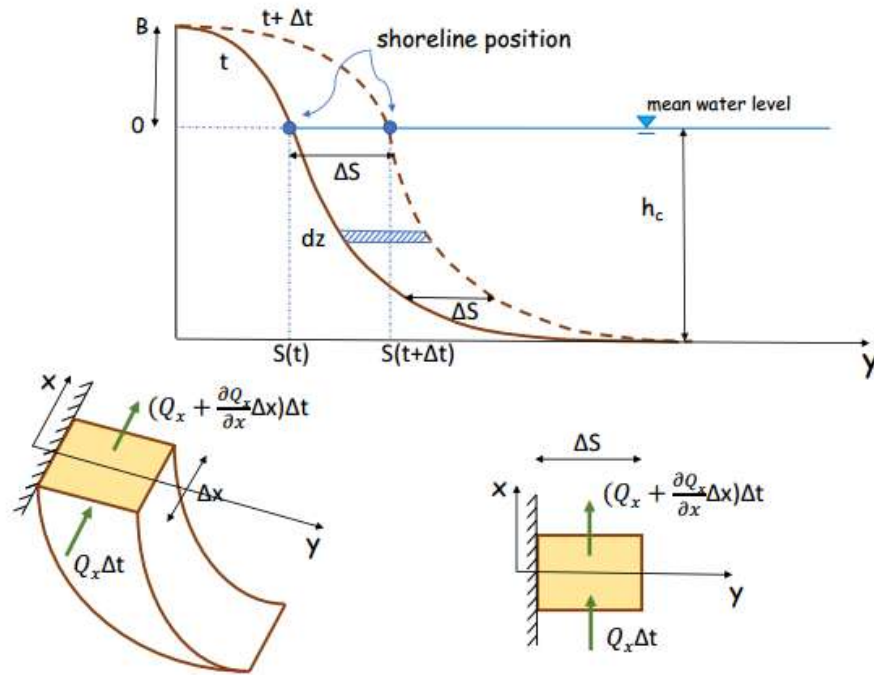


**Figure 1.4** – Sketch of shoreline change due to longshore transport (figure by Tran 2018).

### Genesis model of Hanson (1989)

During the last decades, GENESIS has been used as a standard tool applied by the United States Army Corps of Engineers (USACE), consulting engineering companies, and universities world wide (Hoan, 2010). GENESIS has been used to simulate a wide variety of user-specified offshore wave inputs, initial beach configurations, coastal structures, bypassing operations, and beach fills. The model has been applied at numerous project sites including stretches of coasts in Alaska, California, Louisiana, New Jersey, New York, Texas, and Florida (Chu et al., 1987; Kraus et al., 1988; Gravens et al., 1989; Hanson et al., 1990). GENESIS, which has undergone several phases of development (Kraus et al., 1984; Hanson and Kraus, 1986; Hanson, 1989), is a one-line model with rectilinear cells. Here, the shoreline position changes is predicted over a period of several years and the cross-shore transport effects, such as storm-induced erosion and seasonal changes in shoreline position associated with wave climate, are assumed to cancel over a long simulation period. Input to the model is the nearshore bathymetry and a time series of wave height, period, and direction. Based on these data, the model calculates breaking wave conditions, sediment transport rates using CERC formula, (CERC, 1984) and shoreline positions in rectilinear discretized shoreline cells. Efforts have been made to incorporate into the model sediment transport by tidal currents and/or wind induced current (Hanson et al., 2001, 2006; Bayram et al., 2007). However, there are currently several different versions of the model and it will be very difficult to unify the different improvements of all these versions into one. In addition, the model is only applicable on fairly straight coastlines and where the boundary conditions can be specified, namely, at a groin, jetty, or a uniformly (known) changing shoreline position, which clearly limits its scope (Hoan, 2010).

### The Coastal Evolution Model (CEM) of Ashton et al. (2001)

Ashton et al. (2001), Murray and Ashton (2004) and Ashton et al. (2006) observed that breaking wave heights and angles cannot be considered constant along an undulating coastline, as assumed by the previous models (Hanson, 1989). For example, wave refraction results in small breaking wave angles and causes breaking wave height to vary significantly along a sinuous shoreline. Therefore, extending the concept of previous one-line models, the cellular CEM of Ashton et al. (2001), later refined by Murray and Ashton (2004), integrated a new numerically stable solution scheme to treat the case of high-angle waves, knowing that previous versions assumed small breaking wave angles. The CEM simulates shoreline changes that can generate different types of naturally occurring coastal landforms, including capes, flying spits, and along-shore sand waves. Ashton et al. (2001) observed that longshore sediment transport driven by small angles between the wave crest orientation and the beach orientation smooth the shoreline while large angles result in perturbations of a straight shoreline.

### The model of Hurst et al. (2015)

Hurst et al. (2015) implemented a shoreline evolution model based on a new one-line approach that represents the shoreline as a vector in a cartesian reference frame (Kaergaard and Fredsoe, 2013). The coastline is represented as a series of nodes in Cartesian space  $x$  and  $y$  with subscripts  $i=0,1,2, \dots, n$ , where each nodes is characterized by a local orientation, a cell width and a local shoreface (constant slope extending down to the shoreface depth). To compute efficiently the one-line formulation of recurved coastlines, the model of Hurst et al. (2015) handles coastlines with variable orientation by dividing the shoreline into a series of triangular, trapezoidal, and polygonal cells with known surface area, allowing the mass conservation.

#### 1.4.2 Modeling shoreline changes driven by cross-shore transport

The models presented above have been used in many applications by engineers for the prediction of shoreline position. However, one of their limitations is that short term variations due to storms, rip currents or sea level rise, are considered as temporary disturbances and canceled, while they could result in significant morphological changes. Over the past decades, shoreline models based on cross-shore physical processes have been developed separately to apprehend beach behaviour on shorter time scales, leading to the concept of a beach in equilibrium with wave climate. Equilibrium beach response concepts have been used to model the evolution of beach profiles (Larson and Kraus, 1989), nourishment projects (Dean, 1991), inter-annual variations in the cross-shore location of the sandbar crest (Plant et al., 1999), and shoreline response to sea level rise (Dubois, 1990), storm surges (Kriebel and Dean, 1993), and storms (Miller and Dean, 2004). As the incident wave forcing causes change of the cross-shore profile in time and consequently the shoreline position, a sandy beach tends towards equilibrium if the wave forcing is time invariant. Wright et al. (1985) suggested that for a given beach profile, the forcing that induces no change in shoreline position is called the equilibrium forcing and is represented by the equilibrium Gourlay number  $\Omega_{eq}$ . Wright et al. (1985) assumed that the rate of shoreline change depends on the instantaneous disequilibrium of the wave field  $\Delta\Omega = \Omega_{eq} - \Omega$ . This assumption allowed Miller and Dean (2004) to developed a simple model relating shoreline change to the disequilibrium of the shoreline position, which depends on the wave conditions, water

level (including storm surge, wave setup, and tides), and berm height:

$$\frac{dS(t)}{dt} = K(S_{\text{eq}}(t) - S(t)) \quad (1.7)$$

where  $S(t)$  is the shoreline position in the transect,  $S_{\text{eq}}$  the equilibrium shoreline position,  $t$  is time and  $K$  the rate constant, which can have different values for erosion and accretion and must fulfill simple conditions of beach behavior.

The equilibrium concepts of [Wright et al. \(1985\)](#) and [Miller and Dean \(2004\)](#) form the basis of the most sophisticated and widely used cross-shore shoreline models that were subsequently developed using extensive observations of shoreline location and hourly estimates of the wave field, which resolve even short-lived storms.

### The model of [Yates et al. \(2009\)](#)

The cross-shore model of [Yates et al. \(2009\)](#) uses the energy density  $E = 1/8\rho gH_s^2$  (with  $g = 9.81\text{m}^2/\text{s}$ ) as the descriptor of beach evolution and morphology, with  $E_{\text{eq}}$  the equilibrium wave energy which depends on the initial position of  $S$ . Here, the position of the shoreline  $S(t)$  varies in time according to the instantaneous energy  $E$  and the instantaneous energy disequilibrium  $\Delta E = E - E_{\text{eq}}$  that explicitly included feedback, instead of  $S_{\text{eq}}(t) - S(t)$  as assumed by [Miller and Dean \(2004\)](#):

$$\frac{dS}{dt} = C^\pm E^{1/2} \Delta E \quad (1.8)$$

where  $C^\pm$  are change rate coefficients for accretion ( $C^+$  for  $\Delta E < 0$ ) and erosion ( $C^-$  for  $\Delta E > 0$ ). The equilibrium wave energy  $E_{\text{eq}}$  is inferred from measurements as a linear function of the shoreline position:

$$E_{\text{eq}}(S) = aS + b \quad (1.9)$$

The shoreline model was shown to be transportable to other sites with similar (but not identical) grain size and incident wave energy without significant loss of skill ([Yates et al., 2011](#)). But, it is still a scientific issue to relate this model free parameters to measurable environmental variables, such as grain size.

### ShoreFor model of [Davidson et al. \(2013\)](#)

As [Wright et al. \(1985\)](#) suggested, the ShoreFore model of [Davidson et al. \(2013\)](#) is based on the dimensionless fall velocity  $\Omega$  to encompass different rates of accretion and erosion. The ShoreFor model of [Davidson et al. \(2013\)](#) takes the following form:

$$\frac{dS}{dt} = b + C^\pm P^{0.5} \Delta\Omega \quad (1.10)$$

Where  $P = E.C_g$  is the the incident wave power,  $C_g = \sqrt{gh_b}$  is the shallow wave group velocity,  $h_b = H_s/\gamma$  the water depth at breaking,  $H_s$  the significant wave height at breaking and  $C^\pm$  the free parameter that is indicative of the response rate following [Yates et al. \(2009\)](#).  $C$  is separated into accretion ( $C^+$  for  $\Delta\Omega > 0$ ) and erosion ( $C^-$  for  $\Delta\Omega < 0$ ) components.

The equilibrium dimensionless fall velocity  $\Omega_{\text{eq}}(t)$  is defined as the weighted average of the

antecedent dimensionless fall velocity:

$$\Omega_{\text{eq}}(t) = \frac{\sum_{j=0}^{D/\Delta t} \Omega_j 10^{-j\Delta t/\phi}}{\sum_{j=0}^{D/\Delta t} 10^{-j\Delta t/\phi}} \quad (1.11)$$

where  $\phi$  (in days) is the memory decay,  $D = 2\phi$ ,  $\Delta t$  is the wave forcing data time step,  $j$  is the number of data points in the survey time series prior to the calculation point at time  $t$ . Equation 1.11 indicates that the smaller the  $\phi$ , the more  $\Omega_{\text{eq}}(t)$  is close to  $\Omega(t)$ . On the contrary, the larger  $\phi$ , the more  $\Omega_{\text{eq}}(t)$  is close to the average value of the antecedent Dean numbers.

### The model of Splinter et al. (2014)

The cross-shore model of Splinter et al. (2014) is similar to Davidson et al. (2013) ShoreFor model. The only difference is that Splinter et al. (2014) developed a parametrization of the free parameters of Davidson et al. (2013) model. Here, the rate of shoreline change is simply defined as follows:

$$\frac{dS}{dt} = c(F^+ + rF^-) + b \quad (1.12)$$

where  $c$  ( $m^{1.5} \cdot s^{-1} \cdot W^{-0.5}$ ) is the rate parameter,  $b$  ( $m/s$ ) is the linear term included here to acknowledge longer-term processes not previously and explicitly included in the ShoreFor model of Davidson et al. (2013) (e.g., gradients in longshore transport, cross-shelf sand supply, etc.). The wave-driven parameter  $c$  and  $b$  are tuned by an optimization method to fit at best with shoreline position data. The key forcing term in equation 1.12 is subdivided into accretionary  $F^+$  and erosional  $F^-$  components multiplied by a ratio. The ratio parameter  $r$  (no unit) is defined here to encapsulate that accretionary and erosion responses are governed by different processes (Miller and Dean, 2004; Yates et al., 2009; Splinter et al., 2011).  $r$  is numerically evaluated in the model as:

$$r = \left| \frac{\sum_{i=0}^N F_i^+}{\sum_{i=0}^N F_i^-} \right| \quad (1.13)$$

where  $N$  is the total record length. The forcing term  $F$  is defined as:

$$F = P^{0.5} \frac{\Delta\Omega}{\sigma_{\Delta\Omega}} \quad (1.14)$$

where  $P$  is the breaking wave energy flux and  $\sigma_{\Delta\Omega}$  the standard deviation of  $\Delta\Omega$ .  $\sigma_{\Delta\Omega}$  is used to normalize  $\Delta\Omega$  in equation 1.14, such that the rate parameter  $c$  and wave energy flux  $P$  determine the magnitude of the shoreline response  $\frac{dS}{dt}$ , rather than  $\Delta\Omega$ . If  $F(t) > 0$ ,  $F = F^+$ . Conversely, if  $F(t) < 0$ ,  $F = F^-$ .

The ShoreFor model of Splinter et al. (2014) was applied at 12 study sites including exposed open coastlines and semi-embayed coastlines. The wide range of study sites induces a detailed analysis of calibration parameters ( $c$  and  $\phi$ ) which value ranges seem to depend on quantifiable environmental variables. Besides, it is noted that Splinter et al. (2014) assumed that some physical processes including storm surge, sea level rise and even the longshore transport are constant in time. Therefore, in this model, the shoreline changes due to these processes are just the linear trend modeled by the free parameter  $d$  in equation 1.12.

### 1.4.3 Longshore and cross-shore integrated model

Until now, cross-shore and alongshore processes have been mostly addressed in isolation as observed by [Robinnet et al. \(2018\)](#). To increase our understanding of shoreline change and prediction capabilities from the timescales of hours (i.e. storm) to decades and centuries, cross-shore and alongshore processes might be combined into a single reduced-complexity shoreline model accounting for the complexity of offshore and nearshore wave transformation, by integrating environmental parameters such as sediment size. Following this approach, some models have been developed with more or less important simplifications of cross-shore processes depending on the spatial scale to be solved.

#### CASCADE model of [Larson et al. \(2002a\)](#)

The main feature of CASCADE model ([Larson et al., 2002a](#)) is its capacity to be applied to stretches of coastline covering hundreds of kilometers. CASCADE has been applied at numerous project sites: *e.g.* Moriches and Shinnecock inlets on Long Island ([Larson et al., 2002a](#)), Ocean City and Indian River Inlets on the Delmarva Peninsula ([Larson and Kraus, 2003](#)), Brunswick County, FL ([Kraus, 2008](#)), coastal stretches influenced by beach nourishment in Barra, Portugal, overwash and breaching in Macaneta spit in Mozambique, and dune development in Ängelholm, Sweden ([Palalane et al., 2016](#)). CASCADE simulates longshore sediment transport and coastal evolution at the regional and local scale ([Larson et al., 2002a](#); [Larson and Kraus, 2003](#); [Larson et al., 2006](#)). Instead of integrating all relevant processes into a single module, several modules have been developed in CASCADE model. This modular approach has allowed the model to be developed step by step over the past two decades, integrating several processes such as shoreline evolution taking into account regional trends, evolution of flood shoal and ebb-shoal complexes ([Larson et al., 2002a](#); [Larson and Kraus, 2003](#)), sediment supplies and losses ([Larson et al. 2006](#), *e.g.* beach nourishment, cliff erosion, wind-blown sand, and sediment mining), dune erosion due to overwash ([Larson et al., 2004](#)), channel dredging and material exchange between the bar and the berm ([Larson et al., 2016](#); [Palalane et al., 2016](#)). Most modules have required development of new theory and numerical approaches such as rapid calculation of breaking wave properties ([Larson et al., 2010](#)), generalized longshore sediment transport formula ([Bayram et al., 2007](#)), ebb-shoal dynamics ([Kraus, 2000](#)), inlet shoal ([Larson et al., 2006](#)) and bypassing algorithms ([Larson et al., 2002a](#)). A typical coastal setting to which CASCADE may be applied is barrier islands separated by inlets with and without jetties, where the sediment is transferred around inlets through the inlet shoal complex. The shoreline of the barrier island chain may display a curved trend at the regional scale with local variations in between the inlets. One of the limitations of this model is that at the boundaries, the sediment budget should be stable over the entire study period.

[Hoan et al. \(2011b\)](#) enhanced the capability of the CASCADE model to simulate inlet sediment transport and the evolution of morphological elements at an inlet. Also, the possibility to describe structures in the model was improved and a more general longshore sediment transport formula was implemented that is sensitive to grain size and includes currents that are not only wave-generated.

---

### The CosMos-COAST model of Vitousek et al. (2017)

As CASCADE, the CosMos-COAST model (Vitousek et al., 2017) was recently developed for stretches of coastline covering hundreds of kilometers. The model was applied to the coastline stretching on the length of 500 km in Southern California, which contains cliffs, dunes, bluffs, estuaries and infrastructures. Vitousek et al. (2017) suggested a one-line integrated model of shoreline variation due to cross-shore transport, overland transport and sea-level rise. Longshore transport and shoreline changes due to waves are modelled following the one-line approach (Larson et al., 1997; Vitousek and Barnard, 2015). Cross-shore transport and equilibrium shoreline change due to waves are based on the model of (Yates et al., 2009). The other contribution to shoreline change in this model is from the sea-level rise response model based on Bruun rule (Bruun, 1962b). The model also includes the long-term shoreline trend representing unresolved processes. The model uses the spatial and temporal discretization method to compute the shoreline evolution. A highlight of this model is that the data assimilation by an extended Kalman filter method is used to improve a long-term prediction. However, this model requires a large data set for assimilation. Moreover, the numerical discretization method and data assimilation in the case study were performed with quite complex computations to meet the stability condition and achieve stability results (Tran, 2018).

### The LX-Shore model of Robinet et al. (2018)

The LX-Shore model was developed recently by Robinet et al. (2018) and comprises both longshore and cross-shore processes with concurrent responses of the shoreline. A 2D cellular-based one-line model similar to that of Ashton et al. (2001) is used to compute the longshore transport and the cross-shore transport is based on the model of Splinter et al. (2014). Wave propagation is simulated using the SWAN model. The model was demonstrated to be able to simulate the shoreline evolution of embayed beaches and non-linear evolution of complex shoreline features from small-time scales (hours) to large-time scales (decades). This model shows good skills in allowing users to address the dynamics of 10s km of complex shoreline plan-view shapes, including rocky areas and non-erodible submerged structures, on timescales from hours to years and decades, with reasonably low computational cost. But more relevantly, LX-Shore must be applied on coasts away from the influence of tidal inlets and estuary mouths (Robinet et al., 2018). Coastal effects due to overwash are still neglected in the model, and as most of the models, the main limitation here is due to the fact that shoreline changes are assumed to be controlled only by wave-driven sediment transport occurring over the active and sediment rich shoreface (the shoaling and surf zones).

### The model of Tran and Barthelemy (2020)

This recent modeling tool combines a model for the shoreline changes due to the gradients in longshore drift and a heuristic cross-shore shoreline model. Cross-shore processes are modelled using an up-to-date semi-empirical shoreline evolution model based on the equilibrium beach state assumption with alongshore processes are modelled as the one-line type approach based on the longshore sand budget. The model was developed for closed embayed beaches where no loss of sediment is assumed. The model was calibrated with the wave and shoreline data of the embayed beach of Narrabeen, Australia and the results showed that the equilibrium shoreline orientation depends on the time correlation between the incoming wave power and the difference

---

---

between the instantaneous and the time average wave incidence.

---

## Chapter 1 summary

In this chapter, a review of common knowledge on the main natural oceanic forcing causing shoreline variability (section 1.2) and on the techniques for monitoring beach changes (section 1.3) was conducted. In the last section (section 1.4), a complete review of existing shoreline models has been carried out, based on the longshore and cross-shore sediment transport.

- **Main contributors to beach changes:** waves propagation, storms, wave-induced currents, sediment supply/trap, sea level rise.
- **Sea level variations at the coast:** Only the trend in sea level rise is generally considered in coastal management. But, there is still a great deal of uncertainty as to the real impact of the sea-level rise on the coast. And the knowledge on the beach response to shorter (daily to inter-annual) sea level variations is still scarce.
- **Techniques for monitoring beach changes:** Beyond the traditional techniques, the new video and altimetry monitoring approaches allow high frequency (daily and 5-day, respectively) and large scale (100s meters to 100s km) monitoring of the beach profile changes.
- **Modeling shoreline evolution:** Several models have been developed to integrate a large number of nearshore processes. But only few are capable of integrating sediment transport both on cross-shore and longshore directions at large temporal and spatial scales (CASCADE, CosMos-COAST, LX-Shore and the model of [Tran and Barthelemy 2020](#)).

### 1.5 Conclusion

One of the criteria for the choice of the model to be applied on wave-dominated coasts in the [BoB](#) can be the computational consuming time to enable long-term simulations (decades to centuries) of shoreline change as well as cross-shore processes simplification rate. Following on from this work, the choice of the CASCADE model for modelling the shoreline of the [BoB](#) is justified by the length of the coastline to be studied (which is more than 400 km), the type of the coast (wave-dominated coast formed of sandy beach-ridge barriers and lagoons) and the refinement in the integration of cross-shore coastal processes. CASCADE model encompasses several barrier islands separated by inlets on 100s kilometers of coast, including such phenomena as inlet creation, ebb- and flood-tidal shoal development, bypassing bars between beaches and inlets, channel dredging, regional trends in the shape of the coast, relative change in sea level, wind-blown sand, storms, periodic beach nourishment, and shore-protection structures such as groins and seawalls.

---

# Chapter 2

## Study area, methods and data

### Contents

---

<b>2.1</b>	<b>Introduction</b>	<b>31</b>
<b>2.2</b>	<b>The Bight of Benin, Gulf of Guinea</b>	<b>32</b>
2.2.1	Location and general overview	32
2.2.2	Oceanic forcing	32
2.2.3	Harbors and coastal infrastructure	34
2.2.4	River discharges	34
2.2.5	Grand Popo beach, Benin	35
<b>2.3</b>	<b>Data</b>	<b>35</b>
2.3.1	The Grand Popo 2014 field measurements	35
2.3.2	Waves from Era-Interim global reanalysis	36
2.3.3	Tide gauge and FES2014 model	38
2.3.4	Satellite measurements	38
2.3.5	Video-based station, images and processing	39
<b>2.4</b>	<b>Conclusion</b>	<b>47</b>

---

### 2.1 Introduction

This chapter is devoted to the presentation of the study site, data and processing methods used. Section 2.2 details the main characteristics of the coast in the [BoB](#) in the Gulf of Guinea. The wave climate is presented as well as the characteristics of sea level variations, the different rivers that discharge sediments on the coast and the main coastal structures. Section 2.3 provides an overview of altimetric, tide gauge and model data collected in existing databases. Field measurements carried out during 10 days in Grand Popo, Benin, are presented. The video system installed since February 2013 and the collected images are also presented. Details are given on the methods used to process these video images, in particular wave celerity extraction and depth inversion techniques.

## 2.2 The Bight of Benin, Gulf of Guinea

### 2.2.1 Location and general overview

The BoB, in the Gulf of Guinea, West Africa, is more than 400 km long, ranging between 1 to 5°E in longitude, and 5 to 7°N latitude and facing the South Atlantic Ocean (Fig. 2.1). This embayment covers the coastal environments of four countries: Ghana, Togo, Benin and Nigeria. It is a wave-dominated coast formed of sandy beach-ridge barriers and lagoons, bordered by the Niger River delta in the east and the Volta River delta in the west, and also fed by several small coastal rivers (Anthony and Blivi, 1999; Blivi et al., 2002; Anthony, 2015a). The historical evolution of this sand barrier and its associated lagoon and lacustrine system has been intensely investigated (Anthony, 1995; Anthony and Blivi, 1999; Blivi et al., 2002). Barrier beach and shoreface deposits in prograded single or double sand barriers range in thickness from less than 5 m on their landward edges to 15-20 m offshore seaward. For the case of double sand barriers, Anthony (1995) showed that the segmented inner barrier was formed essentially from nearshore sands while the outer barrier has been constructed from sands supplied by the Volta Delta. Deposits are essentially composed of medium to coarse (0.4–1 mm,  $D_{50} = 0.6$  mm) quartz sand (>80%), with variable minor fractions of feldspars (up to 10%), shelly debris (5–15%) and heavy minerals (1–5%). Recent studies (Almar et al., 2014; Laibi et al., 2014) showed that beaches along this area are mostly in the ‘reflective-to-intermediate’ state classes and often exhibit an alongshore-uniform low-tide terrace and a steep reflective upper beachface. Anthony et al. (2019) observed that the continental shelf is narrow (widths ranging from 15 to 33 km). There, the shoreface is fairly uniform and moderately steep with a gradient of between 1:120 and 1:150 down to 15 m, while seaward, the inner shelf forms a low-gradient (1:350–1:400) plain covered by relict transgressive sands (Anthony and Blivi, 1999).

### 2.2.2 Oceanic forcing

The BoB undergoes the main action of oceanic forcing, i.e. the action of waves and sea level oscillations. Wave forcing was shown to consist of two components with distinct origins and behaviour: locally generated wind waves in the Gulf of Guinea and long swell waves generated in subtropical regions (Almar et al., 2015b). Long swell waves are dominantly generated by the mid- to high (45-60°) latitude westerlies, to which are superimposed, on a lesser extent, the effects of the south-easterly trade winds, blowing off the coast of Namibia (30–35°S). The dominant southwesterly swells impinge slightly obliquely (at angles of 10–15°) on the nearly rectilinear west-east oriented Bight of Benin coast. This wave climate (mean significant wave height  $H_s = 1.36$  m; mean wave period  $T_p = 9.4$  s) drives an easterly longshore sediment transport (one of the largest in the world) ranging between 0 up to 1.2 million m<sup>3</sup>/year, depending on the location (Allersma and Tilmans, 1993; Anthony and Blivi, 1999; Almar et al., 2015b).

Sea level variations in the BoB are characterized by several time scales. The shortest periods correspond to semi-diurnal tides, ranged from 0.3 m to 1.8 m for neap and spring tides, respectively. Polo et al. (2008) revealed intra-seasonal (20 to 90 day periods) recurrent and continuous horizontal propagations of sea level fluctuations, triggered by coastally-trapped Kelvin and Rossby waves, distinguishable poleward along the coasts as far as about 10°N - 15°N, with peak-to-peak amplitudes of 10 cm and phase speed range from 1.5 to 2.1 m/s along the West African coastline. South Atlantic climate variability modes in this tropical region result in  $\sim 25$

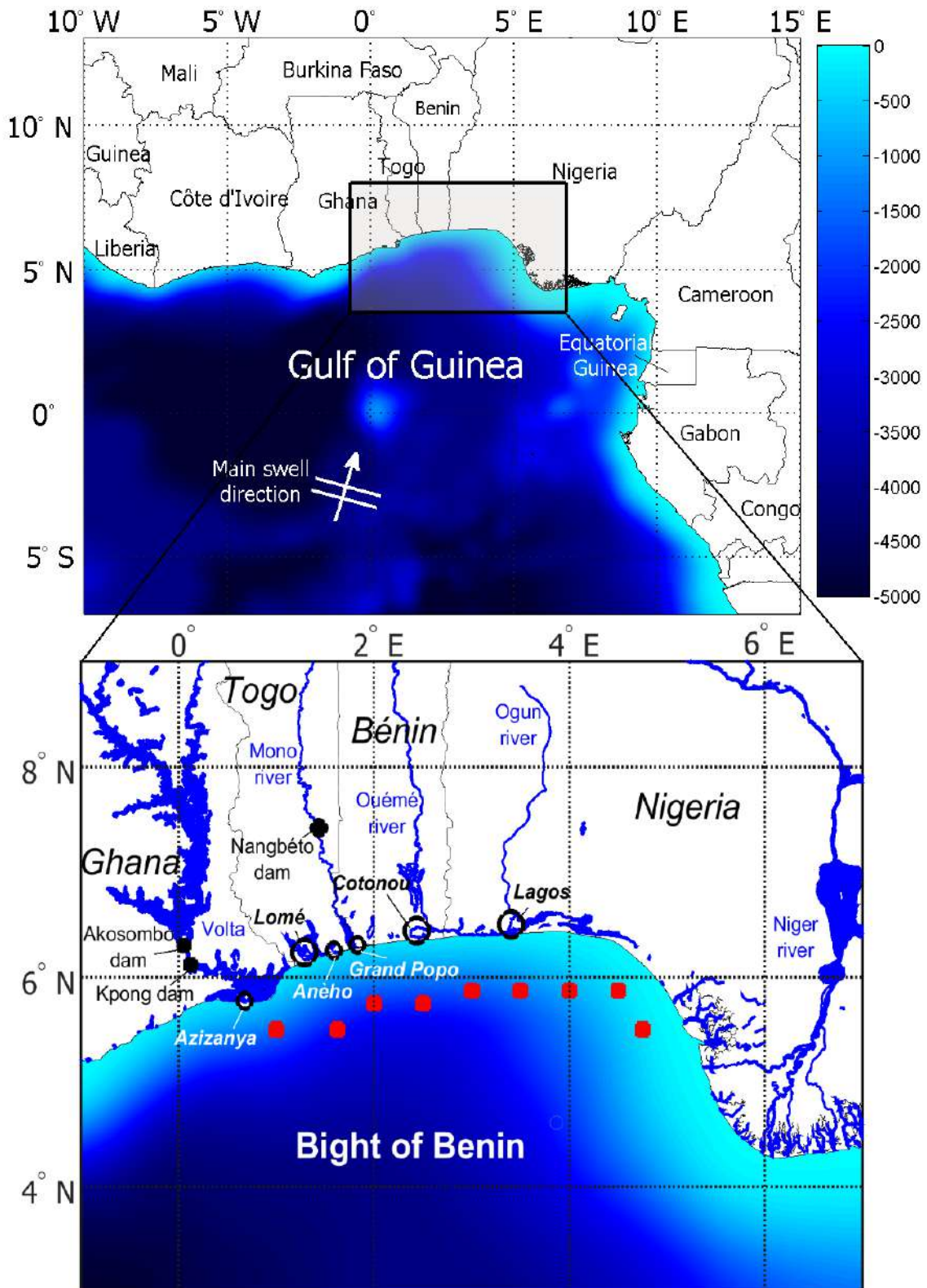


**Figure 2.1** – The Bight of Benin in the Gulf of Guinea, West Africa. The largest circles stand for the three main coastal cities (Lomé, Cotonou and Lagos), each have their deep water harbor and dike. The smaller circles represent some small coastal towns. The black dots represent the location of river dams. The red dots stand for the stations where wave and water levels data have been extracted.

cm seasonal and inter-annual variations in sea level (Ding et al., 2009). And the regional trend in sea level rise is larger than the global rate that has doubled in the last two decades compared to the average rise in the 20th century (Melet et al., 2016).

### 2.2.3 Harbors and coastal infrastructure

Investigations carried out in the BoB (Anthony, 1995; Blivi et al., 2002) showed that before the years 1900, equilibrium was achieved between coastal morphology and the hydrodynamic regime. Recent studies (Laibi et al., 2014; Almar et al., 2015b; Giardino et al., 2018; Anthony et al., 2019) have pointed out the disruption of this stability due to the construction of deep-water harbors in 1957 in Lagos, 1962 in Cotonou and 1967 in Lomé. The three harbors (Fig. 2.1) have impacted alongshore sediment redistribution by segmenting the previously unrestrained longshore sand transport, resulting in long sectors of rampant erosion that endangering parts of the rapidly expanding port cities, coastal infrastructure, and numerous villages (Laibi et al., 2014; Anthony et al., 2019). Recently, coastal defence infrastructures along the coast have been planned to limit the increase of coastal risks. Downstream of the three harbors, series of protective groins were built to limit the observed erosion. And between 2012 and 2016, near the city of Aného (Togo), several groins have been constructed over a distance of  $\sim 10$  km. Human activities, such as plantations and sand mining, have also obliterated the alignment of multiple beach ridges characterizing the barriers, even though can still be identified in places on aerial photographs (Anthony et al., 2019).

### 2.2.4 River discharges

The Volta River delta and the Niger River delta (Fig. 2.1) are among the three largest deltas in West Africa. The Volta delta, situated entirely in Ghana, covers an area of about 5000 km<sup>2</sup> (Boateng et al., 2018) while the Niger delta, much larger and situated in Nigeria, covers an area of 19,135 km<sup>2</sup> (Anthony et al., 2019). Anthony and Blivi (1999) identified the Volta River as the single most important fluvial sediment source for much of the sand barrier system of the BoB. In contrast, the influence of the Niger delta has been limited essentially to the eastern confines of the Bight of Benin coast, as observed by Anthony et al. (2019). A few minor additional sediment inputs have been identified at the mouth of the Mono River.

According to Logah et al. (2017), the Volta sediment concentration at Azizanya station was recently measured at 20 mg/l, which corresponds to a sediment discharge of  $\sim 320000m^3$ /year for a mean water discharge of 1200 m<sup>3</sup>/s (Anthony et al., 2019), assuming that the density of sediment is 2400 kg/m<sup>3</sup>. However, these discharges rates at the Volta delta recorded over the past decade have decreased by 70-90% compared to those recorded before the construction of the Akosombo and Kpong dams across the Volta river (Bollen et al., 2011; Boateng et al., 2012; Anthony et al., 2016, 2019). The sand load supplied by the river to its delta has been estimated at about more than 1 million m<sup>3</sup> prior to the construction of the dam (Delft Hydraulics, 1990). The construction of Akosombo dam 100 km upstream from the sea between 1961 and 1965, and Kpong dam between 1977 and 1982, 24 km downstream of the Akosombo dam, have replaced the natural seasonal high and low flows of the river by an almost constant reduced flow throughout the year. Oguntunde et al. (2006) noted that the decrease in rainfall in the Sahel since 1975 also contributed to the reduction of river discharges. This reduction in Volta river sand supply could be a significant contributing factor to the observed disruption of shoreline stability.

---

Sediment inputs from the Mono River estimated at  $100,000m^3$  during the wet-season months two decades ago, have been significantly reduced with the construction of the Nangbéto Dam, built 180 km upstream from the mouth of the Mono River in 1987 (Ago et al., 2005). The other smaller rivers (e.g. Ogun river) debouch into still infilling lagoons behind the coastal sand barriers, linked to the sea via inlets (Anèho, Cotonou and Lagos) which have been all fixed by engineering structures.



**Figure 2.2** – Grand Popo beach, Benin, Gulf of Guinea, West Africa

### 2.2.5 Grand Popo beach, Benin

**Grand Popo (GPP)** beach is a small coastal town, located in Benin, near the border with Togo, in the **BoB** in West Africa ( $6.28^{\circ}N$ ,  $1.83^{\circ}E$ ; Fig. 2.2) and bounded by the inlet of the *Lagune de Grand Popo* to the east and Aneho harbour to the west ( $\sim 40$  km). GPP beach consists of an open wave-dominated microtidal sandy coast, almost W-E orientated (0.3/1.8 m for neap/spring tidal ranges,  $H_s = 1.36$  m,  $T_p = 9.4$  s,  $D_p = S-SW$ ) (Almar et al., 2014). The coast is exposed to plunging regime of long period swells that originate from high latitudes South Atlantic storms, resulting in a Low tide Terrace to reflective beach which consists of a steep reflective upper beach (slope  $\sim 12-17^{\circ}$ ; often with cusps present) with submerged longshore-uniform sub-tidal terrace. The sediment is primarily of a relatively homogeneous suite of iron-coated medium to coarse sand (0.4–1mm,  $D_{50} = 0.6$  mm) (Almar et al., 2014, 2015b). The slope break occurs around mean spring low water and the tidal level acts to modulate surf zone width and breaker type across the narrow terrace. The persistent southerly swell direction drives a strong easterly-directed longshore current resulting in a reported littoral drift of  $800,000m^3/yr$  (Blivi et al., 2002). GPP is typical and representative (Almar et al., 2014) of the natural undisturbed reflective beaches of the Gulf of Guinea. GPP is hardly affected by human presence, hosting only a few fishermen, far enough from the influence of the major cities: Cotonou (80 km away), and Lome (60 km away).

## 2.3 Data

### 2.3.1 The Grand Popo 2014 field measurements

A 10-day field experiment was conducted in Grand Popo from March 10 to 19, 2014 to provide insight into primary beach-change driving processes at this site. Measurements of topography, bathymetry and water level changes were performed using a differential global positioning

system (DGPS), an echo sounder and an [Acoustic Doppler Current Profiler \(ADCP\)](#), respectively (Fig. 2.3).

Sea level and directional wave spectra were measured by an [ADCP](#) moored at 10 m water depth in surface tracking mode from March 11 to 18, 2014. The device emits sound waves that are reflected by suspended particles moving with the current. The [ADCP](#) then receives these reflected waves and calculates a celerity profile of the current over the entire water column using the frequency difference between the emission and reception. The [ADCP](#) incorporates a piezoresistive sensor that measures the pressure exerted by the water column on the device, thus measuring variations in swell and tide. The height (depth) of the water is calculated as follows :

$$depth = (P_{ADCP} - P_{atm}) / (\rho g) \quad (2.1)$$

where  $P_{ADCP}$  is the pressure measured by [ADCP](#),  $P_{atm}$  the atmospheric pressure,  $\rho$  is the water density and  $g = 9.81m/s^2$ . The tide was extracted by removing the average column height from the [ADCP](#) measurements.

DGPS consists of two stations, one fixed and one mobile. The longitudes, latitudes and altitudes coordinates obtained with the mobile station are instantly corrected by the fixed station, leading to a centimetric precision of the positions. The operator carried a backpack containing the mobile station, and performed several cross-shore transects on the coast at low tide, in order to cover as much as possible the terrace of the beach profile. The transects are about 400 metres long and are spaced 5 to 10 metres apart. Bathymetry was measured on a boat with echo sounder, trying to follow cross-shore and longshore transects.

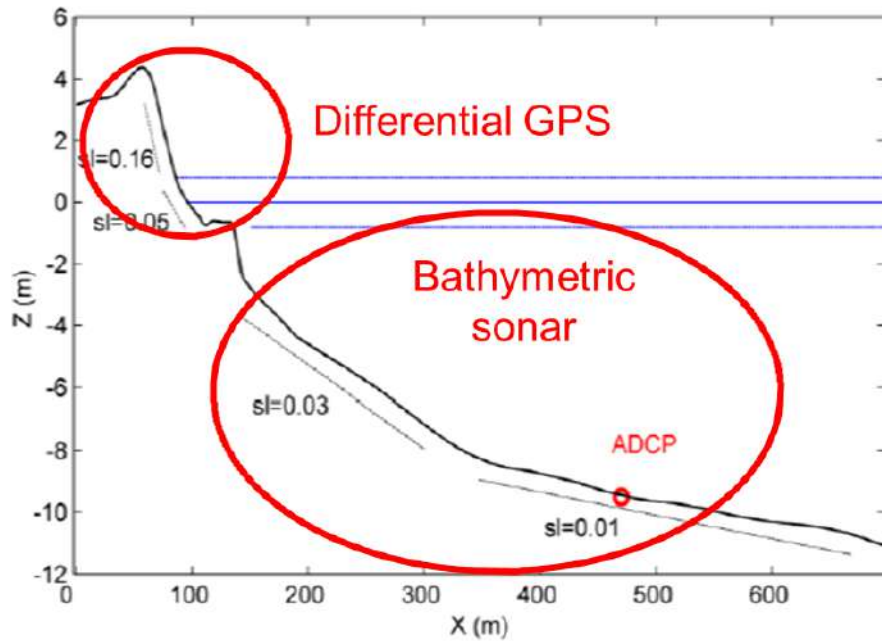


**Figure 2.3** – Data collected during the Grand Popo 2014 field measurements: topographic data with a DGPS, bathymetric data with a sonar and water level variations with an ADCP moored at 10 m-depth. The blue lines represent low, mean and high tide levels respectively.

### 2.3.2 Waves from Era-Interim global reanalysis

Wave characteristics were extracted from ERA-Interim ECMWF re-analyses ([Sterl and Caires, 2005](#)) at 6-hr interval from 1990 to 2016 at nine different nodes along the coast in the

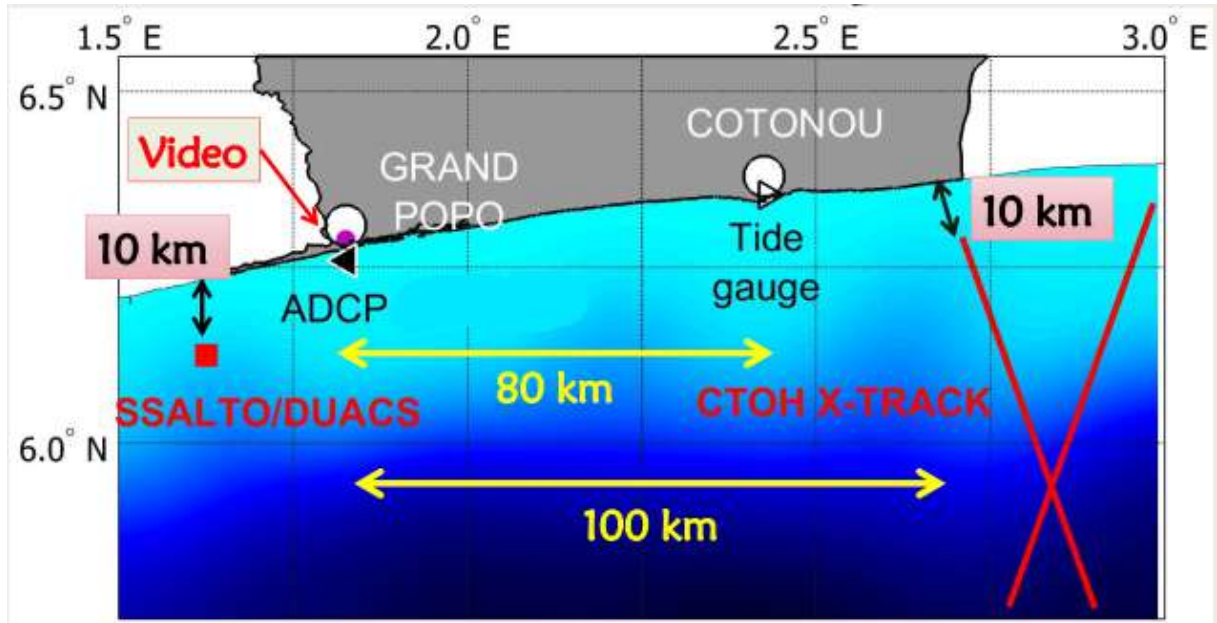


**Figure 2.4** – Location of data sources in the Bight of Benin, next to Grand Popo town.

Bight of Benin. ERA-Interim dataset is a third generation reanalysis dataset produced by much improved atmospheric model and assimilation system from those used in the previous versions (ERA-40). Extracted waves data were propagated from deep water to the breakpoint using the formula by Larson et al. (2010).

This formula directly provides the breaking wave height  $H_b$  and angle  $\theta_b$ , given deep water wave height  $H$ , period  $T$ , direction  $\theta$  and breaker depth ratio  $\gamma = \frac{H_b}{h_b}$  where  $h_b$  is the water depth at breaking:

$$H_b = \gamma \lambda \cdot C^2 / g \quad (2.2)$$

$$\theta_b = \arcsin(\sqrt{\lambda} \cdot \sin(\theta)) \quad (2.3)$$

$$\lambda = \Delta \cdot \lambda_a \quad (2.4)$$

$$\Delta = 1 + 0.1649\xi + 0.5948\xi^2 + 1.6787\xi^3 + 2.8573\xi^4 \quad (2.5)$$

$$\xi = \lambda_a \cdot (\sin(\theta))^2 \quad (2.6)$$

$$\lambda_a = [\cos(\theta) / \varphi]^{2/5} \quad (2.7)$$

$$\varphi = \left( \frac{C}{\sqrt{g \cdot h_b}} \right)^4 \left( \frac{C}{C_g} \right) \gamma^2 \quad (2.8)$$

where the phase celerity is given by  $C = 1.6T$ , group celerity  $C_g = C/2$  and breaker depth index  $\gamma = 0.78$ .

This simplified formulation has been widely used in recent studies in the Gulf of Guinea

(e.g. [Almar et al. 2015b](#); [Angnuureng et al. 2016, 2018](#)). Using nested numerical model (e.g. SWAN) to propagate waves from deepwater to the breakpoint would have been an ideal option for a short-term study, but there are several difficulties when investigating wave propagation in the spatio-temporal scales of this study. In addition, this simplified formulation, already implemented in the CASCADE model, allows a significant reduction in calculation times.

### 2.3.3 Tide gauge and FES2014 model

In situ tide data were collected by the tide gauge located at Cotonou harbor (6.338°N, 2.428°E) with a 5-min acquisition period from June 2011 to March 2015. The tide gauge is approximately 80 km away from the camera location (Fig. 2.4). Considering several malfunctions of the tide gauge, available data were processed for 2 years (February 2013–January 2015). The Finite Element Solution (FES) 2014 tidal atlas is the latest release of the FES atlas series ([Carrere et al., 2016](#)). The FES2014 atlas performance has been assessed and validated with tide gauges and various geophysical applications (satellite altimetry corrections, gravimetry, etc.). It shows significant improvements compared to previous FES releases and other state-of-the-art tidal atlases ([Lyard et al., 2016](#); [Ranji et al., 2016](#)). Hourly tidal estimates were extracted from FES2014 from February 2013.

### 2.3.4 Satellite measurements

#### Altimetry sea level products

Sea level time series were extracted from two altimetry products: the Center for Topographic Studies of the Ocean and Hydrosphere (CTOH) along-track sea level anomalies" provided by CTOH/LEGOS, version X-TRACK 2017 and the SSALTO/Data Unification and Altimeter Combination System (DUACS) multimission gridded and delayed-time products provided by Copernicus Marine and Environment Monitoring Service (CMEMS) (Fig. 2.4). Tide, inverse barometer and atmospheric wind are corrected for in both altimetry products. The CTOH X-TRACK sea level time series are obtained from along-track combined TOPEX/Poseidon, Jason-1, Jason-2, and Jason-3 missions, at a spatial resolution of 6–7 km ([Birol et al., 2017](#); [Marti et al., 2019](#)). In the SSALTO/DUACS products, two available altimeter missions are merged and mapped daily onto a 1/4°-resolution grid ([Arbic et al., 2012](#); [Pujol et al., 2016](#)). Knowing that this study focuses on the coast, both altimetry data were extracted as close as possible to the coast and to the video camera location (Fig. 2.4). CTOH X-TRACK sea level time series were extracted on the track 122, at the location 6.3148°N, 2.7148°E, approximately 98 km away from the camera and 9 km off the coast. SSALTO/DUACS time series of sea level were extracted at the grid node 6.1258°N, 1.6258°E, approximately 28 km away from the camera and 12 km off the coast (Fig. 2.4). The extracted data were then averaged monthly, because of the different sampling frequencies of these altimetric products (CTOH X-TRACK 10-day periodicity and SSALTO/DUACS 1-day periodicity).

#### Shorelines derived from satellite images

Available satellite images that offer not only large individual coverage, given the length of the Bight of Benin coast (> 400 km), but also robust and accurate determinations of shoreline change rates were uploaded. In total, 15 LANDSAT 4–8 images were used. Three images for

each of the years 1990, 2000, 2005, 2010, and 2015 were downloaded from the USGS data portal EarthExplorer. The analysis involved using panchromatic (10 m resolution) and a customized combination of bands maximizing land-water contrast (30 m) to derive the shoreline. We used the most recent images in the time series, and with minimal cloudiness, checked for easy landmarks on those where these could be traced back through time, and georeferenced these using coordinates from Google Earth, from the most recent to the oldest image. The accuracy was typically around 1 pixel (30 × 30 m). To compute rates of change in shoreline position, we used the ArcMap extension module Digital Shoreline Analysis System (DSAS), version 4.3 (Thieler et al., 2009), coupled with ArcGIS 10. The brush/ plantation fringe could be used as a robust shoreline marker on this sandy coast characterized by beaches throughout. The shore-normal distance of the vegetation line to a base line was established at 100-m alongshore spacing for the earliest and most recent images. This distance, chosen as a compromise between quality of the interpretation and the total length of analyzed shoreline (410 km) was then divided by the time in years between the two dates to generate a shoreline change rate, i.e. the End Point Rate in DSAS 4.3. A total of 4100 change rates, each corresponding to a DSAS transect, were thus determined. The annual error (E) of shoreline change rate, which sums up image rectification, extraction of the shoreline, and operator digitization in delimiting the shoreline, was computed from:

$$E = \sqrt{(d_1^2 + d_2^2)} / T \quad (2.9)$$

where  $d_1$  and  $d_2$  are the uncertainty estimates for successive sets of images and  $T$  is time in years between image sets (Hapke et al., 2006). We obtained an error of  $\pm 2.4\text{m/yr}$  between 1990 and 2015. Rates of shore-normal shoreline change along transects are useful in indicating the degree of shoreline mobility.

### 2.3.5 Video-based station, images and processing

#### Video monitoring station and stored images

In February 2013, a low-cost video system was installed on a 15-m-high tower located approximately 70 m from the shoreline (Almar et al., 2014). A VIVOTEK IP 7361 camera (1600 x 728 pixels) continuously collects data at a 2-Hz framerate between 07:00 and 17:00 local time. An on-site computer processes the raw image-frames and stores every 15 minutes three types of images: one snapshot, one time exposure (timex) image and three time-stack images (Fig. 2.5). Timex images are 15 min averaged of snapshot images into a single image (Holland et al., 1997). Timestack images are obtained by stacking the successive traces corresponding to 15 min of snapshots (Aagaard and Holm, 1989; Holland and Holman, 1993), with as many 15-min time-stack images as traces implemented. There is only one cross-shore stack implemented, which is used in the further work. Missing data are due to temporary malfunctions of the camera.

#### Image rectification

The image rectification process is the procedure that transforms an originally oblique image into a plan view equivalent image, also known as rectified image. This corresponds to determining the relationship between the image pixels coordinates  $(x, y)$  and real coordinates  $(X, Y, Z)$  in meters. This technique has been extensively detailed and used in the literature (Holland

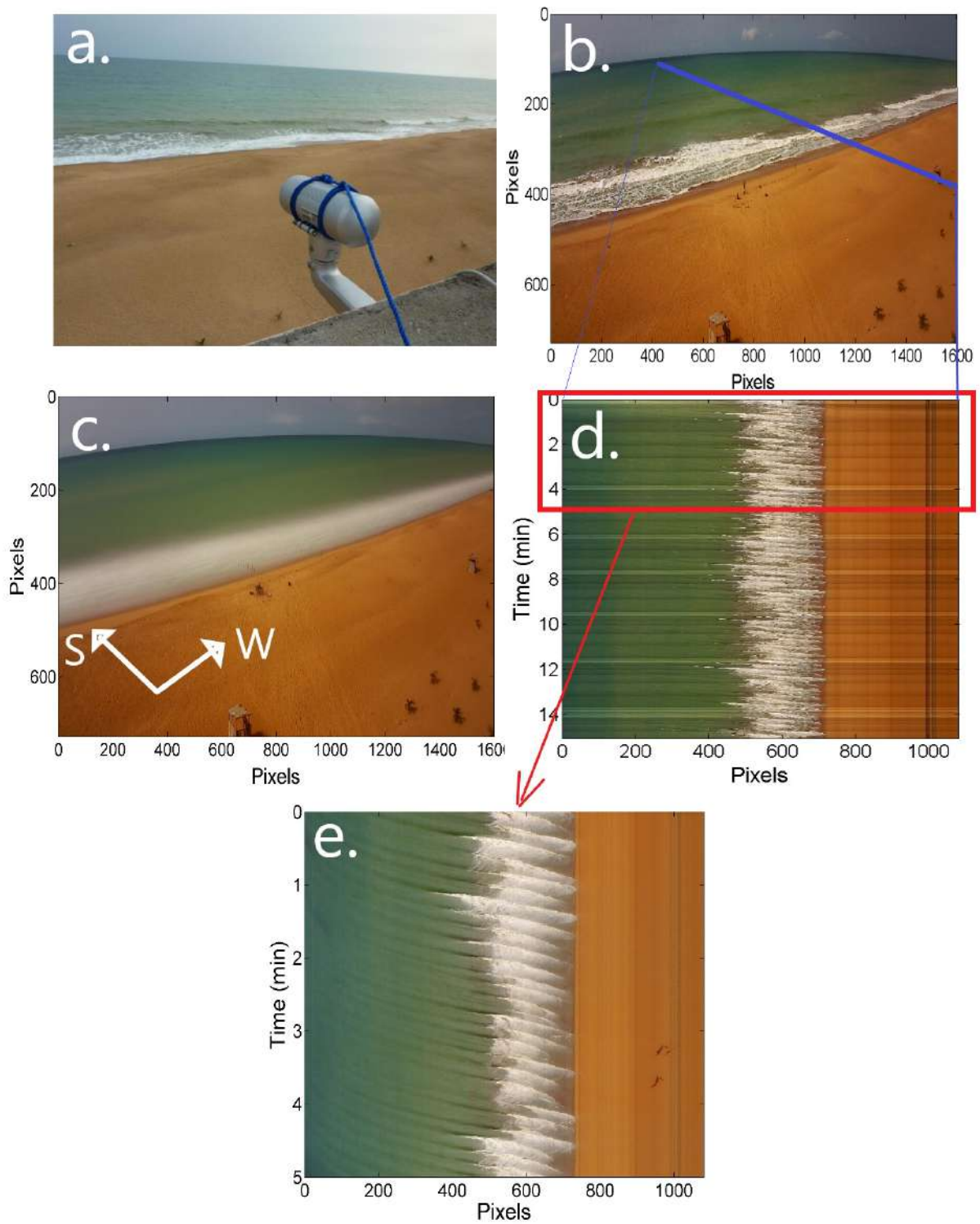


**Figure 2.5** – Grand Popo video system (a) and stored video images: (b) video snapshot (cross-shore time-stack location in blue), (c) timex image, (d) time-stack image, and (e) zoom of time-stack image over 5 min.

et al., 1997; Almar, 2009; Holman et al., 2013; Angnuureng et al., 2017; Thuan et al., 2019). Georeferencing and rectification from image pixels into real-world coordinates was accomplished by direct linear transformation (Holland et al., 1997) using 20 DGPS ground control points (Fig. 2.6) and radial distortion correction of the lens (Heikkila and Silven, 1997).

Determination of camera internal parameters is necessary to correct the image distortion inducted by the lens curvature. Recall that internal parameters are the focal length  $f$  and radial and tangential distortion coefficients  $k_j$ . Focal length is defined as the distance from the center of the lens to the focal points of the lens. It is a measure of how strongly the optical sensor converges or diverges light. The distortion coefficients quantify the deformation that might be inducted on the image by the lens curvature. The optimal focal length and distortion coefficients were computed using least square error minimization method. The rectified distances in meters on the stack and a rectified timex image are shown in the figure 2.6.

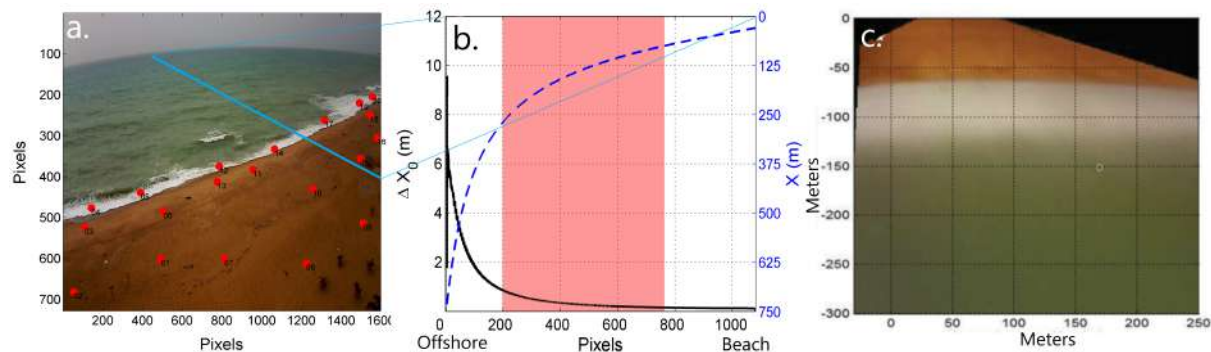


**Figure 2.6** – Image rectification: (a) Grounds control points in red on a snapshot. The blue line indicates the cross-shore time stack location. (b) Averaged pixel footprint  $\Delta X_0$  and cross-shore coordinate  $X$  in meters relative to the camera location, versus pixel coordinate on the cross-shore stack. Shaded area in red indicates the study area, which corresponds to the submerged part of the stack with a pixel foot print less than 1 m. (c) Plan shape timex showing the camera field of view

Using the ground control points located on the beach, the average horizontal error of the rectification method is 3 m. In addition, given the oblique angle of view of the camera, the cross-shore pixel footprint  $\Delta X_0$  increases seaward, ranging from  $\sim 0.05$  m on the beach to approximately 10 m offshore. The footprint  $\Delta X_0$  remains consistently smaller than 1 m in our area of interest (shaded area in red, Fig. 2.6) which corresponds approximately to the region extending from the MSL shoreline seaward to the nearshore profile at 6-m depth. In this area of interest, potential errors due to the camera’s viewing angle are minimal. We assume that the overall horizontal error is smaller than 5 m within the domain of interest.

### Image selection

Many poor quality images can be stored, depending on atmospheric conditions such as dew on the camera lens, fog, and sunlight. A simple criterion based on image intensity is presented here to select images relevant for processing.

As studied by Andriolo (2018), the pixel brightness intensity on a timestack image characterizes the wave transformations domains along the beach profile. For the Grand Popo video system case study, the standard deviation of pixel intensity  $\sigma_{I_{px}}$  has a local minimum in all RGB color bands (Fig. 2.7), which characterizes the surf zone. The single blue band better represents both the dark blue pixel of the background waves and the white pixel of the surfing

waves and was chosen for the relevant image selection scheme (Andriolo, 2018). The standard deviation of the pixel intensity is computed at each position on the stack as follows:

$$\sigma_{I_{px}} = \sqrt{\frac{1}{N-1} \sum_{i=1}^N (I_{x,i} - I_{xmoy})^2} \quad (2.10)$$

where

$$I_{xmoy} = \frac{1}{N} \sum_{i=1}^N I_{x,i} \quad (2.11)$$

$I_{x,i}$  is the pixel intensity at location  $x$  on pixel  $i$ . For the study case of Grand Popo video system,  $N = 1800$  and the cross-shore stack extends approximately 715 m.

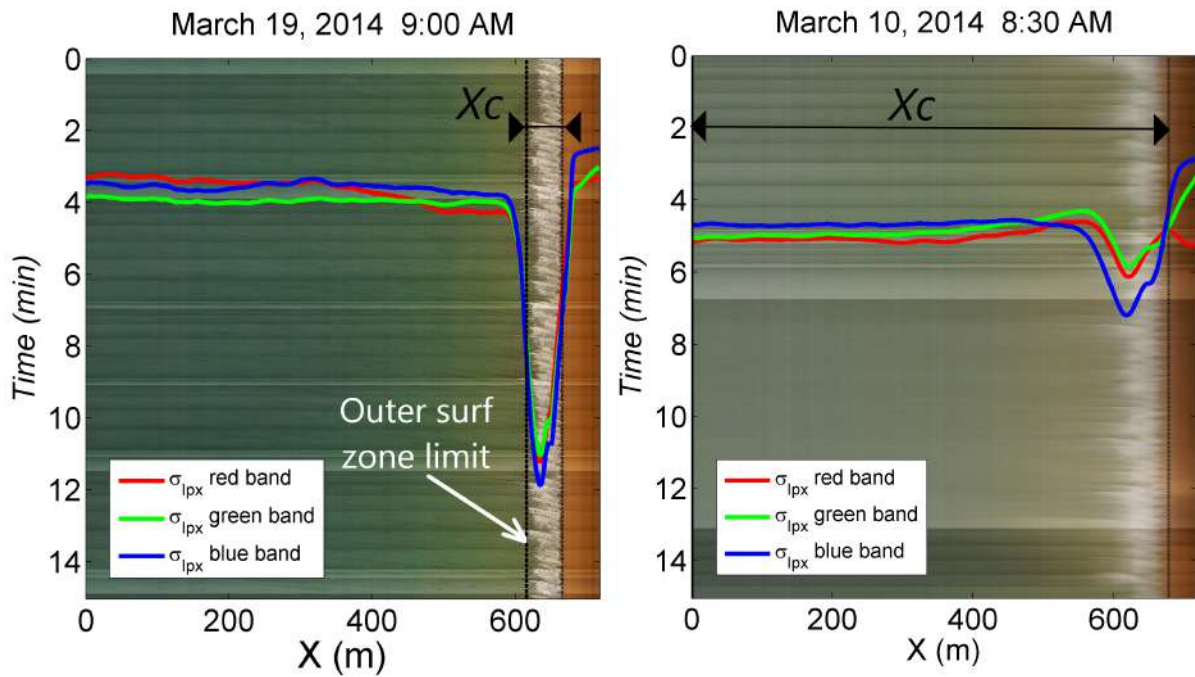


**Figure 2.7** – Standard deviation of pixel intensity  $\sigma_{I_{px}}$  for the red (red line), blue (blue line) and green (green line) bands of a good (March 19, 2014 at 9:00 a.m.) and a bad (March 10, 2014 at 8:30 a.m.) timestack image.

The peak observed in the  $\sigma_{I_{px}}$  variation can therefore be used to delimit the outer and inner surf zone. For this, a simple criterion was applied, consisting in determining the width  $X_c$  of the peak at mid-height (Fig. 2.7). The image is considered relevant if the following is fulfilled:

$$x_{s1} < X_c < x_{s2} \quad (2.12)$$

where  $x_{s1}$  and  $x_{s2}$  are pre-selected threshold distances (in meters). Here,  $x_{s1} = 10$  m and  $x_{s2} = 200$  m.

Otherwise, the image is rejected. For example, on Figure 2.7 the image of March 10, 2014 at 8:30 am is rejected, while the image of March 19, 2014 at 9:00 am is relevant for post-processing.

### Shoreline and intertidal profile

The shoreline, defined as the 15-min water line, is derived from timex video images using the MSV (Minimum Shoreline Variability) method (Almar et al., 2012b), which combines two

intrinsic shoreline properties, that is, (1) the color difference between sea and sand and (2) the presence of swash. Beach pixels usually exhibit high red-channel (R) values and low green-blue-channel (G-B) values (i.e., high R/G-B ratios), whereas sea pixels exhibit intense green-blue-channel values and low red-channel values (i.e., low R/G-B ratios). A first estimate of the shoreline is the local minimum computed as the transition zone between lower and higher R/G-B peaks on sea and beach pixels, respectively. At this step, specific conditions are defined to check the image quality (sufficient light and well-marked local minimum). A second estimate of the shoreline is computed using the swash signature, considering the complexity of the topography and the local occurrence of breaking. Several contour lengths  $S$  are computed for different R/G-B values around the local minimum identified.  $S$  depends on the width of the region of interest and its variation  $\Delta S$  is typically on the order of 1 to 30% of  $S$ . The local minimum of  $\Delta S/S$  for varying R/G-B is used to infer the associated value of R/G-B shoreline and the contour position  $(x, y)$ , while assuming that two close contours of R/G-B values at the shoreline have similar shapes. The shorelines calculated from the original timex images (Fig. 2.8) are then rectified. To reduce the longshore detection error, shoreline video positions are averaged alongshore.

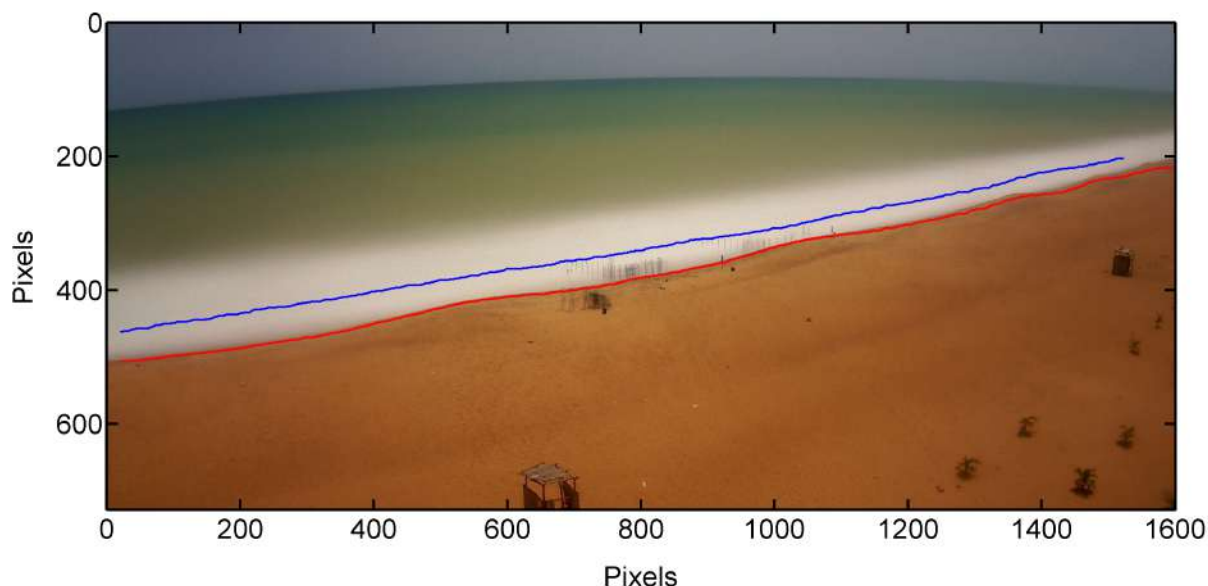


**Figure 2.8** – Example of shoreline detection for a tidal cycle: low tide (blue) and high tide (red).

Determination of the daily intertidal beach profile involves the delineation of the shoreline at different tidal levels and interpolation between low and high tides day by day (Plant and Holman, 1997; Aarninkhof et al., 2003).

### Wave celerity estimation

To estimate wave celerity from video images, only the temporal approach can be used here because of the type of timestack images that have been stored. For this purpose, the rectified timestack images are pre-treated to clean the wave intensity signal. Given that the wave climate is characterized by average period of about 9–10s, a bandpass filter between 0.05 and 0.5Hz is used to remove low-frequency and high-frequency noise (Almar et al., 2008). Low-frequency noise can be induced by light fluctuations due to clouds, or any other process with a periodicity greater than 20 s. High-frequency noise can be induced by wind waves or a rapid adjustment of the camera auto iris, with a periodicity lower than 2 s.

To derive the celerity  $C_{jt}$ , a celerity-sensing method is applied for each filtered image at time  $t$  on cross-shore location  $j$  (Almar et al., 2008; Bergsma and Almar, 2018). Considering an image at time  $t$ , a temporal cross-correlation matrix  $M$  is computed at each pixel  $j$  with the neighboring pixel  $k$ , imposing an arbitrary (but lower than half the wave period) time lag  $\Delta t = 3s$ :

$$M_{j,k} = cor [\eta(j, t_{1:n_t}), \eta(j+k, t_{1:n_t} + \Delta t)], k = 1, 200 \quad (2.13)$$

where  $\eta(j, t_{1:n_t})$  is a time series of water level variations in pixel intensity at position  $j$  for a duration  $t(n_t)$ .

The index  $k_{max}$  with the maximum correlation gives an estimate of the time-integrated distance  $\Delta X_j$  made by waves during  $\Delta t$  at position  $j$ ,

$$\Delta X_j = \sum_{p=j+1}^{j+k_{max}} \Delta X_0(p). \quad (2.14)$$

The pixel footprint  $\Delta X_0$  depends on the pixel location. A local estimate of the celerity at pixel  $j$  at time  $t$  is:

$$C_{jt} = \Delta X_j / \Delta t. \quad (2.15)$$

### Depth inversion scheme

The depth inversion scheme is based on the linear dispersion relation (Eq. 1.1) for free surface waves, which requires two of the three free variables (wavelength  $L$ , wave period  $T$ , and wave celerity  $C$ ) to be solved (Almar et al., 2008; Bergsma and Almar, 2018). After rearranging the linear dispersion relation (Eq. 1.1) for free surface waves, depth can be found as a function of the wave celerity  $C_{jt}$  (Fig. 3.2):

$$d_{jt} = \frac{\tanh^{-1} \left( \frac{2\pi C_{jt}^2}{gL_{jt}} \right)}{\frac{2\pi}{L_{jt}}} \quad (2.16)$$

This equation can be rearranged as follows (considering the wave number  $k_{jt} = 2\pi/L_{jt}$  and the wave pulsation  $w_{jt} = k_{jt}C_{jt}$ ):

$$w_{jt}^2 - gk_{jt}\tanh(k_{jt}d_{jt}) = 0 \quad (2.17)$$

An estimate of the depth  $d_{jt}$  can therefore be given using Newton's algorithm for the computation of non-linear equations :

$$d_{jt(n+1)} = d_{jt(n)} - \frac{w_{jt}^2 - gk_{jt}\tanh(k_{jt}d_{jt(n)})}{\frac{-g(k^2)}{\cosh(k_{jt}d_{jt(n)})^2}} \quad (2.18)$$

with the stop condition:

$$d_{jt(n+1)} - d_{jt(n)} < \alpha; n = 1, \infty. \quad (2.19)$$

$\alpha$  reflects the required accuracy. The initial depth value in the algorithm is chosen for ideal

shallow water conditions:

$$d_{jt(1)} = C_{jt}^2/g \quad (2.20)$$

Following that  $w_{jt} = \frac{2\pi}{T_t}$  and  $L_{jt} = c_{jt}T_t$ , depth inversion requires knowledge of the wave period. Here, the upward zero-crossing method is applied on a rectified and filtered timestack image at time  $t$  to estimate the mean wave period  $T_t$  (Fig. 2.9).

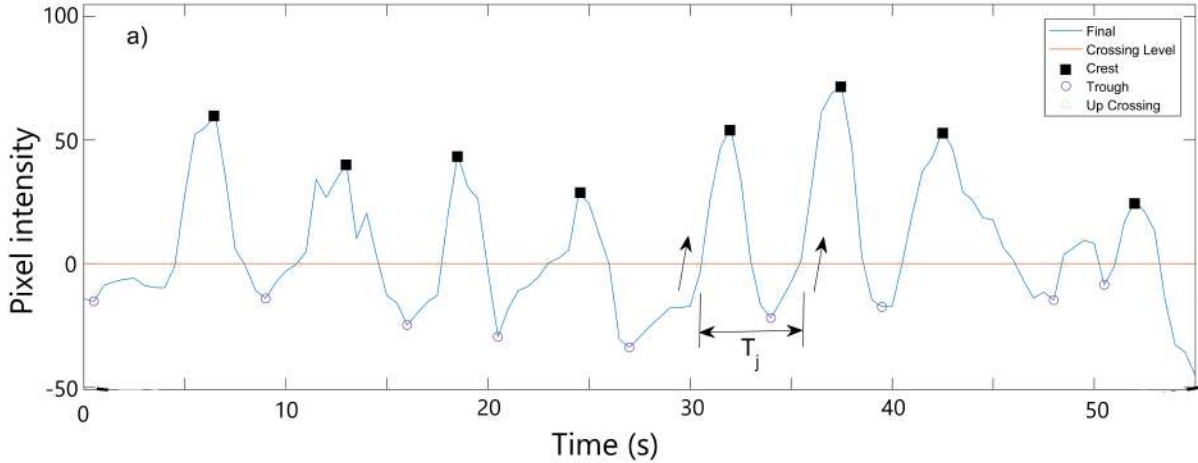


**Figure 2.9** – Wave period estimate using upward zero-crossing method applied to a filtered time series of pixel intensity.

### Error estimates in video-derived shorelines and bathymetry

The accuracy in shoreline detection is limited by horizontal uncertainties caused by the wave-induced set-up (Aarninkhof et al., 2003), image rectification (Plant et al., 2007), and shoreline identification error equal to the pixel footprint  $\Delta X_0$ . The rectification error ranged between 0.5 and 5 m depending on pixel location.  $\Delta X_0$  increases seaward from 0.05 m on the beach to approximately 1 m at 10-m depth, due to the oblique angle of view of the camera within the region of interest. The rectification error and  $\Delta X_0$  also affect the accuracy in video depth estimation. However, Bergsma and Almar (2018) showed that the main source of errors for video depth estimation can be related to the limited validity of the linear dispersion relation in the shallowest parts of the nearshore. Brodie et al. (2018) showed that the effects of pixel saturation due to wave breaking can reduce the accuracy of the method at breaking area. Camera movements are another source of error (Bouvier et al., 2019); but they were deemed small at Grand Popo in Benin, with no influence in the area of interest where  $\Delta X_0$  is lower than 1 meter (Fig. 2.6 b). Bergsma et al. (2016) showed that fluctuations of the sea surface with the tide change the geographical pixel locations on the video image, thus adding an error to the video-derived depth. The overall computation showed a horizontal error that was smaller than 1 m on the upper beach, but varied from less than 1 m to 5 m seaward.

Two estimators have recently been proposed in the literature: wavelength estimate  $L_0$  (Bergsma and Almar, 2018) and tidal error proxy (Thuan et al., 2019). The first measure compares two calculated speed estimates with the cross correlation in the time domain, and the second compares the observed tides with the estimated tides by video. The latter estimator seemed to cover most of the reported types of errors in a single result (Fig. 2.10). Interestingly,

considering these error proxies through assimilation in a filter (such as Kalman filter) could increase the accuracy and robustness of celerities and bathymetry estimates.

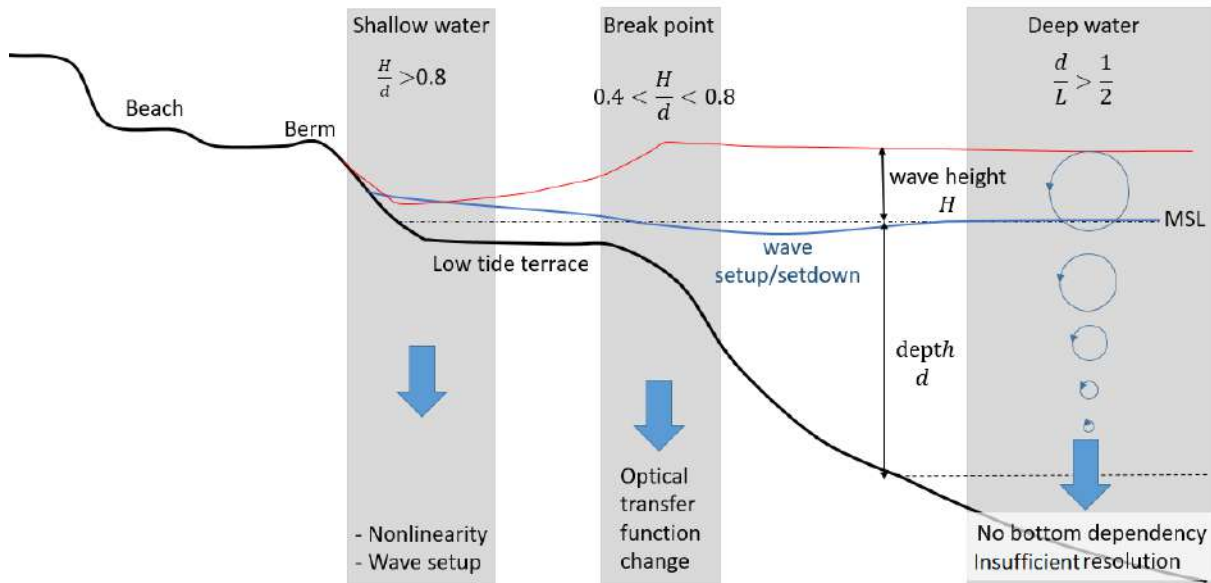


**Figure 2.10** – Description of the main sources of error for the use of video-based depth inversion methods. Namely, non-linearity and wave-setup in shallow area, optical modulation transfer function change at the breakpoint and relative deep water conditions for shortest waves (figure by [Thuan et al. 2019](#)).

## Chapter 2 summary

This chapter focused on the hydrodynamic and morphological characteristics of the coast in the [BoB](#), with particular emphasis on the different data and methods to be used for this thesis.

### The [BoB](#)

- More than 400 km long
- Bordered by the Niger River delta in the east and the Volta River delta in the west
- Sand barrier with lagoonal and lacustrine system
- Dominant southwesterly swells (mean values:  $H_s = 1.36$  m;  $T_p = 9.4$  s)
- Easterly longshore sediment transport (up to 1.2 million m<sup>3</sup>/year)
- Continuous horizontal propagations of sea level fluctuations (Kelvin waves)
- Three main deep-water harbors (Lagos, Cotonou and Lomé)
- Several rivers mouths and reduction of sediment discharges due to dams
- [GPP](#) is representative of the natural undisturbed Low Tide Terrace to reflective beaches of the [BoB](#)

### Data

- 10-days of field measurements at [GPP](#) (hydrodynamic and morphological data)
- Wave data from ERA-Interim ECMWF re-analyses (6-hour frequency)
- Tide data from 2-years Cotonou tide gauge measurements and FES2014 model
- Altimetry provides sea level time series (daily) and shorelines ( $\sim 400km$  every 5 years)
- 15-min video data from February 2013 that were used to derive shorelines ( $\sim 500m$ ) and bathymetry (up to 10 m depth)
- Two estimators recently proposed in the literature could be used to increase the accuracy and robustness of video-derived depths.

## 2.4 Conclusion

Before studying coastal processes in the [BoB](#) at large spatial and temporal scales, it is crucial to understand coastal dynamics at shorter scales, at a suitable pilot site such as the [GPP](#). However, the main data collected during the field measurement campaign are limited to 10 days. And the video data collected since 2013 could help to understand local dynamics, especially since the recent techniques presented here allow to extract several morphological features from the video images (shoreline and bathymetry). From this point of view, the formatting and processing of these data are crucial for the continuation of this thesis. And several improvements can be made to current processing techniques, including the implementation of error proxies in the depth estimation algorithm as suggested in the literature. In the next chapter, we will focus on improving the processing of video image.

---



# Chapter 3

## Improvement of depth inversion scheme and sea level estimation from video imagery

### Contents

---

<b>3.1</b>	<b>Introduction</b>	<b>49</b>
<b>3.2</b>	<b>New approach in the temporal method of estimating wave celerity</b>	<b>50</b>
3.2.1	Approach statement	50
3.2.2	Validation of video-derived depths	51
<b>3.3</b>	<b>Error proxies in video-based depth inversion: temporal celerity estimation</b>	<b>52</b>
3.3.1	Background	53
3.3.2	Depth Error Estimates	54
3.3.3	Kalman filter	54
3.3.4	Results	55
3.3.5	Discussion	57
3.3.6	Conslusion	57
<b>3.4</b>	<b>Sea level at the coast from video-sensed waves</b>	<b>58</b>
3.4.1	Background	58
3.4.2	Water level estimation	60
3.4.3	Results	61
3.4.4	Discussion	64
3.4.5	Conslusions	67
<b>3.5</b>	<b>Conclusion</b>	<b>68</b>

---

### 3.1 Introduction

Although bathymetric estimates derived from video images allow to track the beach profile evolution from the scale of events to decades (Bergsma et al., 2019b), they remain noisy and issues related to the accuracy of these estimates are still relevant. Bergsma and Almar (2018) and Thuan et al. (2019) have introduced two error proxies that could improve the accuracy of depth estimates using the temporal approach if assimilated in a filter (e.g. Kalman). In addition,

these high-frequency depth estimates could provide an estimate of the total water level on the coast, including wave contributions that are difficult to measure with tide gauges and altimetry (Melet et al., 2016, 2018a).

In this chapter, we describe some improvements in video techniques, in particular the temporal method, for estimating nearshore depth and coastal water levels. Section 3.2 presents a new approach for wave celerity estimation. Sections 3.3 addresses the use of the specific proxies reported in the literature to reduce errors in video estimates of bathymetry. Section 3.4 explores the use of bathymetry estimates to derive sea level changes at the coast.

## 3.2 New approach in the temporal method of estimating wave celerity

### 3.2.1 Approach statement

In the temporal method for wave celerity estimation, the rectified timestack images were filtered around the frequency of the incident wave ( $\sim 0.1$  Hz) by defining two cut-off frequencies, high ( $\sim 0.5$  Hz) and low ( $\sim 0.05$  Hz), in order to retain only the incident wave signal. However, the video signal is still noisy due to all the harmonics contained in the filtered signal spectrum (see figure 3.1 according to Almar 2009). Figure 3.1 presents a pixel intensity spectrum that is much wider than that of water height, although they present the same peaks.

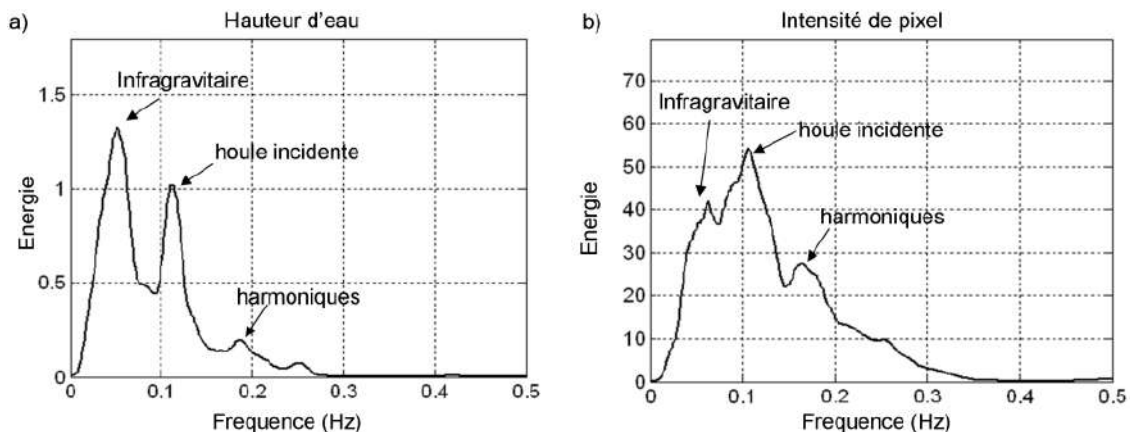


**Figure 3.1** – Spectral distribution. Time series spectra of (a) water height and (b) pixel intensity (figure by Almar 2009).

To remove harmonics other than those involved in wave propagation, the main harmonic components are first extracted from the pixel intensity spectrum on a timestack image. Then, for each spectral component  $f_i$ , a bandpass filter between  $f_i - \Delta f_i$  and  $f_i + \Delta f_i$  is applied to the timestack image that has already been rectified and filtered once.  $\Delta f_i$  is selected manually. The celerity  $C_{ijt}$  associated with the spectral component  $f_i$  at position  $j$  on the cross-shore stack at time  $t$  is estimated using the temporal method (see equations 2.13, 2.14 and 2.15). Depths  $d_{ijt}$  are also extracted for each spectral component  $f_i$  using equations 2.18, 2.19 and 2.20. A specific coefficient  $C_0$  is therefore used to merge depths:

$$d_{jt} = \sum_{i=1}^N \left( \frac{C_{0ijt}}{\sum_{i=1}^N C_{0ijt}} d_{ijt} \right) \quad (3.1)$$

with

$$C_{0ijt} = 1 - \frac{C_{ijt}}{C_\infty} \quad (3.2)$$

where  $C_\infty$  is given by equation 1.2 and  $N$  is the number of the main harmonics.

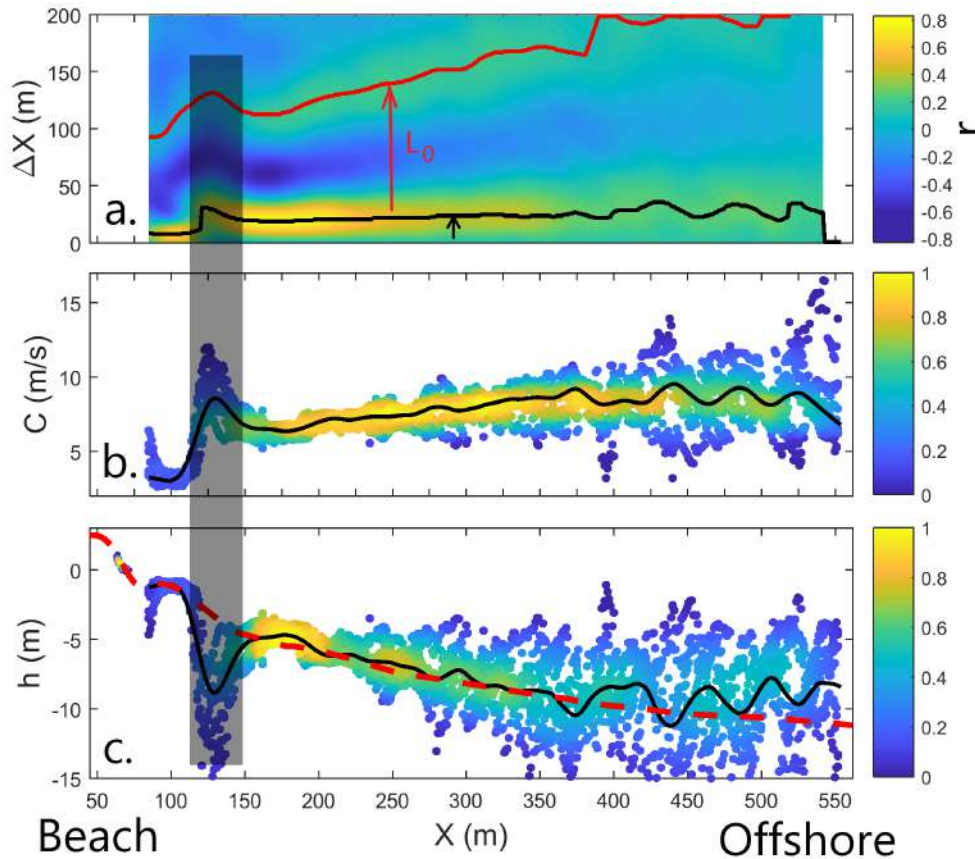


**Figure 3.2** – Temporal approach for depth inversion scheme during the Grand Popo experiment from March 10 to 19, 2014: (a) Cross-correlation matrix. The colors represent the correlation per cross shore  $X$  (from the camera location) for a range of  $\Delta X$ . The color limits represent maxima out-of-phase and in phase correlation. The blackline indicate the first local maximum of correlation ( $\Delta X_0$  is given by the black arrow) and the red line the second successive local maximum correlation. This second local maximum correlation gives an estimate of the wavelength  $L_0$ . (b) Wave celerities and (c) depth estimates. In (b) and (c), the colors represent the relative density of estimates. The dashed red line in (c) represents in-situ topography and bathymetry. The shaded area stands for the breaking zone where pixel saturation limits the capacity to accurately determine depths.

### 3.2.2 Validation of video-derived depths

The validation results were presented in [Abessolo et al. \(2017\)](#) (see Appendix II). The implementation of this approach results in an average profile that correlated 80% with the profile measured during Grand Popo 2014 field measurements (see Fig. 3.2). The results unveiled the maximum vertical error that was about 0.15 m for the daily depth, along the part of the profile covering the upper beach and the lower part of the terrace (50 to 130 m). The whole beach profile can be derived by merging the daily intertidal and bathymetric profiles. Figure 3.3 presents a first daily full depth profile derived from video imagery. The observed depth changes suggest that the beach profile varies as follows. The terrace width increases during the winter period (June-July-August) when wave energy is high and decreases during the austral summer

period (December-January-February) when wave energy is low. In addition, an erosive trend of  $-1.6$  m/yr is observed for the upper beach; this trend seems to be even stronger at the end of the terrace ( $-3.1$  m/yr).

The techniques developed here therefore make it possible to extract from video images significant information about the dynamics of a beach profile. However, this improvement does not remove all depth inversion errors, including the one caused by wave breaking. In Figure 3.2, the effects of pixel saturation (shaded area) due to wave breaking are clearly visible, reducing the accuracy of the method in the breaking area. By limiting the study of the profile between 50 and 130 m, we're then beyond the surf zone, with an averaged error of 0.15 m (Fig. 3.3).

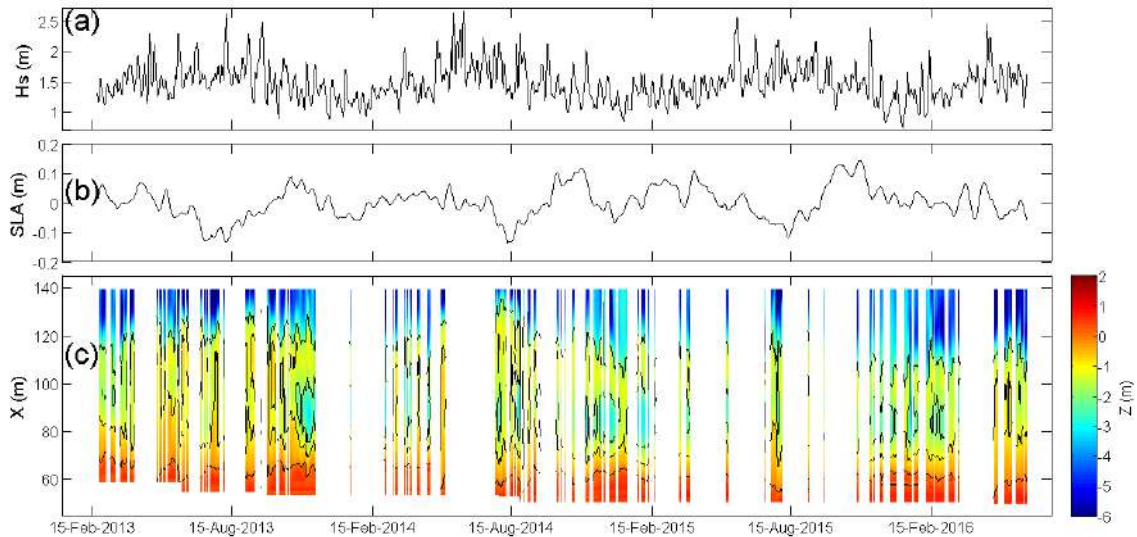


**Figure 3.3** – Forcing parameters and beach evolution at Grand Popo, Benin: (a)  $H_s$ , (b) SLA, and (c) video-derived depths ( $Z$ ), for the period February 2013 to August 2016.  $X$  stands for the cross-shore location from the video camera. Black lines in panel (c) stand for the 0- to 2-m depth contours.

### 3.3 Error proxies in video-based depth inversion: temporal celerity estimation

As discussed in Chapter 1, the temporal celerity-based depth inversion method does not yet have an error proxy to improve the robustness and the accuracy of the estimates. This section presents a first attempt to use of error proxies in the temporal method. The results presented in this section have been accepted for publication.

#### Article's reference

**Abessolo, O.G.**, Almar, R., Bergsma, E. and Bonou, F., 2020. Error Proxies in Video-Based Depth Inversion: Temporal Celerity Estimation. In: Malvárez, G. and Navas, F. (eds.), Proceedings from the International Coastal Symposium (ICS) 2020 (Seville, Spain). Journal of Coastal Research, Special Issue No. 95, pp. 1101–1105. Coconut Creek (Florida), ISSN 0749-0208.

## Abstract of the paper

The accuracy of bathymetric measurements is crucial, especially to understand coastal processes. Video-based depth inversion methods have been widely developed in recent years, but they remain noisy, with typical errors due to the breakpoint optical and non-linear effects. Among the spectral and temporal approaches to video depth inversion, only the spectral approach applies an error criterion to identify erroneous data. Here, two error proxies are assimilated for the first time in the temporal approach, using a Kalman filter applied to 3.5 years (February 2013 to September 2016) of video images. Differences between filtered and unfiltered bathymetries were observed to be correlated with the proxies considered. A validation with field data on a 10-day experiment is performed between the original bathymetries and the filtered bathymetries. The results indicate that the mean square error can be reduced by at least 30%. Both proxies show good ability to correct depth estimates. Although the results are promising, validation of these approximations must be performed under various hydrodynamic and atmospheric conditions.

### 3.3.1 Background

Among the variables useful for understanding and modelling coastal dynamics and variability, bathymetry is probably the most critical (Holman et al., 2013). The boundary conditions of the prediction models must be based on accurate bathymetric information over time (hours to years) and at the spatial scale (local to regional).

Traditionally, coastal depths are measured by the flight time of an acoustic signal reflected by the bed, generated by the on-board echo sounder technology. More recently, video imagery or X-band radar has been used to accurately estimate depths (Bergsma and Almar, 2018). Derived approaches are methods of depth inversion with linear dispersion relationship (Holman and Stanley, 2007; Bergsma and Almar, 2018), non-linear depth inversion (Catalan and Haller, 2008), extended Boussinesq equations (Misra et al., 2003) and coupling video models on wave energy dissipation by wave energy dispersion models (Aarninkhof et al., 2005). In the typical case of depth inversion methods with linear dispersion relationship, two main approaches exist: a time method and a spectral method. Video-based bathymetric inversion methods have been developed for more than 20 years. They have been calibrated and validated in various environments and should withstand various data failures (camera failure, fog or obscure raindrops) or low signal-to-noise ratio (no wave or signal saturation due to solar glare). But the video bathy remains noisy, with typical errors due to the optical and non-linear effects of the breaking points (Thuan et al., 2019; Bergsma and Almar, 2018). Although reducing these errors is difficult (Brodie et al., 2018), their effects can be overcome by assimilation. It is essential to define a robust error criterion, which is fundamental to improving depth estimates.

A fitting error has been implemented in the spectral method (cBathy, see Holman et al. 2013) to identify the erroneous data, extract a set of useful data, using a Kalman filter. The aim is to limit failures and fill gaps with better estimates, using a time-running average. The temporal method does not yet incorporate such a method-based error estimate. A major challenge for the temporal method is to evaluate the validity of the method associated with similar induced errors on bathymetric estimation (Thuan et al., 2019). Two estimators have recently been proposed in the literature: wavelength (Bergsma and Almar, 2018) and tidal error proxies (Thuan et al., 2019). The first measure compares two calculated speed estimates with the cross correlation in

---

the time domain, and the second compares the observed tides with the estimated tides by video.

In this work, the two error proxies are evaluated for the first time in the temporal depth inversion method, using a Kalman filter. First, the two error proxies were derived from a 3.5-year video dataset (February 2013 to September 2016) at 15-min acquisition time. Second, error proxies were used in a Kalman filter to calculate a moving average that smoothes out individual daily estimates. Finally, the effectiveness of the proxies used is evaluated by comparing the original bathymetry and the filtered bathymetries.

### 3.3.2 Depth Error Estimates

Figure 3.2 shows that wave celerity can be estimated using two approaches. The classical approach considers the distance  $\Delta X_0$  to estimate wave celerity (see section 2.3.5). Bergsma and Almar (2018) proposed a new approach based on a direct correlation to estimate the celerity, considering the wavelength  $L$  (illustrated by the second thinner red line in Fig. 3.2). Even though the use of a time lag  $\Delta t$  is preferred to the direct cross-correlation (due to the increase of spatial resolution, see Bergsma and Almar 2018), the wavelength  $L$  for the associated period  $T$  and after  $C = L/T$  can be used to approximate a method-based error, as in the spectral method (cBathy, see Holman et al. 2013). The error proxy associated with  $C = L/T$  can be defined as follows:

$$\Delta_{WL} = |h_{jt} - h'_{jt}| \quad (3.3)$$

where  $h_{jt}$  and  $h'_{jt}$  are depths derived from equation 2.15 and  $C = L/T$  respectively.

Thuan et al. (2019) provided another estimator that seems to cover most of the reported types of errors in a single result. The estimator was based on the comparison of tides between in-situ and video. Tides were derived from video by estimating time-varying total water levels by applying the temporal celerity-based depth inversion method (Thuan et al., 2019; Abessolo et al., 2019). These methods are detailed in the next section. By assuming little and negligible morphological change over a single day, the instant-derived depth  $h_{jt}$  can be separated between the bathymetry  $D_{jt}$  and total water level  $\eta$ :

$$h_{jt} = D_{jt} + \eta \quad (3.4)$$

Then the video-derived tides at pixel  $j$  and time  $t$  are obtained by removing the 1-day (or n-days) moving average from instant depths  $h_{jt}$ .

The error proxy associated with tides can be defined as follows:

$$\Delta_{tide} = |\eta_{in} - \eta'_{vid}| \quad (3.5)$$

where  $\eta_{in}$  and  $\eta'_{vid}$  are tides derived from ADCP and equation 3.4 respectively.

More details on estimating water levels from video are given in the next section.

### 3.3.3 Kalman filter

The Kalman filter consists on computing a time-running average that smoothes instant depths estimates in a way that objectively weights the confidence in the new estimate with that of the prior running average (Holman et al., 2013). At any location, the Kalman filter updates

the prior depth estimate  $\hat{h}_k$  by comparing the believability of the new estimate  $\bar{h}_k$  with that of the prior  $\hat{h}_k$ .

$$\bar{h}_k = \bar{h}_{k-1} + K_k (\hat{h}_k - \bar{h}_{k-1}) \quad (3.6)$$

where  $k$  and  $k-1$  represent an adjacent pair of sampling times. If the Kalman gain  $K_k = 0$ , the new estimate makes no contribution whereas if  $K_k = 1$ , the prior estimate is ignored (Holman et al., 2013).

$$K_k = \frac{P_k^-}{P_k^- + R_k} \quad (3.7)$$

$$P_k^- = P_{k-1} + Q\Delta t \quad (3.8)$$

with  $P_{k-1}$  the error variance of the running average at time  $k-1$ .  $\Delta t$  is the time interval in days between estimates and  $Q$  the process error, representing unmodeled natural variability (depth changes) that occur under the action of waves and currents.  $R_k$  is the error associated with the prior estimate  $\hat{h}_k$ . Details can be found in Holman et al. (2013). In this work, the two error proxies  $\Delta_{tide}$  and  $\Delta_{WL}$  were considered as the error associated with the prior estimate  $\hat{h}_k$  to evaluate Kalman filtering.

### 3.3.4 Results

#### Error proxies variations

The error proxies  $\Delta_{tide}$  and  $\Delta_{WL}$  are shown in Fig. 3.4. The two proxies have different physical characteristics.  $\Delta_{tide}$  is consistent with breakpoint error and nonlinear effects during shoaling and in shallow water, due to the breakpoint optical effect on the video images and the deep water limitation (Thuan et al., 2019, Bergsma and Almar, 2018).  $\Delta_{WL}$  is more marked by the breakpoint error and the nonlinear effects in the surfzone, and less by the deep water limitation.

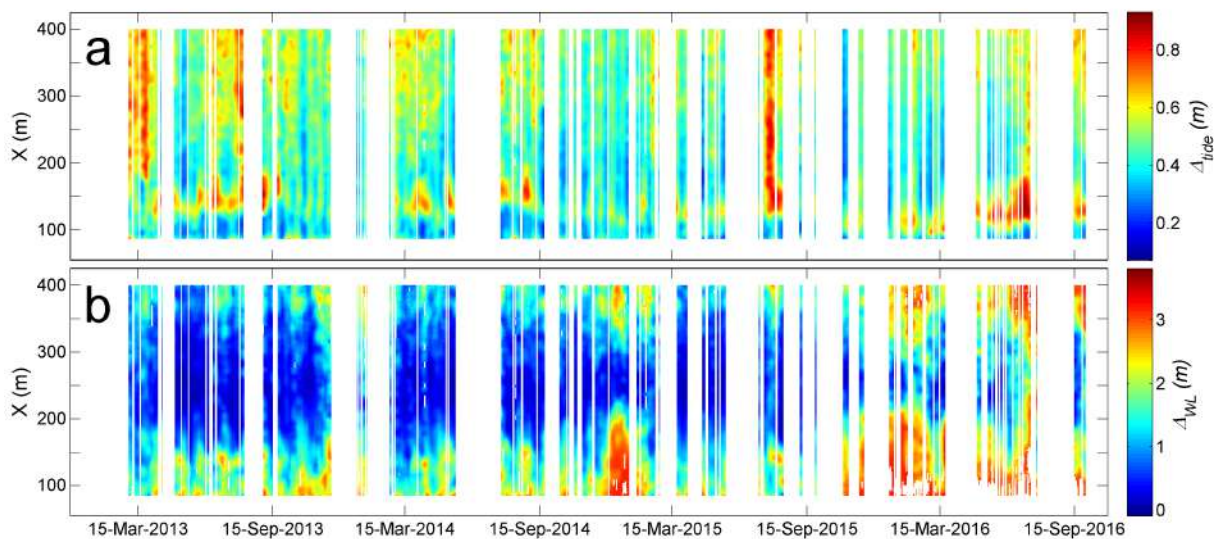


**Figure 3.4** – Errors proxies: a. Tidal differences ( $\Delta_{tide}$ ) between FES2014 and video tide estimates. b. Wavelength differences ( $\Delta_{WL}$ ) from the two celerity estimates.  $X$  extends from the camera location. Timeseries were smoothed over 15 days.

Using the two proxies  $\Delta_{tide}$  and  $\Delta_{WL}$  in a Kalman filter, the corrected bathymetries are derived and shown in Fig. 3.5. The relationship between  $\Delta_{tide}$  and  $\Delta_{WL}$  and the accuracy on depth estimates is investigated in Fig. 3.6 a-b. Overall, there is a good agreement between reconstructed and observed differences between filtered and the original bathymetries throughout the study period (February 2013 to September 2016), with regression coefficients equal to 0.97 and 0.93 (both significant at 95% level). The linear regression shows an important physical link between the proxies and the observed bathymetric differences. For maximum values of error proxies, there are obviously large differences between the original and filtered bathymetries. This suggests that the higher the values of the two proxies  $\Delta_{tide}$  and  $\Delta_{WL}$ , the less reliable the depth estimate should be.

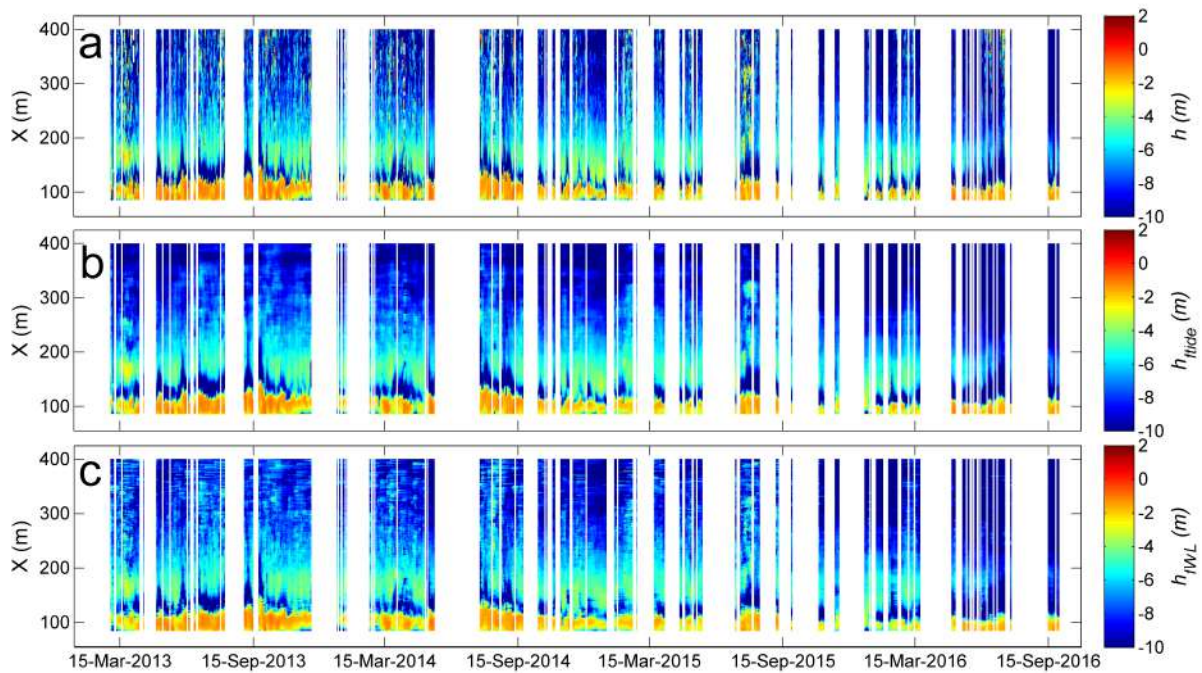


**Figure 3.5** – Daily bathymetry. a. Original bathymetry ( $h$ ) derived from video inversion. b. Bathymetry filtered with Kalman using  $\Delta_{tide}$  proxy ( $h_{ftide}$ ). c. Bathymetry filtered with Kalman using  $\Delta_{WL}$  proxy ( $h_{fWL}$ ).

### Validation of filtered estimated bathymetry with in-situ bathymetry

In this section, the original ( $h$ ) and filtered depth estimates ( $h_{ftide}$  and  $h_{fWL}$ ) are compared with the in-situ measurements of Grand Popo 2014 campaign (Table 1). Three statistical parameters were evaluated: correlation ( $R^2$ ), root mean square error (RMSE) and mean error (ME). The filtered bathymetries show a significant improvement in all statistical parameters. In particular, there is an improvement of 36 % in the RMSE for  $h_{ftide}$  with the  $\Delta_{WL}$  error proxy, while the Kalman-filter using  $\Delta_{tide}$  reduces the ME on depth estimation by 64 %. The two error proxies therefore lead to some improvements.

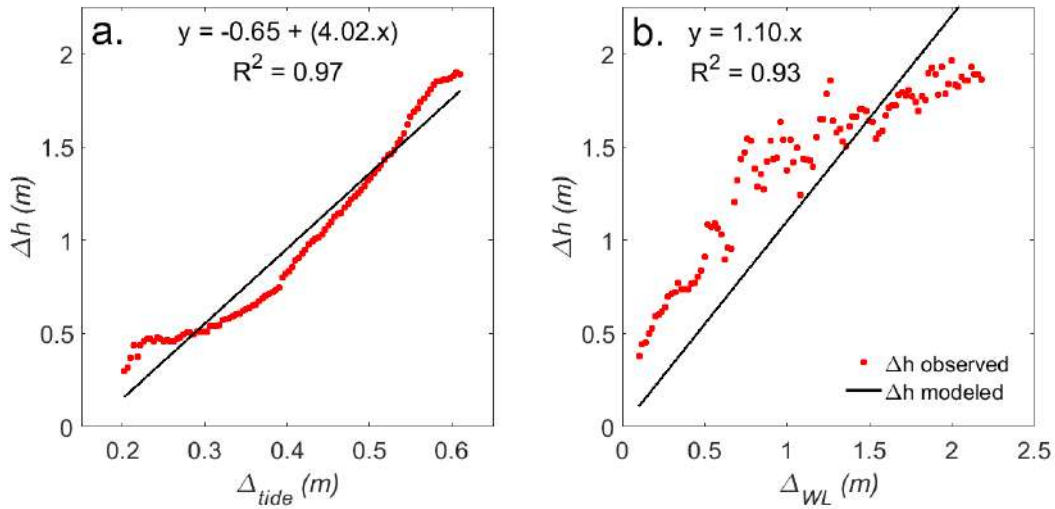


**Figure 3.6** – Comparison between observed and reconstructed differences ( $\Delta h$ ) between original bathymetry and filtered bathymetry using  $\Delta_{tide}$  proxy (a) and  $\Delta_{WL}$  proxy (b) for the study period (February 2013 to June 2016). Observed and reconstructed differences were averaged (using median) over a 0.01 m-window interval on the x-axis. Outliers with values upper than 90th percentile were removed.

Depths	h	$h_{\Delta_{tide}}$		$h_{\Delta_{WL}}$	
$r$	0.67	0.82	+24 %	0.78	+18 %
RMSE (m)	2.33	1.50	-36 %	1.62	-30 %
ME (m)	0.74	0.36	-51 %	0.27	-64 %

**Table 3.1** – Comparison of original (h) and filtered depth ( $h_{\Delta_{tide}}$  and  $h_{\Delta_{WL}}$ ) with measured field-depth measured during Grand Popo 2014 from March 11<sup>th</sup> to 19<sup>th</sup>, 2014

### 3.3.5 Discussion

The two error approximations allow a good evaluation of the errors associated with depth estimates, as observed in Fig. 3.6. Non-linear effects on the terrace and offshore appear to be well resolved. However, at this stage, it is still difficult to choose among the two error proxies the one with the best improvement rates. This requires a validation in various environments with various hydrodynamic and atmospheric conditions. The validation period will have to be extended, as it remains for the moment limited to 10 days. On another point of view, since the two error proxies have different physical bases, it would be possible to make a multi-parameter implementation in a Kalman filter, and to assimilate the data with a model to better constrain the results. It is therefore still necessary to continue to document this work in order to fully understand the effect of these approximations on the bathymetric estimate.

### 3.3.6 Conclusion

This article presents the first time implementation of two error proxies in a video depth time inversion method, using a Kalman filter. The two error proxies were derived for the 3.5-year video data case study in Grand Popo, Benin. The differences between filtered and unfiltered derived bathymetries are observed to be correlated with the proxies considered. By comparing the depths derived from the video with 10-day in situ measurements, the two error proxies

improve the depth estimate. The tidal error proxy reduced the RMSE root mean square error by 36% while the wavelength error proxy reduced the ME root mean error by 64%. However, validation must be implemented for various hydrodynamic and atmospheric conditions in order to select the one with the best improvement rates from the two proxies.

### 3.4 Sea level at the coast from video-sensed waves: comparison to tidal gauges and satellite altimetry

In Chapter 1, we referred to the need of the nearshore research community to develop new observational tools to provide accurate water-level measurements at complex and energetic coasts, including all contributions to total sea level. This section focuses on the capacity of shore-based camera and video systems to obtain total sea levels at an open coast. Here, we utilize a celerity-based depth inversion method, conventionally used to derive bathymetry, to obtain time-varying depth, which under certain assumptions can provide a measure of total sea levels over the period from February 2013 to August 2016 at [GPP](#). The results presented in this section have been published.

#### Article's reference

**Abessolo, G.O.**, Almar, R., Castelle, B., Testut, L., Leger, F., Sohau, Z., Bonou, F., Bergsma, E., Meyssignac, B., Larson, M., 2019. Sea Level at the Coast from Video-Sensed Waves: Comparison to Tidal Gauges and Satellite Altimetry. *Journal of Atmospheric and Oceanic Technology*, 36, 1591-1603.

#### Abstract of the paper

Nearshore complex and energetic hydrodynamic conditions make observing evolving processes during extreme and short-term events difficult. In particular, total sea levels at the coast are hard to measure with current techniques. Sea level is commonly measured with tidal gauges and spaceborne altimetry, which lack essential details of spatial and wave-related sea level variability along the coast. Hence, novel techniques, adapted to nearshore areas, are required. This paper presents the first-time use of video cameras to derive the total sea level at the coast. This novel approach consists of estimating time-varying total water levels by applying a celerity-based depth inversion method, which is conventionally used to estimate bathymetry from video. The video-derived total sea levels are compared to sea levels derived from an in situ acoustic Doppler current profiler (ADCP), the nearest tide gauge, and altimetry. A tidal harmonic analysis is performed on the video-derived water levels, yielding an accurate determination of the dominant tidal harmonics. However, it remains difficult to separate bathymetric changes due to the waves on beaches when rapid morphological changes occur under energetic conditions. Nonetheless, video-derived water-level anomalies are in good agreement with state-of-the-art altimetry products. Although there is still work to be done, the results show the potential to measure total sea level at the coast using video camera systems.

#### 3.4.1 Background

The nearshore coastal zone is the interface between land and the continental shelf ([Komar, 1999](#)). Coastal areas are often densely populated and evolve under an increasing threat from sea

---

level rise, long-term erosion, extreme storms, and anthropogenic influences (Vousdoukas et al., 2018; Anderson et al., 2018). Remote sensing and in situ instrumentation enabled improved understanding of nearshore hydro- and morphodynamic processes. However, complex and energetic hydrodynamic conditions reduce the possibility to observe a range of processes, such as total coastal sea level fluctuations.

There is a need for observations of sea level at the coast (Cazenave et al., 2018; Melet et al., 2018a). More than in other geosciences, nearshore research historically faces difficulties in investigating the complex and energetic environment. Satellite altimetry, optimized for the open ocean, performs poorly within 25 km of the coast since landmasses perturb the radar signal (Cipollini et al., 2017). Over the past 10 years, significant progress has been made to improve available altimetry data at the coast through several projects, for example, X-TRACK (Birol et al., 2017), PISTACH (Prototype Innovant de Système de Traitement pour les Applications Cotières et l’Hydrologie) and Prototype for Expertise on Ka-Band Altimeter (AltiKa) for Coastal, Hydrology and Ice (PEACHI; Valladeau et al. 2015), and Adaptive Leading Edge Sub-waveform (ALES) retracker (Passaro et al., 2014). More is to be expected from the French–U.S. Surface Water and Ocean Topography (SWOT) mission. Despite these efforts, spaceborne altimetry still has a relatively low spatial and temporal resolution compared to coastal spatiotemporal scales. Similarly, most tide gauges are limited to deep water or sheltered harbors and omit part of the natural total sea level variability at open coasts (Melet et al., 2016). New radar gauges are exposed to wave effects nowadays but there remains a challenge to understand wave effects on these sensors. Intensive nearshore field experiments with high spatial and temporal sampling rates are scarce. Bathymetric surveys with echo sounders are time consuming and often contain data gaps between the bathymetry and the topography, especially in the micro- to mesotidal regimes. As a result, bridging the knowledge gap between short-term, small-scale dynamics and long-term evolution is a major challenge. This generally holds for most major recent studies dealing with sea level at the coasts (e.g., Birol et al. 2017; Idzanovic et al. 2018b; Segura et al. 2018; Melet et al. 2018a).

Such limitations also reflect the existing knowledge gap of total sea level propagation across the shelf to the shore during extreme events in which processes vary rapidly. The nearshore research community, therefore, needs new, better suited, observational tools to provide accurate water-level measurements at complex and energetic coasts, including all contributions to total sea level. The total sea level at the coast (SL) is the superposition of oceanographic, meteorological, hydrological, and geological forcing and constraints (Slangen et al., 2017). This includes contributions due to global warming of the ocean and the transfer of water mass from land ice, land water storage, ocean circulation, and water density variations at global and regional scales [sea level anomaly (SLA)], local effects of astronomical tide (AT), atmospheric surges [inverse barometer (DA) and atmospheric wind (Wi)], and wave transformations  $W$  in the surf zone (Melet et al., 2016; Slangen et al., 2017). Therefore, the total sea level can be described by:

$$SL_{jt} = SLA_{jt} + AT_t + DA_t + Wi_{jt} + W_{jt} \quad (3.9)$$

Coastal video monitoring systems provide an excellent response to the challenge of observing the water-level contributions at a larger spatial scale. It now offers access to 15-min frequency and long-term description of the near shore (Holman and Stanley, 2007; Almar et al., 2014; Pianca et al., 2015; Angnuureng et al., 2016; Abessolo et al., 2017; Bergsma et al., 2019b). During the last few decades, progress has been made on estimating variables from shore-based

video imagery, such as shoreline position (Boak and Turner, 2005; Almar et al., 2012b), intertidal beach morphology (Uunk et al., 2010; Osorio et al., 2012), breaking wave height (Almar et al., 2012a), nearshore currents (Radermacher et al., 2014; Almar et al., 2016), water level in the swash zone (Ibaceta et al., 2018), and nearshore bathymetry (Holman et al., 2013; Bergsma et al., 2016; Bergsma and Almar, 2018; Brodie et al., 2018). This paper focuses on the capacity of shore-based camera and video systems to obtain total sea levels at an open coast. Here, we utilize a celerity-based depth inversion method, conventionally used to derivate bathymetry, to obtain time-varying depth, which under certain assumptions can provide a measure of total sea levels. We present a comparison of video-derived water levels with tide gauges and spaceborne altimetry at Grand Popo beach in Benin, Gulf of Guinea, over a period from February 2013 to August 2016.

### 3.4.2 Water level estimation

The littoral zone is defined as the part of the beach profile where sediment can be transported by wave action (Davidson-Arnott, 2010b). On longer time scales (e.g., week, month, year), bathymetry changes significantly, but here, we assume little and negligible morphological change over a single day. Contrary to the conventional use of video-derived depth for bathymetry estimation, we consider here that the instant-derived depth  $h_{jt}$  can be separated between the bathymetry  $D_{jt}$  and total sea level  $SL_{jt}$  (Thuan et al., 2019):

$$h_{jt} = D_{jt} + SL_{jt} \quad (3.10)$$

Thus, any change in  $h_{jt}$  over a day in the nearshore is associated with  $SL_{jt}$  changes, while changes on longer time scales could be associated with both  $h_{jt}$  and  $SL_{jt}$ . Beyond the littoral zone, where there is no significant transport of sediment by wave action,  $h_{jt}$  can be assumed to be constant for longer periods, as there are little changes in bottom elevation. The limit between the two areas can be defined using the depth of closure (DoC) as defined by Kraus et al. (1988). As explained in the previous section, the video-derived water levels at pixel  $j$  and time  $t$  are therefore obtained by removing the 1-day (or  $n$ -days,  $\bar{h}_{jt}$ ) moving average from instant depths  $h_{jt}$ . The daily average is computed with 6.5 h of continuous instant depths  $h_{jt}$  over a day, to cover a high and a low tide.

It remains difficult to fully discriminate all contributions (Eq. 3.9) from video-derived water levels ( $SL_{jt}$ ) without additional assumptions. On the spatial scale of this study (100–200m in the cross-shore direction), tidal (AT) and sea level anomaly (SLA), combined with inverse barometer (DA), are supposed to be constant across the whole profile, while wave contribution (i.e., setdown/setup) is varying in the cross-shore direction. The quantities AT and SLA + DA can be extracted using a spatial median averaged of  $SL_{jt}$  over a chosen area on the profile, which is selected using the maximum correlation between  $SL_{jt}$  and field/altimetry data. The median is used to limit the effect of any single value that is too high or too low compared to the rest of the estimates. The derived time series are filtering over 2 hours, and a spatially constant contribution, representing a "clean" video-derived tide (AT), is obtained. This video-derived tidal signal is compared to the tide derived from ADCP, Cotonou tide gauge and FES2014 data. The Cotonou tide gauge and FES2014 data are interpolated on video time points (15-min period). The video-derived SLA + DA is derived by daily or monthly averaging the  $SL_{jt}$  and is used to perform the comparison with altimetry. The DA is removed from video estimates by

applying the same corrections used in CTOH X-TRACK processing (Biol et al., 2017). The obtained monthly averaged SLA is compared to the monthly averaged altimetry data.

The harmonic analysis of the video-derived water levels is performed using the Python version of the Utide software (Codiga, 2011). The tidal regime estimated from the nearby Cotonou tide gauge is semidiurnal with four constituent amplitudes greater than 10cm ( $M_2$ ,  $S_2$ ,  $K_1$ ,  $N_2$ ). After some tests, we focus our analysis on the main semidiurnals and diurnal constituents ( $M_2$ ,  $S_2$ ,  $N_2$ ,  $K_2$ ,  $K_1$ ,  $P_1$ ,  $O_1$ ).

The data processing scheme is presented in Fig. 3.7, as a synopsis of all processing applied to derive the total coastal sea level from video images.

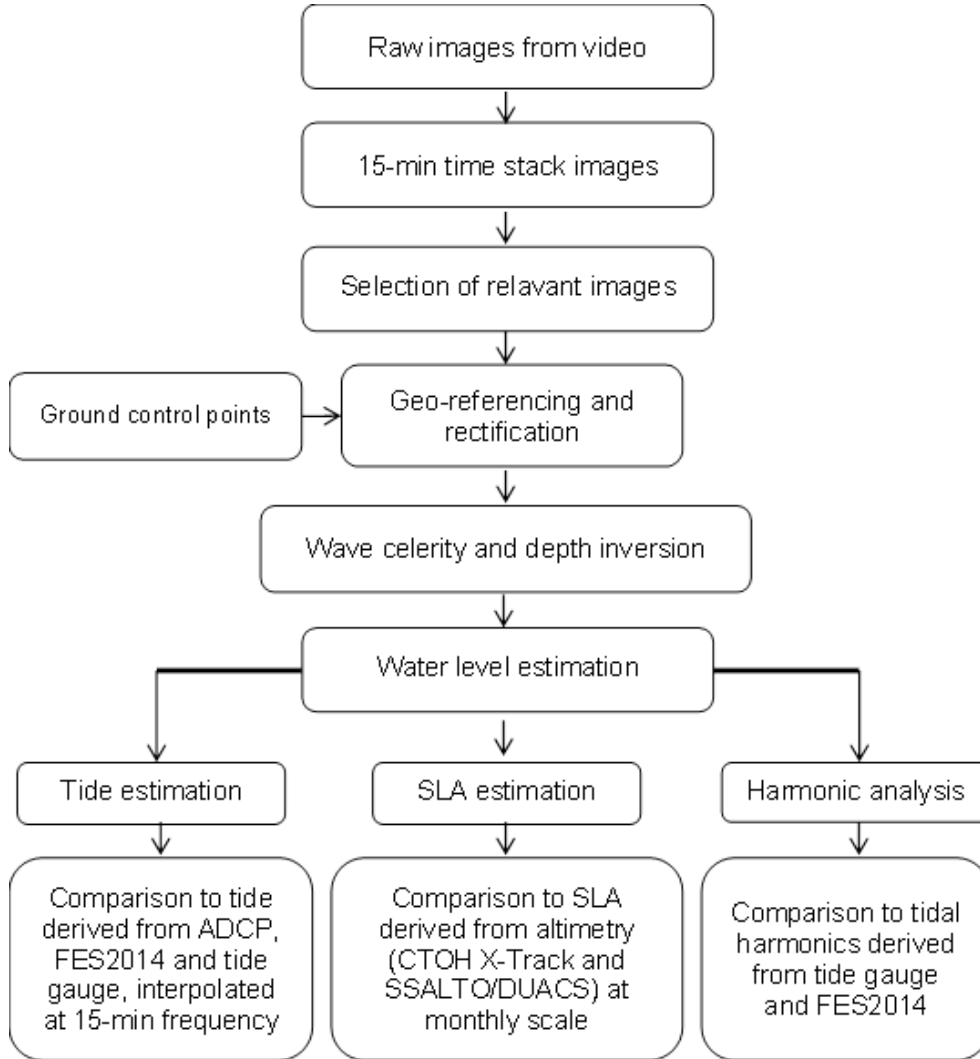


**Figure 3.7** – Data processing scheme for water levels estimation.

### 3.4.3 Results

#### Video-derived water levels along the beach profile

The different water-level components (AT and SLA + DA) are estimated most accurately depending on the cross-shore position as illustrated in Fig. 3.8 (blue-shaded zones). The correlation coefficients between  $SL_{jt}$  and field/altimetry data reveal two main areas at which a high correlation of tide and sea level anomaly can be found. The first area shows that video-based estimation of the tidal constituents is most adequate on the terrace. This holds under the assumption that little changes of  $D_{jt}$  occur over a day, unlike longer periods. The second area

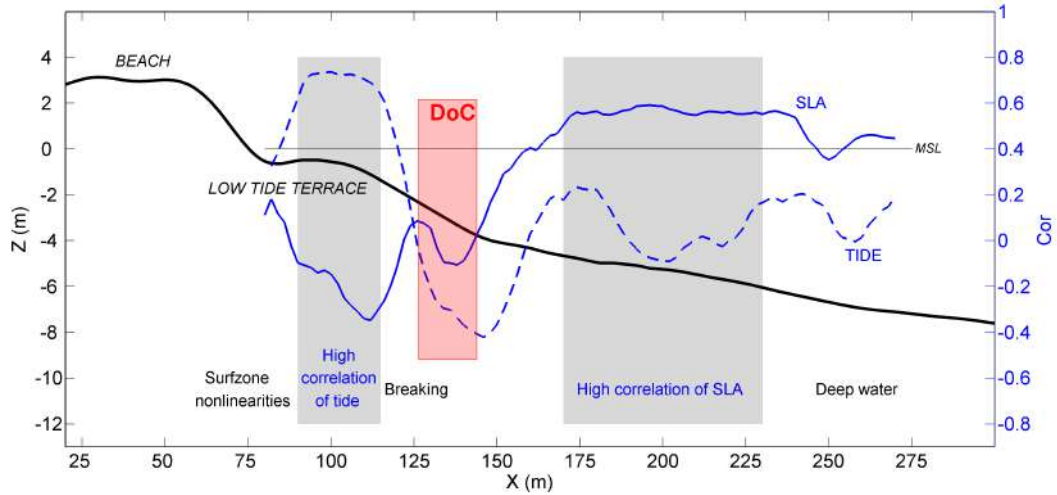


**Figure 3.8** – Evolution of the correlation coefficients between video and field/altimetry data: Dashed blue line shows the correlation between 2-hr-smoothed  $SL_{jt}$  and ADCP measurements, and solid blue line represents the correlation between monthly averaged  $SL_{jt}$  and SSALTO/DUACS data. Red shaded area indicates the depth of closure (DoC) variation zone.

corresponds to the zone beyond the DoC, without morphological changes over longer periods of time. Then  $D_{jt}$  may not change when addressing long-term SLA from video. Areas with low correlation coefficients on the profile correspond to the surfzone, the incipient breaking zone, and deep water. [Thuan et al. \(2019\)](#) presented a full description of the associated errors for the use of video-based depth inversion methods, which are observed to be low where AT and SLA are derived (see Fig. 10 in [Thuan et al. 2019](#)).

### Comparison of the video-derived tide with field measurements and model

The video-derived tide (AT) is computed on the terrace:  $90 < X < 115m$ . From Fig. 3.8, we can see that the video-derived tide (on the terrace) and tide derived from ADCP have correlation coefficients greater than 0.5. Figure 3.9 shows the inter-comparison of the video-derived tide with the tide derived from ADCP, Cotonou tide gauge, and FES2014 model data. Table 3.2 gives corresponding correlation coefficients and rootmean-square (RMS) differences. During the 10-day Grand Popo 2014 field experiment (Fig. 3.9a), the best agreement between video estimates and ADCP-derived tides is found during the last days of the experiment. Important differences (approximately 30cm) are observed during the first three days, which could be related to local atmospheric and oceanic conditions.

	ADCP	Cotonou tide gauge	FES2014
Dates	10 days	2 years	3.5 years
r	0.90	0.58	0.64
RMS difference (m)	0.20	0.38	0.38

**Table 3.2** – Correlations  $r$  and RMS differences in video-derived tide AT with the time series of tides derived from the ADCP, Cotonou tide gauge, and FES2014 model

### Comparison of video-derived sea level anomaly with altimetry

The correlation coefficients of the SLA are found to be high ( $r \geq 0.5$ ) at depths greater than 4m:  $170 < X < 230m$  (Fig. 3.8). This cross-shore range is beyond the depth of closure and

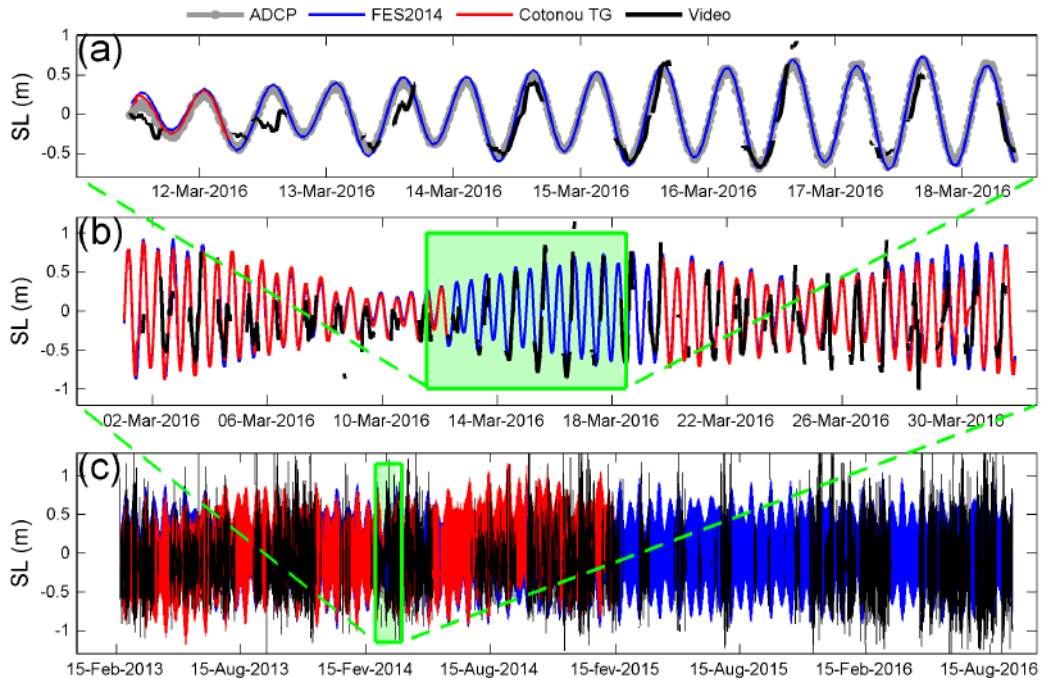


**Figure 3.9** – Comparison of video-derived water levels with time series of tide derived from the ADCP, the Cotonou tide gauge, and the FES2014 model. (c) Time series over the study period. (a),(b) Zooms of the time series over the 10-day Grand Popo 2014 field experiments and the month of March 2014, respectively.

hence we can presume that  $D_{jt}$  is constant on a monthly scale. Also, any temporal variation of the total water level is driven by the SLA + DA components. Figure 3.10 shows the monthly video-derived anomalies SLA compared to monthly SSALTO/DUACS and CTOH X-TRACK sea level anomalies. Table 3.3 shows the corresponding correlation  $r$ , RMS difference, and  $p$  value. It is observed that the video-derived SLA is overall consistent with altimetry products. The three sets of data show the same seasonality, as shown by the correlation values. However, computed RMS differences correspond to 25% of the sea level anomaly and some discrepancies can be observed between video and altimetry. Also, the 3.5-yr video data are not long enough to derive the sea level anomaly trend in the study area.

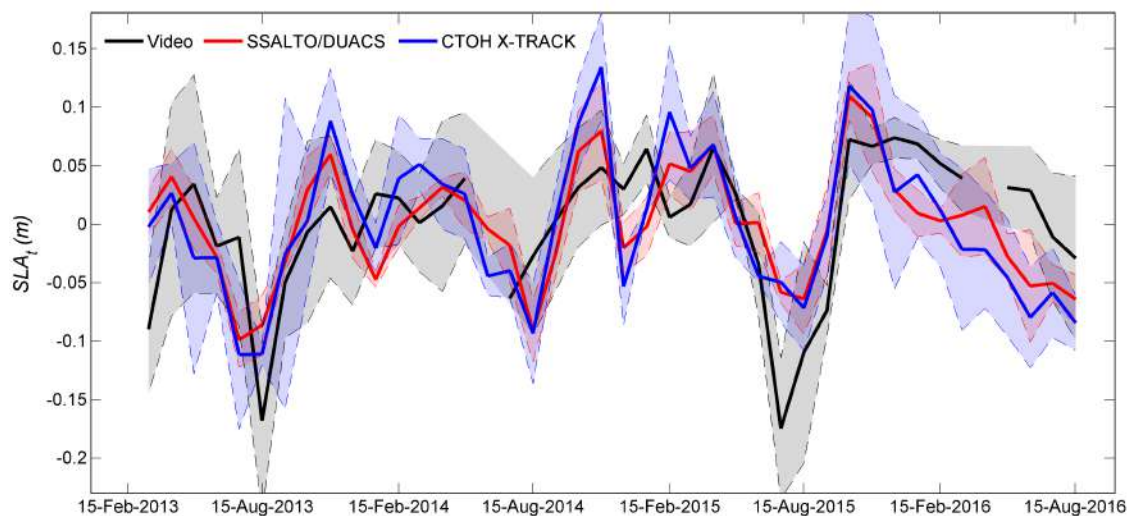


**Figure 3.10** – Comparison of video (black), SSALTO/DUACS (red), and CTOH X-TRACK (blue) monthly derived sea level anomalies. Shaded areas indicate the day-to-day dispersions.

	CTOH X-TRACK	SSALTO/DUACS
r	0.56	0.58
RMS difference (m)	0.06	0.05

**Table 3.3** – Correlations  $r$  and RMS differences between monthly video-derived water-level anomalies with monthly CTOH X-TRACK and monthly SSALTO/DUACS sea level anomalies.

### Comparison of long-term video-derived tidal harmonics components with field data

Figure 3.11 shows the main tidal constituents for the Gulf of Guinea sub-region derived from the video-derived tide, the FES2014 model, and the Cotonou gauge data. It is observed that the video signal well represents the amplitudes of the main semi-diurnal and diurnal tidal constituent. The observed differences in the amplitude of tidal harmonics are likely due to other contributions than tides such as waves, inter-daily morphological changes, local forcing in the coastal area, with interdependence between the various temporal scales, and the errors from the video-derived method.

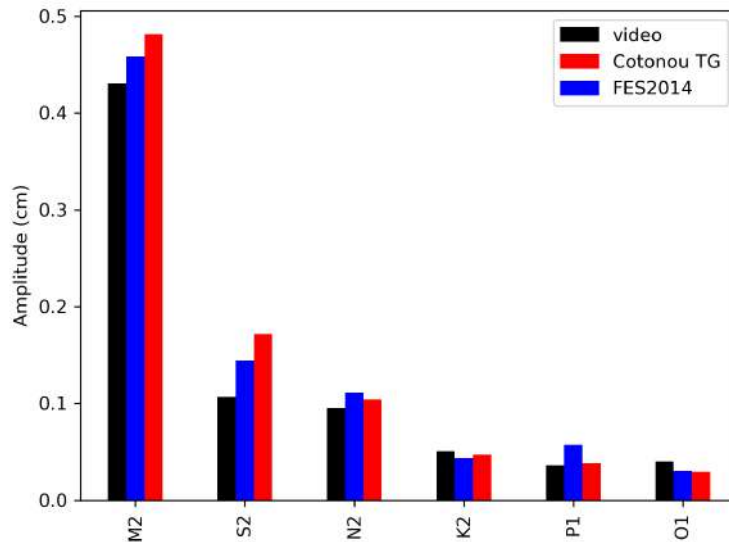


**Figure 3.11** – Tidal constituents derived with the Python version of the Utide software from video (black), Cotonou tide gauge (red), and FES2014 (blue) data.

### 3.4.4 Discussion

#### Errors on celerity estimation and depth inversion

The method presented in this work relies on the precision in the estimation of wave celerity and depth. During the 10-day experiment of Grand Popo (11–20 March 2014), the overall inaccuracies were estimated to be around 10% of the local depths (Abessolo et al., 2017). This error is likely to vary over the total length of the study period (2013–16) according to the main source of errors investigated by (Bergsma and Almar, 2018). Their results show that the main source of errors can be related to the limited validity of the linear dispersion relation in the shallowest parts of the nearshore. As waves shoal, break, and become nonlinear, implementation of linear wave theory may be inaccurate near the shoreline (Brodie et al., 2018).

In addition, Bergsma et al. (2016) showed that video-derived wave celerity may be biased by presuming a fixed free water surface level, while in fact, the water surface alternates with the

tide. The fluctuations of the water surface with the tide change the geographical pixel locations and thus modify the estimated time-integrated distance  $\Delta X$ . Bergsma et al. (2016) showed that the associated error depends on the local video system settings, such as camera height and distance from the camera in combination with the tidal range. At Grand Popo, the rectification was done at mean tide level and this effect leads to a horizontal pixel displacement of 3–25 m, according to the formulation proposed by Bergsma et al. (2016). This might add an error of 0.2–1 m to the depth estimation for a 0.01–0.05 bottom slope. Thus, this error may be large where the bottom slope is steep. The camera viewing angle also introduces an error related to the pixel footprint increasing offshore. Although this error has been estimated at less than 1 m in the area of interest, its impact on depth inversion scheme has not yet been assessed. Camera movements are another source of error in the image rectification process (Bouvier et al., 2019), but camera movements at Grand Popo were deemed small and with no influence on the area of interest where wave information was inferred.

### Limitations and errors on water level

#### LIMITATIONS

Equation 3.10 suggests that the derived instant water depth  $h_{jt}$  can be separated into contributions due to bathymetry  $D_{jt}$  and total sea level ( $SL_{jt}$ ). This means that errors associated with bathymetry may differ from errors associated with water-level variations (AT and SLA + DA). Because of this complexity, it remains difficult to directly estimate the error in the videoderived water levels, since bathymetry changes may affect video-derived water levels.

The validation of the video-derived water levels is also an issue. For that, it would have been necessary to have more frequent measurements of water level and bottom elevation on the cross-shore profile over a long enough time period to allow for water-level estimations/calculations at different time scales. It would have required the deployment of pressure sensors or the use of remote sensing equipment, such as the lidar, covering the field of view of the camera (Brodie et al., 2018). Such data are generally rare and nonexistent at our study site. Altimetry data are available more than 9 km off the coast, whereas tide gauge data have been measured approximately 80 km away from the camera location, and the ADCP data are limited to a 10-day observation. In addition, magnitude of waves propagation and their impact on video estimates of total sea levels are also difficult to assess, because of the lack of buoys in the study site during the study period. Furthermore, video estimation, tide gauge, and altimetry products do not incorporate the same processes nor measure at the same time scales and in the same place. This approach should, therefore, be replicated in other more instrumented sites.

Although the video gives information measured directly on the coast (0–1 km offshore) with a 15-min frequency, one of the main limitations is its inability to measure at night.

#### ERRORS ON TIDE ESTIMATION

The video-derived tide (AT) is assumed to be constant over the cross-shore beach profile, whereas wave (W) and wind (Wi) are affected by wave non-linearities in the nearshore (surfzone) environment (Bergsma and Almar, 2018; Brodie et al., 2018). Since AT is derived on the terrace using a cross-shore median averaged of  $SL_{jt}$ , separating the W and Wi contributions from AT is challenging. In addition, AT is derived over a cross-shore area at which we can assume that morphological evolution is negligible over a day. However, wave-exposed coasts that often experience extreme events are prone to rapid bathymetric changes. This leads to substantial

variations in the video-derived tide (AT) over a day. The RMS differences in AT estimations can be related to  $W + W_i$  contributions during moderate wave conditions and to  $W + W_i$  contributions associated with bathymetry changes during extremes events. A typical example of differences on the order of 30 cm is observed during the first 3 days of the Grand Popo 2014 field experiment. The video RMS difference for the field data represents an average error on the order of 20% of the tide (Table 1). The sum  $AT + W + W_i$  contributes to the total sea level, whereas the bathymetry changes, wave non-linearities, and wave breaking in the near shore lead to uncertainties in the total sea level at the coast. Thus,  $AT + W + W_i$  may be derived more accurately in environments in which bathymetric changes are limited (rocky beaches) and/or relatively slow under moderate wave conditions.

#### ERRORS ON SLA ESTIMATION

At depths greater than the DoC, the contributions of bathymetry changes to the total sea level are assumed to be negligible. Kraus et al. (1998) provided a definition of the DoC, based on the available literature, as the depth beyond which there is no significant change in bottom elevation. At such a location, the error on the SLA estimation may be related to the wave celerity and inversion error described by Bergsma and Almar (2018). In addition, gaps in the video data within a month will affect the monthly averaged values. This is not only the case for video. CTOH X-TRACK data are limited to one sample approximatively every 10 days while SSALTO/DUACS data were re-interpolated daily from available satellite tracks with several days of periodicity. These three data sources show the same seasonality and must be used in complementarity in order to avoid the problem of data gaps due to the different measuring time scales. The differences identified could also be explained by the non-linearities at the coast. Likewise, separating  $W$  and  $W_i$  contributions from  $SLA + DA$  is challenging. The video RMS difference with altimetry data represents an average error on the order of 25% of the sea level anomaly (Table 3.3).

#### Potential of video coastal network: Ground truth for spatial studies and early warning systems

There is a clear need to understand sea level propagation in the near shore. The results obtained in this study show that video systems have good skills in observing sea level variability at the event and monthly scales. It is a low-cost technique suitable for nearshore areas where the installation of traditional measuring devices turns out to be difficult and expensive. Nonetheless, there are still some parts of the method that can be improved, since the computed RMS differences with field/altimetry data remain high compared to the errors of other conventional devices. However, the technique is promising, regarding the complexity of nearshore areas.

Altimetry products have great difficulty measuring close to the coast. Marti et al. (2019) investigated the rate of sea level change, combining ALES retracked altimetry data (Passaro et al., 2018a) and geophysical corrections dedicated to coastal areas (Biol et al., 2017). The obtained X-TRACK/ALES 20-Hz products allow to get a little closer to the coasts (up to 3km), but not so close to observe wave undergoing transformations within depths of less than 10m. The impact of wave transformations on sea level is still poorly understood and validated, as tide gauges are limited to sheltered places (Melet et al., 2016, 2018a). The challenge remains on understanding waves effects in new radar gauges measurements. Shore-based video systems can, therefore, be used to supplement existing tide gauges and altimetry. Combining the future

French–U.S. SWOT (for example) mission to the video-based estimation of water levels opens the possibility to address and fill in the existing knowledge gap between deep and coast waters: 0–1km from the coast with video and 1–10km with new and future altimetry products.

Video-derived water levels can be used to investigate processes related to storm surge and coastal flooding while supporting high-frequency and localized validation of wave forecasts and reanalysis of ocean forcing. Moreover, video capabilities can be used for longer periods of time, providing long-term coastal water level time series in order to validate the method to estimate the coastal contribution to water levels proposed by [Melet et al. \(2018a\)](#) or [Anderson et al. \(2018\)](#). A regional network of video cameras along the West African coast, for example, would densify the waterlevel monitoring network at long-term time scale. It could be the backbone of a real-time, early-warning system for coastal disasters, as shown in [Sembiring et al. \(2017\)](#).

### 3.4.5 Conslusions

In this study, we present a novel method to measure total sea level at the coast using for the first time a shore-based video-monitoring system. For the case study in Grand Popo, Benin (Gulf of Guinea), video-derived water levels showed similar characteristics with (i) 10-day field data:  $r = 0.9$ , RMS difference = 0.2 m; (ii) 2-yr tide gauge data 80km far away:  $r = 0.58$ , RMS difference = 0.38 m; and (iii) 3.5-yr altimetry products: SSALTO/DUACS  $r = 0.58$ , RMS difference = 0.05 m; CTOH X-TRACK samples:  $r = 0.56$ , RMS difference = 0.06 m. The most important tidal harmonics ( $M_2$ ,  $S_2$ ,  $K_1$ ,  $N_2$ ,  $K_1$ ,  $P_1$ , and  $O_1$ ) are well estimated from the video. Therefore, this novel approach to derive the total sea level at the coast from video (i) is particularly (with greater certainty) suitable for environments in which bathymetric changes are limited (rocky beaches) and/or relatively slow under moderate wave conditions and (ii) should be used at cross-shore positions where waves and wind non-linearity errors are low. This pioneering study highlights the potential of low-cost video cameras in observing sea level at the coast. Furthermore, combining future altimetry products with observations of the total sea level at the coast derived from shore-based video systems would give new insights to close the knowledge gap from the continental shelf to the coast.

---

## Chapter 3 summary

This chapter focused on the improvements in temporal approach to celerity-based depth inversion method to derive depths and sea level variations at the coast.

### Improvement of wave celerity estimation from video imagery

- Consists of (1) filtering the pixel intensity signal of a timestack image around the main frequencies, (2) applying to it the conventional temporal method for wave celerity and depth estimation and (3) calculating weighted averages of the depths obtained for each of the main frequencies
- Validation with 10-days in-situ measurements at [GPP](#)
- Mean video-derived beach profile correlates 80% with 10-days field data collected at [GPP](#)
- Vertical error of 0.15m for the upper beach and the terrace
- First daily full depth profile evolution

### Assimilation of two error proxies in a Kalman filter for depth estimation accuracy

- The tide related-error proxy is calculated as the difference between field-measured tides and video-derived tides
- The wavelength related-error proxy is computed as the differences between inverted depths derived from two wave celerity estimates
- Validation with 10-days in-situ measurements at [GPP](#)
- The mean square error can be reduced by at least 30% and both proxies show good ability to correct depth estimates

### Novel approach to extract water levels at the coast from video-derived depth estimates

- Consists of estimating time-varying total water levels by applying a celerity-based depth inversion method
- Validation with 10-days in-situ measurements at [GPP](#)
- Video-derived tides correlate 90% and 58% with [ADCP](#) and tide gauge data, respectively
- Video-derived sea level anomalies correlate 50-60% with altimetric data
- Accurate determination of the dominant tidal harmonics

## 3.5 Conclusion

The results presented in this chapter improve the accuracy of bathymetric estimates by reducing errors by at least 30%. Moreover, these estimates allow the derivation of the water levels at the coast with all the contributions that were difficult to obtain with conventional tools such as tide gauges and altimetry. These results demonstrate the potential of video cameras in monitoring coastal variability. In the next chapter, bathymetric estimates coupled with intertidal profiles will be processed to study the behaviour of beaches facing the multi-scale (event to inter-annual) wave forcing and sea level variations in the equatorial Atlantic.

# Chapter 4

## Beach response to multi-scale wave forcing and sea level variations

### Contents

---

<b>4.1</b>	<b>Introduction</b>	<b>69</b>
<b>4.2</b>	<b>Beach response to wave forcing from event to inter-annual time scales</b>	<b>70</b>
4.2.1	Background	70
4.2.2	Methods	71
4.2.3	Results	73
4.2.4	Discussion	77
4.2.5	Conclusions	78
<b>4.3</b>	<b>Beach adaptation to intra-seasonal sea level changes</b>	<b>79</b>
4.3.1	Background	80
4.3.2	Sea Level Data	81
4.3.3	Intra-seasonal sea level forcing	82
4.3.4	Detection algorithm for intraseasonal sea level event and Kelvin waves	82
4.3.5	Intra-seasonal beach response	83
4.3.6	Influence of intraseasonal sea level variations on beach morphology	84
4.3.7	Conclusions	86
<b>4.4</b>	<b>Conclusion</b>	<b>87</b>

---

### 4.1 Introduction

In order to identify the natural causes of shoreline variability and beach morphology at our pilot site in [GPP](#), video data were compiled and analyzed using the techniques presented in the previous chapters. [Almar et al. \(2015b\)](#) showed that the beach of Grand Popo was mainly affected by the long swell generated by westerlies in the 40 – 60°S zone and to a lesser extent by trade winds at 30 – 35°S. In addition, [Polo et al. \(2008\)](#) showed that recurrent coastally-trapped waves (Kelvin waves) were observed on the coasts in the [BoB](#). In this chapter, the morphological estimates obtained (shorelines and beach profiles) are analysed relatively to this multi-scale oceanic forcing. Section 4.2 focuses on wave action, while section 4.3 focuses on the impact of intra-seasonal water level variations on the coast.

## 4.2 Beach response to wave forcing from event to inter-annual time scales at [GPP](#), Benin, Gulf of Guinea

This section assesses different time scales of beach response to wave forcing at Grand Popo beach (Benin) using wave evolution and video-derived shoreline over a 3.5 year period (February 2013 to August 2016). The beach response was first investigated during and after storm-events, including the impact of storm duration and post-storm beach recovery. At seasonal scale, the link between beach adjustment and wave variability was investigated. Finally, inter-annual trends were computed in order to identify the role of wave climate in long term shoreline evolution. The results presented in this section have been published.

### Article's reference

**Abessolo, G.O.**, Bonou, F., Tomety, F.S., Du Penhoat, Y., Perret, C., Degbe, C.G.E., and Almar, R., 2017. Beach response to wave forcing from event to inter-annual time scales at Grand Popo, Bénin (Gulf of Guinea). *Water*, 9, 447.

### Abstract of the paper

This paper assesses the morphological wave events impact, seasonal cycles, trends of wave forcing, and beach's response at the coastal area of Grand Popo, Benin. Three and a half years' worth of data were collected from 2013 to 2016, using a video system calibrated with field data collected during a 10 day experiment. A comparison was carried out with Wavewatch III IOWAGA wave hindcast data. The along-shore-averaged shoreline position exhibited a seasonal pattern, which was related more to the average wave height than the average storm intensity. Wave events occur in austral winter (June, July, August, and September). Based on 12 wave events, the results revealed that the average event duration was 1.6 days, with a mean erosion of 3.1 m. The average post-event beach recovery duration was 15 days, and the average recovery rate was 0.4 m/day. The impact of wave events was more or less amplified depending on the eroding and accreting periods of the wave climate. There was an inter-annual eroding trend of about -1.6 m/year, but the causes of this trend could not be explained.

### 4.2.1 Background

The coastal zone of West Africa is under increasing pressure of overpopulation, as it is a zone of economic interest. Human settlements and livelihood activities have been developing on the shores of the Atlantic Ocean, where the beach evolution varies according to a wide range of different temporal and spatial scales. In this region, beaches are microtidal and swell-dominated environments, where waves and tides are the main drivers of nearshore dynamics ([Stive et al., 2004](#)). Several findings suggest that along wave-dominated coastlines, regionally-varying wave climates will have an increasing impact on the shoreline in the coming decades, and cannot be ignored in forecasting shoreline variability ([Ranasinghe et al., 2012a](#); [Le Cozannet et al., 2019](#)). This highly dynamic behaviour is essentially due to the fact that sandy coasts can undergo adjustments in form and processes, which can change rapidly. Periods of accretion and erosion are generally associated with low- and high-energy wave conditions, respectively, but they also exhibit strong site-specific variations ([Senechal et al., 2015](#)). For many coastal regions, both sea-level rise and changes in the storm-wave climate would result in coastal erosion and an increased

---

frequency with a high intensity of coastal flooding. Storm-events represent a major factor of modulating short- and medium-term morphological evolutions of many sandy shorelines. In the event of changing storm regimes associated with climate change (Zhang et al., 2002), it is important to understand the potential effects of storms on beaches, and how they recover after these high-energy events. Many studies have been carried out on assessing the impact of storms, beaches' responses, and post-storm morphological adjustments in storm-dominated coastlines (Morton et al., 1994, 1995; Zhang et al., 2002; Almeida et al., 2012; Castelle et al., 2015; Masselink et al., 2016; Angnuureng et al., 2017). Managing erosion-induced problems will depend on the resilience of the beach to extreme events, and universal threshold conditions are not likely to be found (Senechal et al., 2015). Establishing storm thresholds is difficult, especially because they are generally site-specific (Almeida et al., 2012; Ba and Senechal, 2013); this is as well as the beach recovery period (Morton et al., 1994), which has not yet been clearly addressed in the literature. Available literature regarding beaches' responses to storms on tropical microtidal coastlines and the potential impacts of climate change remains scarce.

Along the wave-dominated coastlines of the Gulf of Guinea, the influence of South Atlantic high-energy swells drives strong, eastward longshore sediment transport (Laibi et al., 2014; Almar et al., 2015b). This littoral drift in the Bight of Benin is one of the largest in the world, with estimations of approximately 400,000–1,000,000 m<sup>3</sup>/year (Anthony and Blivi, 1999; Almar et al., 2015b). This transport is mostly driven by swell waves due to the Southern Annular Mode (SAM), rather than wind waves due to the Inter-Tropical Convergence Zone (ITCZ) (Almar et al., 2015b). This equatorial fluctuation presents a large seasonal and inter-annual variability as well as wave climate (Laibi et al., 2014). This implies a high seasonal variability in the beaches' responses to equatorial Atlantic forcing, given that seasonal processes dominate the shoreline changes due to seasonal variations of the wave height at several specific sites (Yates et al., 2009; Senechal et al., 2015). These findings need to be confirmed, but few measurements are available on the high-frequency evolution of shoreline and beach states in the West and Central African regions.

This study assesses different time scales of beach responses to wave forcing at Grand Popo Coast, Benin, using video-derived shoreline and wave evolution data over a 3.5 year observation period (February 2013 to August 2016). We first investigate an average beach response during and after storm-events. Secondly, we evaluate the impact of storm durations and recurrence with seasonal variability. And finally, we estimate the inter-annual trends.

## 4.2.2 Methods

### Hydrodynamic data derived from video

Recent methods were used to extract hydrodynamic parameters: significant wave height  $H_s$ , mean period  $T_m$  and direction  $Dir$ .

$H_s$  video estimations were obtained from the time-stack images (Almar et al., 2012a). Following the wave signature induced by breaking, wave heights were detected from the pixel intensity threshold  $I_{pix} = 40$ . The intensity of breaking pixels was significantly larger ( $I_{pix} > 80$ ) than that of non-breaking pixels ( $I_{pix} \sim 10$ ). The pixel intensity peak, which appeared at the wave crests, was calculated by the standard deviation  $\delta$  of the pixel intensity of each time series. The width of the peak of  $\delta$  marked the horizontal projection of the wave face covered by the roller (L), which was subsequently projected into the vertical direction for a simple rough estimation:

$H_b = L \cdot \tan(\beta)$  where  $\beta$  is the camera view angle. The fact that the wave-front slope ( $\alpha_b$ ) at breaking differed significantly from the vertical direction was taken into account. The common value  $\alpha_b \approx 30^\circ$  used as a breaking criterion in numerical breaking parameterizations, according to [Almar et al. \(2012a\)](#). The wave height could therefore be estimated from the equation ([Almar et al., 2012a](#)):

$$H_b = (L - Cor) \tan(\beta), \quad (4.1)$$

$Cor$  being a geometrical correction defined as:

$$Cor = \frac{L}{\tan(\alpha_b)} \tan(\beta) \quad (4.2)$$

The mean wave period  $T_m$  was computed from the offshore pixel intensity time series using the mean zero-crossing method on the time-stack images (see Fig.2.9 and [Almar et al. 2008](#)). Wave direction was estimated from the snapshots and 15 min averaged images. The technique consisted of, firstly, subtracting the average image from the snapshot (removing the background, which does not move); secondly, highlighting the wave crests (the time-varying part); then rectifying on a regular grid; and finally, recovering the angle of the crest of the waves by the Radon transform ([Almar et al., 2012a](#)).

### Event Scale

The definition of storm-event is site-specific ([Senechal et al., 2015](#); [Castelle et al., 2015](#)), and the  $H_s$  threshold used to define storm conditions or wave events was selected to produce clear and identifiable events. Three-hourly  $H_s$  time series were used, and the 5% exceedance probability of the  $H_s$  time series over the study period ( $H_{s5\%} = 1.85m$ ) was considered as the threshold for wave events. A single event is defined as a continuous period of  $H_s$  exceeding this threshold and lasting at least one tidal cycle (12 h), following [Senechal et al. \(2015\)](#); [Angnuureng et al. \(2017\)](#). The overall impact of wave events is assessed through the daily-averaging maximum shoreline moving during the event. Wave event intensity  $I$  ( $m^2 \cdot h$ ) is computed as the integration of time-varying  $H_s$  over the storm duration:

$$I = \int_{t_1}^{t_2} H_s(t)^2 \cdot dt \quad (4.3)$$

where  $t_1$  and  $t_2$  are times corresponding to the beginning and the end of the event ([Angnuureng et al., 2017](#)).

There are several ways to define the recovery duration after each wave event. It can be defined as the time taken by the nearshore morphology to evolve from a post-storm state (e.g., dissipative/longshore bar and trough) to its modal state (i.e., the most frequently occurring beach state, e.g., rhythmic bar and beach or transverse bar and rip, [Almeida et al. 2012](#); [Castelle et al. 2015](#); [Masselink et al. 2016](#)). In this study, the time duration taken to reach the first maximum recovery value of the along-shore-averaged shoreline location  $\langle X \rangle$  after each event was accepted as the recovery duration ([Masselink et al., 2016](#); [Angnuureng et al., 2017](#)). This duration referred to the post-storm period of continuous accretion towards its equilibrium pre-storm state (Tr), and did not depend on any forcing parameter. The overall recovery duration for the study period was computed as the time for daily-averaging post-event evolution of continuous accretion ([Senechal et al., 2015](#)).

## Seasonal Signal and Trends

To obtain the seasonal signal, monthly nearshore estimations were computed. The test of Mann Kendall was used to check if the time series showed substantial trends (Hamed and Rao, 1998). The null hypothesis of trend absence in a time series was tested, against the alternative of having a trend. Each time series was reorganized as a matrix  $M_{ij}$  where  $1 \leq i \leq N_y$  with  $N_y$  representing the number of years of video observation, and  $1 \leq j \leq 12$ . The seasonal signal  $S_j$  was obtained as follows:

$$S_j = \frac{1}{N_y} \sum_{i=1}^{N_y} M_{ij} \quad (4.4)$$

The monthly residual or anomaly  $R_{ij}$  of each parameter was estimated by removing the seasonal monthly value from each monthly averaged value computed over the 3.5 years. The annual anomaly or trend  $R_a$  was computed by averaging monthly anomaly values  $R_{ij}$ .

### 4.2.3 Results

#### Hydrodynamic and Morphological Variability

Figure 4.1.a–c provides an overview of monthly video and WW3 data (Rascle and Ardhuin, 2013) over the study period. The same  $H_s$  seasonality for the two sets of data was observed (Figure 4.1.a), with more energetic waves during the April–October period and less energetic waves during the November–March period. These observations are consistent with the wave climate of the area because of northward migration, by a few degrees, of the wave-generating zone in the high latitudes of the South Atlantic ( $\sim 40^\circ$  to  $60^\circ S$ ) during the summer period (Laibi et al., 2014; Almar et al., 2015b). Table 4.1 gives correlations and errors between the WW3 video and model data on the time series of  $H_s$ ,  $T_m$ , and the wave direction. There is strong correlation between the two time series of  $H_s$  ( $R^2 = 0.80$ ). Direction and  $T_m$  are less correlated ( $R^2 = 0.44$  and  $R^2 = 0.19$ ; Figure 4.1.b,c), with a low observed variability.

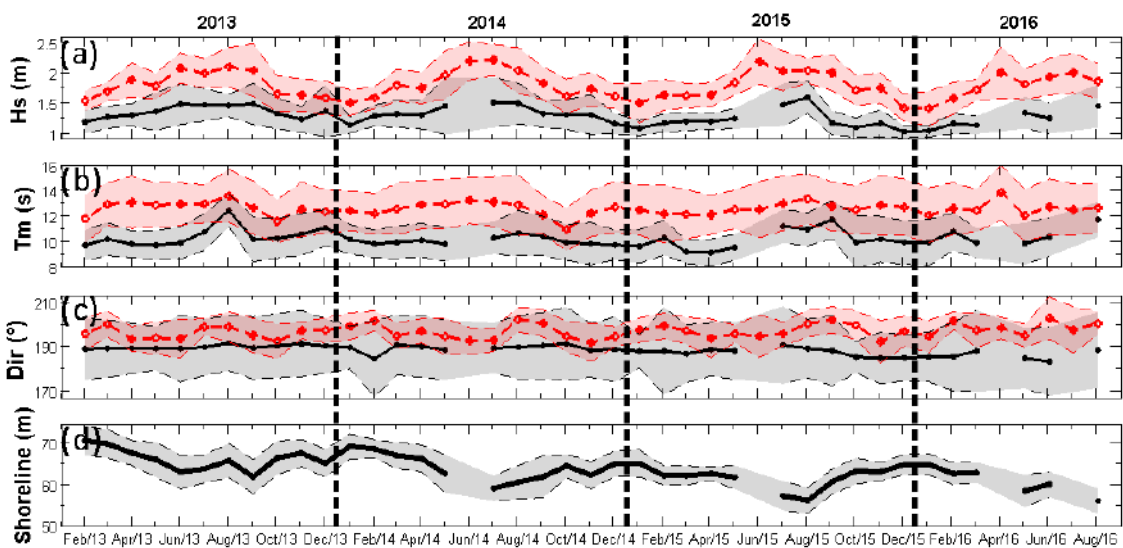


**Figure 4.1** – Monthly-averaged video estimates (black) and Wavewatch III data (red): (a) wave significant height  $H_s$ ; (b) wave mean period  $T_m$ ; (c) wave direction  $Dir$ ; and (d) shoreline location  $X$ . Shaded zones stand for day-to-day dispersion (standard deviation).

Video-WW3	$H_s$ (m)	$T_m$ (s)	$Dir$ ( $^\circ$ )
Correlation	0.8	0.4	0.2
RMSE	0.3	2.4	9.4
ME	0.3	2.3	8.5

**Table 4.1** – Comparison of daily hydrodynamic video data and WW3 model outputs. WW3 data were propagated from deep water to breakpoint using an empirical direct formula (Larson et al., 2010). The root-mean-square error (RMSE) and the mean error (ME) were computed between the two sets of data.

It should be noted here that the IOWAGA WW3 ocean wave hindcast had not been assimilated with any observations (satellite or buoy). For the previous versions of WW3, random averaged errors between  $H_s$  model outputs (WW3) and satellite data ranged from 0.3 to 0.4 m for low wave heights ( $<2$  m), and 0.15 m for higher waves (Tolman, 2002). An improvement was made on the recent version used in this work, integrating new parameterizations for the wind–sea and wave dissipation. However, the normalized RMSE for  $H_s$  remained  $\sim 20\%$ , compared to the satellite data in our study area, with biases of more than 0.1 m (Rascle and Ardhuin, 2013). This was consistent with the overestimation observed in the model outputs (Figure 4.1), which were likely amplified due to local unresolved effects of bathymetry for the wave propagation from deep water to breaking point. However, WW3 results were improved even more from linear regression correction than from bias correction, as shown in Woodcock and Greenslade (2007). Gaps in  $H_s$  video data could therefore be estimated using a linear regression between the two sets of data.

### Wave events and Morphological Impact

32 storms were identified over the study period (Fig. 4.2.a) and only 12 wave events were further considered, due to gaps in shoreline data. The mean peak storm  $H_s$  was 2.05 m (standard deviation  $\sigma = 0.05m$ ) and the mean wave height throughout the storms was 1.99 m ( $\sigma = 0.12m$ ). The average duration of a wave event was 1.6 days and storms were recorded from April to September, corresponding to austral winter. Individual wave events resulted in a wide range of shoreline impacts (Fig. 4.2.b), from no change on July 2, 2013 (1 day event), to significant erosion ( $-8.7$  m) during a 4 day wave event (September 21-25, 2013). The maximum number of wave events was recorded in July. In 2014 for example, 12 wave events were counted, with four in July. The strongest wave events impacts were recorded at the end of austral fall (in May) with an average onshore migration of  $-3.7$  m during a storm of less than 1 day. This impact decreased with the increase of events numbers until the beginning of austral winter (June and July).

The overall impact of wave events is assessed through the daily-averaging maximum shoreline moving during the storm (see Fig. 4.3). Figure 4.3 shows an ensemble-averaged analysis of the shoreline evolution during the wave event and post-event recovery period, with this period referring to the post-event period of continuous accretion, at the end of which the beach was assumed to be stabilized (Senechal et al., 2015; Castelle et al., 2015; Angnuureng et al., 2017). The day "0" stands for the beginning of the wave event, according to the 5% exceedance (1.85 m) of  $H_s$ . The average wave event intensity was  $155 m^2.h$  and induced an average beach erosion of 3.1 m. After the end of the wave event, the beach attempted to recover during a continuous accretive phase: the shoreline moved offshore (0.46 m/day) and the time needed

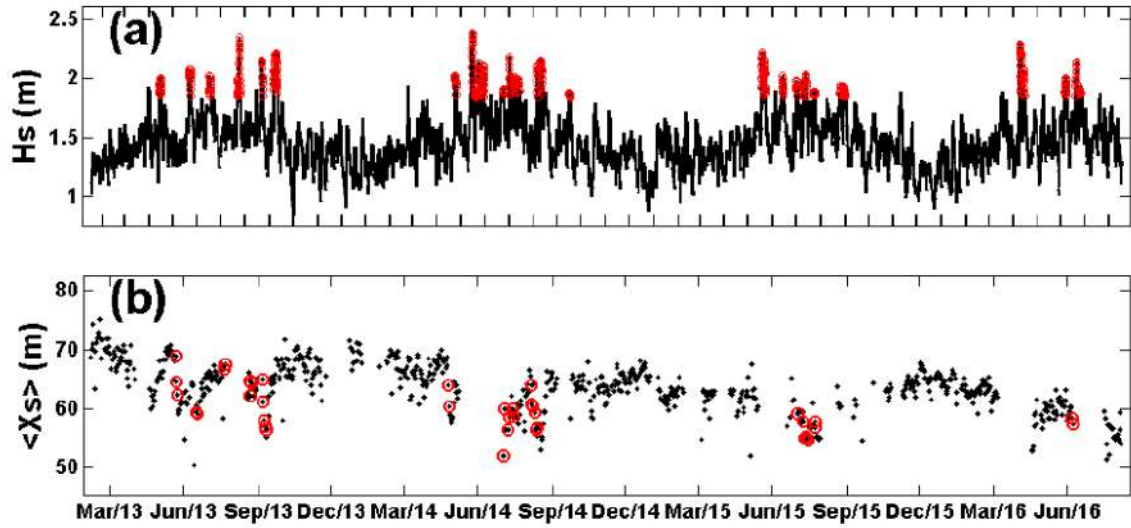


**Figure 4.2** – Time series of: (a) significant wave height, and (b) along-shore-averaged location  $\langle X_s \rangle$  from the tower of camera location. Storm periods are marked in red.

to reach stabilization was approximately 15 days. This time was considered as the post-event recovery duration  $T_r$ .

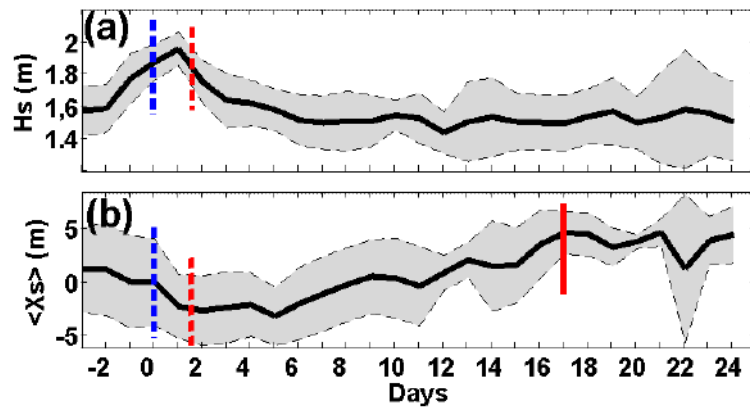


**Figure 4.3** – Ensemble-averaged evolution during the wave event and post-event recovery period for: (a)  $H_s$ , and (b) shoreline location  $\langle X_s \rangle$ . Blue dashed lines stand for the beginning of the averaged-event, red dashed lines for the end of the wave event (1.6 day storm duration), and the solid red line stands for the post-event recovery duration for beach stabilization (15 days).

### Seasonal cycle

Figures 4.4 and 4.5 present the seasonal cycle of several monthly nearshore forcing parameters and beach morphology. The maximum monthly-averaged  $H_s$  (1.51 m) was obtained in July, corresponding to the maximum monthly-averaged wave flux (15400 J/m · s). The seasonal pattern was highlighted in the along-shore-averaged shoreline position, which was strongly correlated to the monthly  $H_s$  seasonal cycle ( $R^2 = -0.94$ ), and in contrast, less correlated to the monthly-averaged beach slope ( $R^2 = -0.25$ ). The maximum beach slope was 0.14 rad at the end of April. For the 32 identified storms, the greatest number of storms was recorded in July, but these were shorter (average duration of 1.34 days), leading to a lesser average intensity compared to the other months. Figure 4.4.a,d and Figure 4.5.a show that the beach response (shoreline location) was most related to the monthly-averaged  $H_s$  rather than the intensity of

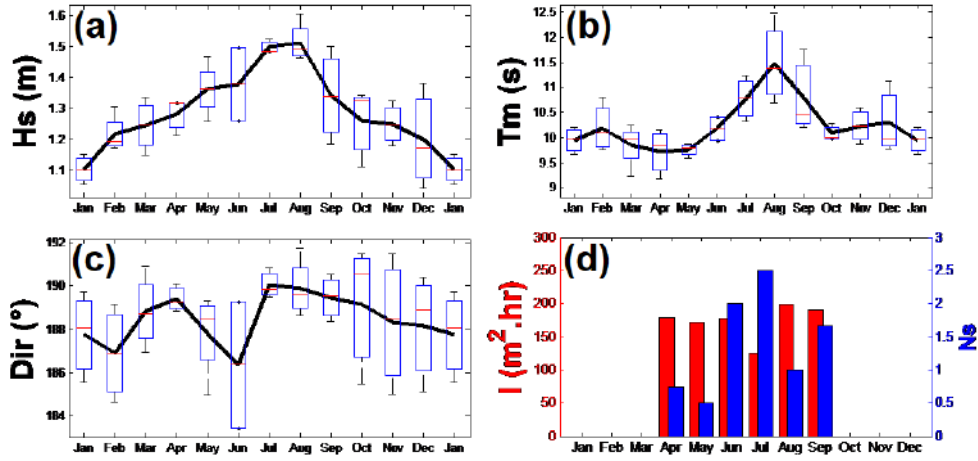


**Figure 4.4** – Seasonal variability (monthly average) of: (a)  $H_s$ , (b)  $T_m$ , (c) wave direction ( $Dir$ ), and (d) wave event intensity in  $m^2.h$  (red) and the number of wave events  $N_s$  (blue). For each box, the central mark (red line) is the median, the edges of the box (blue) are the 25<sup>th</sup> and 75<sup>th</sup> percentiles, and the whiskers extend to the most extreme data points not considered outliers.

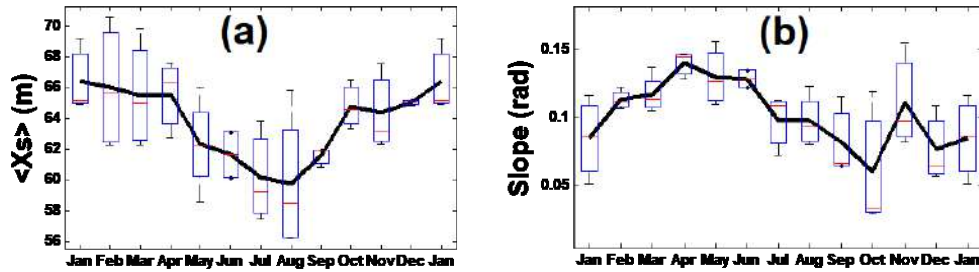


**Figure 4.5** – Monthly average seasonal variability: (a) mean shoreline location  $\langle X_s \rangle$  from video camera location, and (b) beach slope. For each box, the central mark (red line) is the median, the edges of the box (blue) are the 25<sup>th</sup> and 75<sup>th</sup> percentiles, and the whiskers extend to the most extreme data points not considered outliers.

storm-events.

The seasonal cycle of the shoreline presented two main different phases, the erosive phase (January to August) and the accretive phase (August to December), due to the changes of  $H_s$  (Figure 6.a) and  $T_m$  (Figure 4.5.b), which were driven by swell waves. The standard deviation of the beach slope variation was smaller during the eroding period, reflecting the low variability of the beach slope according to low-energy waves.

Wave events occurred at the end of the eroding period (April to July) and at the beginning of the accreting period (August to September). The beach exhibited particular responses to wave events, depending on the concerned period, as shown in Figure 4.6, where only 12 wave events were considered with their corresponding shoreline data. During this eroding period, the recovery duration seemed to be shorter ( $\sim 10$ days). In contrast, in the accreting period, the time recovery duration seemed to be longer and the storm impact increased with the storm duration, consistent with Yates et al. (2009). The post-event recovery was more significant in the accreting period than in the eroding period. In August, the beach experienced an onshore migration of 2.4 m during a 1.4 day averaged-duration wave event, while in September, a 3.7 day averaged-duration wave event caused an erosion of -5.4 m. The beach response was therefore influenced by the erosive or accretive period of the wave climate oscillation.

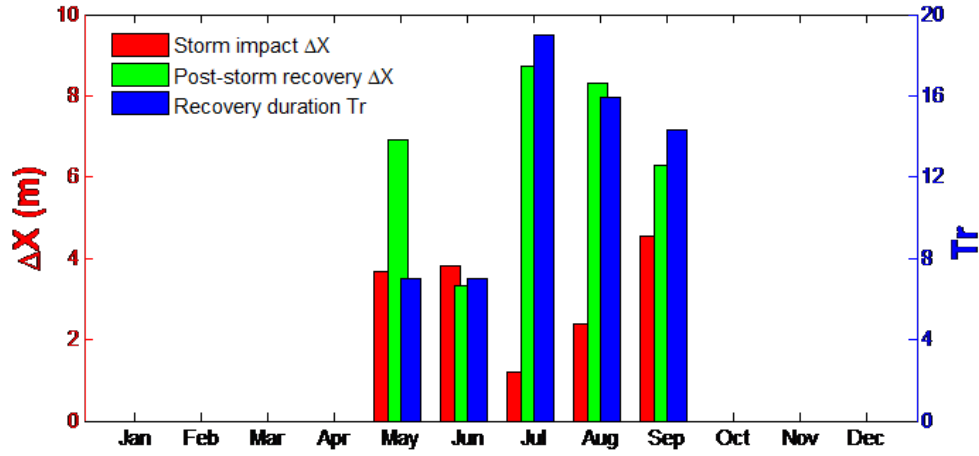


**Figure 4.6** – Ensemble-averaged shoreline variation  $\langle \Delta X_j \rangle$  during and after wave events: wave events impact (red), beach recovery (green), and recovery duration (blue) per month.

### Trends and Inter-Annual Evolution

Trends of waves and the shoreline were investigated using the test of Mann Kendall (Hamed and Rao, 1998). The results showed that the shoreline position  $H_s$  and wave direction data presented substantial trends. A failure to reject the null hypothesis (absence of trend) at 95 % significance level was obtained for the wave period and energy, and the beach slope. The residual signal reflected trends over the study period and was obtained by removing the seasonal cycle from the daily data. Table 4.2 shows the annual average and residuals of each studied parameter. During the 3.5 year study period, the shoreline migrated 6 m onshore. The annual anomaly or residual of the shoreline decreased from +2.8 m in 2013 to -2.9 m in 2016, while the annual residual of the beach slope did not change. A decrease of  $3^\circ$  in the wave direction was observed during the study period.

Study period	2013		2014		2015		2016 (Jan-Aug)	
	Mean	$R_a$	Mean	$R_a$	Mean	$R_a$	Mean	$R_a$
$H_s$ (m)	1.35	+0.05	1.34	+0.04	1.23	-0.07	1.28	-0.06
$T_m$ (s)	10.4	+0.2	10.1	-0.2	10.2	-0.1	10.6	+0.3
Dir ( $^\circ$ )	188.9	+1.4	188.2	+0.5	186.4	-1.3	185.2	-1.8
Shoreline position (m)	66.4	+2.8	63.9	+0.2	61.8	-1.9	60.1	-2.9
Beach slope (rad)	0.098	-0.006	0.101	0	0.109	+0.008	0.113	-0.04

**Table 4.2** – Annual averaged values and anomalies ( $R_a$ ) for the study period.

#### 4.2.4 Discussion

The results presented here are consistent with the wave climate observations in the studied area (Laibi et al., 2014; Almar et al., 2015b). A seasonal pattern was clearly observed in the shoreline position, beach slope, and wave characteristics. Data exhibited two specific periods: an accreting period (August to December), where  $H_s$  and  $T_m$  decreased; and an eroding period, where  $H_s$  and  $T_m$  increased (January to July). This was consistent with the oscillation of the Southern Annular Mode (SAM), which has a predominant influence on transport induced by swell waves (Almar et al., 2015b). The low values of the beach slope standard deviation observed during February to April reflected a stabilization reached during low wave-energy conditions.

Computing the beach slope variability could lead to an understanding of the nature of the waves breaking, as the beach slope is connected to the surf-similarity parameter. A recent finding (Almar et al., 2015a) suggested that the wave reflection is mostly governed by swash dynamics, whereby the reflected spectrum essentially depends on the swash slope.

The 3.5 years of video of the shoreline location suggests that beach dynamics observed at GPP Beach are affected by wave events. This study revealed that the impact on shoreline migration can be significant: -8.7 m on 21 September 2013, during a 4 day sequence of wave events. The mean duration of the 12 observed wave events was 1.6 days, with an average event-erosion of -3.1 m. At the end of the wave event, the shoreline migrated offshore at an average distance of 6 m within 15 days. However, the wave event impact and post-event recovery were very dependent on the observed seasonal pattern, consistent with Yates et al. (2009). The recovery duration in the eroding period was shorter (10 days) than in the accreting period (>15 days). The end of the period of stabilization observed between February and April was marked by short wave events of an average duration of less than 1 day, which caused significant erosion on the beach, averaging 3.7 m. During the accreting period, it took longer storms to observe a significant impact (mean of 3.7 days for -5.4 m). The beach's response was therefore mostly related to the energy of average wave conditions, rather than to the energy of extreme wave conditions.

The study of inter-annual trends in this work demonstrated a gradual decline of the shoreline cross-shore location during the period 2013–2016. However, the length of the data set was not enough to assess the inter-annual variability. A field of nine groins of 100 m lengths and 20 m widths was constructed between 2012 and 2014 over a distance of 3.5 km, near the city of Aneho (Togo), about 20 km from the video system at GPP Beach. This field could reduce the sediment supply of the eastward coastal drift in the direction of GPP. The impact of the field of groins could therefore be investigated, but no clear conclusions can be drawn on its impacts on the coastal area of GPP; although immediately downstream from the groynes, the region is experiencing significant visual erosion.

The trend of oceanic forcing (wave direction of  $-3^\circ$  for the period 2013–2015) is another possible factor of the observed erosion. The diminution of the wave direction from  $188.9^\circ$  to  $185.2^\circ$  during the study period increased the importance of cross-shore processes compared to along-shore processes, resulting in a decrease in the along-shore sediment transport ( $\sim 5\%$  per year), computed with an empirical formula (Larson et al., 2010) presented, in our study area. The longshore sediment transport is very dependent on the shore's normal wave direction, and the resulting littoral drift in the BoB is one of the largest in the world, following (Laibi et al., 2014; Almar et al., 2015b). Nevertheless, the video estimates of the wave direction had uncertainties. A comparison of video and WW3 wave direction outputs showed that the video data presented a larger standard deviation than the model output, respectively  $13.4^\circ$  (video) and  $6.4^\circ$  (WW3), and the video wave direction trend was not observed in the WW3 data. A previous study estimated the root mean square error with field ADCP measurements to be about  $9.25^\circ$ , and the mean error (ME) to be  $2.25^\circ$ , within the range of observed variation from 2013 to 2016 ( $-3^\circ$ ).

#### 4.2.5 Conclusions

3.5 years of video-derived shoreline and wave evolution data at GPP Beach was used to investigate the beach's response to wave forcing from event to inter-annual time scales in the

coastal area of Grand Popo Beach, Benin. The beach exhibited a seasonal pattern in wave conditions and the along-shore-averaged shoreline position was most related to the monthly-averaged wave height rather than the average storm intensity. The seasonal pattern of the shoreline indicated an eroding period and an accreting period, corresponding to austral and winter periods, respectively. 32 wave events were identified for the period 2013–2016. The mean wave event duration was 1.6 days for the 12 considered wave events due to gaps in video data, and the average event erosion was -3.1 m. Ensemble-averaged wave event recovery conditions showed that the beach recovered within 15 days, and the average recovery rate was 0.4m/day. This study underlines that the impact of wave events is more or less amplified depending on the eroding and accreting periods of the wave climate: (i) the recovery duration is longer in the accreting period than in the eroding period, (ii) the wave event impact is more significant in the eroding period than in the accreting period, (iii) wave events are longer in the accreting period than in the eroding period, and (iv) the number of wave events is high during the transition from the eroding to accretive phases. A trend on the along-shore-averaged shoreline location was observed (-1.6 m/year), however our data were not enough to draw conclusions at inter-annual time scales.

### 4.3 Beach adaptation to intra-seasonal sea level changes

As previously hypothesized that sea-level changes may actually play a part in beach variability (see chap 1), here we combine regional observation of coastal sea level variations (derived from satellite altimetry) with local beach profile evolution (derived from shore-based video) to investigate the nearshore response to intra-seasonal sea level variations in the BoB, Gulf of Guinea. The results presented in this section have been submitted for publishing and the revised article is currently under review.

#### Article's reference

**Abessolo, G.O.**, Almar, R., Jouanno, J., Bonou, F., Castelle, B., Larson, M., 2020. Beach Adaptation to Intraseasonal Sea Level Changes. *Environmental Research Communications*, 2, 051003.

#### Abstract of the paper

Coastal areas such as beaches with steep upper slope and flat low-tide terrace, are expected to be increasingly affected by sea level changes. Related impacts due to the paramount rise in sea level have been intensively investigated, but there is still little evidence of the impact of shorter timescales variations on the coast, particularly those induced by trapped coastal waves. Using the latest advances in video bathymetric estimation, daily observations over 3.5 years (February 2013 to June 2016) on Grand Popo Beach (West Africa) reveal that intraseasonal sea level variations impact the beach profile. The intraseasonal sea level variations are dominated by the propagation of wind forced coastal trapped waves with periods ranging 15-95 days. It is shown that the beach goes through a transient state with a deformation of the profile: an intraseasonal sea level rise leads to a 2m erosion of the upper beach and a widening of the flat terrace at the lower beach. Although the underlying mechanism must be tested through beach profile modelling, this study highlights the active adaptation of the beach profile to variations

---

in sea level.

### 4.3.1 Background

Most of the world's coasts are subject to changes because of their vulnerability to climate change as well as human development. Climate change drives variations in mean sea level, wave conditions, storm surge, that result in the destruction of socio-economical and environmental systems (Stive et al., 2004; Rueda and et al., 2017). Understanding the factors responsible for beach erosion and flooding has become a main concern. There is a need to assess and evaluate the trends under present climate conditions, which will be fundamental for predicting future impacts (McInnes et al., 2016) and for developing effective management policies (Leonard et al., 2014).

Global sea-level rise is well known to lead to a recession of the shoreline (Bruun, 1954, 1962b,a, 1988; Ranasinghe et al., 2012a; Rosati et al., 2013; Shand et al., 2013; Le Cozannet et al., 1962; Dean and Houston, 2016; Atkinson et al., 2018). It is an important contributor to erosion hotspots at decadal to centenary scales (Nicholls and Cazenave, 2010; Le Cozannet et al., 2019). Conventionally, it is thought that at shorter time scales, from hours to years, waves, tides, sedimentary processes, and anthropogenic factors drive beach changes that surpass sea level impact (Stive, 2004; Ranasinghe, 2016; Anthony et al., 2019). This is relevant at mid-to-high latitudes where storm-induced coastal dynamics is dominant. However, this can be different in the inter-tropical band where sea level presents large fluctuations at seasonal and interannual scales (Komar and Enfield, 1987; Feng et al., 2003; Ding et al., 2009; Komar et al., 2011), and intraseasonal scales (Polo et al., 2008; Echevin et al., 2014; Ezer, 2016; Kim et al., 2018; Ding et al., 2018). While the seasonal and interannual scales are related to the tropical climate modes, the intraseasonal variability is characterized by the poleward propagation of coastal disturbances triggered by coastally-trapped Kelvin and Rossby waves. These coastally-trapped waves can be caused by wind stress variability, atmospheric disturbances and variations in the intensity of oceanic currents. For instance, Kelvin waves have been intensively described in the equatorial Atlantic and in the equatorial Pacific. Echevin et al. (2014) reported  $\pm 0.20$  m of intraseasonal sea level variations on the nearshore Peru ecosystem, within the 60–120 day time periods. At  $15^\circ N$  on the western coast of India,  $\pm 0.25$  m intraseasonal variations of alongshore currents were observed in the 55–110 day time periods (Vialard et al., 2009). In West Africa, Gulf of Guinea, Polo et al. (2008) observed recurrent and continuous wave propagations distinguishable over thousands of kilometers poleward along the coast, in the period range 20–90 days. The observed characteristics were close to those of equatorial Kelvin wave propagations with a variance of 0.02 m and a phase speed ranging from 1.5 to 2.1 m/s without any substantial differences and no remarkable property changes following the coastline along different isobaths (200 to 1000 m-depth).

Such transient sea-level changes may actually play a part in beach variability (Komar and Enfield, 1987). But, how they operate in the coastal zone is still a scientific issue (McInnes et al., 2016). Segura et al. (2018) investigated such dynamics at a reef-fringed beach at seasonal scale. Their results suggested that, contrary to general observation on open beaches, the seasonal beach response is primarily influenced by seasonal variations in offshore water level rather than by wave heights. However, this result is specific to reef-fringed beaches. At intraseasonal scale, there is still very little knowledge about the impact of sea levels on the beach, as little attention has been given to it. We hypothesize that intraseasonal sea level variability could drive

beach changes, in particular for storm-free and tropical environments, where these intraseasonal sea level changes were reported to be large. However, the lack of suitable measurements and the historical cloisoning of the nearshore and coastal oceanography communities have led to a knowledge gap on transient sea level change impacts. Here we combine regional observation of coastal sea level from satellite altimetry with local scale beach evolution from shore-based video to investigate the nearshore response to intraseasonal sea level variations in the Gulf of Guinea. In this paper, the term "upper beach" will refer to the steepest part of the beach corresponding to the swash zone at high tide, according to [Miller and Dean \(2004\)](#).

### 4.3.2 Sea Level Data

Sea level anomalies (SLA) time series were extracted at daily scale from the SSALTO/DUACS multi-mission gridded and delayed-time products ([Arbic et al., 2012](#); [Pujol et al., 2016](#)) provided by Copernicus Marine and Environment Monitoring Service (CMEMS). In these products, available altimeter missions (Saral/AltiKa, Cryosat-2 and OSTM/Jason-2 for the period from 2013 to 2016) are merged and mapped daily onto a  $1/4^\circ$ -resolution grid. In order to identify propagating sea level variations along the coast, data were extracted along a track of 54 grid nodes in the Bight of Benin (see Figure ), close enough to the coast, but not too close to prevent land-masses disturbances in radar signal (see [Polo et al. 2008](#)). The distance between consecutive selected nodes was  $1/4^\circ$  ( $\sim 27.5$  km, according to SSALTO/DUACS grid) and each node was taken approximately 75 km from the coast. Contributions to sea level variations driven by local wind, atmospheric pressure, and waves were neglected, despite their possible importance ([Melet et al., 2016](#); [Slangen et al., 2017](#); [Melet et al., 2018a](#)). The ocean forcing ( $H_s$  and SLA) for the 3.5 years period is shown in Figure 3.3.

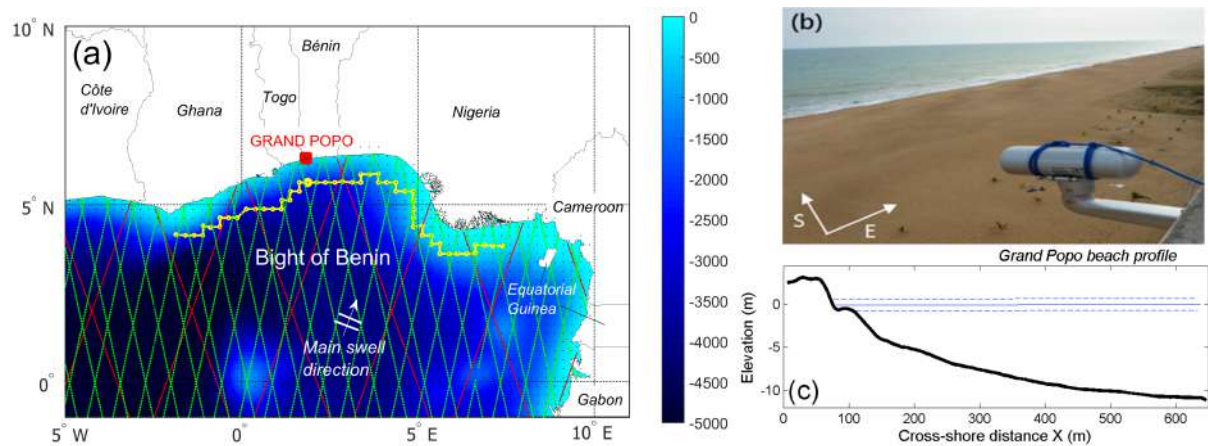


**Figure 4.7** – Study site. (a) Bight of Benin, West Africa, Gulf of Guinea. Yellow points stand for selected nodes along the coast used to track propagating sea level variations. Black dots stand for SSALTO/DUACS grid nodes. The tracks of the satellite missions merged in the SSALTO/DUACS gridded product used for the altimetric sea level are indicated: in red for Jason-3 and in green for Saral/AltiKa. The Cryosat-2 mission is non-sun-synchronous and moves along drifting tracks ( $92^\circ$ -orbit inclination) that have not been shown. The color bar gives the bathymetry in meters (GEBCO gridded bathymetry data). Node 34 ( $5.6271^\circ N$ ,  $1.6375^\circ E$ ) is the closest point to Grand Popo. (b) Video camera system deployed on a tower made available by the Beninese Navy at Grand Popo. (c) Average beach profile (solid black line) obtained during the Grand Popo experiment (March 10 to 19, 2014), with mean sea level (solid blue line) and high and low (blue dashed blue lines) tide levels.

### 4.3.3 Intra-seasonal sea level forcing

Sea level anomalies along the coast of West and Central Africa observed from altimetry show large variability, with main peaks at the annual, semi-annual, and 120-day period (Polo et al., 2008; De Coetlogon et al., 2010; Jouanno et al., 2013). The annual and semi-annual components dominate the sea level variability (Aman et al., 2007). For periods smaller than 100 days, a relative maximum is observed at a 60-day period (Polo et al., 2008). This temporal band corresponds to coastal trapped waves that propagate from the equator north to Senegal, and whose properties resemble that of a pure coastal Kelvin wave in the limit where the continental margin tends to zero. The study by Polo et al. (2008) used Topex/Poseidon products at 7-day time resolution and retained the range 25–95 day for detecting these intraseasonal waves. Here, the use of SSALTO/DUACS products with daily temporal resolution allowed for the broadening of the identification range to 15-95 days. A 15-95 day band-pass filter was performed by subtracting the time series obtained from two low-pass filters, consisting of median averages over running windows of 15 and 95 days, particularly suited for time series with missing data. Seasonal harmonics (120 days, semi-annual and annual) have been previously removed. The 15-95 day filter was used to derive intraseasonal variations of sea level ( $SLA_i$ ), significant wave heights at breaking ( $H_{si}$ ), and depth-contours ( $X_i$ ) in beach profile evolution.

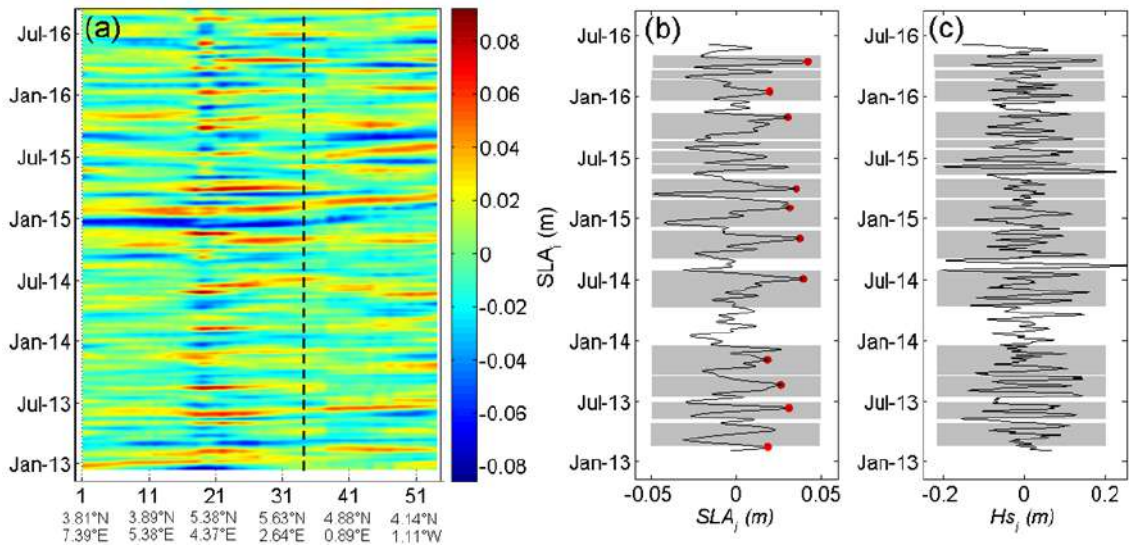


**Figure 4.8** – Intra-seasonal variations in sea level anomalies  $SLA_i$  and wave height  $H_{si}$ : (a) Longitude/latitude-time diagram of intraseasonal anomalies, following nodes on the track in Figure 4.7. Dashed black line corresponds to node 34, near Grand Popo town, and the corresponding intraseasonal sea level and wave height variations are shown in (b) and (c), respectively. Shaded gray areas stand for considered intraseasonal sea level events. Red points stand for detected propagating peaks of intraseasonal sea levels, with an average speed of 1.1 m/s.

### 4.3.4 Detection algorithm for intraseasonal sea level event and Kelvin waves

The intraseasonal sea level propagations corresponding were detected automatically along the track of 54 nodes shown on Figure 4.7. The first step consists of spatially averaging the filtered sea level anomalies  $SLA_i$  time series for nodes 1 to 5. With the averaged signal, the positive and negative peaks of the amplitude are detected. The peaks are considered to be detected for node 5. For further steps,  $P_{k_i}$  corresponds to the high peak detected at node  $k$  at time  $t_{k_i}$ , with  $1 \geq i \geq N$  and  $N$  is the number of considered peaks.

The second step consists of verifying which of the considered peaks  $P_{5_i}$  is propagating along the coast. Polo et al. (2008) observed that continuous propagations of  $SLA_i$  along the coast suggested Kelvin wave propagation with phase speed ranging from 1.5 to 2.1 m/s. For the detection algorithm, we choose  $V_{min} = 0.5$  m/s and  $V_{max} = 3$  m/s as speed limits, and  $V_{moy} = 1.8$  m/s as mean speed. If the peak  $P_{5_i}$  corresponds to a Kelvin wave propagation, a peak will be detected at node 6 at time  $t_{6_i} \in [t_{5_i} + (d_{56}/V_{max}); t_{5_i} + (d_{56}/V_{min})]$  with  $d_{56}$  the distance between nodes 5 and 6. If no peak is detected, the algorithm continues by considering the theoretical peak at time  $t_{6_i} = t_{5_i} + d_{56}/V_{moy}$  at node 6. This allows for not stopping the algorithm prematurely. By starting at node 6 at the considered time  $t_{6_i}$ , another peak is searched for at node 7 at time  $t_{7_i} \in [t_{6_i} + (d_{67}/V_{max}); t_{6_i} + (d_{67}/V_{min})]$ . If no peak is detected, a theoretical peak is considered again at time  $t_{7_i} = t_{6_i} + d_{67}/V_{moy}$ . The same algorithm is applied at nodes 8 to 54.

The last step consists of evaluating whether the peaks correspond to a propagating coastal-trapped wave, considering the discrepancies or discontinuities in the time series. For that, the ratio of the number of detected peaks to the number of nodes along the track must be above a fixed threshold of 75 %.

Fifteen intraseasonal sea level events ( $SLA_i$ ) have been identified along the 3.5 years' time series (Figure 4.8). About 80% of the intraseasonal events that have been identified are associated with coastal trapped waves propagating westward with an average speed of 1.1 m/s computed manually, an average period of 59 days and an average amplitude of 6.6 cm.

#### 4.3.5 Intra-seasonal beach response

The correlation computed between the intraseasonal wave energy (Figure 4.8.c) and the associated intraseasonal depth contours variations suggests that the intensity of the wave's action on beach response is linearly dependent on sea level at intraseasonal scale. The highest correlation values ( $r = -0.73$  and  $r = +0.41$  for the upper beach and terrace, respectively), computed significant at 95% confidence level ( $p - value < 10^{-4}$  and  $p - value = 0.0097$ , respectively), are observed when intraseasonal sea level is high ( $SLA_i > +0.02m$ ). Correlations values decrease with intraseasonal sea level to reach the lowest values ( $r = -0.05$  and  $r = -0.09$ ) when intraseasonal sea level is low ( $SLA_i < -0.02m$ ). This observation suggests that the combination of waves and sea level events would result in a modulation of wave action on the beach at intraseasonal scale as a function of intraseasonal sea level and thus a response of the beach profile to intraseasonal sea level. However, this dependence remains less marked on the terrace, as the highest correlation value obtained ( $r = +0.41$ ) explains only 17% of the variance.

In order to understand the action of  $SLA_i$ , morphological changes on beach profile were measured during  $SLA_i$  events. Figure 4.9 presents the relationship between changes in intraseasonal sea level events ( $\Delta SLA_i$ ) and associated morphological changes ( $\Delta X_i$ ). Correlations between  $\Delta SLA_i$  and  $\Delta X_i$  were computed statistically significant at the 95% confidence level. Interestingly, the changes in  $SLA_i$  are significantly related to changes on the upper beach ( $r = -0.81$ ), even if less related to changes on the terrace ( $r = +0.49$ ). Correlation values suggest that morphological changes at the intraseasonal scale are not only due to wave conditions and coastal currents, but also to sea level variations. Waves and coastal currents (e.g. rip currents) may explain the dispersion of the events observed with the error bars in Figure 4.9.

These observations are confirmed by combining all the intraseasonal events (Figure 4.10). This consists on median-averaging all the considered events, previously interpolated on the same number of samples. The observed impact of the  $SLA_i$  ensemble event is the deformation of the

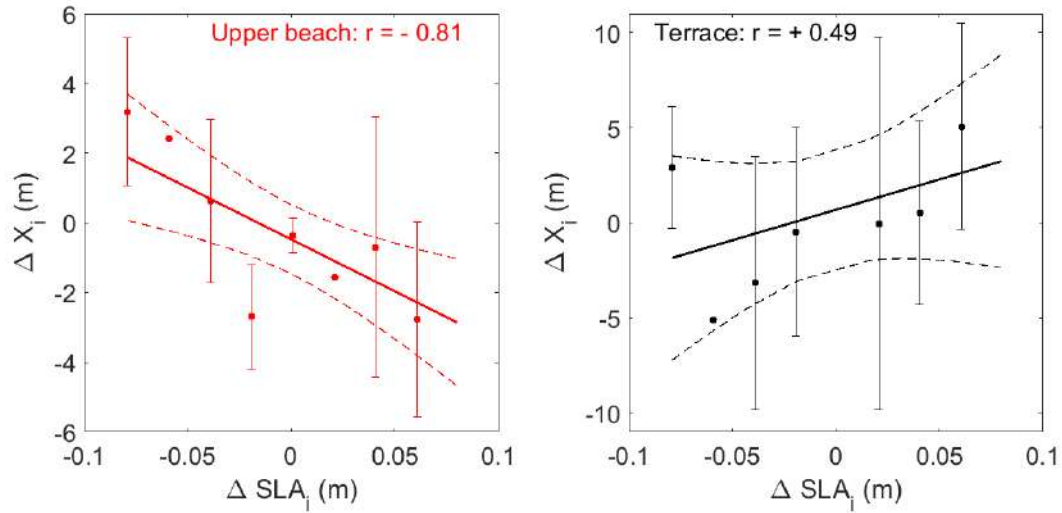


**Figure 4.9** – Intraseasonal sea level ( $\Delta SLA_i$ ) and corresponding morphological ( $\Delta X_i$ ) changes during  $SLA_i$  events. Solid lines are linear regression and dashed lines indicate the 95% confidence levels. Dots stand for changes ( $\Delta SLA_i$  and  $\Delta X_i$ ) computed between the end and the beginning of the ascending and descending phases of an  $SLA_i$  event, and averaged (using median) over a 0.02 m-window interval on the x-axis, for upper beach and terrace, respectively. Error bars indicate the dispersion of events within the window

beach profile with a rise or fall in the sea level. A phase shift of about 9 days is observed between the response of the terrace and the  $SLA_i$  event. The correlations between the  $SLA_i$  event and the beach changes are  $-0.93$  and  $0.76$ , respectively for the upper beach and the terrace (considering a 9-day lag for the terrace response). Therefore, two phases can be clearly identified (Figure 4.10.c). During a 30-day period of rising sea level, the upper beach is eroded. On the terrace, the concurrent seaward migration of the 1 to 2-m depth-contour lines indicates terrace widening and therefore suggests offshore sand transport. During a 30-day period of lowering sea level, observations indicate upper beach accretion and deeper terrace and therefore suggest onshore sand transport from the terrace to the upper beach. The 9-day lag could represent the time required for sediment to move from the upper beach to the terrace and vice versa. On average, a 7-cm change in sea level leads to nearly 2 m of horizontal terrace deformation as shown in Figure 4.10.d.

#### 4.3.6 Influence of intraseasonal sea level variations on beach morphology

Our observations show a deformation of the beach profile with varying intraseasonal sea level, rather than a translation of the profile, corresponding to a retreat of the upper beach and a terrace widening during a high event. The predominant control of wave events on the beach is found to be higher during high sea levels than during low levels. This suggests that sea level variations modulate the magnitude of wave action on the beach. Some studies (Miles and Russell, 2004; Almeida et al., 2017) have already highlighted this specific behavior at terraced beaches when looking at shorter intra-tidal variations. The combination of a two-slope beach and varying tidal heights brings a complex situation where the separate sections of the beach respond as quite different systems (Huntley and Bowen, 1975), despite being exposed to the same offshore waves. The two sections do interact depending on the water depth on the terrace, with a shallow terrace breaking incident waves as spilling breakers before they reach the upper part of the beach (Miles and Russell, 2004). It is hypothesized that during high sea levels, higher

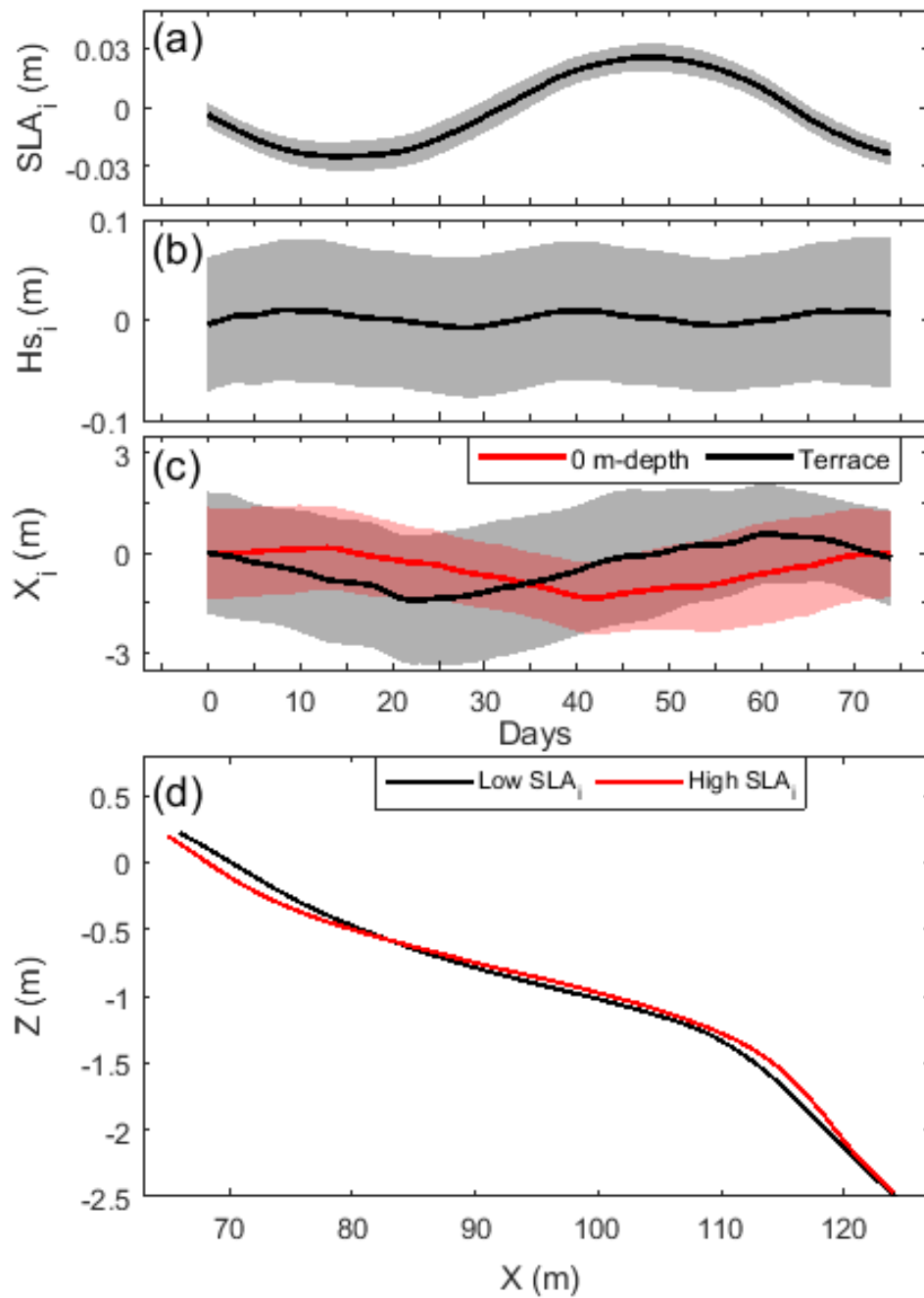


**Figure 4.10** – Ensemble-averaged evolution over intra-seasonal events and morphological changes with shaded areas representing one standard deviation: (a) Sea level  $SLA_i$ , (b) wave height  $H_{s_i}$ , (c) depth-contours  $X_i$  corresponding to upper beach (blue) and terrace (black), (d) Mean profiles for high (red) and low (black) sea levels during a 7-cm mean change in  $SLA_i$ .

average water level across the entire terrace results in less depth-induced breaking wave energy dissipation and, in turn, more energetic waves at the beach face. This can drive more pronounced upper beach erosion, with sediment further supplying the outer edge of the terrace, resulting in terrace enlargement. This explanation needs to be tested and validated, given the complex interplay and the feedback between cross-shore sediment transport driven by undertow and wave non-linearities. Field measurements of sand transport using similar approach to [Miles and Russell \(2004\)](#) would provide more insight into sediment fluxes between the upper beach and the terrace. However, maintaining such measurements during 10s days is challenging. State-of-the-art beach profile process-based models have the potential to address the underlying mechanisms, but this remains out of scope of the present study.

Multi-scale coastal evolution, due to sea level variations, remains poorly known. As noted earlier, only the sea-level rise is well known to lead to a recession of the shoreline at decadal to centenary scales ([Le Cozannet et al., 2019](#)). At shorter time scales, from hours to years, sea level variations also influence the beach variability. But, there is still very little literature on their impact on the coast, especially since waves and tide were traditionally the only two forcings studied to understand beach dynamics at open coasts. In this work, focus has been given to intraseasonal sea level variations, which affect the entire African tropical coast ([Polo et al., 2008](#)). And the wave energy was observed to be modulated by sea level variations. A recent study ([Segura et al., 2018](#)) has investigated the role of water level at a reef-fringed beach, which is modulated by wave heights, wave set-up and wave-driven flows, due to saturation of the surf zone and the corresponding variability in depth-limited wave breaking. The beach response was shown to be primarily dictated by the variability in subtidal water levels at seasonal scale, comparatively to wave energy. Although these studies were conducted on sites with very different characteristics (sandy beach and reef-fringed beach), the results suggest that the multi-temporal coupling between water level and wave energy must be considered to understand beach dynamics. Such studies should also be investigated on various sites, including coasts where meteotsunamis have been reported ([Carvajal et al., 2017](#)). This requires the development of tools and devices for measuring and modelling coastal dynamics at different time and spatial scales.

#### 4.3.7 Conclusions

This study investigated beach changes to intraseasonal sea level variations using 3.5 years of daily video-derived beach profiles and altimetry. The results reveal that sea level variations of order tens of cm at intraseasonal scale drive beach changes: the beach response is not a simple translation of the profile from sea level but a deformation of the profile. As a hypothesis, the intraseasonal sea levels modulate wave action on the beach, inducing erosion of the upper beach and transfer of sediments to the outer part of the terrace during high sea levels. The underlying mechanisms will be tested and validated using detailed process-based beach profile models. The coupling between wave energy and sea level variations could be the key mechanism for multi-temporal understanding of the beach dynamics at open coasts, in particular in the context of current changes of wave regimes and sea level with climate changes. However, further works are needed to investigate the variability of the total sea level at the coast and the associated morphological changes.

---

## Chapter 4 summary

In this chapter, the behavior of the beach at the Grand Popo pilot site was assessed in response to wave forcing from event to interannual scales and to intra-seasonal sea level variations, that are characteristic of this region.

### Beach response to wave forcing from event to inter-annual time scales at **GPP**

- Potential of video cameras in assessing wave characteristics and beach morphology
- 3.5 years of video-derived shoreline evolution
- 1.6-days average storm duration results in 3.1 m-mean shoreline erosion and 15-days post-storm beach recovery duration
- The shoreline position exhibited a seasonal pattern, related to the average wave height
- An inter-annual eroding trend -1.6 m/year not explained by the wave climate

### Beach adaptation to intra-seasonal sea level changes

- 3.5 years of video-derived beach profile evolution
- Intra-seasonal sea level variations dominated by the propagation (1.1 m/s) of wind forced coastal trapped (Kelvin waves) with 15 to 95-days periodicity in the **BoB**
- Intra-seasonal sea level propagations detected using altimetry
- An intra-seasonal sea level rise leads to a 2m erosion of the upper beach and a widening of the flat terrace at the lower beach
- ***Hypothesis needed to be tested and validated with process-based models:*** Intra-seasonal sea levels modulate wave action on the beach.

## 4.4 Conclusion

The results obtained in this chapter show that the **GPP** pilot beach responds significantly to wave forcing on all time scales (from event to interannual). Furthermore, when subjected to propagation of coastally-trapped waves, such as Kelvin waves, its response could be more or less accentuated, due to the modulation of the wave action by water level at the coast. Although these studies demonstrate the importance of natural factors, they focused on short time scales and cannot explain the erosive inter-annual trend of -1.6 m/year observed at **GPP**. A more global long-term approach is needed to apprehend the coupling of these natural forcings with the various human actions on this coast, including harbors and sediment discharges from rivers. In the following chapter, based on the five Landsat-derived shorelines (see chapter 2), the variations in the **BoB** will be analysed in order to understand the trends and investigate possible causes.



# Chapter 5

## The Bight of Benin coast evolution from 1990 to 2015

### Contents

---

<b>5.1</b>	<b>Introduction</b>	<b>89</b>
<b>5.2</b>	<b>Sedimentary cell dynamics in the Bight of Benin</b>	<b>90</b>
<b>5.3</b>	<b>Trends in shoreline evolution</b>	<b>91</b>
<b>5.4</b>	<b>Causes of shoreline mobility in the Bight of Benin</b>	<b>92</b>
5.4.1	EOF Analysis	92
5.4.2	Longshore sediment transport, coastal infrastructures and rivers sand supply	94
5.4.3	Influence of South Atlantic climate dynamics	96
5.4.4	Localized sand mining	98
5.4.5	Outer shoreface/inner shelf sand supply	98
5.4.6	Future management and climate change	98
<b>5.5</b>	<b>Conclusion</b>	<b>100</b>

---

### 5.1 Introduction

Understanding the links between shoreline change, oceanic forcing, sediment transport, rivers sand supply, human activities, and climate change is by no means easy, but is an important pre-requisite before starting the construction of a model to simulate/predict the evolution of the shoreline, in order to establish effective coastal management frameworks in the face of increasingly intensive occupation of the coast in a rapidly changing world ([Ranasinghe and Stive, 2012](#); [Jongejan et al., 2016](#)).

In this chapter, the analysis of 25-years shoreline evolution (1990 to 2015) is carried out. For this purpose, the five Landsat-derived shorelines have been compiled (see chapter 2). Section 5.2 therefore presents the dynamics of the different cells identified ([Laibi et al., 2014](#)). Section 5.3 analyses the trends in the evolution of the coasts, taking into account the results of previous studies. Based on an Empirical Orthogonal Function (EOF) analysis, a discussion is then conducted in section 5.4 on the causes of this variability. The results presented in this chapter have been published.

## Article's reference

Anthony, E., Almar, R., Besset, M., Reyns, J., Laibi, R., Ranasinghe, R., **Abessolo O. G.**, Vacchi, M., 2019. Response of the Bight of Benin (Gulf of Guinea, West Africa) coastline to anthropogenic and natural forcing, Part 2: Sources and patterns of sediment supply, sediment cells, and recent shoreline change. *Continental Shelf Research*, 173, 93–103.

## Abstract of the paper

The Bight of Benin in the Gulf of Guinea, West Africa, forms an embayment between the Volta River delta in the west (Ghana) and the Niger River delta (Nigeria) in the east. The bight coast comprises sandy beaches backed by Holocene beach-ridge barriers. Incident swell waves, beachface gradient and the unidirectional longshore sand transport from west to east are intimately linked, generating a classic example of a strongly wave-dominated drift-aligned coast. The stability of this coast, which hosts several major cities in addition to three large international deepwater ports, has been strongly affected by human activities. We analyzed shoreline mobility and coastal area change over the period 1990–2015. Our results show how the stability of this coast has been strongly affected by the three ports therein, and by natural and human-altered shoreline dynamics related to the Volta River delta and to distributaries at the northwestern flank of the Niger delta. The combination of these factors has impacted alongshore sediment redistribution by segmenting the previously unrestrained longshore transport of sand that prevailed along this open coast. The result is a mixture of natural and artificial sediment cells increasingly dominated by shoreline stretches subject to erosion, endangering parts of the rapidly expanding port cities of Lomé (Togo), Cotonou (Benin) and Lagos (Nigeria), coastal roads and infrastructure, and numerous villages. Post-2000, the entire bight shoreline has undergone a significant decrease in accretion, which is here attributed to an overall diminution of sand supply via the longshore transport system. We attribute this diminution to the progressive depletion of sand-sized bedload supplied to the coast through the main Volta river channel downstream of the Akosombo dam, built between 1961 and 1965. Sand mining to cater for urban construction in Lomé, Cotonou and Lagos has also contributed locally to beach sediment budget depletion. Although alongshore sediment supply from the Volta River has been the dominant source of sand for the stability or progradation of the Bight of Benin coast, potential sand supply from the shoreface, and the future impacts of sea-level rise on this increasingly vulnerable coast are also important. The continued operation of the three ports and of existing river dams, and sea-level rise, will lead to sustained shoreline erosion along the Bight of Benin in the coming decades.

## 5.2 Sedimentary cell dynamics in the Bight of Benin

The BoB coast shows overall net advance (accretion) when averaged over the 25-year period of analysis, but also a varying alongshore pattern of shoreline change (Fig. 5.1). Five main sectors were identified (see Fig. 5.1), four of which (S1 to S4) correspond with major sediment cells. The identified sectors and their associated cells are built on the cell structure identified by Laibi et al. (2014). Sector S1 (cell 1), associated with the Volta delta, and sector S5 (unidentified multiple cells), along the westernmost flank of the Niger delta, are dominated by natural shoreline change patterns inherent to large deltas (Anthony, 2015b; Anthony et al., 2016; Dada et al.,

2016), whereas the remaining sectors S2-S4 (cells 2–4) between these deltas are dominated by the effects of port engineering structures (Fig. 2.1), but S3 is also impacted by the mouth of the Mono River and the Aneho inlet.

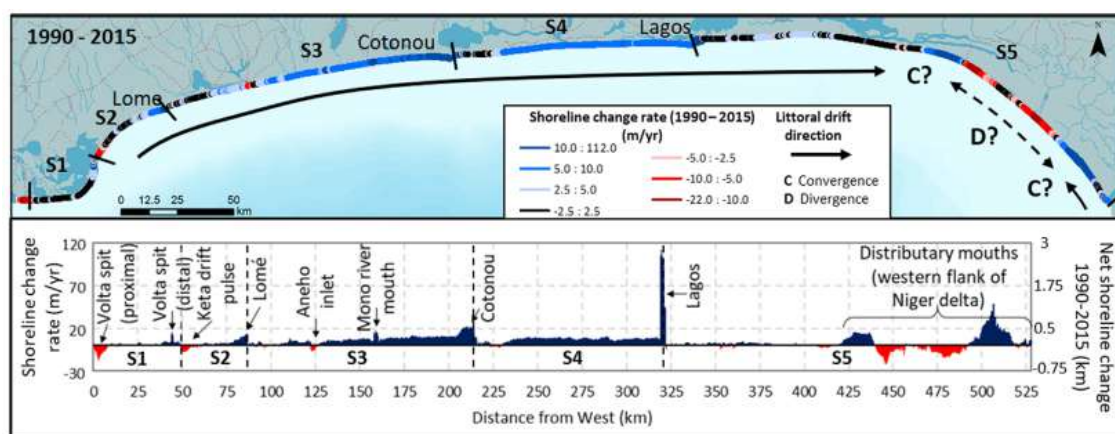


**Figure 5.1** – Shoreline change rates and net change in the Bight of Benin between 1990 and 2015, showing a spiky alongshore pattern. Significant changes are associated with identified features. Arrows show present dominant longshore sediment transport directions (dashed arrows = hypothetical directions). The shoreline has been divided into five sectors (S1 to S5), of which S1 to S4 correspond to individual sediment cells with boundaries (Anthony et al., 2019).

In cell S1, the combination of river sediment input, delta dynamics and strong sand transport appears to be responsible for the formation (after 1880?) and transformation of the Volta delta spit (Fig. 5.1, Anthony et al. 2016). S2 marks the transition of the delta transition with the rest of the bight coast, and is typically marked by erosion since the mid-1880s (Kumapley, 1989), before the construction of the Akosombo dam (Ly, 1980). This area of upward drift corresponds to what was initially a natural drift pulse, probably characterised by the highest potential rate of coastal transport in the Gulf of Benin (over 1 million  $m^3/year$ , Anthony and Blivi 1999). The amount of sand bypassing the Volta spit was not sufficient to compensate for the high coastal sand transport potential in this area, hence the strong and chronic erosion of the Keta area. Sector S3, artificially delimited by the ports of Lomé (west) and Cotonou (east), was fed by the sand bypassing the Volta spire and by the sand released by coastal erosion in the pulse zone of the Keta drift. Sector 4 is also bounded by ports, notably to the east by the port of Lagos. Sector 5 is bounded to the west, immediately downstream of Lagos port, by a major discharge structure, Eko Atlantic, an urban complex launched in 2007. To the east of this landfill, the multiple cells associated with S5 along the Nigerian coast (Fig. 5.1) include converging (shoreline accretion) or diverging (shoreline erosion) natural boundaries, but with a sand budget that has probably been affected by the large Lagos port. In this area, the many small distribution mouths that are part of the Niger Delta tend to favour a highly segmented multi-cellular structure. Each cell corresponds to a sand barrier with sets of beach bridges characterised by upward erosion and downward arrow curves associated with accumulation (Anthony, 2015b).

### 5.3 Trends in shoreline evolution

When the variability of the coastline is analysed in detail, an alarming erosive trend appears, even becoming dominant over the 2010-2015 period on the scale of the entire bay. Figures 5.2 and 5.3 show the evolution of the coastline for the four distinct analysis periods (1990-2000,

200-2005, 2005-2010 and 2010-2015) as well as the associated gains and losses in the coastal zone for each of the five sectors identified (S1 to S5). These results describe a clear trend of net advance over the decade during the decade 1990-2000, followed by a sharp decline in growth between 2000 and 2005, and a further decline until 2010. It is interesting to note that although S1 incorporates the coastline of the Volta delta and the river mouth, and thus corresponds to the main sand supply area of the bay the coastline, the advance recorded in this sector over the period 1990-2000 was much lower than that of sectors S3 to S5 (Fig. 5.3). S2 similarly exhibited only mild accretion between 1990 and 2000 (Fig. 5.3), whereas the other three sectors accreted significantly over this interval. Since 2000, all sectors have fluctuated more or less markedly, but the interval 2010–2015 has been characterized by retreat in S4 and especially S5.

The temporal trend of shoreline change is in agreement with the findings of Ozer et al. (2017) for Togo and Benin, where, between 2000 and 2015, 52% of an analyzed shoreline length of 170 km was eroding, 34% stable, and only 14% still advancing. A dominantly erosive trend from 2007 to 2013 was also highlighted by Addo (2015) for the Volta delta shoreline corresponding to our sectors S1 and S2 (Fig. 5.5).

The Hovmöller diagram of spatio-temporal shoreline change (Fig. 5.2) denotes a strong mean erosion trend between 2010 and 2015, highlighting two observations: (1) the strong erosion is largely accounted for by S5, whereas S1 to S3 showed mild recovery, and (2) is offset by the massive Eko Atlantic landfill. Other accretion spots are associated with the Lomé and Cotonou port breakwaters. Since 2010, long tracts of erosion prevail along much of the bight coast of Ghana, Togo and Benin, and especially in S5 east of Lagos (Fig. 5.2).

## 5.4 Causes of shoreline mobility in the Bight of Benin

Sharp gradients in, or interruptions of, longshore sand transport are expressed, as expected, by switches from accretion to erosion, or vice versa, as on either side of each of the three ports (Fig. 5.1). The Volta delta cell bounding S1 evinces a similar effect on shoreline stability in S2. The synchronicity of the changes throughout the bight coast, illustrated by the downward shift in accretion after 2000 (Fig. 5.3), suggests, however, the operation of through-drift across the artificial port cell boundaries which are, therefore, permeable. This permeability is also confirmed by the dredging operations to keep the port accesses free of sand transported alongshore (Lihoussou, 2014), and by periodic alarming reports in the regional press on the deleterious effects, on port activity, of inadequate dredging of these accesses.

### 5.4.1 EOF Analysis

In order to highlight spatial and temporal structure from the patterns of shoreline change, and, subsequently to further investigate causative factors, an Empirical Orthogonal Function (EOF) analysis of the generated shoreline change data. EOF analysis, or principal components analysis, is a commonly used technique to analyze spatial and temporal patterns of shoreline change (e.g., Anthony 1994; Wijnberg and Terwindt 1995; Kroon et al. 2008; Hapke et al. 2016). The EOF analysis brings out two modes (Fig. 5.4). Mode 1 accounts for 64% of the variability, and represents small spatial scales associated with relatively sharp local changes in accretion/erosion caused by the three ports and by natural shoreline dynamics, notably associated with distributary mouths debouching from the Niger delta, the Aneho inlet in Togo, and the Volta spit (Fig. 5.4.a). These features explain the spiky pattern of shoreline change between

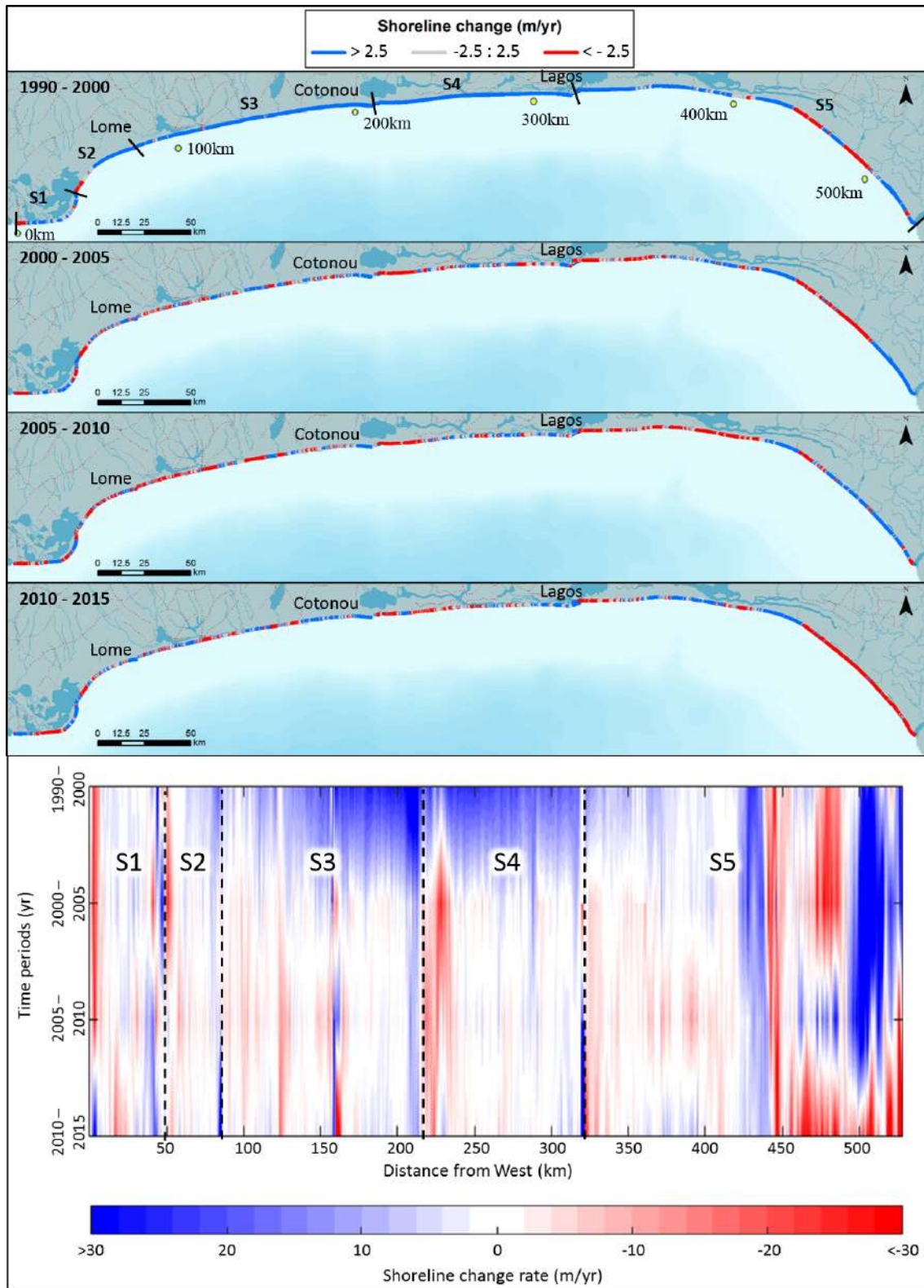


**Figure 5.2** – Maps of shoreline change in the Bight of Benin for the four individual intervals of analysis, and Hovmöller diagram of the spatio-temporal change pattern highlighting the increasing tendency towards dominant erosion (Anthony et al., 2019).

1990 and 2015 (Fig. 5.1). From almost 0 in the intervals 1990–2000 and 2000–2005, the intensity expressed by this mode increased clearly in the interval 2005–2010 (Fig. 5.4.b), reflecting the increasingly more segmented and variable shoreline pattern caused by the afore-mentioned features. Mode 2 explains 36% of the variability, and is interpreted as representing a larger scale (Fig. 5.4.a) associated with the gradual regional diminution in accretion over the study

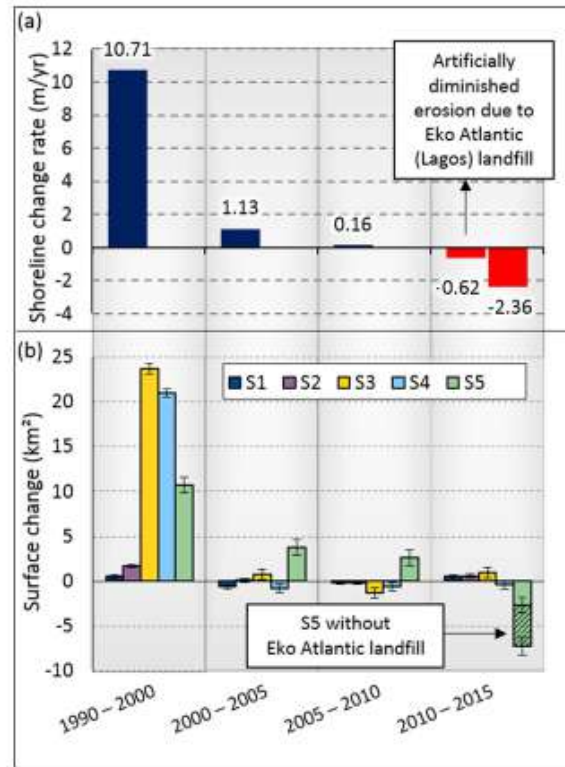


**Figure 5.3** – Shoreline change rates in the Bight of Benin over the intervals of analysis between 1990 and 2015, showing the switch in 2010–2015 from net accretion to net erosion across the entire bight shoreline (a), and changes in coastal surface area over these intervals for the five sectors (b). The two bars representing the 2010–2015 interval (a), and sector S5 (b) show the mitigating effect of artificial landfill near Lagos harbour on shoreline retreat, and the large shoreline retreat rate when this landfill is excluded from the analysis. (Anthony et al., 2019).

period (Fig. 5.4.b). This mode brings out the influence of the two longest sectors, S3 and S5, impacted, respectively, by sand inputs from the Mono River in addition to updrift accretion caused by the port of Cotonou (S3), and the significant fluctuations related to artificial landfill and fluctuations in sediment supply by distributary mouths (S5). Figures 5.1. and 5.4.a suggest that, apart from the inordinately large shoreline advance induced by the port of Lagos in S4 and the artificial landfill in S5 (Fig. 5), the effect on shoreline change by river/distributary mouths (Mono in S3 and Niger delta distributaries in S5) has been as important as that of the ports of Lomé and Cotonou.

#### 5.4.2 Longshore sediment transport, coastal infrastructures and rivers sand supply

The spiky pattern of shoreline change highlights, thus, the effect, on longshore sand transport, of artificial and natural cell boundaries, within a context of diminished advance since 2000 (Fig. 5.2). The alongshore alternations of eroding/stable/advancing sectors occurring along much of the cell segments away from the immediate vicinity of the three ports highlight intra-cell alongshore sand reworking within this context. Diminished shoreline advance has involved a west-east progression of erosion along the Bight of Benin coast, with increasingly longer stretches of eroding shoreline releasing sand that accumulates in shorter segments of accretion. This erosion threatens coastal communities, roads and infrastructure, entailing their successive landward displacements, and generates geopolitical tensions as the erosion wave, recognized in

each country as being caused by the port updrift in the neighbouring country, crosses country borders (Ozer et al., 2017).

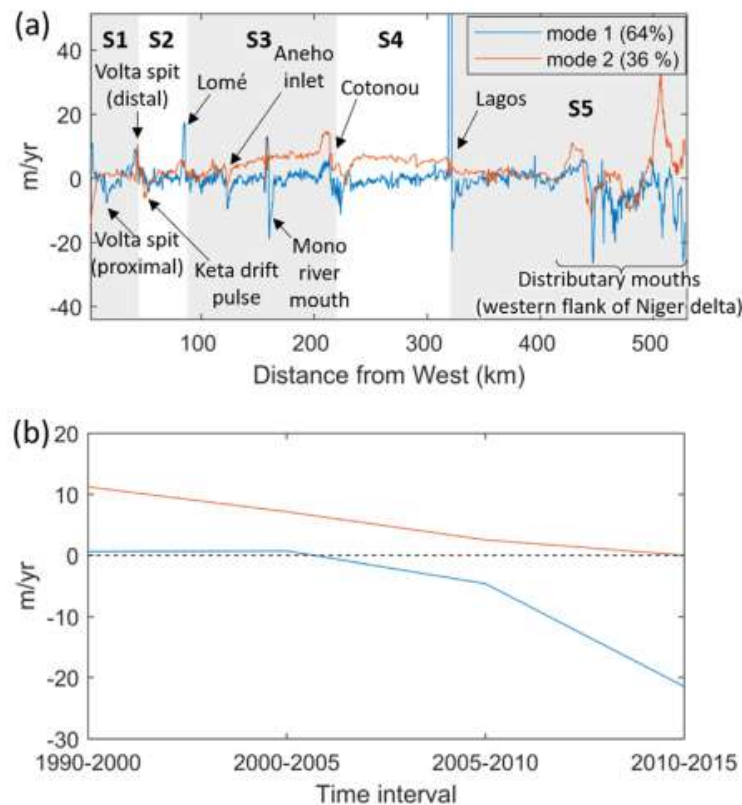


**Figure 5.4** – EOF modes of shoreline change in the Bight of Benin from 1990 to 2015: (a) spatial pattern, showing two modes representing, respectively, the pronounced local influence of features identified in Fig. 5.1 (mode 1), and the more regional (larger-scale) influence (mode 2) of the two longest two sectors, S3, dominated by the port of Cotonou, and S5, characterized by delta distributary mouths at the western flank of the Niger delta; (b) temporal pattern expressing each of these modes. Note the relatively marked decline expressed by mode 1 at the local level, and the gentler bight-wide decline by mode 2 mitigated by overall accretion in S3 and by two segments of strong accretion in S5 (one of which is the Eko Atlantic landfill), despite longer segments of erosion (Anthony et al., 2019).

The relatively moderate advance recorded in S1, which includes the main Volta mouth source for sand supply to the bight shoreline, compared to sectors S2 to S5 over the period 1990–2000 (Fig. 5.3.b), suggests the operation of efficient longshore transport eastward towards the rest of the bight shoreline. Erosion and accretion have largely alternated in this sector since 1990 (Fig. 5.5), probably in response to variations in sand supply from the Volta River and in wave conditions that are discussed later. Changes in shoreline orientation associated with spit development, and with an eastward shift of 12 km of the mouth of the Volta since the commissioning of the Akosombo dam (Addo et al., 2018) may also have had an impact on alongshore variations in accretion and erosion. S2 has been impacted both by drift acceleration in the Keta area and by the Aneho inlet, an erosion hotspot (Fig. 5.1). The infilling Aneho lagoon captures sand transported alongshore. Groynes were employed in this area in 1988 to protect the town of Aneho and a nearby phosphate export facility threatened by erosion (Anthony and Blivi, 1999). Significant accretion in S3 in the interval 1990–2000 was likely favoured by additional sand supply by the Mono River (Laibi et al., 2014). This sector has fluctuated since, probably in response to a diminution in sand supply downstream of the Nangbeto dam on the Mono,

and fluctuations in river discharge combined with periodic engineered breaching of the sand spit diverting the mouth of the river eastward (Ndour et al., 2018). Erosion has been dominant in S4 which is far downdrift of the Volta source and not associated with any direct river sand inputs. The marked changes that have affected S5, excluding the Lagos city expansion landfill (Fig. 5.3), and the clear shift to dominant erosion, may reflect the joint impacts, on fluvial sand supply to the coast, of river dams in the Niger catchment and of fluctuations in the hydrology of the Niger and its delta (Dada et al., 2018).

The large-scale shift, since about 2000, and especially since 2010, to a dominantly erosional bight shoreline and increasing losses in coastal area (Figs. 5.2 and 5.3) is due to an overall diminution of sand supply via the longshore transport system, although the bight averaged erosion between 2010 and 2015 is largely accounted for by the net retreat in S5 in eastern Nigeria (Fig. 5.3.b), impacted not only by interception of alongshore sand supply from the west by the large port of Lagos, but also by Niger delta distributaries. The most likely explanation for the downswing in significant advance in the decade 1990–2000 is an overall diminution of sand supplied by the Volta River. The continuous seaward growth of the large Volta spit over several decades (Anthony and Blivi, 1999; Anthony, 2015b), the significant accretion throughout the Bight of Benin in the decade 1990–2000, and the downswing in this accretion after 2000 (Fig. 5.3), including in growth of the Volta spit, all suggest that the negative effect of dams on sediment supply from the Volta River to the Bight of Benin was offset for several decades by the progressive transfer of channel bedload from the  $\sim 100$  km-long Volta channel downstream of these dams to the delta shoreline. This hypothesis, which concerns the adjustment time and dynamics of the Volta channel downstream of the Akosombo and Kpong dams, will require further research. Petts and Gurnell (2005) showed that river channel adjustment downstream of dams may occur over long periods (decades to centuries). The changes recorded since 2000 also coincided with enhanced but temporary sand trapping in the Keta drift pulse (Fig. 5.5) following the completion, in 2004, of a shoreline stabilization project to protect Keta. This project comprised several groynes, beach nourishment between groynes, a seawall, and landfill. The Keta project generated an artificial but permeable cell boundary that replaced part of the original drift pulse, which has shifted alongshore, resulting in erosion well downdrift of Keta. Although some interception by the Keta groynes no doubt contributed to a decrease in the volume of sand in transit to the BoB from the mouth of the Volta after 2000, we do not deem this interception as having played an important role in the decline in shoreline advance along the rest of the bight shoreline because: (1) spaces between these groynes were nourished in the course of the project (Fig. 5.5) to minimise aggravated downdrift erosion caused by sand trapping by the groynes, (2) erosion has occurred in recent years (2010–2015) in this protected segment of S2, an aspect also reported by Angnuureng et al. (2013) and Addo (2015), and (3) the longshore transport potential impacted by these structures would have been offset, anyway, by erosion of a large updrift segment of S2.

### 5.4.3 Influence of South Atlantic climate dynamics

An additional moderating influence on the alongshore sediment supply has been identified by Almar et al. (2015b) who highlighted an eastward longshore transport decay of -5% over the 1979–2012 period of analysis of the ERA wave dataset (Fig. 2). The authors linked this to a decrease in the intensity of westerly winds associated with the southward shift of pressure centres, and a strengthening of the trade winds, both of which reduce the eastward sediment transport

---

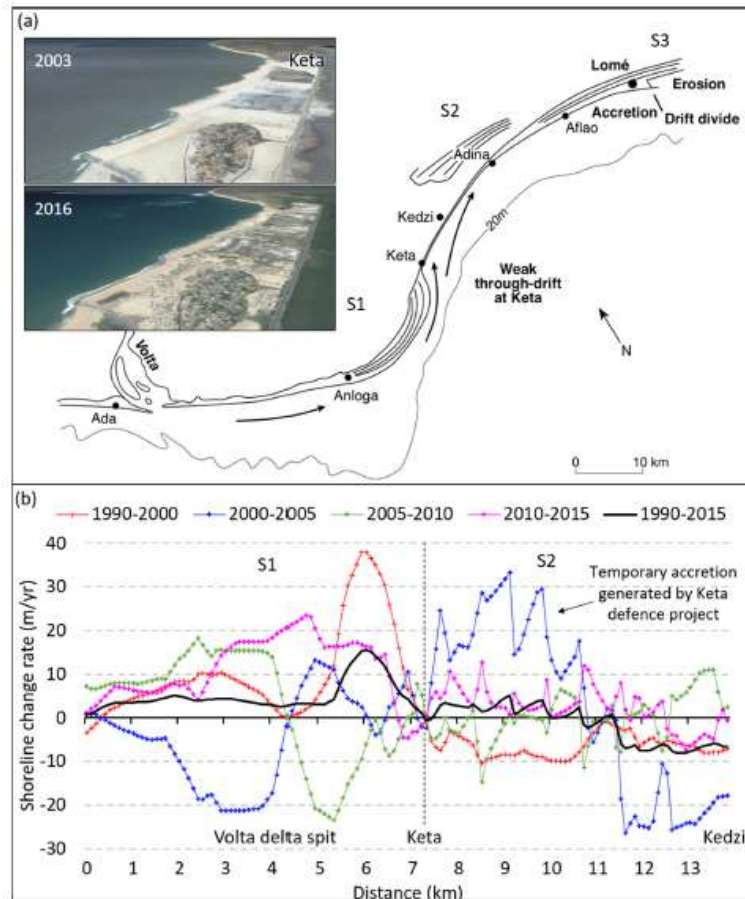


**Figure 5.5** – Schematic morphology and cell dynamics downdrift of the mouth of the Volta delta (a), and shoreline changes between 1990 and 2015 (b). A single longshore drift cell is presumed to have existed up to, and after, the 1880s, allowing transport of sand from the mouth of the Volta to the Bight of Benin (Anthony et al., 2016). The current cell (S1) between the delta mouth and Keta has been characterized by trapping of an unknown proportion of Volta sand by a distinct spit, resulting in the formation of a drift divide in the area of Keta and erosion of the Keta-Kedzi barrier sector downdrift of which occurs a second cell (S2) bounded eastward by the deepwater port of Lomé. The shoreline in this transition zone between S1 and S2 has fluctuated markedly since 1990, especially along the Volta spit. A coastal defence project involving groynes, a seawall, and landfill was implemented in Keta in the early 2000s (2003 and 2016 Google Earth photos inset), resulting in temporary accretion, and transformation of part of the natural Keta drift pulse into a fixed permeable artificial cell boundary accompanied by aggravated erosion downdrift towards Kedzi (Anthony et al., 2019).

potential. The equatorial fluctuation of the Inter-Tropical Convergence Zone (ITCZ) was found to explain most of the variability in transport induced by wind waves, while the Southern Annular Mode (SAM), an extratropical mode, had a predominant influence on transport induced by swell waves Almar et al. (2015b). The ITCZ and SAM had, respectively, a negative and positive trend over the period 1979–2012 that explain the decrease in both wind- and swell-wave-induced transport. The effect of this slight drop in transport may also have contributed to the attenuation of transport gradients in the BoB since it goes along with either a slight drop in wave energy or a slight decrease in wave approach angle.

#### 5.4.4 Localized sand mining

In addition to the deduced foregoing effects on sand supply from the Volta, the sediment budget of the bight coast has also been impacted negatively in the last decades by localized extractions of beach sand to cater for aggregate needs in urban construction (Dossou and Glehouenou-Dossou, 2007; Rutten, 2011; Ozer et al., 2017; Ndour et al., 2018) in all the bight countries, and especially for the cities of Cotonou and Lagos. Although legislation has been passed since 2000 in both Togo and Benin to regulate and even forbid beach sand extraction, the practice still continues, albeit at an apparently reduced rate.

#### 5.4.5 Outer shoreface/inner shelf sand supply

Alongshore sediment transport is fundamental to the stability of many open wave-dominated coastlines, in as much as sediment supply for coastal progradation (or to maintain stability) is commonly derived from rivers, which are the main suppliers of sediments to coasts globally (Milliman and Farnsworth, 2011). One unanswered aspect of the sand supply on the BoB coast is to what extent does outer shoreface/inner shelf sand supply still prevail along this coast? Sand supply from the shelf is thought to have been important in the early phases of barrier progradation as shoreface gradients in West Africa adjusted to the sea-level still stand (Anthony, 1995). Active sand supply from the shoreface to the coast in wave-dominated settings has been identified on a number of coasts exposed to swell (e.g., Cowell et al. 2003; Stive et al. 2010; Ruggiero et al. 2016). Quantifying sand supply from the shoreface is, however, technically very tricky, and fraught with difficulties (Aagaard, 2014). The BoB is fronted by a narrow shelf 15-33 km wide, and characterized by a fairly uniform, moderately steep shoreface with a gradient of between 1:120 and 1:150 down to -15 m, the hypothetical maximum closure depth for significant wave-induced sand transport on this coast (Delft Hydraulics, 1990). This closure depth leaves a significant shoreface zone over which sand stored on the inner shelf can be reworked and driven onshore by the constant SW swell waves impinging on this microtidal coast. The operation of such a potential shoreface sand source needs to be confirmed through high-resolution bathymetric and seismic surveying, but such data are not available. Seaward of the shoreface, the inner shelf forms a low-gradient (1 : 350 – 1 : 400) plain covered by relict transgressive sands (Anthony and Blivi, 1999).

#### 5.4.6 Future management and climate change

The extent to which the contemporary dominant erosion will continue to prevail on the Bight of Benin coast in the next decades will depend on: (1) the management choices implemented by the regional governments regarding the construction (likely) or removal (unlikely) of river dams in the future, and (2) climate change (Giardino et al., 2018). Meanwhile, ports, maintained and extended in the pursuit of economic development, will continue to fragment longshore sand transport on this coast, with localized accretion near downdrift sectors adjacent to cell boundaries and increasingly more prevalent erosion along much of the bight coastline.

Regarding climate change, Giardino et al. (2018) anticipate only a minor contribution from change in river hydrology to the stability of the BoB coast. Two other aspects that need further consideration are: (1) the effects of climate change on the hydrodynamic regime, and (2) sea-level rise. Regarding the influence of climate change on wave climate, General Circulation Models predict a stabilization of the SAM, evoked earlier, and, thus, a non-substantial or weak change

in alongshore sediment transport can be expected on the coast of the BoB (Almar et al., 2015b). Over the period 1993–2012, mean sea-level rise in Cotonou has been estimated at 3.2 mm/yr (Melet et al., 2016), a value close to that of the recent global trend (Church and al., 2013). A continuation of this trend in the future will adversely affect the BoB shoreline as sea-level rise will lead to landward translation of the coastline and an increase in sediment accommodation space on the shoreface. According to the sediment budget model of Giardino et al. (2018), the effect of coastal area loss due to the three ports will be approximately of the same order of magnitude as the effect of coastal retreat due to sea level rise (SLR) with a SLR scenario of 0.3 m by 2100, but the latter will become the overarching cause of erosion in a SLR scenario of 1.0 m. Given the likelihood of the continued operation of the existing ports, the continued presence of river dams, and ongoing SLR, shoreline erosion will continue to affect the BoB and the lives and livelihood of its cities and people.

---

## Chapter 5 summary

In this chapter, the shoreline mobility and the changes in coastal area in the **BoB** were analyzed over the period 1990–2015 using 5 shorelines (1990, 2000, 2005, 2010 and 2015) derived from Landsat images.

### Trends in shoreline evolution

- Post-2000, the entire bight shoreline has undergone a gradual retreat
- Since 2010, an alarming erosive trend on the scale of the entire bight is observed
- Since 2010, long tracts of erosion prevail along much of the bight coast

### Causes of shoreline mobility

- The coast has been strongly affected by the three ports therein, and by natural and human-altered shoreline dynamics related to the Volta River delta and to distributaries at the northwestern flank of the Niger delta, by segmenting the previously unrestrained longshore transport that prevailed along the open coast
- Diminution of sand supply via the longshore transport system, due to progressive depletion of sand-sized bedload supplied to the coast through the main Volta river channel downstream of the Akosombo dam
- Decrease in sediment inputs to rivers due to dams
- Sand mining to cater for urban construction has also contributed locally to beach sediment budget depletion
- Potential future impacts of climate change and sea level rise
- Potential sand supply from the shoreface and influence of South Atlantic climate dynamics

**The continued operation of the three ports and of existing river dams, and sea-level rise, will lead to sustained shoreline erosion along the **BoB** in the coming decades.**

## 5.5 Conclusion

This chapter provides an exhaustive list of all natural and anthropogenic factors whose combination could lead to the observed mobility of the shoreline in the **BoB**. Although it was not easy to identify these factors, it is even less easy to determine the proportions of the factors causing this variability, and their relative contributions to future anthropogenic and climate change. Depending on the degree of sophistication, modelling can meet this expectation and provide guidelines for effective coastal management frameworks. In the following chapter, the CASCADE coastline equilibrium model will be applied in the **BoB**, taking into account a maximum of identified variability factors.

## Chapter 6

# Modeling regional coastal evolution in the Bight of Benin

### Contents

---

<b>6.1</b>	<b>Introduction</b>	<b>102</b>
<b>6.2</b>	<b>Data form employed</b>	<b>103</b>
<b>6.3</b>	<b>Modeling regional coastal evolution</b>	<b>103</b>
6.3.1	Background and theoretical formulations	103
6.3.2	Model set-up	105
6.3.3	Model calibration	105
6.3.4	Model validation	106
<b>6.4</b>	<b>Simulation results for selected scenarios</b>	<b>108</b>
6.4.1	Overview	108
6.4.2	Transport pattern without harbor structures	109
6.4.3	Nourishment to remedy downdrift erosion	110
6.4.4	Influence of reduced boundary transport	110
<b>6.5</b>	<b>Discussion</b>	<b>111</b>
<b>6.6</b>	<b>Conclusions</b>	<b>114</b>

---

The 400-km long coast of the [BoB](#), formed by sand barriers and lagoons, is bordered to the east by the Niger River Delta and to the west by the Volta Delta and is characterized by several coastal infrastructures, of which the most important are the deep water harbors of Lomé, Cotonou, and Lagos. In this work, an enhanced version of the CASCADE coastal evolution model was implemented in order to reproduce the evolution of the coast over the period 2000-2015, considering the presence of coastal infrastructure, inlets, and the reduced sediment influx from rivers. The model results showed simulated coastal response around the main coastal infrastructure in agreement with observed data. In addition, the validated model was used to estimate the amount of sediment needed to control erosion through beach nourishment downstream of the harbors. The impact of reducing sediment input on coastal evolution was investigated through model parameterization of the influx at the boundary. Overall, the model may be a useful tool for improving regional coastal policies in the Bight of Benin.

The results presented in this chapter have been submitted for publication.

## Article's reference

**Abessolo O. G.**, hoan L.X., Almar, R., Larson M., 2020. Modeling the Bight of Benin (Gulf of Guinea, West Africa) coastline response to natural and anthropogenic forcing. *Regional Studies in Marine Sciences*, in Review.

### 6.1 Introduction

Decision-making for coastal development is still a challenge today due to multi-scale adjustments of the coast to changes in wave climate, sea level rise, and sediment supply (Ranasinghe, 2016). Shoreline management and policies are increasingly concerned with adaptive responses to coastal change (Nicholls et al., 2012, 2013) and related plans are invariably framed by projections of climate change and their anticipated consequences for the coast (Nicholls and Cazenave, 2010).

Major barriers for sustainable coastal planning are therefore the limited understanding of the primary controls on coastal behavior over time scales relevant to management and the difficulty of implementing an integrated coastal management plan on a large scale across geographic boundaries, aiming at creating awareness between policy makers in different countries about current and future challenges (Giardino et al., 2018). For instance, in the BoB, which is a part of Gulf of Guinea, West Africa, disturbances to the stability of a 400-km long shoreline have been observed over the last few decades, mainly due to the three deep water harbors and their jetties together with the reduction in sediment supply from adjacent rivers (Laibi et al., 2014; Almar et al., 2015b; Giardino et al., 2018; Anthony et al., 2019). However, there are few local indicators that enable the prediction of regional spatial scale impact of large settlements/infrastructure and changes in oceanic forcing, as the multi-scale interplay between natural and anthropogenic processes and influences is complex (French and Burningham, 2009; Del Rio et al., 2013). Sea-level rise, elevated storm-surge water levels, high-energy storm waves, depletion of sediment budgets from rivers, and the construction of sea walls are all capable of promoting large-scale beach change. In addition, Giardino et al. (2018) observed that the fragmentation of actors and responsibilities between West African countries, and even within the same country, have hampered the planning of effective and sustainable solutions for decades. Integrated large-scale spatial and temporal prediction of the evolution of this coastal system is therefore important to decisions-makers in the concerned countries, which are low-income countries with 70% of the population in the coastal zone (Ndour et al., 2018). As shoreline evolution is the combined effect of natural and human activities, which vary over space and time, numerical models are vital to understand shoreline change behavior that will eventually lead to large-scale integrated coastal zone management.

A wide variety of coastal evolution models have been developed for this purpose, each having attributes that reflect specific application areas. Until now, models, whether physics-based, process-based or empirical, inevitably rely on more or less extensive approximations of complex and multi-scale systems. Cross-shore and longshore processes have mostly been described separately in these models, where the latter is typically the largest contributor to coastal change. Thus, when considering coastline evolution at large spatial scales (1 to 100s km of coast), the representation of the cross-shore sediment exchange has been simplified, employing sources and sinks with schematized values in time and space (e.g. Larson et al. 2002a,b; Hoan et al. 2011a).

---

To improve the predictive capability of these models from the time scales of hours (i.e. storm) to decades, longshore and cross-shore processes have been combined in a more rigorous manner, using physics-based formulations (Larson et al., 2016; Vitousek et al., 2017; Robinet et al., 2018). However, further simplifications are required to reduce the computational time since simulations are performed for large areas (more than 100 km of coast) over long time periods, i.e., decades to centuries (Larson et al., 2016).

In order to provide assistance to decision-makers regarding coastal development in West Africa, this chapter aims to model the observed evolution of a 400-km long coastal stretch (covering Togo, Benin and Nigeria) in the Bight of Benin from 2000 to 2015. Based on this modeling, the importance of anthropogenic influences on the coastal evolution in the BoB is investigated in a more rigorous manner. The validated model may be used to predict the evolution of the studied coast in the light of different scenarios and management policies. For this purpose, we used a regional coastal evolution model that can be applied to stretches of coastline covering hundreds of kilometers, encompassing several barrier islands separated by inlets, including such phenomena as inlet creation, ebb- and flood-tidal shoal development, bypassing bars between beaches and inlets, channel dredging, regional trends in the shape of the coast, and shore-protection structures and activities, for example groins, seawalls, and beach nourishment. Cross-shore related processes such as relative change in sea level, wind-blown sand, cliff erosion, and storms may be included as sources and sinks with strengths varying in time and space.

## 6.2 Data form employed

Wave characteristics were extracted and daily-averaged from ERA-Interim ECMWF re-analyses (Sterl and Caires, 2005) at eight different stations along the coast (Fig. 6.1), at 6-hr interval. In order to determine the coastline evolution over the 15 years, available 4-8 Landsat images were analyzed. The criteria for image selection focused on individual spatial coverage with minimal cloudiness, and on the robust and accurate determination of shoreline location. Twelve images were chosen and downloaded from the USGS data portal Earth Explorer, three for each of the years 2000, 2005, 2010, and 2015. The shoreline was derived with an accuracy of around 1 pixel (30 x 30m), using panchromatic at 10 m resolution and a customized combination of bands maximizing land-water contrast. Then, shorelines were digitized at 100-m alongshore spacing using the ArcMap extension module Digital Shoreline Analysis System (DSAS), version 4.3, coupled with ArcGIS 10. An error of  $\pm 2.4m/year$  between 1990 and 2015 was obtained, considering image rectification, extraction of the shoreline, and operator digitization in delimiting the shoreline.

## 6.3 Modeling regional coastal evolution

### 6.3.1 Background and theoretical formulations

The Cascade model (Larson et al., 2002a) was established to address time and space scales associated with regional coastal processes, providing predictions suitable in the planning and preliminary design phase of a project. As the first step towards modeling regional coastal evolution, Cascade was developed to bridge the gap between a sediment budget approach and a shoreline evolution model. The dynamics of selected processes and controls of importance for

---

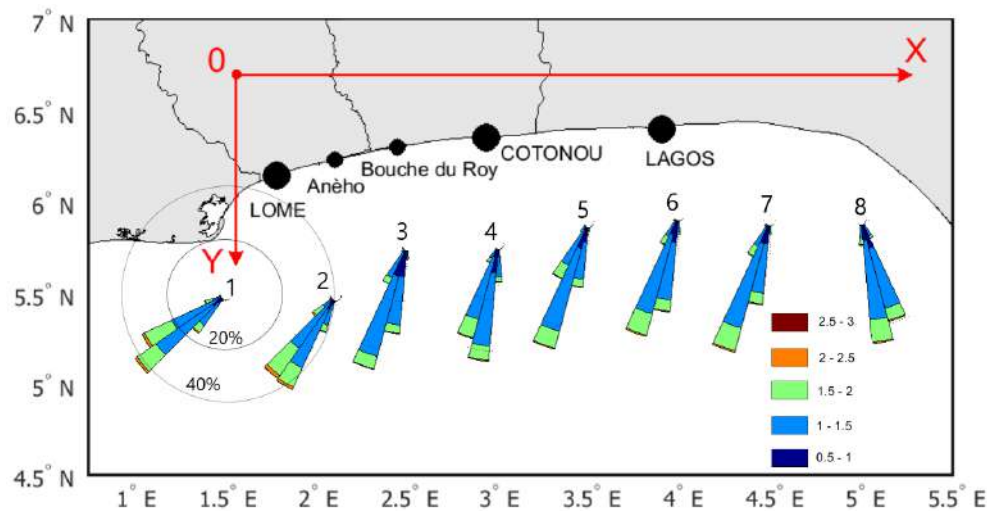


**Figure 6.1** – Grid reference (0, X, Y) used to model the shoreline evolution in the Bight of Benin together with the locations of wave input stations (1 to 8) with wave roses and of the main cities in the bight. The wave roses computed for the period from 1990 to 2015, show the predominant directions of waves and their significant heights ( $H_s$ ) with color bands.

the regional coastal evolution were modeled based on physical representations, whereas other processes were parameterized through time- and space-varying sources and sinks. Cascade was calibrated and validated against high-quality data sets from three coasts that describe the regional coastal evolution after the creation of multiple inlets on open barrier-island coasts (Larson and Kraus, 2003; Larson et al., 2006). These successful long-term simulations were made for the opening of Moriches and Shinnecock Inlets on Long Island, and Ocean City and Indian River Inlets on the Delmarva Peninsula.

(Hoan et al., 2011b) enhanced the capability of the Cascade model to simulate inlet sediment transport and the evolution of morphological elements at an inlet. Also, the possibility to describe structures in the model was improved and a more general longshore sediment transport formula was implemented that is sensitive to grain size and includes currents that are not only wave-generated. The improved model was employed to reproduce the regional coastal evolution along the coast of Long Island as well as for predicting the progression of linear spits at several sites (Hoan et al., 2011a). An earlier version of this model was used to reproduce the observed evolution at Hai Hau Beach in Vietnam (Hoan et al., 2010).

The model by Hoan et al. (2011b), employed in this study, consists of the following main components:

- Nearshore wave transformation including breaking
- Longshore current and sediment transport
- Inlet sediment transport and morphological evolution
- Cross-shore sediment exchange through sources and sinks
- Impact from human intervention due to structures and activities
- Coastal evolution from sediment conservation

The wave conditions at breaking are computed based on linear wave theory assuming locally straight and parallel bottom contours, where an arbitrary number of wave input station can be employed. Based on the breaking conditions, the longshore current and sediment transport are determined using the formula proposed by Bayram et al. (2007), expanded for tidal- and wind-induced currents following Hanson et al. (2006). The inlet sediment transfer and storage,

schematized through a number of morphological elements are simulated using the reservoir model suggested by Kraus (2000), further refined by Hoan et al. (2011b). Cross-shore sediment exchange is handled through sources and sinks with strengths that may vary in time and space, including sediment supply from rivers. Different structures and activities to control the sediment transport and coastal evolution are possible to include, for example jetties, groins, and beach nourishment. The evolution of the coastline is determined based on the sediment conservation equation after the longshore sediment transport has been computed together with contribution from sink and sources, and with application of the appropriate boundary conditions.

### 6.3.2 Model set-up

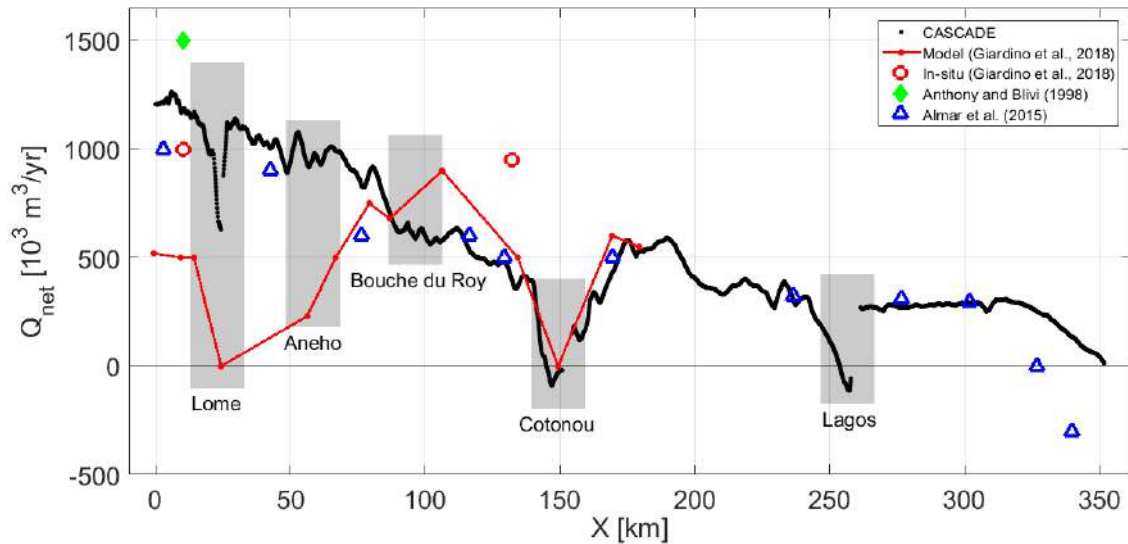
The evolution of a 400 km-long stretch of coastline along the BoB was simulated using a grid size of 100 m and a time step of 3 hr (equal to a half of the wave input time step). A grid was placed on land with the x-axis pointing in the eastern direction and the y-axis offshore. Fig. 6.1 displays the grid employed together with the input stations from the derived wave climates. The wave roses are shown at each station illustrating the bimodal wave climate, also indicating the prevalence for easterly sediment transport, except at the most easterly located station. The boundaries of the grid were placed at locations where the shoreline exhibited almost no change in the observed data, corresponding to boundary conditions with fixed shoreline positions, implying zero transport gradients. Thus, the longshore transport is free to move over the boundaries, attaining values that ensure no shoreline change.

In order to calibrate the model, the shoreline change between 2000 and 2010 was used, whereas the period from 2010 to 2015 was employed for validation. The main calibration parameters were the two transport coefficients (see Hoan et al. 2011b, for which the optimum values were  $K1 = 0.15$  and  $K2 = 0.1$ ). These values are considered typical and in agreement with previous studies. The wave conditions between the stations were linearly interpolated at each time step and allowed to vary along the grid. The sediment supply from various rivers in the modeled stretch was added as continuous sources with a constant strength following the values reported by (Allersma and Tilmans, 1993). The supply from the Volta and Niger River was represented through the boundary values for the longshore sediment transport obtained at the right- (west) and left-hand (east) side of the grid, respectively. The main structures along the coast, especially around the harbors, where described in the model employing their physical dimensions as determined from aerial photos, also including changes to structural properties through time. Some of the minor groin fields were not included in the simulations, since they have limited influence on the evolution at the regional scale.

### 6.3.3 Model calibration

Fig. 3 illustrates the calculated mean annual net longshore sediment transport rate ( $Q_{net}$ ) in the study area for the calibration period, where eastward transport is positive. In the figure are also results from other studies shown, derived through different means. Overall the agreement between the present study and the previous investigations is good, although some deviations occur. The present modeling show that  $Q_{net}$  decreases from more than a million  $m^3/year$  in the eastward direction at the western end of the grid to  $Q_{net}$  about 0  $m^3/year$  at the eastern end. The influence of the three harbors are clearly seen, where Lagos and Cotonou causes zero transport at their locations, whereas the influence of Lomé is more limited, although still

pronounced.



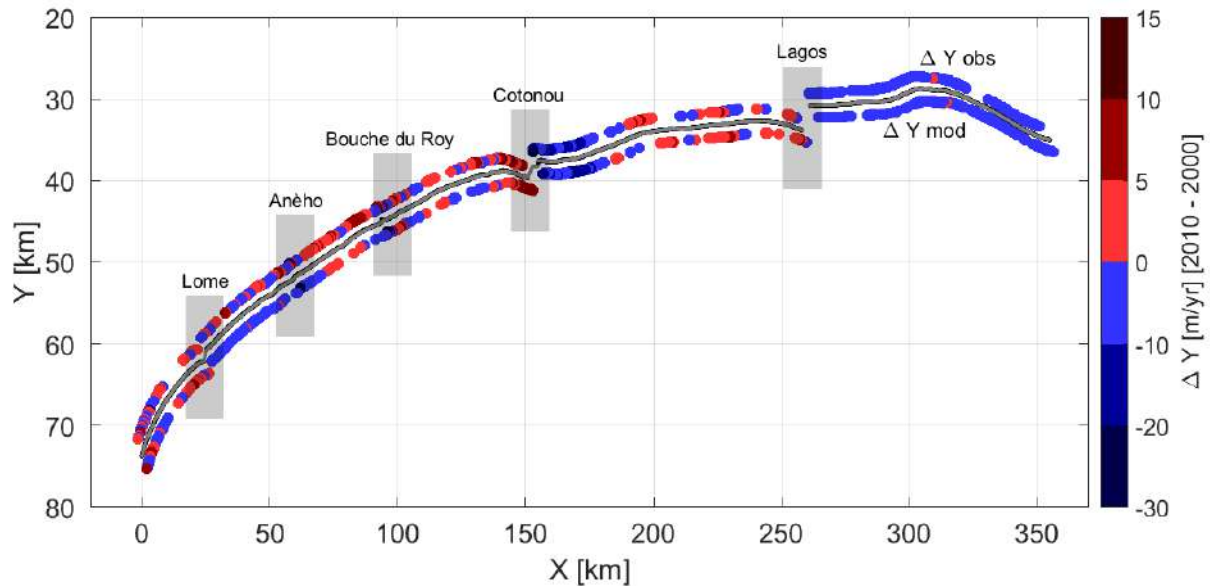
**Figure 6.2** – Calculated mean annual net longshore sediment transport rate along the study area in the Bight of Benin for the calibration period from 2000 to 2010, together with estimated transport rates in previous investigations through various means.

Fig. 6.3 displays the initial shoreline at year 2000 together with the modelled and observed shorelines at 2010. The differences is hard to assess at the scale of the entire bight, so detailed results are shown in Figs. 6.4a-c for the three harbor areas, including difference plots for selected regions with the most pronounced change. An important aspect of the modeling is the ability of the model to maintain the regional shape without any large-scale diffusion and shoreline smoothing. This lends credibility to the calculated large-scale alongshore sediment transport pattern based on the wave input station, since the transport gradients produce the correct regional shape of the shoreline. The harbor areas are clearly displayed as gaps in the shorelines with distinct offsets. For some of the harbors the updrift structure may experience bypassing, but typically this sediment is not transferred to the downdrift area because of the harbor configurations not promoting this.

Figs. 6.4a, 6.4b, and 6.4c display the shoreline evolution in the vicinity of the harbors at Lagos, Cotonou, and Lomé, respectively. The initial shoreline at year 2000 together with the modelled and observed shorelines at 2010, as well as the modelled and observed shoreline change, is shown in these figures. The focus is on the areas around the harbors since the largest changes occur here; it was difficult in some cases to exactly determine the harbor configuration and properly represent it in the model, especially on the downdrift side. It can be seen from the plots that the main features of the shoreline change is reproduced satisfactorily some distance away from the harbor area at Cotonou and Lagos ( $r = 0.91$  and  $r = 0.96$  significant at 95% confidence level, respectively); however, this is not the case around Lomé harbor ( $r = 0.09$ ).

### 6.3.4 Model validation

The optimized model parameters based on the calibration period 2000-2010 were used to simulate the evolution 2010-2015 to validate the model. The agreement between the modelled and observed shoreline change during the validation period was somewhat less good ( $r = 0.74$  significant at 95% confidence level), as the model shows a higher variance and seems to miss parts of the largest erosion ( $\Delta Y_{obs} \leq -13m/yr$ ), as displayed in the validation panel (2010 -



**Figure 6.3** – The initial shoreline (black line) at year 2000 together with the modelled and observed shorelines at 2010 (grey lines, respectively), as well as the modelled and observed shoreline change represented with dots ( $\Delta Y_{mod}$  and  $\Delta Y_{obs}$ , respectively). Only changes greater than 20 m have been shown. Red indicates accretion, blue indicates erosion.

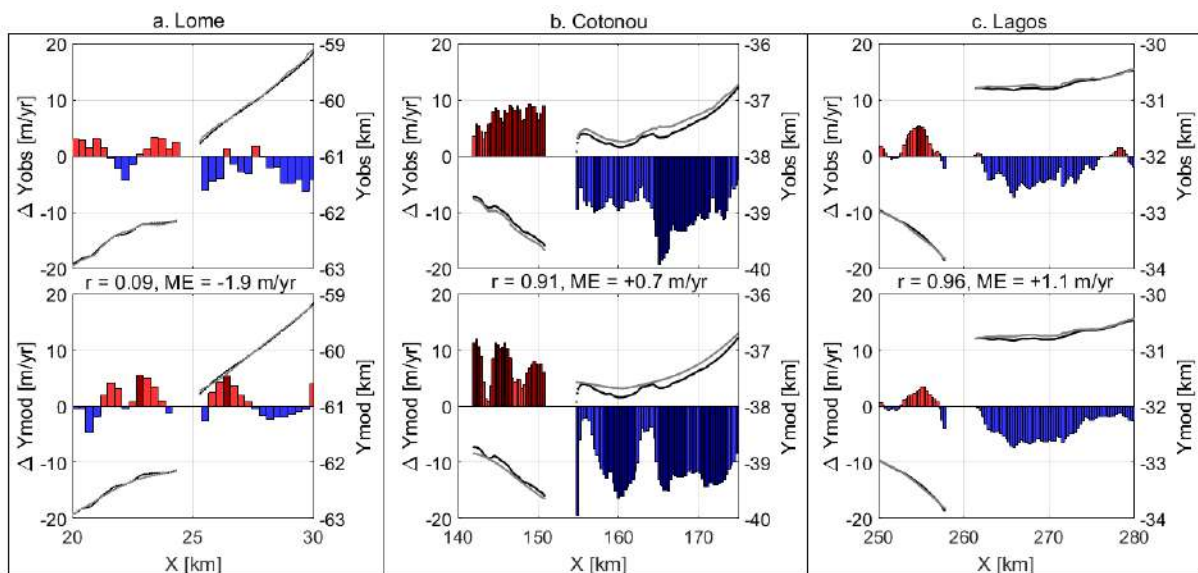


**Figure 6.4** – Shoreline changes for the areas around the harbors of (a) Lome, (b) Cotonou, and (c) Lagos for the calibration period from 2000 to 2010. Left y-axis: observed and modelled shoreline changes ( $\Delta Y_{obs}$  and  $\Delta Y_{mod}$ , respectively) represented with bars. Red indicates accretion, blue indicates erosion. Right y-axis: the black line represents the initial shoreline at year 2000, the grey line represents the modelled or observed shorelines ( $Y_{mod}$  or  $Y_{obs}$ , respectively) at 2010.  $r$  and  $ME$  stand for the correlation and the difference between modelled and observed changes.

2015) in Fig. 6.5. Overall, the agreement remains similar to the calibration period, which gives confidence to the ability of the model to simulate shoreline evolution in the study area (Fig. 6.5). Furthermore, the main feature of the calculated annual net longshore transport rate for the validation period was identical to the calibration period, with only minor, local differences. One noteworthy difference was obtained;  $Q_{net}$  was close to negative at the eastern boundary, indicating some sediment influx from the Niger Delta during this time period (see Fig. 6.7; also,

compare with the estimate in this region by [Almar et al. 2016](#) shown in Fig. 3). The transport on the western side, reflecting the supply of sediment from the Volta River side was similar to what is shown in Fig. 6.2.

Figs. 6.6a, 6.6b, and 6.6c display the shoreline evolution in the vicinity of the harbors at Lagos, Cotonou, and Lomé, respectively, for the validation period. The initial shoreline at year 2010 together with the modelled and observed shorelines at 2015, as well as the modelled and observed shoreline changes, are displayed in these figures. Again, the figures emphasize the areas in the vicinity of the harbors where the largest changes occurred. As for the calibration period (see Figs. 6.4a-c) the main features of the shoreline change is reproduced satisfactorily.

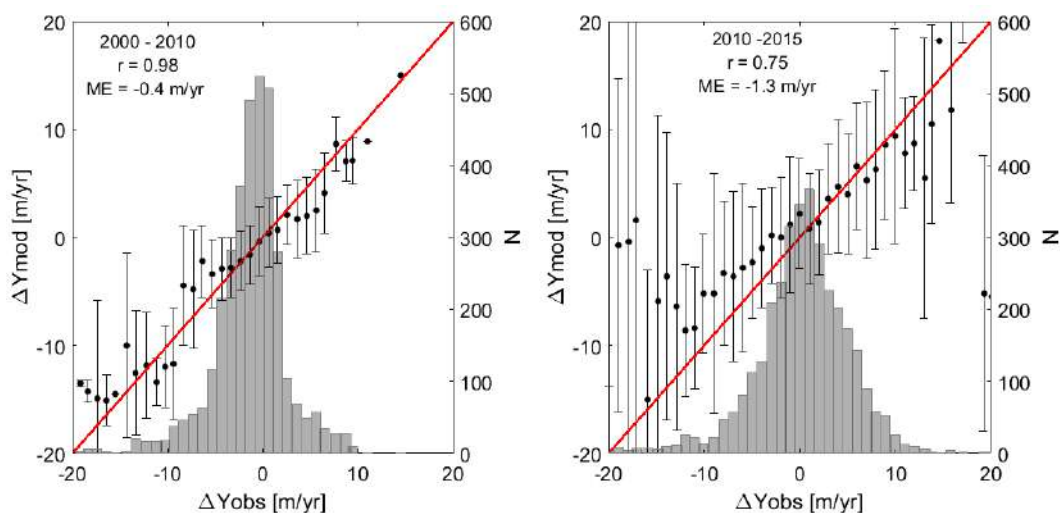


**Figure 6.5** – Comparison of observed (x-axis) and modelled (left y-axis) shoreline changes for calibration (2000-2010) and validation (2010-2015) periods. Changes were averaged over a 1 m-window interval on the x-axis and the error bar gives the dispersion within the window. The number of samples (N) considered within the window is given on the right y-axis. Correlations were computed at 95% confidence level.

## 6.4 Simulation results for selected scenarios

### 6.4.1 Overview

In order to quantify the importance of anthropogenic influences on the coastal evolution in the BoB, different scenarios were simulated where the impact of man-made structure and activities were investigated. Three different scenarios are discussed here focusing on the impact of:

- Harbor structures
- Nourishment operations
- Reduced sediment influx due to dam construction

In the case of the harbor structures, the effects of Lagos, Cotonou, and Lomé harbors were investigated by removing the structures completely. The nourishment operations were employed to determine the amount needed to combat downdrift erosion at Lagos Harbor, where the most severe erosion was observed. Finally, the boundary condition for sediment influx on the western boundary was modified to mimic the effects of reduced sediment supply due to dam construction in the Volta River system. All simulations were made for the validation period 2010-2015.

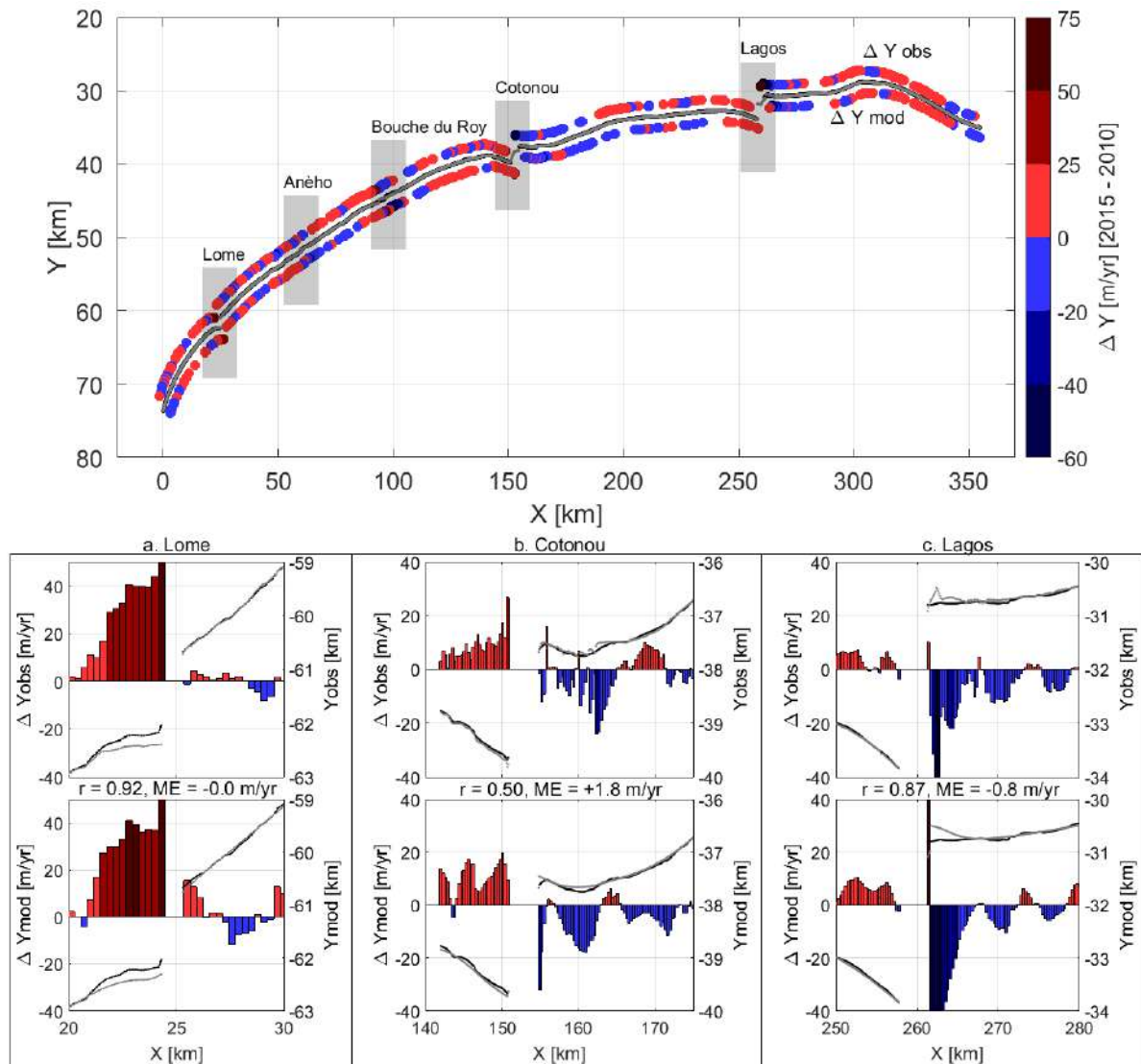


**Figure 6.6** – Panel above: shoreline changes for the validation period from 2010 to 2015. Black and grey lines represent the initial shoreline at year 2010 together with the modelled and observed shorelines at 2010, respectively. Dots indicate the modelled and observed shoreline change ( $\Delta Y_{mod}$  and  $\Delta Y_{obs}$ , respectively). Red indicates accretion, blue indicates erosion. Panel below: corresponding shoreline changes for the areas around the harbors of (a) Lome, (b) Cotonou, and (c) Lagos. Left y-axis: observed and modelled shoreline changes ( $\Delta Y_{obs}$  and  $\Delta Y_{mod}$ , respectively) represented with bars. Right y-axis: the black line represents the initial shoreline at year 2000, the grey line represents the modelled or observed shorelines ( $Y_{mod}$  or  $Y_{obs}$ , respectively) at 2010.  $r$  and  $ME$  stand for the correlation and the difference between modelled and observed changes.

#### 6.4.2 Transport pattern without harbor structures

In this simulation, the three main harbors in the bight were removed as well as inlets at Anèho and Bouche du Roy. The input shoreline was smoothed in accordance with its natural shape. Fig. 6.7 shows  $Q_{net}$  for the cases with and without the harbors at Lagos, Cotonou, and Lome. The plot clearly illustrates the influence of the harbors, in terms of magnitude, gradients, and spatial extent. The mean annual net transport rate without harbors and inlets influence represents the averaged net transport due to waves from 2010 to 2015. The difference between  $Q_{net}$  computed with and without harbors represents the transport fluctuations introduced by harbors and inlets. Using the implementation of a multiple linear regression, relative contributions to the variation in

shoreline computed for the coast show that total shoreline changes are significantly influenced by harbors and inlets (60%) with regard to direct effects from the waves (40%). When analyzing the areas around the harbors, relative contributions show that harbors (84%) are dominant drivers of shoreline migration up and downstream in comparison to the waves (16%).

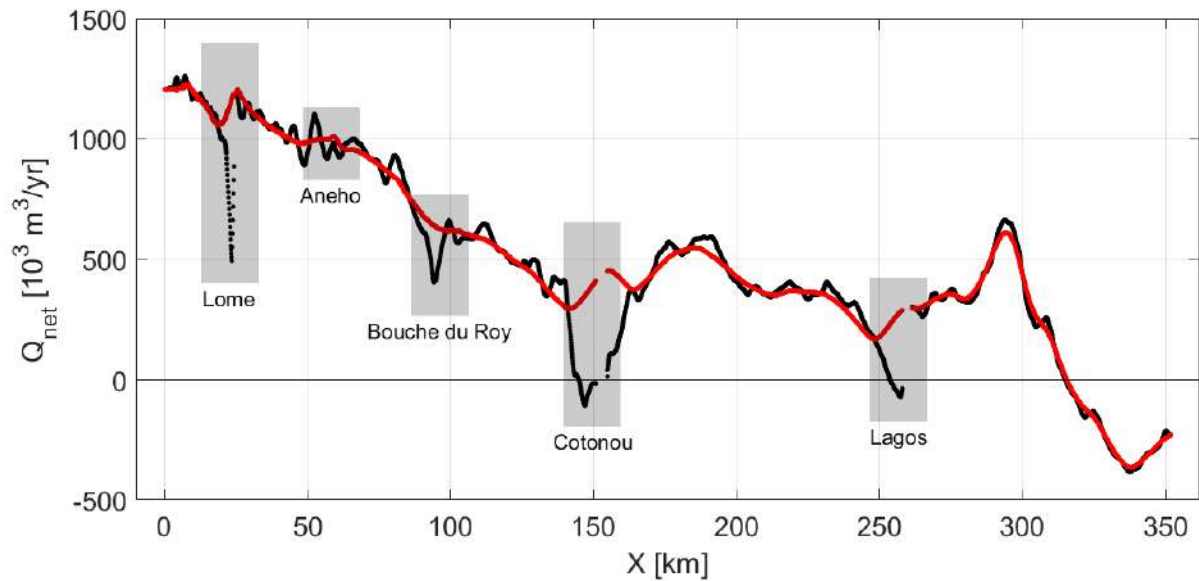


**Figure 6.7** – Mean annual net transport rate for the validation period (2010 – 2015) for the cases with (black) and without (red) the harbors at Lagos, Cotonou, and Lomé and inlets.

### 6.4.3 Nourishment to remedy downdrift erosion

A common and popular method to remediate erosion is beach nourishment, where sand is added to the beach, typically to compensate for sand that is lost because of unfavorable gradients in the longshore sediment transport. The nourishment can be put in different parts of the beach and at different time intervals. Here, in order to estimate the amount of nourishment needed to compensate for downdrift erosion at Lagos Harbor, a constant source of sediment was added over a specific distance downdrift the harbor. The magnitude of the source was determined through calibration with the purpose to achieve a stable shoreline during the study period with limited erosion.

The model shows that the inlet jetty blocks the sediment transport to a large degree, producing downdrift erosion; thus, net sediment transport updrift the inlet is small (see Fig. 6.2), but net transport increases significantly along the erosion area (see Fig. 6.7, where  $\Delta Y < -100m$ ). The construction on the east side of the jetty, started from 2011 and modelled with a seawall condition, is another reason for the erosion. To maintain the beach, the total nourishment volume needed is about 3 300 000 m<sup>3</sup> for the period from 2010 to 2015, as observed in Fig. 6.8. This corresponds to a nourishment of 650 000 m<sup>3</sup>/year.

### 6.4.4 Influence of reduced boundary transport

A large amount of sediment enters into the study area from the western side, presumably originating from the Volta River Delta. The calculations showed varying input of sediment on the eastern side, related to the Niger River Delta, with a negligible net contribution during the calibration period, whereas the input was significant for the validation period. In order to

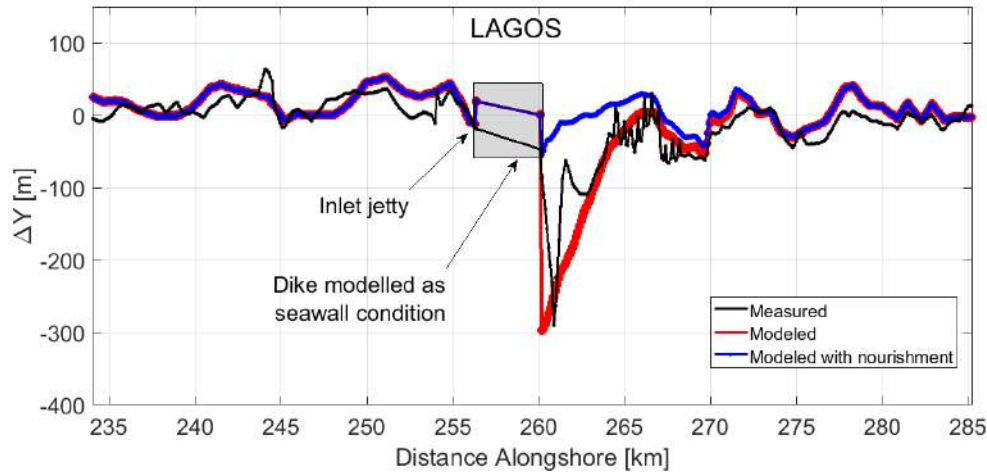


**Figure 6.8** – Nourishment simulation at Lagos Harbor for the period from 2010 to 2015.  $\Delta Y$  represents the shoreline changes modelled and modelled in 2015 compared to the 2010 shoreline.

evaluate the effects of a reduced boundary inflow of sediment, presumably replicating the case with less sediment being supplied from the Volta River Delta, a modified boundary condition was developed. Instead of allowing for a free inflow of sediment at the boundary, maintaining a stable shoreline, the inflow is restricted according to a specific function.

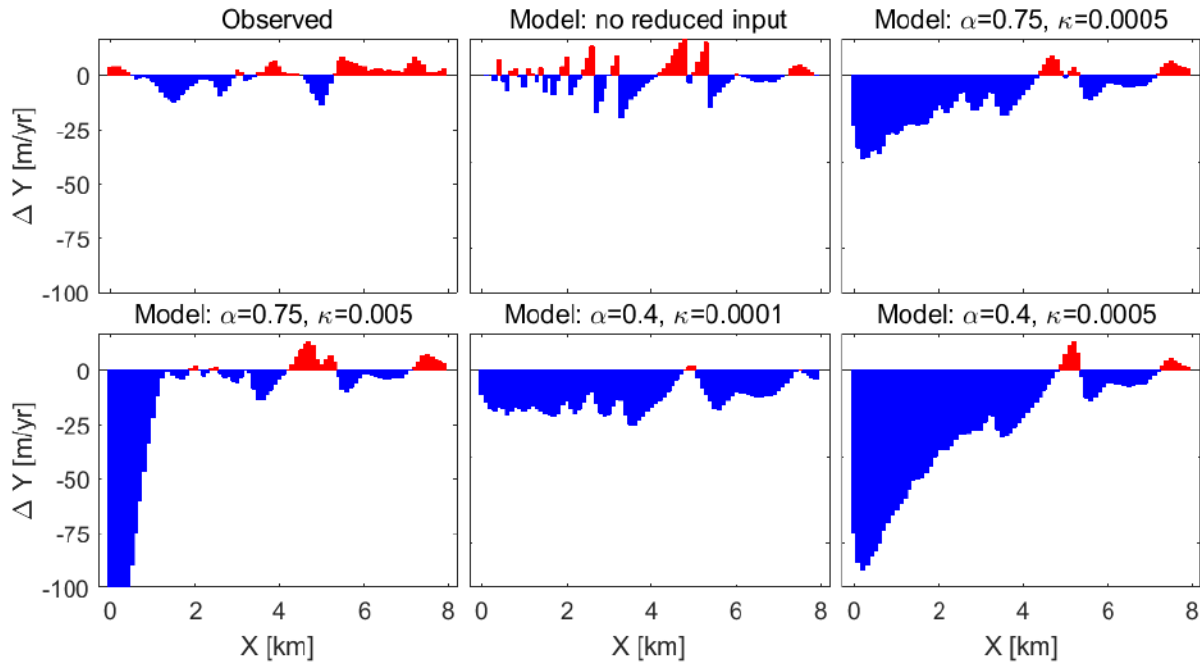
A specific multiplier ( $\alpha$ ) was employed to the transport rate obtained at the boundary with a fixed shoreline position, lowering the rate in order to represent a reduced inflow of sediment. To mimic the spatial influence of the reduced transport at the boundary, an exponential growth function was used from the boundary in towards the grid, where the influence on the local transport rate decayed from  $\alpha$  to 0 (the latter implies no influence). The rate of the decay was determined by a coefficient  $\kappa$  having the units  $m^{-1}$ .

Fig. 6.9 illustrates the effect of different values on  $\alpha$  and  $\kappa$  on the shoreline evolution. A larger  $\alpha$  implies a larger reduction in the sediment influx and a smaller  $\kappa$  a larger spatial influence. For a given  $\alpha$ , a smaller  $\kappa$  would expand the erosion area, but causing a smaller retreat at the boundary where the maximum effect occurs.

## 6.5 Discussion

In this study, the effects of the major man-made interventions (harbor dikes and river dams) on coastal evolution in the Bight of Benin were assessed using an enhanced version of the CASCADE. The application of the model to the studied coast shows good overall performance in the vicinity of the harbors, reproducing well the erosion and accumulation areas (Laibi et al., 2014; Anthony et al., 2019) and showing a robust behavior during the simulation period. With the validated model and its capability, it is possible to estimate the amount of sediment that would be required to control erosion through beach nourishment. The example of Lagos harbor illustrates this feature of the model. Since the massive landfill and the construction of the seawall at Lagos harbor (Fig. 6.8) in 2011, erosion has accelerated downstream and the model shows that nearly  $650,000 m^3/year$  of sediment would be required to keep the coastline stable. The model was also used to assess the expected shoreline changes resulting from the removal of the major ports, providing an indicative net transport anomaly induced by the harbors, as well as of the effects of the use of sediment by-pass systems at the harbor jetties.

At regional scale, the model maintains the shape of the bight well and reproduces the trend



**Figure 6.9** – The effect of reduced boundary influx on the shoreline evolution through a multiplier  $\alpha$  with different spatial influence determined by a coefficient  $\kappa$ . Red indicates accretion, blue indicates erosion.

over the calibration (observed  $-0.9$  m/year and modelled  $-0.7$  m/year) and validation (observed  $+0.4$  m/year and modelled  $+1.2$  m/year) periods, which is consistent with previous observations (Anthony et al., 2019); however, some discrepancies were noted during model validation. In Fig. 6.5, for example, the model seemed to miss parts of the largest erosion ( $\Delta Y_{obs} \leq -13$  m/yr). These discrepancies can be explained by factors that were not considered in this work. Giardino et al. (2018) and Anthony et al. (2019) investigated a list of factors to be taken into account, such as climate change and reduced sediment flow due to dams on rivers, all contributing at the same time to the total longshore transport and shoreline changes. The overall reduction of sand supplied by the Volta River is probably an important factor in coastline variability in the BoB, as suggested by previous works (Boateng et al., 2012; Anthony et al., 2016; Giardino et al., 2018; Anthony et al., 2019). Here, the effects of a reduced boundary inflow of sediments from the Volta river delta were partly investigated in a simplistic manner. The results suggested that a reduced sediment input ratio by at least 40% can significantly affect shoreline with erosion rate higher than  $+20$  m/year over 8 km of coast. However, these results require further investigation for the choice of  $\alpha$  and  $\kappa$ , two parameters introduced to describe the effects of reduced boundary inflow of sediment at the shoreline evolution.

The scenarios studied in this work were mainly used to assess the capability of the model to simulate coastal evolution in the BoB. The model implementation results in a well-resolved coastal response around coastal infrastructures and inlets. Fig. 6.7 clearly shows the influence of sediment discharges from the Mono River at the Bouche du Roy, although this remains small compared to the influence induced by harbors. However, a number of potentially interesting scenarios were not considered. Effects due to climate change, such as sea level rise, were not taken into account despite its potential strong influence at long timescales (Le Cozannet et al., 2019; Vousdoukas et al., 2020); this would require new model developments, but also improved, fundamental understanding of the physical processes and much more input data on the coastal

---

topography and its properties. Quantifying the relative contributions of reduced sediment inputs, sea level rise and the development of harbor on the coastal evolution still remains an open question and this can only be addressed by a comprehensive study combining comprehensive observations and modeling of coastal evolution, as well as its drivers.

---

## Chapter 6 summary

An enhanced version of the numerical simulation model CASCADE, which simulates regional coastal evolution, including effects of infrastructures and inlets, was successfully implemented in the Bight of Benin over the period 2000 to 2015.

### **An enhanced version of the numerical simulation model CASCADE**

- Nearshore wave transformation including breaking
- Longshore current and sediment transport
- Inlet sediment transport and morphological evolution
- Cross-shore sediment exchange through sources and sinks
- Impact from human intervention due to structures and activities
- Coastal evolution from sediment conservation

### **Modeling the BoB coastline response with CASCADE**

- The model reproduces well the global trend
- The model clearly shows a well-captured shoreline behavior in the vicinity of the harbors in agreement with the data
- Model capabilities were used to address the amount of sediment required to control erosion downdrift Lagos harbor
- The model provides an indicative net transport anomaly induced by the harbors and the inlets
- The effect of a reduced discharge of sediment by the rivers was investigated

## **6.6 Conclusions**

The model performance was tested by employing a 10-year calibration period (2000-2010) followed by a 5-year validation (2010-2015) period. Also, a number of specific scenarios were investigated to assess the importance of natural and anthropogenic influences. Overall, the model may be a useful tool for improving regional coastal policies in the Bight of Benin.

---

# Conclusions and Future Research

## Main contributions

This thesis was set out to investigate the primary drivers of shoreline changes in the [BoB](#), Gulf of Guinea. The work carried out covered a wide range of measurements, processing and modelling techniques, from local to regional scale, ranging from daily to decadal time scales. The drivers of shoreline changes were investigated through multi-temporal and spatial analyses and implemented in a coastal evolution model. In this final chapter, we highlight the main research contributions of this thesis, as well as discuss directions for future research.

### **First full depth daily profile evolution from video imagery**

Among the nearshore monitoring techniques, video cameras are the least expensive, the easiest to implement and, above all, show the potential to monitor simultaneously several hydrodynamic and morphological nearshore parameters. In the past 10 years, video processing techniques have been increasingly used for nearshore depth estimation through wave celerity. In this thesis, as a first part of the work, concrete improvements were proposed for depth estimates robustness and accuracy:

- The first full depth daily profile evolution (0 to 5 m-depth) was derived. The depth estimates were validated with a vertical averaged mean error of 0.15 m.
- The temporal method for depth inversion did not have an error proxy to increase the accuracy of depth estimates, such as its spectral equivalent (cBathy). Here, two error proxies were assimilated for the first time in a Kalman filter in the temporal approach, thus improving depth estimation accuracy and robustness.

### **New scheme to derive water level at the coast from video imagery**

Total sea levels at the coast are hard to measure with current techniques (tidal gauges and spaceborne altimetry), which lack essential details of spatial and wave-related sea level variability along the coast. Here, we introduced a novel approach of estimating time-varying total water levels by applying a celerity-based depth inversion method, which is conventionally used to estimate bathymetry from video. The video-derived total sea levels were compared to sea levels derived from an in situ [ADCP](#), the nearest tide gauge, and altimetry. A tidal harmonic analysis has been performed on the video-derived water levels, yielding an accurate determination of the dominant tidal harmonics.

### **Waves are the primary drivers of shoreline variability at the event and seasonal scales**

Using coastal morphology derived from the local shore-based video camera installed at the

**GPP** pilot site, the beach is primarily dictated by waves at event (daily) and seasonal scale. Based on 12 storms, the results reveal that the average storm duration was 1.6 days, with a mean erosion of 3.1 m. The average post-storm beach recovery duration is 15 days, and the average recovery rate is 0.4 m/day. But, the inter-annual eroding trend -1.6 m/year could not be explained by the wave climate.

### **Beach responds to intraseasonal sea level changes**

The **BoB** is characterized by intraseasonal sea level variations dominated by the propagation (1.1 m/s) of wind forced coastal trapped (Kelvin waves) with periods ranging from 15 to 95 days. But literature is scarce about the impact of shorter timescales variations on the coast. In this thesis, using the latest advances in video bathymetric estimation, daily observations over 3.5 years (February 2013 to June 2016) on Grand Popo Beach (West Africa) reveal that intraseasonal sea level variations impact the beach profile. It is shown that the beach goes through a transient state with a deformation of the profile: an intraseasonal sea level rise leads to a 2m erosion of the upper beach and a widening of the flat terrace at the lower beach. However, the underlying mechanism needs to be tested through beach profile modelling.

### **Human settlements strongly affect shoreline evolution in the Bight of Benin**

Over longer periods (decades), shorelines derived from regional satellite remote sensing were analysed to assess the main anthropogenic drivers of shoreline changes:

- The coast has been strongly affected by the three ports therein
- The diminution of sand supply via the longshore transport system, due to progressive depletion of sand-sized bedload supplied to the coast through the main Volta river channel downstream of the Akosombo dam
- The decrease in sediment inputs to rivers due to dams
- Sand mining
- Potential future impacts of climate change and sea level rise

### **Large scale modeling in the Bight of Benin, a useful tool for improving regional coastal policies**

In this study, the effects of the major man-made interventions (deep water harbors and river dams) on coastal evolution have been assessed using an enhanced version of the CASCADE model. The model performance was tested by employing a 10-year calibration period (2000-2010) and a 5-year validation (2010-2015) period applied to specific scenarios. The model clearly shows a well-resolved output shoreline in the vicinity of the harbors. The model reproduces well the global trend and its capabilities were used to address the amount of sediment required to control erosion downdrift Lagos harbor.

## **Future work**

### **Central and West Africa Coastal Observation Network**

Regarding the regional wave climate in West and Central Africa, important morphological beach changes occur with low to moderate wave energy conditions. The West African region is under the influence of both north and south Atlantic climate dynamics and local generated wind-waves while coasts in Central Africa are only affected by energetic swells, coming from the South Atlantic. But, all these coasts show broadly similar behavior. The coast dynamics

---

were assessed through video systems that have been installed at Mbour (Senegal), Grand Popo (Benin), James Town (Ghana) and Kribi (Cameroon), and recently Elmina and Dzita (Ghana). And the erosive trend observed along the coast from Senegal to Cameroon demonstrates the urgent need to extend this local high-frequency observation network.

A regional network of video cameras along the West African coast, for example, would densify the beach morphology, waves and sea level monitoring network and provide long-term coastal time series which can be used to promote validation of wave contributions to total sea levels at the coast (proposed by [Melet et al. 2018b](#)). It could be the backbone of a real-time, early warning systems for coastal disasters.

A proceeding outlining the first available video observations has been published (see Appendix II).

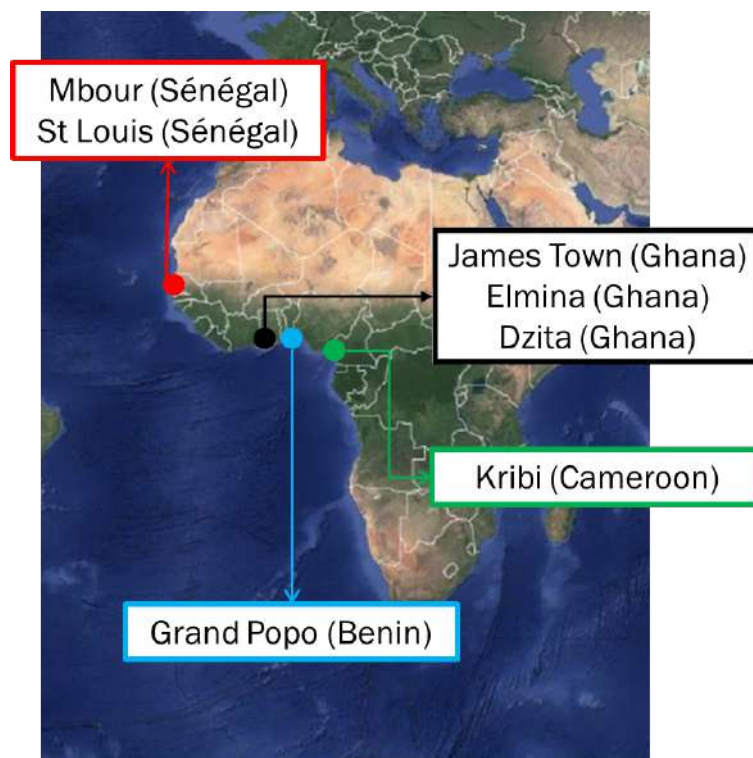


Fig. 7.1. Existing video systems location in the Gulf of Guinea (West and Central Africa).

### Merging video and altimetric-derived water level at the coast

There is a clear need to understand sea level propagation in the nearshore. In this thesis, a novel approach consisting of estimating time-varying total water levels by applying a celerity-based depth inversion method, was presented. This approach provides insights in the water level variations at the coast over a cross-shore distance ranging from 100 m and less than one km off the coast.

In contrast, altimetry products have great difficulty measuring close to the coast. [Marti et al. \(2019\)](#) investigated the rate of sea level change, combining ALES retracked altimetry data and geophysical corrections dedicated to coastal areas. The obtained X-TRACK/ALES 20-Hz products allow to get a little closer to the coasts (up to 3 km), but not so close to observe wave undergoing transformations within depths of less than 10m. The impact of wave transformations on sea level is still poorly understood and validated, as tide gauges are limited to sheltered places.

Shore-based video systems can, therefore, be used to supplement altimetry. Combining the

future French–U.S. SWOT (for example) mission to the video-based estimation of water levels opens the possibility to address and fill in the existing knowledge gap between deep and coast waters: 0–1km from the coast with video and 1–10km with new and future altimetry products.

### **Regional coastal response to sea level changes**

Intraseasonal sea level variations, particularly those induced by trapped coastal waves with periods ranging 15–95 days, locally modulate the magnitude of wave action on the beach, as observed in chapter 4. In West Africa, Gulf of Guinea, [Polo et al. \(2008\)](#) observed that such transient sea-level changes were recurrent, continuous and distinguishable over thousands of kilometers poleward along the coast in the Gulf of Guinea. They might therefore play a role in the regional coastal variability. The topic is very relevant in the sense that it links regional oceanography with coastal dynamic which are not usually jointly covered and it might be of potential benefit in terms of coastal hazard assessments.

"Google Earth Engine" (GEE), for example, can provide a robust platform to process the available Sentinel 2 images and derive regional coastlines with considerable computing power. Combining the morphological changes obtained from GEE and local video cameras (for example in the Gulf of Guinea) with regional sea level observations in a regional approach, similar to that presented in Chapter 4, can provide new insights to better understand the complex combined effect of waves and surf waves on coastal erosion and flooding.

### **Large scale shoreline modeling including high level sophistication of cross-shore processes**

In Chapter 5, several possible causes of the evolution of the coastline were outlined. However, only the presence of harbors, beach nourishment and inlets was fully taken into account in the coastal modelling presented in Chapter 6. Effects due to climate change, such as sea level rise, were not taken into account. Quantifying the relative contributions of reduced sediment inputs, sea level rise and harbors to coastal change remains a scientific issue in the [BoB](#).

A similar investigation by [Giardino et al. \(2018\)](#) derived a large-scale sediment budget analysis on the western part of the coast in the Gulf of Guinea (Republic of Côte d'Ivoire, Ghana, Togo and Benin coasts) and pointing out the effects of major human interventions and climate change in this large common sediment system. The effect of climate change (i.e. increase in wave conditions, change in wave direction, SLR, and variations in temperature and precipitation at the river catchments) on the large scale sediment transport and consequent shoreline changes was analyzed, showing how some of the man-made interventions have had major effects on the large-scale sediment budget and consequent shoreline changes.

Based on this thesis results and those of [Giardino et al. \(2018\)](#), integrate in a more rigorously manner sea level variations and reduction in sediment input into regional shoreline evolution model (CASCADE or CosMos-COAST or LX-Shore or the model by [Tran and Barthelemy 2020](#)) may improve coastal modelling and thus provides practical solutions to regional coastal policies in the [BoB](#) in terms of prediction. As sandy shoreline change projections inherit the uncertainties of future mean sea-level changes, there is also a need to understand uncertainties in projections in order to ultimately support coastal land-use planning and adaptation.

### **Deep learning for nearshore evolution**

Bathymetry is an important factor in determining wave and current transformation in coastal

---

and surface areas but is often poorly understood. However, its knowledge is crucial for hydro-morphodynamic forecasting and monitoring. Available for a long time only via in-situ measurement, the advent of video and satellite imagery has allowed the emergence of inversion methods from surface observations. However, the inversion methods have certain limitations:

- they are based on Airy's linear theory and therefore do not give a clear picture of the evolution of the surf zone
- from a perspective of global application, they are not well adapted to large volumes of data, and processing time becomes prohibitive

With the advent of methods and architectures adapted to big data, a treatment via a deep learning approach seems now promising to remove these locks. Deep learning has so far shown impressive capabilities in image processing tasks, particularly in object classification, but it has only recently been applied to regression tasks from satellite images. The estimation of coastal systems using video or satellite imagery is therefore a specific application of deep learning methods, for which the development of new learning architectures and techniques may be necessary. The possibility of simulating different coastal scenarios is also possible in our case, by generating large datasets using numerical simulators, which are then used for training artificial neural networks.

A proceeding investigating those capabilities has been published (see Appendix V).



# Conclusions et perspectives

## Principales contributions

Cette thèse avait pour but d'identifier les principaux facteurs responsables des changements du littoral dans la Baie du Bénin, dans le Golfe de Guinée. Le travail a couvert un large éventail de mesures, de techniques de traitement et de modélisation, de l'échelle locale à l'échelle régionale, de l'échelle journalière à l'échelle décennale. Les facteurs conduisant aux variations du trait de côte ont été appréhendés à travers des analyses multitemporelles et spatiales et intégrés dans un modèle d'évolution côtière. Dans ce dernier chapitre, nous mettons en évidence les principales contributions scientifiques de cette thèse et discutons des perspectives.

### **Première observation de l'évolution journalière d'un profil de plage à partir d'images vidéo**

Parmi les techniques d'observation du littoral, les systèmes d'observation vidéo sont les moins coûteux, les plus faciles à utiliser et, surtout, ils permettent le suivi simultané de plusieurs paramètres hydrodynamiques et morphologiques. Au cours des dix dernières années, les systèmes vidéo ont été de plus en plus utilisés pour l'estimation de la profondeur en milieu littoral par la méthode d'estimation de la célérité des vagues. Dans cette thèse, dans la première partie du travail, des améliorations concrètes ont été proposées pour la robustesse et la précision des estimations de profondeur :

- La première évolution journalière d'un profil de plage (0 à 5 m de profondeur) a été obtenue. Les estimations de profondeur ont été validées avec une erreur moyenne verticale de 0,15 m.
- La méthode temporelle d'inversion de la célérité pour estimer la profondeur n'intégrait pas de "proxy" d'erreur pour améliorer la précision, contrairement à son équivalent spectral (cBathy). Ici, deux "proxy" d'erreur ont été assimilés pour la première fois à travers un filtre de Kalman dans cette méthode temporelle, améliorant ainsi la précision et la robustesse de l'estimation de la profondeur.

### **Nouvel algorithme pour l'estimation du niveau d'eau à la côte à partir de l'imagerie vidéo**

Le niveau total de la mer à la côte est difficile à mesurer avec les techniques actuelles (marégraphes et altimétrie), qui ratent les contributions essentielles des vagues dans la variabilité spatiale du niveau de la mer le long de la côte. Nous avons introduit dans cette thèse une nouvelle approche pour estimer les variations temporelles du niveau total de la mer en appliquant une méthode d'inversion bathymétrique basée sur la mesure de la célérité des vagues, traditionnellement utilisée pour estimer les profondeurs à partir de la vidéo. Les niveaux d'eau

obtenus de la vidéo ont été comparés aux niveaux mesurés in situ à l'aide d'un ADCP, du marégraphe le plus proche et de l'altimétrie. Une analyse des harmoniques de marée, effectuée sur les niveaux d'eau obtenus de la vidéo, a permis déterminer avec précision les harmoniques de marée dominantes.

### **Les vagues sont les principaux facteurs de variabilité du littoral aux échelles évènementielle et saisonnière**

En utilisant les mesures morphologiques côtière obtenues à l'aide du système vidéo local installé sur le site pilote de GPP, les observations suggèrent que la plage répond principalement aux vagues à l'échelle de évènementielle (journalière) et saisonnière. A partir des 12 évènements extrêmes détectés, les résultats révèlent que la durée moyenne de la tempête était de 1,6 jours, avec une érosion moyenne de 3,1 m. Le temps moyen de récupération de la plage après la tempête est de 15 jours, avec un taux de récupération moyen de 0,4 m/jour. Cependant, la tendance interannuelle à l'érosion de -1,6 m/an n'a pas pu être expliquée par le climat des vagues.

### **La plage réagit aux variations intrasaisonnières du niveau de la mer**

La Baie du Bénin est caractérisée par des variations intrasaisonnières du niveau de la mer dominées par la propagation (1,1 m/s) d'ondulations forcés par les vents et piégés à la côte (ondes de Kelvin) avec des périodes allant de 15 à 95 jours. Mais il existe peu de littérature sur l'impact de ces variations sur la côte. Dans cette thèse, en utilisant les dernières avancées en terme de mesures bathymétriques par vidéo, 3,5 années d'observations journalières (février 2013 à juin 2016) sur la plage de Grand Popo (Afrique de l'Ouest) révèlent que les variations intrasaisonnières du niveau de la mer ont une influence sur l'évolution du profil de la plage. Il est montré que la plage passe par un état transitoire avec une déformation du profil : une élévation intrasaisonnière du niveau de la mer provoque une érosion de 2 m de la partie supérieure de la plage et un élargissement de la terrasse (partie inférieure de la plage). Cependant, le mécanisme sous-jacent doit encore être testé par des modèles d'évolution du profil de la plage.

### **Les infrastructures côtières influent fortement sur l'évolution du littoral dans la baie du Bénin**

Sur de longues périodes de temps (décennies), les traits de côtes mesurés par télédétection satellitaire régionale ont été analysées pour évaluer les principaux facteurs anthropiques responsables des changements côtiers :

- La côte a été fortement affectée par la présence des trois ports qui s'y trouvent
- La réduction de l'apport sédimentaire, en raison de l'épuisement progressif du stock de sable sur la rivière Volta, en aval du barrage d'Akosombo.
- La diminution des apports sédimentaire par les rivières en raison de la présence des barrages
- L'extraction du sable sur les plages
- Les impacts potentiels futurs du changement climatique et de l'élévation du niveau de la mer

### **La modélisation à grande échelle dans la baie du Bénin, un outil très utile pour améliorer les politiques côtières régionales**

Dans cette étude, les effets des principales infrastructures construites par l'homme (ports en eau profonde et barrages fluviaux) sur l'évolution de la côte ont été évalués à l'aide d'une

version améliorée du modèle CASCADE. La performance du modèle a été testée en utilisant une période d'étalonnage de 10 ans (2000-2010) et une période de validation de 5 ans (2010-2015), appliquée à des scénarios spécifiques. Le modèle montre clairement une bonne résolution autour des ports. Le modèle reproduit bien la tendance générale et ses capacités ont été utilisées pour calculer la quantité de sédiments nécessaires pour contrôler l'érosion en aval du port de Lagos.

## Perspectives

### Réseau d'observation des côtes d'Afrique Centrale et de l'Ouest

En considérant le climat régional des vagues en Afrique centrale et de l'Ouest, des changements significatifs dans la morphologie des plages se produisent alors que les vagues présentent des conditions énergétiques faibles à modérées. La région de l'Afrique de l'Ouest est sous l'influence de la dynamique climatique de l'Atlantique Nord et Sud, et des vagues de vent générées localement, tandis que les côtes d'Afrique centrale sont touchées uniquement par les houles énergétiques de l'Atlantique Sud. Cependant, toutes ces côtes présentent un comportement plus ou moins similaire. La dynamique côtière a été évaluée à l'aide de systèmes vidéo qui ont été installés à Mbour (Sénégal), Grand Popo (Bénin), James Town (Ghana) et Kribi (Cameroun), et récemment à Elmina et Dzita (Ghana). Et la tendance érosive observée le long de la côte, du Sénégal au Cameroun, démontre l'urgence d'étendre ce réseau local d'observation.

Un réseau régional de caméras le long de la côte Ouest africaine, par exemple, permettrait de densifier le réseau de surveillance de la morphologie des plages, des vagues et du niveau de la mer, et de fournir des séries chronologiques côtières à long terme pouvant être utilisées pour promouvoir la validation de la contribution des vagues au niveau total de la mer à la côte (proposé par [Melet et al. 2018b](#)). Il pourrait constituer l'épine dorsale d'un système d'alerte précoce en temps réel pour les catastrophes côtières.

Un papier de conférence décrivant les premières observations vidéo a été publié (Voir Annexe II).

### Combiner les observations vidéo et altimétriques à la côte

Il existe un réel besoin dans la communauté scientifique pour comprendre la propagation des variations du niveau de la mer dans le littoral. Dans cette thèse, une nouvelle approche d'estimation du niveau d'eau total à la côte a été appliquée, en utilisant une méthode d'inversion bathymétrique basée sur l'estimation de la célérité des vagues. Cette approche permet de mesurer les variations du niveau de l'eau à la côte sur des distances allant de 100 m à près d'un kilomètre au large.

En revanche, les mesures altimétriques près des côtes ne sont pas précises. [Marti et al. \(2019\)](#) a étudié la variabilité du niveau de la mer près des côtes, en combinant les données altimétriques suivies par ALES aux corrections géophysiques dédiées aux zones côtières. Les produits X-TRACK/ALES 20-Hz obtenus permettent de se rapprocher un peu plus des côtes (jusqu'à 3 km), mais malheureusement pas assez près pour observer la transformation des vagues à des profondeurs de moins de 10 mètres. L'impact des transformations des vagues sur le niveau de la mer reste encore mal compris sachant qu'en plus les marégraphes restent limités aux zones côtières protégées.

Les systèmes d'observation vidéo du littoral peuvent donc être utilisés en complément à l'altimétrie. La combinaison de la future mission franco-américaine SWOT (par exemple) avec

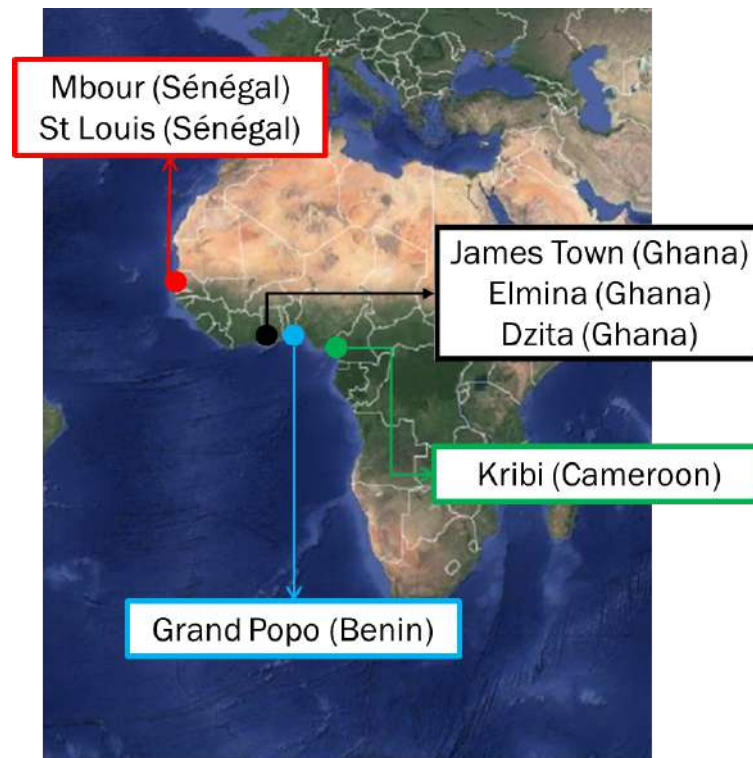


Fig. 7.1. Localisation des systèmes vidéo existants dans le Golfe de Guinée (Afrique Centrale et de l'Ouest).

l'estimation vidéo des niveaux d'eau ouvre la possibilité de combler le fossé des connaissances entre les eaux profondes et les eaux côtières : 0-1 km de la côte avec la vidéo et 1-10 km avec les nouveaux et futurs produits altimétriques.

### **Evolution régionale de la côte face aux variations du niveau de la mer**

Les variations intrasaisonnières du niveau de la mer, en particulier celles induites par les ondulations côtières forcées par le vent et piégées à la côte, dont la période varie de 15 à 95 jours, modulent localement l'ampleur de l'action des vagues sur la plage, comme observé au chapitre 4. En Afrique de l'Ouest, dans le Golfe de Guinée, [Polo et al. \(2008\)](#) a observé que ces variations du niveau de la mer étaient récurrentes, continues et perceptibles sur des milliers de kilomètres vers le pôle le long de la côte du Golfe de Guinée. Elles pourraient donc jouer un rôle dans la variabilité côtière régionale. Le sujet est très pertinent dans la mesure où il relie l'océanographie régionale à la dynamique côtière, qui ne sont généralement pas étudiées de façon conjointe, et pourrait être utile en termes d'évaluation des risques côtiers.

"Google Earth Engine" (GEE), par exemple, pourrait fournir une plate-forme robuste pour traiter les images Sentinel 2 disponibles et produire des traits de côte à l'échelle régionale avec une puissance de calcul considérable. En combinant les changements morphologiques obtenus grâce à GEE et aux systèmes vidéo locaux (par exemple dans le Golfe de Guinée) avec les observations régionales du niveau de la mer dans une approche régionale, similaire à celle présentée au chapitre 4, de nouvelles informations pourraient être obtenues pour mieux comprendre l'effet combiné complexe des vagues et du niveau d'eau sur l'érosion côtière et sur les inondations.

### **Modélisation côtière à grande échelle, intégrant les processus locaux à petite échelle**

Au chapitre 5, plusieurs causes possibles des changements observés du littoral ont été ex-

posées. Cependant, seuls la présence de ports, le rechargement des plages en sédiments et les embouchures des rivières a été pleinement prise en compte dans la modélisation côtière présentée au chapitre 6. Les effets dus au changement climatique, tels que l'élévation du niveau de la mer, n'ont pas été pris en compte. La quantification des contributions relatives de la réduction des apports de sédiments, de l'élévation du niveau de la mer et des ports au changement côtier reste donc une question scientifique dans la Baie du Bénin.

Une étude similaire menée par [Giardino et al. \(2018\)](#) a fourni une analyse du bilan sédimentaire à grande échelle sur la partie Ouest de la côte dans le Golfe de Guinée (côtes de la République de Côte d'Ivoire, du Ghana, du Togo et du Bénin) et a mis en évidence les effets des principales interventions humaines et du changement climatique dans ce grand système sédimentaire commun. L'effet du changement climatique (c'est-à-dire l'augmentation des conditions énergétiques des vagues, le changement de direction des vagues, l'élévation du niveau de la mer et les changements de température et de précipitation dans les bassins versants des rivières) sur le transport sédimentaire à grande échelle et les changements de littoral qui en résultent a été analysé, montrant comment certaines des interventions humaines ont eu des effets majeurs sur le bilan sédimentaire de la région.

Sur la base des résultats de cette thèse et de ceux de [Giardino et al. \(2018\)](#), une intégration plus rigoureuse des variations du niveau de la mer et de la réduction de l'apport sédimentaire dans le modèle régional d'évolution côtière (CASCADE ou CosMos-COAST ou LX-Shore ou le modèle de [Tran and Barthelemy 2020](#)) peut améliorer la modélisation côtière et ainsi apporter des solutions pratiques aux politiques côtières régionales dans la région en termes de prévision. Étant donné que les projections de l'évolution des côtes sableuses héritent des incertitudes des prévisions du niveau de la mer, il est également nécessaire de comprendre les incertitudes de ces projections afin de soutenir de façon adéquate la planification et l'aménagement des côtes.

### **Evolution du littoral par "deep learning"**

La bathymétrie est un facteur important pour déterminer la transformation des vagues et des courants dans les zones côtières, mais elle est souvent mal estimée. Pourtant, elle est cruciale pour la prévision et la surveillance des paramètres hydro-morphodynamiques. Longtemps disponible uniquement par des mesures in situ, l'avènement de la vidéo et de l'imagerie satellitaire a permis l'émergence de méthodes d'inversion basées sur l'estimation de la célérité de la vagues. Cependant, les méthodes d'inversion ont certaines limites :

- Ils sont basés sur la théorie linéaire d'Airy et ne donnent pas une image nette de l'évolution dans la zone de surf
- dans une perspective d'application régionale et globale, ils ne sont pas bien adaptés à de grands volumes de données, et les temps de traitement deviennent considérablement grands

Avec l'avènement des méthodes et des architectures adaptées aux grands ensembles de données, le traitement via une approche dite de "deep learning" semble désormais prometteur pour contourner ces limites. Le deep learning a jusqu'à présent montré des capacités impressionnantes dans les tâches de traitement d'images, en particulier dans la classification des objets, mais il n'a été appliqué que récemment aux tâches de régression basées sur des images satellites. L'estimation des systèmes littoraux à l'aide d'images vidéo ou satellitaires est donc une application spécifique des méthodes de deep learning, pour laquelle le développement de nouvelles architectures et techniques d'apprentissage peut être nécessaire. La possibilité de simuler dif-

férents scénarios côtiers est également possible dans notre cas, en générant de grands ensembles de données à l'aide de simulateurs numériques, qui sont ensuite utilisés pour la formation de réseaux neuronaux artificiels.

Un papier de conférence évaluant les capacités du deep learning dans l'estimations de la bathymétrie a été publiée (voir Annexe V).

# Bibliography

- Aagaard, T. (2014). Sediment supply to beaches: cross-shore sand transport on the lower shoreface. *Journal of Geophysical Research*, 119:913–926.
- Aagaard, T. and Holm, J. (1989). Digitization of wave run-up using video records. *Journal of Coastal Research*, pages 547–551.
- Aarninkhof, S. G., Ruessink, B. G., and Roelvink, J. A. (2005). Mean currents and sediment transport in a rip channel. *Journal of Geophysical Research*, 110:1–13.
- Aarninkhof, S. G., Turner, I. L., Dronkers, T. D., Caljouw, M., and Nipius, L. (2003). A video-based technique for mapping intertidal beach bathymetry. *Coastal Engineering*, 49(4):275–289.
- Abessolo, O. G., Almar, R., Castelle, B., Testut, L., Leger, F., Sohou, Z., Bonou, F., Bergsma, E. W. J., Meyssignac, B., and Larson, M. (2019). Sea level at the coast from video-sensed waves: Comparison to tidal gauges and satellite altimetry. *Journal of Atmospheric and Oceanic Technology*, 36:1591–1603.
- Abessolo, O. G., Almar, R., Kestenare, E. and Bahini, A. H. G.-H., Jouanno, J., Du Penhoat, Y., Castelle, B., Melet, A., Meyssignac, B., E., A., Laibi, R., Alory, G., and R., R. (2016). The grand popo beach 2013 experiment, benin, west africa: from short timescale processes to their integrated impact over long-term coastal evolution. *VilaConcejo, A.; Bruce, E.; Kennedy, D.M., and McCarroll, R.J. (eds.), Proceedings of the 14th International Coastal Symposium (Sydney, Australia). Journal of Coastal Research, Special Issue, No.75. Coconut Creek (Florida), ISSN 0749-0208., Special Issue no 70:442–446.*
- Abessolo, O. G., Almar, R., Kestenare, E., Bahini, A., and Co-authors (2017). Development of a west and central africa regional video camera network to monitor coastal response to multiscale ocean forcing. In *Proc. Coastal Dynamics, Helsinghor, Denmark, University of Copenhagen, 1540–1550.*
- Addo, K. A. (2015). Assessment of the volta delta shoreline change. *J. Coast. Zone Manag*, 18:408.
- Addo, K. A., Nicholls, R. J., Codjoe, S. N., and Abu, M. (2018). A biophysical and socioeconomic review of the volta delta, ghana. *Journal of Coastal Research*, 34(5):1216–1226.
- Ago, E. E., Petit, F., and Ozer, P. (2005). Analyse des inondations en aval du barrage de nangbeto sur le fleuve mono (togo et au bénin). *Geo-Eco-Trop*, 29:1–14.
- Allersma, E. and Tilmans, W. M. K. (1993). Coastal conditions in west africa - a review. *Ocean and Coastal Management*, 19(3):199–240.

- Almar, R. (2009). Morphodynamique littorale haute fréquence par imagerie vidéo. Ph.d. dissertation, University of Bordeaux I.
- Almar, R., Bergsma, E. W. J., Maisongrande, P., and Almeida, L. P. (2019). Wave-derived coastal bathymetry from satellite video imagery: A showcase with pleiades persistent mode. *Remote Sensing of Environment*, 213:111263.
- Almar, R., Cienfuegos, R., Catalan, P. A., Michallet, H., Castelle, C., Bonneton, P., and Marieu, V. (2012a). A new breaking wave height direct estimation from video. *Coastal Engineering*, 61:42–48.
- Almar, R., Honkonnou, N., Anthony, E. J., Castelle, B., Senechal, N., Laibi, R., Mensah-Senoo, T., Degbe, G., Quenum, M., Dorel, M., Chuchla, R., Lefebvre, J. P., Du Penhoat, Y., Laryea, W. S., Zodehougan, G., Sohoun, Z., Addo, K. A., Ibaceta, R., and Kestenare, E. (2014). The grand popo beach 2013 experiment, benin, west africa: from short timescale processes to their integrated impact over long-term coastal evolution. In: *Green, A.N. and Cooper, J.A.G. (eds.), Proceedings 13th International Coastal Symposium (Durban, South Africa), Journal of Coastal Research*, Special Issue no 70:651–656.
- Almar, R., Ibaceta, R., Blenkinsopp, C., Catalan, P., Cienfuegos, R., Viet, N. T., Duong Hai, T., Uu, D., Lefebvre, J., Laryea, W. S., and al. (2015a). Swash-based wave energy reflection on natural beaches. In *In Proceedings of the Coastal Sediments 2015, San Diego, CA, USA, 11–15 May 2015*.
- Almar, R., Kestenare, E., Reyns, J., Jouanno, J., Anthony, E., Laibi, R., Hemmer, M., Penhoat, Y., and Ranasinghe, R. (2015b). Response of the bight of benin (gulf of guinea, west africa) coastline to anthropogenic and natural forcing, part 1: wave climate variability and impacts on the longshore sediment transport. *Continental Shelf Research*, 110:48–59.
- Almar, R., Larnier, S., Castelle, B., Scott, T., and Floc’h, F. (2016). On the use of the radon transform to estimate longshore currents from video imagery. *Coastal Engineering*, 114:301–308.
- Almar, R., Ranasinghe, R., Senechal, N., Bonneton, P. and Roelvink, D., Bryan, K. R., Marieu, V., and Parisot, J. P. (2012b). Video-based detection of shorelines at complex meso–macro tidal beaches. *Journal of Coastal Research*, 28 (5):1040–1048.
- Almar, R., Senechal, N., Bonneton, N., and Roelvink, J. A. (2008). Wave celerity from video imaging: A new method. In *Proceedings of the 31st International Conference Coastal Engineering*, 1(5), 661–673.
- Almeida, L. P., Almar, R., Bergsma, E. W. J., Berthier, E., Baptista, P., Garel, E., Dada, O. A., and Alves, B. (2019). Deriving high spatial-resolution coastal topography from sub-meter satellite stereo imagery. *Remote Sensing*, 11:590.
- Almeida, L. P., Almar, R., Blenkinsopp, C., Martins, K., Benschila, R., and Daly, C. (2017). Swash dynamics of a sandy beach with low tide terrace. In *Proceedings of Coastal Dynamics, 11 – 16 June 2017, Helsingør, Denmark, pp 258-267*.
-

- Almeida, L. P., Vousdoukas, M. V., Ferreira, O., Rodrigues, B. A., and Matias, A. (2012). Thresholds for storm impacts on an exposed sandy coastal area in southern portugal. *Geomorphology*, 143:3–12.
- Aman, A., Testut, L., Woodworth, P., Aarup, T., and Dixon, D. (2007). Seasonal sea level variability in the gulf of guinea from altimetry and tide gauge. *Revue Ivoirienne des Sciences et Technologie*, 9:105–118.
- Anderson, T. R., Fletcher, C. H., Barbee, M. M., Romine, B. M., Lemmo, S., and Delevaux, J. M. S. (2018). Modelling multiple sea level rise stresses reveals up to twice the land at risk compared to strictly passive flooding methods. *Scientific Reports*, 8:14484.
- Andriolo, U. (2018). Nearshore hydrodynamics and morphology derived from video imagery. Ph.d. dissertation, Faculty of Sciences, University of Lisbon.
- Angnuureng, D. B., Addo, K. A., Almar, R., and Dieng, H. (2018). Influence of sea level variability on a micro-tidal beach. *Natural Hazards*, 68:DOI 10.1007/s11069-018-3370-4.
- Angnuureng, D. B., Addo, K. A., and Wiafe, G. (2013). Impact of sea defense structures on downdrift coasts: the case of keta in ghana. *Acad. J. Environ. Sci.*, 1:104–121.
- Angnuureng, D. B., Almar, R., Appeaning Addo, K., Senechal, N., Castelle, B., Laryea, S. W., and Wiafe, G. (2016). Video observation of waves and shoreline change on the microtidal james town beach in ghana. In *In: Vila-Concejo, A. and Bruce, E. and Kennedy, D. M. and and McCarroll, R.J. (eds.), Proceedings of the 14th International Coastal Symposium (Sydney, Australia). Journal of Coastal Research, Special Issue, No. 75, pp. 1022 – 1026, Coconut Creek (Florida).*
- Angnuureng, D. B., Almar, R., Senechal, N., Castelle, B., Addo, K. A., Marieu, V., and Ranasinghe, R. (2017). Shoreline resilience to individual storms and storm clusters on a meso-macrotidal barred beach. *Geomorphology*, 290:265–276.
- Anthony, E., Almar, R., Besset, M., Reyns, J., Laibi, R., Ranasinghe, R., Abessolo Ondo, G., and Vacchi, M. (2019). Response of the bight of benin (gulf of guinea, west africa) coastline to anthropogenic and natural forcing, part 2: Sources and patterns of sediment supply, sediment cells, and recent shoreline change. *Continental Shelf Research*, 173:93–103.
- Anthony, E. J. (1994). Natural and artificial shores of the french riviera: an analysis of their inter-relationship. *Journal of Coastal Research*, 10:48–58.
- Anthony, E. J. (1995). Beach-ridge progradation in response to sediment supply: examples from west africa. *Marine Geology*, 129:175–186.
- Anthony, E. J. (2015a). Patterns of sand spit development and their management implications on deltaic, drift-aligned coasts: the cases of the senegal and volta river delta spits, west africa. In Randazzo, G., Jackson, D. W. T., and Cooper, J. A. G., editors, *Sand and Gravel Spits*, volume 12 of *Coastal Research Library*, chapter 2, pages 21–36. Springer.
- Anthony, E. J. (2015b). Wave influence in the construction, shaping and destruction of river deltas: a review. *Marine Geology*, 361:53–78.
-

- Anthony, E. J., Almar, R., and Aagaard, T. (2016). Recent shoreline changes in the volta river delta, west africa: The roles of natural processes and human impacts. *African Journal of Aquatic Science*, 41(1):81–87.
- Anthony, E. J. and Blivi, A. B. (1999). Morphosedimentary evolution of a delta-sourced, drift-aligned sand barrier-lagoon complex, western bight of benin. *Marine Geology*, 158:161–176.
- Arbic, B. K., Scott, R. B., Chelton, D. B., Richman, J. G., and Shriver, J. F. (2012). Laboratory investigation of the bruun rule and beach response to sea level rise. *Journal of Geophysical Research*, 117:C03029.
- Ashton, A., Murray, A. B., and Arnoult, O. (2001). Formation of coastline features by large-scale instabilities induced by high-angle waves. *Nature*, 414(6861):296.
- Ashton, A. D., Murray, A. B., and Arnoult, O. (2006). High-angle wave instability and emergent shoreline shapes: 1. modeling of sand waves, flying spits, and capes. *Journal of Geophysical Research*, 111:F04011.
- Atkinson, A., Baldock, T. E., Birrien, F., Callaghan, D., Nielson, P., Beuzen, T., Turner, I., Blenkinsopp, D., and Ranasinghe, R. (2018). Laboratory investigation of the bruun rule and beach response to sea level rise. *Coastal Engineering*, 136:183–202.
- Ba, A. and Senechal, N. (2013). Extreme winter storm versus summer storm: Morphological impact on a sandy beach. *Journal of Coastal Research*, 1:648–653.
- Bayram, A., Larson, M., , and Hanson, H. (2007). new formula for the total longshore sediment transport rate. *Coastal Engineering*, 54:700–710.
- Bergsma, E. and Almar, R. (2018). Video-based depth inversion techniques, a method comparison with synthetic cases. *Coastal Engineering*, 138:199–209.
- Bergsma, E. W. J., Blenkinsopp, C. E., M. K., Almar, R., and Almeida, L. P. (2019a). Bore collapse and wave run-up on a sandy beach. *Continental Shelf Research*, 174:132–139.
- Bergsma, E. W. J., Conley, D. C., Davidson, M. A., and O’Hare, T. J. (2016). Video-based nearshore bathymetry estimation in macro-tidal environments. *Marine Geology*, 374:31–41.
- Bergsma, E. W. J., Conley, D. C., Davidson, M. A., O’Hare, T. J., and Almar, R. (2019b). Storm event to seasonal evolution of nearshore bathymetry derived from shore-based video imagery. *Remote Sensing*, 11:519.
- Bindoff, N. L., Willebrand, J., and al. (2007). Observations: Oceanic climate change and sea level. In Solomon, S., Qin, D., Manning, N., Chen, Z., Marquis, M., Averyt, K. B., Tignor, M., and Miller, H. L., editors, *Climate Change 2007: The Physical Science Basis. Contribution of Working Group I to the Fourth Assessment Report of the Intergovernmental Panel on Climate Change*, chapter 5, page 385–432. Cambridge University Press, Cambridge, UK.
- Birol, F., Fuller, N., Lyard, F., Cancet, M., Niño, F., Delebecque, C., Fleury, S., Toubanc, F., Melet, A., Saraceno, M., and Léger, F. (2017). Coastal applications from nadir altimetry: Example of the x-track regional products. *Advance Space Research*, 59:936–953.
-

- Blivi, A., Anthony, E. J., and Oyédé, L. M. (2002). Sand barrier development in the bight of benin, west africa. *Ocean and Coastal Management*, 45:185–200.
- Boak, E. H. and Turner, I. L. (2005). Shoreline definition and detection: A review. *Journal of Coastal Research*, 21(4):688–703.
- Boateng, I., Addo, K. A., Nicholls, R. J., Codjoe, S. N. A., and Mumuni, M. (2018). A biophysical and socio-economic review of the volta delta, ghana. *Journal of Coastal Research*, 34:1216–1226.
- Boateng, I., Bray, M., and Hooke, J. (2012). Estimating the fluvial sediment input to the coastal sediment budget: A case study of ghana. *Geomorphology*, 138(1):100–110.
- Bollen, M., Trouw, K., Lerouge, F., Gruwez, V., Bolle, A. and Hoffman, B., and et al. (2011). Design of a coastal protection scheme for ada at the volta river mouth (ghana). In *Proceedings of 32nd Conference on Coastal Engineering*, Shanghai, China.
- Bouvier, C., Balouin, Y., Castelle, B., and Holman, R. A. (2019). Modelling camera viewing angle deviation to improve nearshore video monitoring. *Coastal Engineering*, 147:99–106.
- Bowen, A. J. and Inman, D. L. (1966). *Budget of Littoral Sands in the Vicinity of Point Arguello, California*. Technical Report 19, 41 pp., Coastal Engineering Research Centre, Technical Memorandum.
- Brander, R. W. (1999). Field observations on the morphodynamic evolution of a low-energy rip current system. *Marine Geology*, 157:199–217.
- Brodie, K. L., Palmsten, M. L., Hesser, T. J., Dickhudt, P. J., Raubenheimer, B., Ladner, H., and Elgar, S. (2018). Evaluation of video-based linear depth inversion performance and applications using altimeters and hydrographic surveys in a wide range of environmental conditions. *Coastal Engineering*, 136:147–160.
- Bruun, P. (1954). *Coast erosion and the development of beach profiles*. Technical Report Technical Memorandum 44, Beach Erosion Board, Corps of Engineers, 82 pp.
- Bruun, P. (1962a). Review of conditions for uses of the bruun rule of erosion. *Coastal Engineering*, 7:77–89.
- Bruun, P. (1962b). Sea-level rise as a cause of shore erosion. *Journal of the Waterways and Harbors Division*, 88:117–130.
- Bruun, P. (1988). The bruun rule of erosion by sea-level rise: a discussion of large-scale two- and three-dimensional usages. *Journal of Coastal Research*, 4:627–648.
- Carrere, L., Lyard, F., Cancet, M. and Guillot, A., and Picot, N. (2016). Fes 2014, a new tidal model—validation results and perspectives for improvements. In *Living Planet Symp., Prague, Czech Republic, ESA*.
- Carvajal, M., Contreras-Lopez, M., Winckler, P., and Sepulveda, I. (2017). Meteotsunamis occurring along the southwest coast of south america during an intense storm. *Pure and Applied Geophysics*, June 2017:DOI 10.1007/s00024-017-1584-0.
-

- Castelle, B. (2004). Modélisation de l'hydrodynamique sédimentaire au-dessus des barres sableuses soumises à l'action de la houle : application à la côte aquitaine. mathesis, University of Bordeaux I.
- Castelle, B., Marieu, V., Bujan, S., Splinter, K. D., Robinet, A., Senechal, N., and Ferreira, S. (2015). Impact of the winter 2013–2014 series of severe western europe storms on a double-barred sandy coast: Beach and dune erosion and megacusp embayments. *Geomorphology*, 238:135–148.
- Castelle, B., Marieu, V., Bujan, S. and Ferreira, S., Parisot, J., Capo, S., Senechal, N., and Chouzenoux, T. (2014). Equilibrium shoreline modelling of a high energy mesomacro-tidal multiple-barred beach. *Marine Geology*, 347:85–94.
- Castelle, B., Scott, T., Brander, R., and McCarroll, R. (2016). Rip current types, circulation and hazard. *Earth-Sciences Review*, 163:1–21.
- Catalan, P. and Haller, M. (2008). Remote sensing of breaking wave phase speeds with application to non-linear depth inversions. *Coastal Engineering*, 55:93–111.
- Catalán, P. A. and Haller, M. C. (2008). Remote sensing of breaking wave phase speeds with application to non-linear depth inversions. *Coastal Engineering*, 55(1):93–111.
- Cazenave, A. and Le Cozannet, G. (2013). Sea level rise and its coastal impacts. *Earth's Future*, 2:15–34.
- Cazenave, A., Palanisamy, H., and Ablain, M. (2018). Contemporary sea level changes from satellite altimetry: What have we learned? what are the new challenges? *Advance in Space Research*, 62:1639–1653.
- CERC (1984). *Shore Protection Manual, volume I*. Dept. of the Army, Waterways Experiment Station, Corps of Engineers, Coastal Engineering Research Center, For sale by the Supt. of Docs., U.S. G.P.O., Vicksburg, 4th ed. edition.
- Chowdhury, M. R., Chu, P.-S., Schroeder, T., and Colasacco, N. (2007). Seasonal sea-level forecasts by canonical correlation analysis—an operational scheme for the u.s.-affiliated pacific islands. *International Journal of Climatology*, 27(10):1389–1402.
- Chowdhury, M. R. and Chu, P. S. and Guard, C. C. (2014). An improved sea level forecasting scheme for hazards management in the us-affiliated pacific islands. *International Journal of Climatology*, 34(7):2320–2329.
- Chu, Y., Gravens, M. B., Smith, J. M., Gorman, L. T., and Chen, H. S. (1987). *Beach Erosion Control Study, Homer Spit, Alaska*. Technical Report Miscellaneous Paper CERC-87-15, U.S. Army Engineer Waterways Experiment Station, Coastal Engineering Research Center, Vicksburg, MS.
- Church, J. and Thornton, E. (1993). Effects of breaking wave induced turbulence within a longshore current model. *Coastal Engineering*, 20:1–28.
- Church, J. A. and al. (2013). Sea level change. In Stocker, T. F., Qin, D., Plattner, G. K., Tignor, M., Allen, S. K., Boschung, J., and et al., editors, *Climate Change 2013: The Physical*
-

- Science Basis. Contribution of Working Group I to the Fifth Assessment Report of the Intergovernmental Panel on Climate Change*, chapter 13, page 1137–1216. Cambridge University Press, Cambridge, UK.
- Church, J. A., White, N. J., Konikow, L. F., Domingues, C. M., Cogley, J. G., Rignot, E., Gregory, J. M., van den Broeke, M. R., Monaghan, A. J., and Velicogna, I. (2011). Revisiting the earth's sea-level and energy budgets from 1961 to 2008. *Geophysical Research Letters*, 38:L18601.
- Ciavola, P., Ferreira, O., Dongeren, A. P., de Vries, J. V. T., Armaroli, C., and Harley, M. (2015). Prediction of storm impacts on beach and dune systems. In Quevauviller, P., editor, *Hydrometeorological Hazards*, volume 1, chapter 3.4, pages 227–252. John Wiley and Sons, Ltd.
- Cipollini, P., Calafat, F., Jevrejeva, S., Melet, A., and Prandi, P. (2017). Monitoring sea level in the coastal zone with satellite altimetry and tide gauges. *Surveys in Geophysics*, 38:33–57.
- Clarke, J. E. H., Mayer, L. A., and Wells, D. E. (1996). Shallow-water imaging multibeam sonars: a new tool for investigating seafloor processes in the coastal zone and on the continental shelf. *Marine Geophysical Researches*, 18:607–629.
- Coco, G., Senechal, N., Rejas, A., Bryan, K. R., Capo, S., Parisot, J., Brown, J. A., and MacMahan, J. H. (2014a). Beach response to a sequence of extreme storms. *Geomorphology*, 204:493–501.
- Coco, G., Senechal, N., Rejas, A., Bryan, K. R., Capo, S., Parisot, J. P., Brown, J. A., and MacMahan, J. H. M. (2014b). Beach response to a sequence of extreme storms. *Geomorphology*, 204:493–501.
- Codiga, D. L. (2011). *Unified tidal analysis and prediction using the UTide MATLAB functions*. Technical Report Tech. Rep. 2011-01, 59 pp., <ftp://www.po.gso.uri.edu/pub/downloads/codiga/pubs/2011Codiga-UTide-Report.pdf>, University of Rhode Island Graduate School of Oceanography.
- Costas, S., Alejo, I., Vila-Concejo, A., and Nombela, M. A. (2005). Persistence of storm-induced morphology on a modal low-energy beach: a case study from nw-iberian peninsula. *Marine Geology*, 224 (1–4):43–56.
- Cowell, P. J., Stive, M. J. F., Niedoroda, A. W., Swift, D. J. P., Vriend, H. J., de Buijsman, M. C., Nicholls, R. J., Roy, P. S., Kaminsky, G., Cleveringa, J., Reed, C. J., and de Boer, P. L. (2003). The coastal-tract (part 2): applications of aggregated modeling of lower-order coastal change. *Journal of Coastal Research*, 19:828–848.
- Dada, O., Li, G., Qiao, L., Ding, D., Ma, Y., and Xu, J. (2016). Seasonal shoreline behaviours along the arcuate niger delta coast: complex interaction between fluvial and marine processes. *Continental Shelf Research*, 122:51–67.
- Dada, O. A., Guangxue, L., Qiao, L., Asiwaju-Bello, Y. A., and Anifowose, A. Y. B. (2018). Recent niger delta shoreline response to niger river hydrology: conflict between forces of nature and humans. *J. Afr. Earth Sci*, 139:222–231.
-

- Davidson, M. A., Splinter, K. D., and Turner, I. L. (2013). A simple equilibrium model for predicting shoreline change. *Coastal Engineering*, 73:191–202.
- Davidson-Arnott, R. (2010a). *Introduction to coastal processes and geomorphology*. Cambridge University Press.
- Davidson-Arnott, R. (2010b). *Introduction to coastal processes and geomorphology*. Cambridge University Press.
- De Coetlogon, G., Janicot, S., and Lazar, A. (2010). Intraseasonal variability of the ocean – atmosphere coupling in the gulf of guinea during boreal spring and summer. *Quarterly Journal of the Royal Meteorological Society*, 136(s1):426–441.
- Dean, R. and Houston, J. (2016). Determining shoreline response to sea level rise. *Coastal Engineering*, 114:1–8.
- Dean, R. G. (1991). Equilibrium beach profiles: characteristics and applications. *Journal of Coastal Research*, pages 53–84.
- Dean, R. G. and Dalrymple, R. A. (2004). *Coastal processes with engineering applications*. Cambridge University Press.
- Del Rio, L., Gracia, F. J., and Benavente, J. (2013). Shoreline change patterns in sandy coasts. a case study in sw spain. *Geomorphology*, 196:252–266.
- Delft Hydraulics (1990). *National and regional aspects of coastal erosion in the Bight of Benin*. Technical Report Project 6607.43.94.155, European Development Fund, Brussels.
- Demir, N., Oy, S., Erdem, F., Seker, D. Z., and Bayram, B. (2017). *Integrated shoreline extraction approach with use of MS and SENTINEL-1A SAR Images*. Technical report, ISPRS Annals of Photogramm. Remote Sens. Spa. Inf. Sci.
- Deronde, B., Houthuys, R. and Henriët, J. P., and Lancker, V. V. (2008). Monitoring of the sediment dynamics along a sandy shoreline by means of airborne hyperspectral remote sensing and lidar: A case study in belgium. *Earth Surface Processes and Landforms*, 33:280–294.
- Ding, H., Keenlyside, N. S., and Latif, M. (2009). Seasonal cycle in the upper equatorial atlantic ocean. *Journal of Geophysical Research*, 114:C09016.
- Ding, Y., Bao, X., Yao, Z., Song, D., Song, J., Gao, J., and Li., J. (2018). Effect of coastal-trapped waves on the synoptic variations of the yellow sea warm current during winter. *Continental Shelf Research*, 167:14–31.
- Dingemans, M. W. (1997). *Water wave propagation over uneven bottoms*. Technical Report Advanced Series on Ocean Engineering, 13: 25769, ISBN 978-981-02-0427-3, NASA Sti/Recon Technical Report N.
- Dodet, G., Castelle, B., Masselink, G., Scott, T., Davidson, M., Floc’h, F., Jackson, D. W. T., and Suanez, S. (2019). Beach recovery from extreme storm activity during the 2013/14 winter along the atlantic coast of europe. *Earth Surface Processes and Landforms*, 44 (1):393–401.
-

- Dolan, R., Hayden, B. P., , and May, S. (1983). Erosion of the us shorelines. In Komar, P., editor, *CRC Handbook of Coastal Processes and Erosion*, volume – of *CRC series in marine science*, chapter 2, page 285–299. CRC Press, Boca Raton, Florida.
- Dossou, K. M. and Glehouenou-Dossou, B. (2007). The vulnerability to climate change of cotonou (benin): the rise in sea level. *Environ. Urban.*, 19:65–79.
- Dubois, R. N. (1990). Barrier-beach erosion and rising sea level. *Geology*, 18:1150–1152.
- Echevin, V., Albert, A., Lévy, M., Graco, M., Aumont, O., Piétri, A., and Garric, G. (2014). Intraseasonal variability of nearshore productivity in the northern humboldt current system: The role of coastal trapped waves. *Continental Shelf Research*, 73:14–30.
- Ezer, T. (2016). Can the gulf stream induce coherent short-term fluctuations in sea level along the us east coast? a modeling study. *Ocean Dynamics*, 66:207–220.
- Feng, M., Meyers, G., Pearce, A., and Wijffels, S. (2003). Annual and interannual variations of the leewind current at 32 s. *Journal of Geophysical Research*, 108(C11):3355.
- Ferreira, Ó. (2005a). Storm groups versus extreme single storms: predicted erosion and management consequences. *Journal of Coastal Research*, pages 221–227.
- Ferreira, O. (2005b). Storm groups versus extreme single storms: predicted erosion and management consequences. *Journal of Coastal Research*, SI 42:221–227.
- French, J. R. and Burningham, H. (2009). Coastal geomorphology: trends and challenges. *Progress in Physical Geography*, 33:117–129.
- Giardino, A., Schrijvershofa, R., Nederhoffa, C., de Vroega, H., Brièrea, C., Tonnona, P.-K., Cairesa, S., Walstra, D., Sosac, J., van Versevela, W., Schellekensa, J., and Sloffa, C. (2018). A quantitative assessment of human interventions and climate change on the west african sediment budget. *Ocean Coastal Management*, 156:249–265.
- Gomez-Pujol, L., Orfila, A., Canellas, B., Alvarez-Ellacuria, A., Méndez, F. J., Medina, R., and Tintoré, J. (2005). Morphodynamic classification of sandy beaches in low energetic marine environment. *Marine Geology*, 242(4):235–246.
- Gourlay, M. R. (1968). *Beach and dune erosion tests*. Technical Report Report No. M935/M936, Delft Hydraulics Laboratory, Delft, The Netherlands.
- Gravens, M. B., Scheffner, N. W., and Hubertz, J. M. (1989). *Coastal Processes from Asbury Park to Manasquan, New Jersey*. Technical Report Miscellaneous Paper CERC-89-11, U.S. Army Engineer Waterways Experiment Station, Coastal Engineering Research Center, Vicksburg, MS.
- Hamed, K. H. and Rao, A. R. (1998). A modified mann-kendall trend test for autocorrelated data. *Journal of Hydrology*, 204:182–196.
- Hanson, H. (1989). Genesis - a generalized shoreline change numerical model. *Journal of Coastal Research*, 5(1):1–27.
- Hanson, H. and Kraus, N. C. (1986). Forecast of shoreline change behind multiple coastal structures. *Coastal Engineering in Japan*, 29:195–213.
-

- Hanson, H., Kraus, N. C., and Nakashima, L. (1990). *Shoreline Change Behind Transmissive Detached Breakwaters - Shoreline Change and Storm-Induced Beach Erosion Modeling: A collection of Seven Papers*. Technical Report Miscellaneous Paper CERC-90-2, U.S. Army Engineer Waterways Experiment Station, Coastal Engineering Research Center, Vicksburg, MS.
- Hanson, H., Larson, M., , and Kraus, N. C. (2001). A new approach to represent tidal currents in the one-line model concept. In *Proceedings of Coastal Dynamics '01, American Society of Civil Engineers*.
- Hanson, H., Larson, M., Kraus, N. C., and Gravens, M. B. (2006). Shoreline response to detached breakwaters and tidal current: Comparison of numerical and physical models. In *Proceeding of the 30th Coastal Engineering Conference, World Scinetific, pp. 3357-3369*.
- Hapke, C. J., Plant, N. G., Henderson, R. E., Schwab, W. C., and Nelson, T. R. (2016). Decoupling processes and scales of shoreline morphodynamics. *Journal of Coastal Research*, 381:42–53.
- Hapke, C. J., Reid, D., Richmond, B. M., and Ruggiero, P. and List, J. (2006). *National assessment of shoreline change. Part 3: historical shoreline change and associated coastal land loss along sandy shorelines of the California coast*. Technical Report 13-14, USGS Report.
- Harley, M. (2017). Coastal storm definition. In Ciavola, P. and Coco, G., editors, *Coastal Storms: Processes and Impacts*, volume 1, chapter 1, pages 1–22. John Wiley and Sons., ISBN 978-1-118-93710-5.
- Hegge, B., Eliot, I., and Hsu, J. (1996). Sheltered sandy beaches of southwestern australia. *Journal of Coastal Research*, 12 (3):748.
- Heikkila, J. and Silven, O. (1997). A four-step camera calibration procedure with implicit image correction. In *Computer Vision and Pattern Recognition, 1997. Proceedings., 1997 IEEE Computer Society Conference on*, pages 1106–1112. IEEE.
- Hoan, L. X. (2010). Long-term simulation of coastal evolution. mathesis, Lund University.
- Hoan, L. X., Hanson, H., and Larson, M. (2011a). A mathematical model of spit growth and barrier elongation. *Estuarine Coastal and Shelf Science*, 93 (4):468–477.
- Hoan, L. X., Hanson, H., Larson, M., and Nam, P. T. (2011b). Modeling regional sediment transport and shoreline reponse in the vicinity of tidal inlets on the long island coast, united states. *Coastal Engineering*, 58:554–561.
- Holland, K. T. and Holman, R. A. (1993). The statistical distribution of swash maxima on natural beaches. *Journal of Geophysical Research*, 98:10271–10278.
- Holland, K. T., Holman, R. A., Lippmann, T. C., Stanley, J., and Plant, N. (1997). Practical use of video imagery in nearshore oceanographic field studies. *IEEE Journal of oceanic engineering*, 22(1):81–92.
- Holman, R., Plant, N., and Holland, T. (2013). cbathy: a robust algorithm for estimating nearshore bathymetry. *Journal of Geophysical Research*, 118:2595–2609.
-

- Holman, R. A. and Stanley, J. (2007). The history and technical capabilities of argus. *Coastal Engineering*, 54:477–491.
- Holthuijsen, L. H. (2010). *Waves in oceanic and coastal waters*. Cambridge university press.
- Huntley, D. A. and Bowen, A. J. (1975). Comparison of the hydrodynamics of steep and shallow beaches. In Hails, J. and Carr, A., editors, *Nearshore Sediment Dynamics and Sedimentation*, volume -, chapter -, page 69–109. Wiley, London.
- Hurst, M. D., Barkwith, A., Ellis, M. A., Thomas, C. W., and Murray, A. B. (2015). Surf zone characterization using a small quadcopter: technical issues and procedures. *Journal of Geophysical Research*, 120:2586–2608.
- Ibaceta, R., Almar, R., Catalán, P. A., Blenkinsopp, C. E., Almeida, L. P., and Cienfuegos, R. (2018). Assessing the performance of a low-cost method for video-monitoring the water surface and bed level in the swash zone of natural beaches. *Remote Sensing*, 10(1):49.
- Idzanovic, M., Ophaug, V., and Andersen, B. (2018a). Coastal sea level from cryosat-2 sarin altimetry in norway. *Advance Space Research*, 62:1344–1357.
- Idzanovic, M., Ophaug, V., and Andersen, B. (2018b). Coastal sea level from cryosat-2 sarin altimetry in norway. *Advance Space Research*, 62:1344–1357.
- Inman, D. L. and Frautschy, J. (1966). Littoral processes and the development of shorelines. In *Proceedings Coastal Engineering Conference, ASCE*, pages 511–536.
- Intergovernmental Oceanographic commission (IOC) (2006). *Manual of sea level - Measurement and interpretation. Volume IV: An Update to 2006. JCOMM Technical Report No. 31, WMO/TD. No. 1339, Manual and guides, Vol. 14*. Technical Report no1339, Intergovernmental Oceanographic commission (IOC).
- Jackson, D. W. T., Cooper, J. A. G., and del Rio, L. (2005). Geological control of beach morphodynamic state. *Marine Geology*, 216(4):297–314.
- Jevrejeva, S., Moore, J. C., Grinsted, A., and Woodworth, P. L. (2008). Recent global sea level acceleration started over 200 years ago? *Geophysical Research Letters*, 35:L08715.
- Jimenez, J., Guillén, J., and Falqués, A. (2008). Comment on the article “morphodynamic classification of sandy beaches in low energetic marine environment” by Gómez-pujol, L., Orfila, A., Cañellas, B., Alvarez-Ellacuria, A., Méndez, F.J., Medina, R. and Tintoré, J. *Marine Geology*, 255(1–2):96–101.
- Jongejan, R., Ranasinghe, R., Wainwright, D., Callaghan, D., and Reyns, J. (2016). Drawing the line on coastline recession risk. *Ocean Coastal Management*, 122:87–94.
- Jouanno, J., Marin, F., du Penhoat, Y., and Molines, J. M. (2013). Intraseasonal modulation of the surface cooling in the gulf of guinea. *Journal of Physical Oceanography*, 43:382–401.
- Kaergaard, K. and Fredsoe, J. (2013). A numerical shoreline model for shorelines with large curvature. *Coastal Engineering*, 74:19–32.
- Kamphuis, J. W. (1991). Alongshore sediment transport rate. *Journal of Waterway, Port, Coastal, and Ocean Engineering*, 117(6):624.
-

- Karunaratna, H., Pender, D., Ranasinghe, R., Short, A., and Reeve, D. E. (2014). The effects of storm clustering on beach profile variability. *Marine Geology*, 348:103–112.
- Kim, J. K., Choi, B. J., and Lee, S.-H. (2018). Non-seasonal sea level variations in the korea strait and regional atmospheric conditions. *Journal of Coastal Research*, SI 85:581–585.
- Klemas, V. (2013). Airbone remote sensing of coastal features and processes: An overview. *Journal of Coastal Research*, 29(2):239–255.
- Komar, P. D. (1999). *Beach processes and sedimentation (2nd edition)*. Prentice Hall.
- Komar, P. D., Allan, J. C., and Ruggiero, P. (2011). Sea level variations along the u.s. pacific northwest coast: tectonic and climate controls. *Journal of Coastal Research*, 27(5):808–823.
- Komar, P. D. and Enfield, D. B. (1987). Short-term sea-level changes and coastal erosion. In Nummedal, D., Pilkey, O. H., and Howard, J. D., editors, *Sea-Level Fluctuations and Coastal Evolution*, volume 41, chapter 2, pages 17–27. SEPM Society for Sedimentary Geology.
- Kraus, N. C. (2000). Reservoir model of ebb-tidal shoal evolution and sand bypassing. *Journal of Waterway, Port, Coastal and Ocean Engineering*, 126(3):305–313.
- Kraus, N. C. (2008). *Regional analysis for beach nourishment planning, Brunswick County, North Carolina*. Technical Report Memorandum for Record CEERD-HV-B, Coastal and Hydraulics, Laboratory. U.S. Army Engineer Research and Development Center, Vicksburg, MS.
- Kraus, N. C., Hanson, H., , and Harikai, S. (1984). Shoreline change at oarai beach, japan: Past, present and future. In *Proceedings of 19th Coastal Engineering Conference, American Society of Civil Engineers*, pp 2107-2123.
- Kraus, N. C., Larson, M., and Wise, R. A. (1998). *Depth of closure in beach-fill design*. Technical Report Coastal Engineering Tech. Note CETN II-40, 14 pp., Laboratory. U.S. Army Engineer Research and Development Center, Vicksburg, MS.
- Kraus, N. C., Scheffner, N. W., Hanson, H., Chou, L. W., Cialone, M. A., Smith, J. M., , and Hardy, T. A. (1988). *Coastal Processes at Sea Bright to Ocean Township, New Jersey, Volume 1: Main Text and Appendix A*. Technical Report Miscellaneous Paper CERC-88-12, U.S. Army Engineer Waterways Experiment Station, Coastal Engineering Research Center, Vicksburg, MS.
- Kriebel, D. L. and Dean, R. G. (1993). Convolution method for time-dependent beach profile response. *Journal of Waterway, Port, Coastal and Ocean Engineering*, 119:204–226.
- Kroon, A., Larson, M., Möller, I., Yokoki, H., Rozynski, G., Cox, J., and Larroude, P. (2008). Statistical analysis of coastal morphological data sets over seasonal to decadal time scales. *Coastal Engineering*, 55:581–600.
- Kumapley, N. K. (1989). The geology and geotechnology of the keta basin with particular reference to coastal protection. In *Proceedings, KNGMG Symposium on Coastal Lowlands. Geol. Geotechnol.* 311–320.
-

- Kuriyama, Y. and Nakatsukasa, T. (2000). A one-dimensional model for undertow and longshore current on a barred beach. *Coastal Engineering*, 40:39–58.
- Laibi, R., Anthony, E., Almar, R., Castelle, B., Senechal, N., and Kestenare, E. (2014). Longshore drift cell development on benin sand barrier coast, west africa. In: *Green, A.N. and Cooper, J.A.G. (eds.), Proceedings 13th International Coastal Symposium (Durban, South Africa), Journal of Coastal Research*, Special Issue no 70:122–129.
- Lamb, H. (1994). *Hydrodynamics, 6th edition*. Cambridge University Press.
- Laporte-Fauret, Q., Marieu, V., Castelle, B., Michalet, R., Bujan, S., and Rosebery, D. (2019). Low-cost uav for high-resolution and large-scale coastal dune change monitoring using photogrammetry. *Journal of Marine Sciences and Engineering*, 7(3):63.
- Larson, M., Hanson, H., and Kraus, N. (1997). Analytical solutions of one-line model for shoreline change near coastal structures. *Journal of Waterway, Port, Coastal and Ocean Engineering*, 123(4):180–191.
- Larson, M., Hoan, L. X., and Hanson, H. (2010). A direct formula to compute wave properties at incipient breaking. *Journal of Waterway, Port, Coastal and Ocean Engineering*, 136(2):119–122.
- Larson, M. and Kraus, N. C. (1989). *SBEACH: Numerical Model for Simulating Storm-Induced Beach Change, Report 1: Empirical Foundation and Model Development*. Technical Report Technical Report CERC-89-9, U.S. Army Engineer Research and Development Center, Vicksburg, MS.
- Larson, M. and Kraus, N. C. (2003). Modeling regional sediment transport and coastal evolution along the delmarva peninsula. In *Proceedings Coastal Sediments '03, ASCE*.
- Larson, M., Kraus, N. C., and Connell, K. L. (2006). Modeling sediment storage and transfer for simulating regional coastal evolution. In *Proceeding of the 30th Coastal Engineering Conference (California, USA), World Scientific*, pp. 3924-3936.
- Larson, M., Kraus, N. C., and Hanson, H. (2002a). Simulation of regional longshore sediment transport and coastal evolution- the cascade model. In *Proceeding of the 28th Coastal Engineering Conference. World Scientific Press*.
- Larson, M., Palalane, J., Fredriksson, C., and Hanson, H. (2016). Simulating cross-shore material exchange at decadal scale. theory and model component validation. *Coastal Engineering*, 116:57–66.
- Larson, M., Rosati, J. D., and Kraus, N. C. (2002b). *Overview of regional coastal processes and controls*. Technical Report Coastal and Hydraulics Engineering Technical Note CHETN XIV-4, U.S. Army Engineer Research and Development Center, Vicksburg, MS.
- Larson, M., Wise, R. A., and Kraus, N. C. (2004). Modeling dune response due to overwash transport. In *Proceedings 29th Coastal Engineering Conference, World Scientific Press*, pp. 21.
-

- Le Cozannet, G., Bulteau, T., Castelle, B., Ranasinghe, R., Woppelmann, G., Rohmer, J., Bernon, N., Idier, D., Louisor, J., and Salas-y Mélia, D. (2017). Quantify uncertainties of sandy shoreline change projections as sea level rises. *Natural Hazards and Earth Systems Sciences*, 17:1075–1089.
- Le Cozannet, G., Bulteau, T., Castelle, B., Ranasinghe, R., Woppelmann, G., Rohmer, J., Bernon, N., Idier, D., Louisor, J., and Salas-y Mélia, D. (2019). Quantify uncertainties of sandy shoreline change projections as sea level rises. *Scientific reports*, 9:42:1–14.
- Le Cozannet, G., Garcin, M., Yates, M., Idier, D., and Meyssignac, B. (2014). Approaches to evaluate the recent impacts of sea-level rise on shoreline changes. *Earth-Science Reviews*, 138:47–60.
- Le Cozannet, G., Oliveros, C., Castelle, B., Garcin, M., Idier, D., Pedreros, R., and Rohmer, J. (1962). Uncertainties in sandy shorelines evolution under the bruun rule assumption. *Frontiers in Marine Science*, 3:49:1—14.
- Leatherman, S. P., K., Z., and C., D. B. (2017). Sea level rise shown to drive coastal erosion. *Eos, Transactions American Geophysical Union*, 81(6):55–57.
- Leonard, M., Westra, S., Phatak, A., Lambert, M., van den Hurk, B., McInnes, K., Risbey, J., Schuster, S., and Jakob, D. and Stafford-Smith, M. (2014). A compound event framework for understanding extreme impacts. *WIREs Climate Change*, 5:113–128.
- Lihoussou, M. (2014). Ports et désenclavement territorial: Cas de l’arrière-pays du port de cotonou. Phd dissertation, University du Havre.
- Lippmann, T. and Thornton, E. and Reniers, A. (1995). Wave stress and longshore current on barred profiles. In *In : Proceedings of Coastal Dynamics, ASCE*, pp. 401–412.
- Lippmann, T. C. and Holman, R. A. (1990). The spatial and temporal variability of sand bar morphology. *Journal of Coastal Research*, 95:575–590.
- Logah, F. Y., Amisigo, A. B., Obuobie, E., and Kankam-Yeboah, K. (2017). Floodplain hydrodynamic modelling of the lower volta river in ghana. *Journal of Hydrology: Regional Studies*, 14:1–9.
- Lombard, A., Cazenave, A., Le Traon, P. Y., and Ishii, M. (2005). Contribution of thermal expansion to present-day sea-level change revisited. *Global and Planetary Change*, 47:1—16.
- Ly, C. K. (1980). The role of the akosombo dam on the volta river in causing erosion in central and eastern ghana (west africa). *marine Geology*, 35:323–332.
- Lyard, F. H., Carrere, L., Cancet, M., Boy, J. P., Gegout, P., and Lemoine, J. M. (2016). The fes2014 tidal atlas, accuracy assessment for satellite altimetry and other geophysical applications. In *EGU General Assembly, Vienna, Austria, European Geosciences Union, 17693*.
- Mancini, F., Dubbini, M., Gattelli, M., Stecchi, F., Fabbri, S., and Gabbianelli, G. (2013). Using unmanned aerial vehicles (uav) for high-resolution reconstruction of topography: the structure from motion approach on coastal environments. *Remote Sensing*, 5:6880–6898.
-

- Marti, F., Cazenave, A., Birol, F., Passaro, M. and Leger, F., Beneviste, J., and Legeais, J. (2019). Altimetry-based sea level trends along the coasts of western africa. *Advances in Space Research*, xxx:In press.
- Masselink, G. and Hughes, M. G. (2014). *An introduction to coastal processes and geomorphology*. Routledge.
- Masselink, G., Scott, T., Poate, T., Russell, P., Davidson, M., and Conley, D. (2016). The extreme 2013/2014 winter storms: hydrodynamic forcing and coastal response along the south-west coast of england. *Earth Surface Processes and Landforms*, 41(3):378–391.
- McInnes, K., White, C., Haig, I., Hemer, M., Hoeke, R., Holbrook, N., Kiem, A., Oliver, E., Ranasinghe, R., Walsh, K., Westra, S., and Cox, R. (2016). Natural hazards in australia: sea level and coastal extremes. *Climatic Change*, 139:69—83.
- McIntosh, P. C., Church, J. A., Miles, E. R., Ridgway, K., and Spillman, C. M. (2015). Seasonal coastal sea level prediction using a dynamical model. *Geophysical Research Letters*, 42:6747—6753.
- McIntyre, M. L., Naar, D. F., Carder, K. L., Donahue, B. T., and Mallinson, D. J. (2006). Coastal bathymetry from hyperspectral remote sensing data: comparisons with high resolution multibeam bathymetry. *Marine Geophysical Researches*, 27:129–136.
- Melet, A., Almar, R., and Meyssignac, B. (2016). What dominates sea level at the coast: A case study for the gulf of guinea. *Ocean Dynamics*, 66:623—636.
- Melet, A., Meyssignac, B., Almar, R., and Le Cozannet, G. (2018a). Under-estimated wave contribution to coastal sea-level rise. *Nature Climate Change*, 8:234—239.
- Melet, A., Meyssignac, B., Almar, R., and Le Cozannet, G. (2018b). Under-estimated wave contribution to coastal sea-level rise. *Nature Climate Change*, 8(3):234.
- Merrifield, M. A., Merrifield, S. T., and Mitchum, G. T. (2009). An anomalous recent acceleration of global sea level rise. *Journal of Climate*, 22:5772—5781.
- Meyssignac, B. and Cazenave, A. (2012). Sea level: A review of present-day and recent-past changes and variability. *Journal of Geodynamics*, 58:96—109.
- Meyssignac, B., Slangen, A., Melet, A., Church, J., Fettweis, X., Marzeion, B., Agosta, C., Ligtenberg, S., Spada, G., Richter, K., Palmer, M., Roberts, C., and Champollion, N. (2017). Evaluating model simulations of twentieth-century sea-level rise. part ii: Regional sea-level change. *Journal of Climate*, 17:8565–8593.
- Miles, J. and Russell, P. (2004). Dynamics of a reflective beach with a low tide terrace. *Continental Shelf Research*, 24(11):1219–1247.
- Miller, J. K. and Dean, R. G. (2004). A simple new shoreline change model. *Coastal Engineering*, 51:531–556.
- Milliman, J. D. and Farnsworth, K. L. (2011). *River Discharge to the Coastal Ocean*. Cambridge, University Press, Cambridge.
-

- Misra, S. K., Kennedy, A. B., and Kirby, J. T. (2003). An approach to determining nearshore bathymetry using remotely sensed ocean surface dynamics. *Coastal Engineering*, 47:265–293.
- Mitchum, G. T., Nerem, R. S., Merrifield, M. A., and Gehrels, W. R. (2010). Modern sea-level-change estimates. In Church, J. A., Woodworth, P. L., Aarup, T., and Wilson, W. S., editors, *Understanding Sea-Level Rise and Variability*, chapter 5, page 122–142. Wiley-Blackwell, Oxford, UK.
- Morton, R. A., Gibeaut, J. C., and Paine, J. G. (1995). Meso-scale transfer of sand during and after storms: Implications for prediction of shoreline movement. *Marine Geology*, 126:161–179.
- Morton, R. A., Paine, J. G., and Gibeaut, J. C. (1994). Stages and durations of post-storm beach recovery, southeastern texas coast, usa. *Journal of Coastal Research*, 10:884–908.
- Murray, A. B. and Ashton, A. (2004). Extending a 1-line modeling approach to explore emergent coastline behaviors. In *Proceedings of the International Conference of Coastal Engineering, 29th, 2035–2047*.
- Ndour, A., Laïbi, R., Sadio, M., Degbé, C. D. E., Diaw, A. T., Oyédé, L. M. and Anthony, E. J., Dussouillez, P., Sambou, H., and Dièye, E. H. B. (2018). Management strategies for coastal erosion problems in west africa: Analysis, issues, and constraints drawn from examples from senegal and benin. *Marine Geodesy*, 156:92–106.
- Nerem, R. S., Chambers, D. P., Choe, C., and Mitchum, G. T. (2010). Estimating mean sea level change from the topex and jason altimeter missions. *Marine Geodesy*, 33(1):435—446.
- Ngom, H., Ndour, A., and Niang, I. (2018). Impacts of protective structures on sandy beaches: Example of the saly balnear station, petite côte, senegal. In: *Almar, R.; Almeida, L.P.; Trung Viet, N., and Sall, M. (eds.), Tropical Coastal and Estuarine Dynamics. Journal of Coastal Research*, Special Issue No. 81:114–121.
- Nicholls, R. J., Bradbury, A., Burningham, H., Dix, J. K., Ellis, M., French, J., Hall, J. W., Karunarathna, H. U., Lawn, J., Pan, S., Reeve, D. E., Rogers, B., Souza, A., Stansby, P. K., Sutherland, J., Tarrant, O., Walkden, M. J. A., and Whitehouse, R. (2012). icoast - integrating coastal sediment systems. In *ICCE2012 International Conference on Coastal Engineering, Santander, ES, 01–06 Jul 2012 (15 pp.)*.
- Nicholls, R. J. and Cazenave, A. (2010). Sea level rise and its impact on coastal zones. *Science*, 328(5985):1517—1520.
- Nicholls, R. J., Townend, I., Bradbury, A. P., Ramsbottom, D., and Day, S. A. (2013). Planning for long-term coastal change: experiences from england and wales. *Ocean Engineering*, 71:3–16.
- Oguntunde, P. G., Friesen, J., van de Giesen, N., and Savenije, H. H. G. (2006). Hydroclimatology of the volta river basin in west africa: trends and variability from 1901 to 2002. *Physics and Chemistry of the Earth*, 31:1180—1188.
- Osorio, A. F., Medina, R., and Gonzalez, M. (2012). An algorithm for the measurement of shoreline and intertidal beach profiles using video imagery: Psdm. *Computers and Geosciences*, 46:196–207.
-

- Ozer, P., Hountondji, Y. C., and de Longueville (2017). Evolution récente du trait de côte dans le golfe du Bénin. exemples du Togo et du Bénin. *Geo-Eco-Trop*, SI 41(3):529–541.
- Paine, D. P. and Kiser, J. D. (2012). *Aerial photography and image interpretation*, volume 3. John Wiley and Sons, Inc.
- Palalane, J., Fredriksson, C., Marinho, B., Larson, M., Hanson, H., and Coelho, C. (2016). Simulating cross-shore material exchange at decadal scale. model application. *Coastal Engineering*, 116:26–41.
- Passaro, M., Cipollini, P., Vignudelli, S., Quartly, G. D., and Snaith, H. M. (2014). Ales: A multi-mission adaptive subwave form retracker for coastal and open ocean altimetry. *Remote Sensing of Environment*, 145:173–189.
- Passaro, M., Rose, M. K., Andersen, O. B., Boergens, E., Calafat, F. M., Dettmering, D., and Benveniste, J. (2018a). Adapting a homogeneous ocean retracker for satellite altimetry to sea ice leads, coastal and inland waters. *Remote Sensing of Environment*, 211:456—471.
- Passaro, M., Zulfikar Adlan, N., and Quartly, G. D. (2018b). Improving the precision of sea level data from satellite altimetry with high frequency and regional sea state bias corrections. *Remote Sensing of Environment*, 218:245—254.
- Petts, G. E. and Gurnell, A. M. (2005). Dams and geomorphology: research progress and future directions. *Geomorphology*, 71:22–47.
- Pianca, C., Holman, R., and Siegle, E. (2015). Shoreline variability from days to decades: Results of long-term video imaging. *Journal of Geophysical Research*, 120:2159–2178.
- Plant, N. G., Aarninkhof, S. G. J., Turner, I. L., and Kingston, K. S. (2007). The performance of shoreline detection models applied to video imagery. *Journal of Coastal Research*, 23(3):658–670.
- Plant, N. G., Holland, K. T., and Haller, M. C. (2008). Ocean wavenumber estimation from wave-resolving time series imagery. *IEEE Transactions on Geoscience and Remote Sensing*, 46(9):2644–2658.
- Plant, N. G. and Holman, R. A. (1997). Intertidal beach profile estimation using video images. *Marine Geology*, 140:1–24.
- Plant, N. G., Holman, R. A., and Freilich, M. H. (1999). A simple model for interannual sandbar behavior. *Journal of Geophysical Research*, 104(C7), 15:755–776.
- Polo, I., Lazar, A., Rodriguez-Fonseca, B., and Arnault, S. (2008). Oceanic Kelvin waves and tropical Atlantic intraseasonal variability: 1. Kelvin wave characterization. *Journal of Geophysical Research*, 113:C07009.
- Pujol, M. I., Faugère, Y., Taburet, G., Dupuy, S., Pelloquin, C., Ablain, M., and Picot, N. (2016). Duacs dt2014: The new multimission altimeter data set reprocessed over 20 years. *Ocean Sciences*, 12:1067–1090.
- Quartel, S., Kroon, A., and Ruessink, B. (2008). Seasonal accretion and erosion patterns of a microtidal sandy beach. *Marine Geology*, 250(1-2):19–33.
-

- Radermacher, M., Wengrove, M. E., Van Thiel de Vries, J. S. M., and Holman, R. A. (2014). Applicability of video-derived bathymetry estimates to nearshore current model predictions. *Journal of Coastal Research*, 70:290–295.
- Ranasinghe, R. (2016). Assessing climate change impacts on open sandy coasts: a review. *Earth-Sciences Reviews*, 160:320–332.
- Ranasinghe, R., Callaghan, D., and Stive, M. J. F. (2012a). Estimating coastal recession due to sea level rise: beyond the bruun rule. *Climatic Change*, 110:561–574.
- Ranasinghe, R., Holman, R., de Schipper, M., Lippmann, T., Wehof, J., Duong, T. M., Roelvink, D., and Stive, M. (2012b). Quantifying nearshore morphological recovery time scales using argus video imaging: Palm beach, sydney and duck, north carolina. *Coastal Engineering Proceedings*, 1(33):24.
- Ranasinghe, R. and Stive, M. J. F. (2012). Rising seas and retreating coastlines. *Climatic Change*, 97:465–468.
- Ranji, Z., Hejazi, K., Soltanpour, M., and Allahyar, M. (2016). Intercomparison of recent tide models for the persian gulf and oman sea. In *Proc. 35th Conf. on Coastal Engineering, Antalya, Turkey, Coastal Engineering Research Council*, 443–454.
- Rasclé, N. and Ardhuin, F. (2013). Global wave parameter data base for geophysical applications. part ii: Model validation with improves source term parameterization. *Ocean Modelling*, 70:145–151.
- Reniers, A. and Battjes, J. (1997). A laboratory study of longshore currents over barred and non-barred beaches. *Coastal Engineering*, 30:1–22.
- Robinet, A., Idier, D., Castelle, B., and Mariou, V. (2018). A reduced-complexity shoreline change model combining longshore and cross-shore processes: The lx-shore model. *Environmental Modelling and Software*, 109:1–16.
- Rosati, J. D. (2005). Concepts in sediment budgets. *Journal of Coastal Research*, 21:207–322.
- Rosati, J. D., Dean, R., and Walton, T. (2013). The modified bruun rule extended for landward transport. *Marine Geology*, 340:71–81.
- Roy, P. S., C. P. J. F. M. A. and Thom, B. G. (1994). Wave-dominated coasts. In Carter, R. W. C. and Woodrofe, C. D., editors, *Coastal evolution – Late Quaternary Morphodynamics*, volume 1 of *Integrated series in information systems*, chapter xx, pages 121–186. Cambridge: Cambridge University Press, New York.
- Rueda, A. and et al. (2017). Global classification of coastal forcing climates. *Scientific Reports*, 7:5038.
- Ruggiero, P., Kaminsky, G. M., Gelfenbaum, G., and Cohn, N. (2016). Morphodynamics of prograding beaches: a synthesis of seasonal- to century-scale observations of the columbia river littoral cell. *Marine Geology*, 376:51–78.
- Rutten, G. L. (2011). *Interactions Between Beachrock Formations and Shoreline Evolution. Case study: Togo*. Technical Report Delft, pp. 95, Delft University of Technology, The Netherlands.
-

- Sallenger, A. H. (2000). Storm impact scale for barrier islands. *Journal of Coastal Research*, 16:890–895.
- Segura, L. E., Hansen, J. E., and Lowe, R. J. (2018). Seasonal shoreline variability induced by subtidal water level fluctuations at reef fringed beaches. *Journal of Geophysical Research*, 123:433–447.
- Semiring, L., Van Ormondt, M., Van Dongeren, A. R., and Roelvink, J. A. (2017). Operational prediction of rip currents using numerical model and nearshore bathymetry from video images. *AIP Conf. Proc.*, 1857:080004.
- Senechal, N., Castelle, B., and Bryan, K. R. (2017). Storm clustering and beach response. In Ciavola, P. and Coco, G., editors, *Coastal Storms: Processes and Impacts*, volume 1, chapter 8, pages 151–174. John Wiley and Sons., ISBN 978-1-118-93710-5.
- Senechal, N., Coco, G., Castelle, B., and Marieu, V. (2015). Storm impact on the seasonal shoreline dynamics of a meso-to macrotidal open sandy beach (biscarrosse, france). *Geomorphology*, 228:448–461.
- Senechal, N., Gouriou, T., Castelle, B., Parisot, J., Capo, S., Bujan, S., and Howa, H. (2008). Morphodynamic response of a meso- to macro-tidal intermediate beach based on a long-term data set. *Geomorphology*, 107(3–4):263–274.
- Senechal, N. and Laibi, R., Almar, R., Castelle, B., Biaisque, M., Lefebvre, J.-P., Anthony, E., Dorel, M., Chuchla, R., Houkonnou, M., and du Penhoat, Y. (2014). Observed destruction of a beach cusp system in presence of a double-coupled cusp system: the example of grand popo, benin. In Green, A.N. and Cooper, J.A.G. (eds), *Proceedings 13th International Coastal Symposium (Durban, South, Africa)*, *Journal of Coastal Research, Special Issue No 70*, pp. 669-674.
- Serafin, K. A., Ruggiero, P., and Stockdon, H. F. (2017). The relative contribution of waves, tides, and non-tidal residuals to extreme total water levels on us west coast sandy beaches. *Geophysical Research Letters*, 44:1839—1847.
- Shand, T., Shand, R., Reinen-Hamill, R., Carley, J., and Cox, R. (2013). A review of shoreline response models to changes in sea level. In *Coasts And Ports Australasian Conference*, Sydney.
- Short, A. and Aagaard, T. (1993). Single and multi-bar beach change models. *Journal of Coastal Research*, SI 15:141–157.
- Short, A. D. (1999). *Handbook of beach and shoreface morphodynamics*. Wiley.
- Short, A. D. (2012). Coastal processes and beaches. *Nature Education Knowledge*, 3(10):15.
- Slangen, A., Meyssignac, B., Agosta, C., Champollion, N., Church, J., Fettweis, X., Ligtenberg, S.R.M. and Marzeion, B., Melet, A., Palmer, M., Richter, K., Roberts, C., and Spada, G. (2017). Evaluating model simulations of twentieth-century sea level rise. part i: Global mean sea level change. *Journal of Climate*, 30:8539—8563.
- Splinter, K. D., Carley, J. T., Golshani, A., and Tomlinson, R. (2014). A relationship to describe the cumulative impact of storm clusters on beach erosion. *Coastal Engineering*, 83:49–55.
-

- Splinter, K. D., Holman, R., and Plant, N. (2011). A behavior-oriented dynamic model for sand bar migration and 2dh evolution. *Journal of Geophysical Research*, 116:C01020.
- Stammer, D., Cazenave, A., Ponte, R. M., and Tamisiea, M. E. (2013). Causes for contemporary regional sea level changes. *Annual Review of Marine Science*, 5:21–46.
- Sterl, A. and Caires, S. (2005). Climatology, variability and extrema of ocean waves- the web-based knmi/era-40 wave atlas. *International Journal of Climatology*, 25:963–977.
- Stive, M. J. F. (2004). How important is global warming for coastal erosion? *Climate Change*, 64:27–39.
- Stive, M. J. F., Aarninkhof, S., Hamm, L., Hanson, H., Larson, M., Wijnberg, K. M., Nicholls, R., and Capobianco, M. (2004). Variability of shore and shoreline evolution. *Coastal Engineering*, 47:211–235.
- Stive, M. J. F., Ranasinghe, R., and Cowell, P. (2010). Sea level rise and coastal erosion. In Kim, Y., editor, *Handbook of Coastal and Ocean Engineering*, volume 1, chapter -, page 1023–1038. World Scientific, -.
- Stockdon, H. F. and Holman, R. A. (2000). Estimation of wave phase speed and nearshore bathymetry from video imagery. *Journal of Geophysical Research: Oceans*, 105(C9):22015–22033.
- Tamisiea, M. E. (2011). Ongoing glacial isostatic contributions to observations of sea level change. *Geophysical Journal International*, 186:1036–1044.
- Tano, R., Aman, A., Kouadio, K., Toualy, E., Ali, K., and Assamoi, P. (2016). Assessment of the ivorian coastal vulnerability. *Journal of Coastal Research*, 32(6):1495–1503.
- Teodoro, A. C. (2016). Optical satellite remote sensing of the coastal zone environment. an overview. In Marghany, M., editor, *Environmental Applications of Remote Sensing*, volume 1, chapter 6, pages 165–180. IntechOpen, Croatia.
- Thieler, E. R., Himmelstoss, E. A., Zichichi, J. L., and Ergul, A. (2009). The digital shoreline analysis system (dsas) version 4.0—an arcgis extension for calculating shoreline change. <http://woodshole.er.usgs.gov/project-pages/DSAS/version4/index.html>.
- Thuan, D. H. and Almar, R., Marchesiello, P., and Viet, N. T. (2019). Video sensing of nearshore bathymetry evolution with error estimate. *Journal of Marine Science and Engineering*, 7:233.
- Toimil, A., Losada, I. J., Camus, P., and Díaz-Simal, P. (2017). Managing coastal erosion under climate change at the regional scale. *Coastal Engineering*, 128:106–122.
- Tolman, H. L. (2002). Addressing the challenges of climate change risks and adaptation in coastal areas: A review. *The Global Atmosphere and Ocean System*, 8:67–83.
- Tran, H. Y. (2018). Modélisation des évolutions à long terme du trait de côte et de l'érosion côtière. mathesis, University Grenoble Alpes.
- Tran, Y. H. and Barthelemy, E. (2020). Combined longshore and cross-shore shoreline model for closed embayed beaches. *Coastal Engineering*, In press:103692.
-

- Uunk, L., Wijnberg, K. M., and Morelissen, R. (2010). Automated mapping of the intertidal beach bathymetry from video images. *Coastal Engineering*, 57:461–469.
- Valladeau, G., Thibaut, P., Picard, b., Poisson, J. C., Tran, N., Picot, N., and Guillot, A. (2015). Using saral/altika to improve ka-band altimeter measurements for coastal zones, hydrology and ice: The peachi prototype. *Marine Geodesy*, 38:124–142.
- Vialard, J., Shenoi, S. S. C., McCreary, J. P., Shankar, D., Durand, F., Fernando, V., and Shetye, S. R. (2009). Intraseasonal response of the northern indian ocean coastal waveguide to the madden-julian oscillation. *Geophysical Research Letters*, 36:L14606.
- Vitousek, S. and Barnard, P. L. (2015). A nonlinear, implicit one-line model to predict long-term shoreline change. In *The Proceedings of the Coastal Sediments 2015*, World Sci., San Diego, Calif.
- Vitousek, S., Barnard, P. L., Limber, P., Erikson, L., and Cole, B. (2017). A model integrating longshore and cross-shore processes for predicting long-term shoreline response to climate change. *Journal of Geophysical Research, Earth Surface*, 122:782—806.
- Vitousek, S. and et al. (2017). Doubling of coastal flooding frequency within decades due to sea level rise. *Scientific Reports*, 7:1399.
- Vousdoukas, M. I., Mentaschi, L., Voukouvalas, E., Verlaan, M., and Feyen, L. (2020). Extreme sea levels on the rise along europe’s coasts. *Earth’s Future*, 5:doi:10.1002/2016EF000505.
- Vousdoukas, M. I., Mentaschi, L., Voukouvalas, E., Verlaan, M., Jevrejeva, S., Jackson, L. P., and Feyen, L. (2018). Global probabilistic projections of extreme sea levels show intensification of coastal flood hazard. *Nature Communications*, 9:2360.
- West African Economic and Monetary Union (2012). *Staff Report on Common Policies of Member Countries*. Technical Report no12/59, International Monetary fund Country Report.
- White, S. and Wang, Y. (2003). Utilizing dems derived from lidar data to analyze morphologic change in the north carolina coastline. *Remote Sensing Environment*, 85:39–47.
- Wijnberg, K. M. and Terwindt, J. H. J. (1995). Extracting decadal morphologic behaviour from high resolution, long-term bathymetric surveys along the holland coast using eigen function analysis. *Marine Geology*, 126:301–330.
- Wilkowski, W., Lisowski, M. and Wszyński, M., and Wierzbicki, D. (2017). The use of unmanned aerial vehicles (drones) to determine the shoreline of natural watercourses. *Journal Of Water And Land Development*, 35 (X–XII):259–264.
- Woodcock, F. and Greenslade, D. J. M. (2007). Consensus of numerical model forecasts of significant wave heights. weather forecast. *Marine Geology*, 22:792–803.
- Wright, L. D. and Short, A. D. (1984). Morphodynamic variability of surf zones and beaches: a synthesis. *Marine Geology*, 56(1):93–118.
- Wright, L. D., Short, A. D., and Green, M. O. (1985). Short-term changes in the morphodynamic states of beaches and surf zones: An empirical pre-dictive model. *Marine Geology*, 62:339–364.
-

- Wu, L., Tajima, Y., Yamanaka, Y., Shimozone, T., and Sato, S. (2019). Study on characteristics of sar imagery around the coast for shorelinedetection. *Coastal Engineering Journal*, 61:2:152–170.
- Wunsch, C., Ponte, R. M., and Heimbach, P. (2007). Decadal trends in sea level patterns: 1993-2004. *Journal of Climate*, 20(24):5889—5911.
- Yates, M. L., Guza, R. T., and O'Reilly, W. C. (2009). Equilibrium shoreline response: observations and modeling. *Journal of Geophysical Research*, 114:C09014.
- Yates, M. L., Guza, R. T., O'Reilly, W. C., Hanson, J. E., and Barnard, P. L. (2011). Equilibriumshoreline response of a high wave energy beach. *Journal of Geophysical Research*, 116:C04014.
- Yeu, Y., Yee, J. J., Yun, H. S., and Kim, K. B. (2018). Evaluation of the accuracy of bathymetry on the nearshore coastlines of western korea from satellite altimetry, multi-beam, and airborne bathymetric lidar. *Sensors*, 18:2926.
- Zhang, K., Douglas, B., and Leatherman, S. (2002). Do storms cause long-term beach erosion along the u.s. east barrier coast? *The Journal of Geology*, 110:493–502.
-

# Appendix I : Potential of Video Cameras in Assessing Event and Seasonal Coastline Behaviour: Grand Popo, Benin (Gulf of Guinea)

In: VilaConcejo, A.; Bruce, E.; Kennedy, D.M., and McCarroll, R.J. (eds.),  
Proceedings of the 14th International Coastal Symposium (Sydney,  
Australia). *Journal of Coastal Research*, 2016, Special Issue, No.75, pp.  
442-446. Coconut Creek (Florida), ISSN 0749-0208.

## Potential of Video Cameras in Assessing Event and Seasonal Coastline Behaviour: Grand Popo, Benin (Gulf of Guinea)

Abessolo Ondoa<sup>†,\*</sup>, G., Almar<sup>‡</sup>, R., Kestenare<sup>‡</sup>, E., Bahini<sup>#</sup>, A., Hougue<sup>@</sup>, G-H, Jouanno<sup>‡</sup>, J., Du Penhoat<sup>‡#</sup>, Y., Castelle<sup>§</sup>, B., Melet<sup>‡</sup>, A., Meyssignac<sup>‡</sup>, B., Anthony<sup>¶</sup>, E.J., Laibi, R., Alory<sup>‡#</sup>, G., and Ranasinghe, R.<sup>§,°,~</sup>



www.cerf-jcr.org

<sup>†</sup>JEAI RELIFORME, Université de Douala, Cameroun  
<sup>@</sup> IRHOB, Cotonou, Benin

<sup>‡</sup>LEGOS (CNRS/CNES/IRD/Université de Toulouse), France

<sup>#</sup>University of Abomey-Calavi, ICMIPA-UNESCO Chair, Cotonou, Benin

<sup>§</sup>EPOC (Université de Bordeaux/CNRS) Talence, France

<sup>°</sup>UNESCO-IHE, Delft, The Netherlands

<sup>¶</sup>CEREGE Aix-Marseille Université, Aix en Provence, France

<sup>~</sup>Harbour, coastal and offshore engineering, Deltares, Delft, The Netherlands

<sup>+</sup> Université Abomey Calavi, Département des Sciences de la Terre, Faculté des Sciences et Techniques, Cotonou, Benin

<sup>§</sup>Research School of Earth Sciences, The Australian National University, Canberra, Australia



www.JCRonline.org

### ABSTRACT

Abessolo Ondoa, G.; Almar, R.; Kestenare, E.; Bahini, A.; Hougue, G-H.; Jouanno, J.; Du Penhoat, Y.; Castelle, B.; Melet, A.; Meyssignac, B.; Anthony E.; Laibi, R.; Alory, G., and Ranasinghe R., 2016. Potential of video cameras in assessing event and seasonal coastline behaviour: a case study at Grand Popo, Benin (Gulf of Guinea). *In: Vila-Concejo, A.; Bruce, E.; Kennedy, D.M., and McCarroll, R.J. (eds.), Proceedings of the 14th International Coastal Symposium* (Sydney, Australia). *Journal of Coastal Research*, Special Issue, No.75, pp. 442-446. Coconut Creek (Florida), ISSN 0749-0208.

In this study, we explore the potential of a nearshore video system to obtain a long-term estimation of coastal variables (shoreline, beach slope, sea level elevation and wave forcing) at Grand Popo beach, Benin, West Africa, from March 2013 to February 2015. We first present a validation of the video system with field data over a 10-day experiment conducted on Grand Popo beach in 2014. Secondly, 2-years daily and monthly timeseries are extracted and their variability is described as a function of regional forcing and climatic modes. All variables show large monthly variability. The longshore sediment transport estimated locally from video is in agreement with that derived from Era-Interim wave data re-analyses. Results show that the shoreline responds predominantly to tides at the event scale and to waves. Overall, this study suggests that video stations are efficient tools to monitor coastal processes over the long term, in complement with other conventional approaches. Although no clear conclusions can be drawn on inter-annual variability, the results show that it is important to build up extended coastal observation networks to address coastline changes over a wide range of scales.

**ADDITIONAL INDEX WORDS :** *Bight of Benin, video remote sensing, shoreline, longshore sediment transport, sea level, waves, tide, regional climate*

### INTRODUCTION

Description and understanding of the processes that link coastal dynamics and regional meteorological-ocean forcing is still an important challenge. This must provide insights on the temporal and spatial scales of coastal response and long-term trends in a changing climate. Specifically, the link between high frequency (short-term events, <30 days) and longer term (i.e. inter-annual) evolution remains unclear, due to the lack of appropriate modeling tools to describe these different temporal scales. This can now be partly addressed via shore-based video stations, which allows the important variables of the near-shore environment to be derived at high frequency and large spatial scales.

The Gulf of Guinea coastline, in West Africa, is exposed to South Atlantic high-energy oblique swells which drive strong longshore sediment transport ( $\sim 500\,000\text{ m}^3\text{yr}^{-1}$ , Almar *et al.*, 2015). This stretch of coast is currently affected by severe erosion that reaches up to 10 m/yr at Cotonou, Benin, attributed to the development of large harbours that trap sand transported alongshore (Dossou and Glehouenou-Dossou, 2007). Recent analysis of model based studies and open ocean altimetry data suggest a large temporal variability of longshore transport and local sea-level elevation with trends reaching  $-103\text{ m}^3\text{yr}$  (1979-2012 period) and  $+4.6\text{ mm/yr}$  (1993-2012 period) respectively over recent decades (Almar *et al.*, 2015; Melet *et al.*, 2015). These findings need to be confirmed with direct observations. For this purpose, a permanent low-cost video system was deployed since February 2013 at Grand Popo, Benin.

In contrast with costly in-situ field measurements limited in both time and space, a low-cost video camera-based video system is advantageous in measuring nearshore hydrodynamics

DOI: 10.2112/SI75-089.1 received 15 October 2015; accepted in revision 15 January 2016.

\*Corresponding author: gregsolo55@yahoo.fr

©Coastal Education and Research Foundation, Inc. 2016

(waves, tides, setup, currents) and morphology (shoreline, bathymetry and

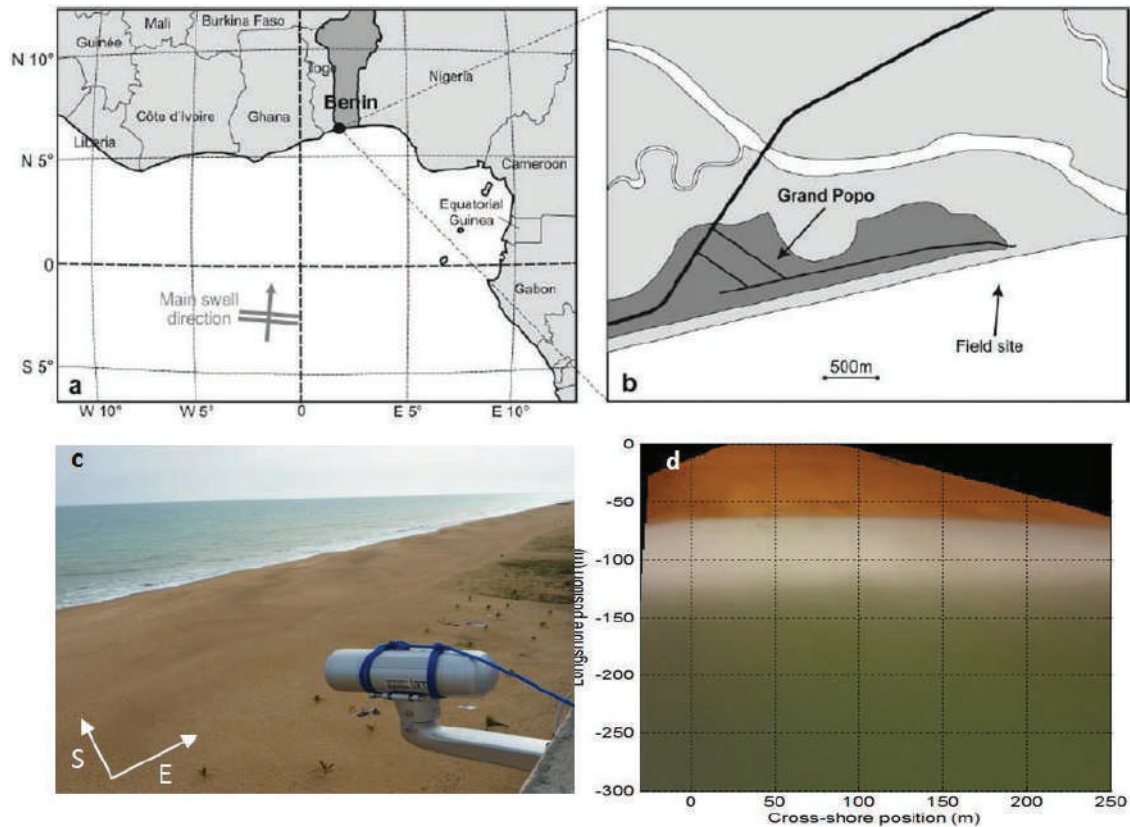


Figure 1. Study site, (a-b) Grand Popo beach in Benin, (Gulf of Guinea, West Africa), facing the South Atlantic. (c) video camera system deployed on a tower made available by the Beninese Navy, and (d) plan shape timex showing the camera field of view. White part is breaking zone and shoreline clearly appears as transition between white to red-band dominated sandy beach.

topography) (see Almar *et al.*, 2012b; Holman and Haller, 2013). In addition, this video imagery technique offers an interesting alternative to coastal tidal gauges or spatial altimetry, because it can give an estimation of waterline elevation.

In this study we explore the potential of nearshore video systems in describing and linking the long-term variability of waves, alongshore currents, sea level elevation and the shoreline. This study includes a comparison with field data over a short period (10 days), which allowed for properly extrapolating the variables over the full observation period. The modes of variability of waves, sea level and shoreline position over the observation period (2.5 years) are analyzed and positioned in a regional climate context.

#### Site description

The beach of Grand Popo, Benin, is located in the Bight of Benin (Gulf of Guinea, West Africa), an open sandy stretch of coast facing the South Atlantic Ocean. Grand Popo is hardly affected by human presence, hosting only a few fishermen, and far enough (80 km) from the influence of Cotonou and

Lome harbours. The beach dynamics are dominated by the influence of waves of moderate energy (mean significant wave height  $H_s = 1.36$  m, mean peak period  $T_p = 9.4$  s) coming from mid-latitude with a S-SW incidence (Laibi *et al.*, 2014, Almar *et al.* 2015). Tides are semi-diurnal with a micro to meso-tidal range, from 0.8 to 1.8 m for neap and spring tides, respectively. Sediment size is medium to coarse, 0.4 to 1 mm, ( $D_{50} = 0.6$ mm). According to the classification proposed by Wright and Short (1984), Grand Popo is an intermediate Low Tide Terrace (LTT) to reflective beach.

#### METHODS

In February 2013, a low-cost video system was deployed on a 15-m high semaphore of the navy of the Republic of Benin, 80 m from the shore (which is the approximate beach width). It comprises a VIVOTEK IP 7361 camera (1600 x 1200 pixels) that collects data continuously at 2 Hz. This autonomous system is powered by solar panels. An on-site computer processes the raw images and stores the data. Three types of secondary images are stored: instant, 15-min average and time stacks. Three time stacks are generated (two across-shore and one along-shore, Almar and *al.*, 2014).

Two field experiments were conducted at Grand Popo beach, Benin, on February 2013 and March 2014. Field data collected during the Grand Popo 2014 experiment (Almar *et al.*, 2016) are used in this study to validate the video system. Measurements included both sea and beach morphological surveys with Differential GPS and bathymetric sonar, while offshore forcing (waves and tide) was characterized using an Acoustic Doppler Current Profiler (ADCP) moored at 10-m depth.

ERAInterim re-analyses (Sterl and Caires, 2005) data were extracted over the 2013-2015 period at the daily scale to compute wave heights at Grand Popo (propagated from deep water to the breakpoint using the formula by Larson *et al.*, 2010), and to compute 3 daily indexes standing as proxies of the dominant climatic modes of the South Atlantic. The Inter-Tropical Convergence Zone (ITCZ) and El Nino Atlantic (AMM) were computed from local wind and sea level off Grand Popo, and Southern Annular Mode (SAM) was computed from mid-latitude winds. Longshore Sediment Transport was estimated using the formula by Kaczmarek *et al.*, (2005) (see Almar *et al.*, 2015).

In this paper, several important nearshore parameters were estimated daily : cross-shore and longshore wave energy fluxes, surface elevation, shoreline location and beach slope. Several video methods were used to estimate the corresponding parameters: wave height (Almar *et al.*, 2012a), period and surface elevation (inversed from celerity, see Catalan and Haller, 2008; Stockdon and Holman, 2000) were measured from spatio-temporal images; wave direction and shoreline location were estimated from average images (Almar *et al.*, 2012). Determination of the intertidal beach profile involved the delineation of the shoreline at different tidal levels (Aarninkhof *et al.*, 2003) and interpolation between low and high tides. Kaczmarek *et al.* (2005) formula is used to estimate longshore current within the surf zone.

**RESULTS**

Table 1 shows the RMSE errors and the mean error (ME) obtained during Grand Popo 2014 measurements for wave parameters ( $H_s$ ,  $T_p$  and  $Dir$ ), elevation, intertidal topography and bathymetry. The average RMS error of the beach profile is relatively low (0.28 m). The accuracy of the method is within the error range of existing methods (0.3-0.7 m reported in Plant and Kingston, 2007).

Figure 2 shows the comparison for hydrodynamics (wave and tide) using the ADCP data and Era-Interim wave estimates. Errors for  $H_s$ ,  $T_p$  and  $Dir$  are reasonable though the correlations are rather weak, showing the difficulties in describing high-frequency behavior. The day-to-day dynamics are well captured. It must be noted that ERAInterim estimates show substantial discrepancies (more than 50 % overestimation of  $H_s$  and period shorter by 2-4s), which argues in favor of using local video-based measurements rather than hindcast products because of local unresolved effects of bathymetry hydrodynamics (or adverse conditions for the Larson *et al.*, (2010) formula).

On the whole, this validation proves that video methods have reasonable errors and can be used in a stand-alone mode

for longer-term estimates of waves, sea level and beach morphological evolution.

**Beach and forcing evolution over the 2013-2015 period**

The five following parameters: cross-shore and longshore wave energy fluxes, surface elevation, shoreline location and

Table 1. Comparison of hourly hydrodynamic video estimates and Grand Popo 2014 field measurements. The root mean square error (RMSE) and the mean error (ME) are computed from the difference between the two sets of data. Intertidal profile error computed from 7 daily comparisons.

Hydrodynamic parameters	RMSE	ME
$H_s$ (m)	0.14	-0.02
$T_p$ (s)	1.31	-0.18
Direction (°)	9.25	2.25
Elevation (m)	0.12	0.02
Intertidal profile	0.28	0.23

beach slope, were computed at daily and monthly scales over the 2-yr period, providing a long enough timeseries to determine the relative contributions of wave and tide forcing to beach response, using a multiple linear regression. In this analyze, waves and tide are considered independent, and the shoreline response approximated as linear, though it might slightly differ (see Davidson *et al.*, 2013; Yates *et al.*, 2009). Table 2 shows that short-term shoreline evolution is dominated by tidal range modulation (spring/neap tide cycle) while waves are rather steady at this scale (which is typical of a storm-free area). At the seasonal scale, the shoreline responds preferentially to the summer/winter modulation of waves, with larger waves during the southern hemisphere winter.

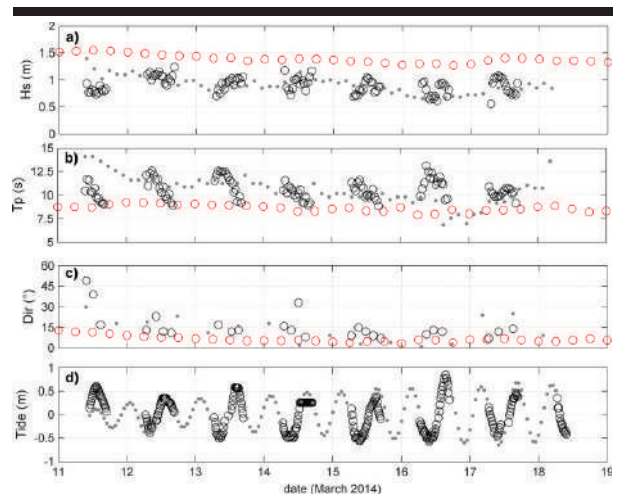


Figure 2. Comparison of 15-min video estimates with Grand Popo 2014 hourly field measurements for (a)  $H_s$ , (b)  $T_p$ , (c)  $Dir$  and (d) tide. Red circles stand for ERAInterim waves propagated to the shore using formula by Larson *et al.*, (2010). Grey dots and black circles are in-situ data (ADCP) and video data, respectively.

Table 2. Relative contribution (percent) of significant wave height and tide to the evolution of shoreline at monthly and event scale.

Hydrodynamic forcing parameters	$H_s$ (%)	Tide (%)
Monthly scale	72	28
Event scale	21	79

Figure 3 shows that all variables have substantial monthly variability. Wave flux (both cross and alongshore) peak in the southern hemisphere winter, while slope decreases and shoreline retreats. In the meantime, elevation and shoreline behavior seem linked and present a substantial trend, though it is too early to draw significant conclusions.

Since the dynamics of this coastline is dominated by longshore processes (Almar *et al.*, 2015; Laibi *et al.*, 2014), we computed Longshore Sediment Transport (LST) from locally video-derived wave parameters. Interestingly, results in Figure 4 shows that Era-Interim (from total swell and wind waves) and local estimates are in good agreement, both in average value (444397 and 496993 m<sup>3</sup>/yr, respectively) and variability, though some discrepancies exist (RMSE=0.23).

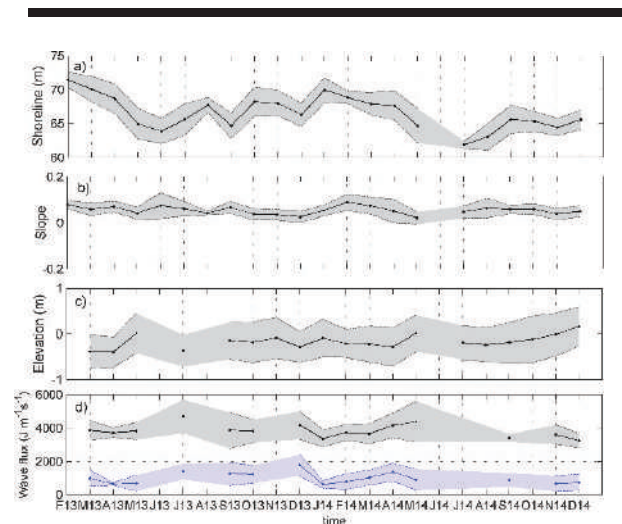


Figure 3. Monthly video estimates of : (a) shoreline location, (b) beach slope, (c) surface elevation, and (d) wave energy flux, cross-shore in grey and longshore in blue. Shaded zones stand for day-to-day dispersion (standard deviation).

Even though it is too early to determine the influence of regional climatic modes, SAM, ITCZ and AMM (Almar *et al.*, 2015) (Figure 5) on these coastal variables, our paper puts forward the potential of video-based techniques for such long-term oriented investigations.

**DISCUSSION AND CONCLUSIONS**

In this paper, 2 years of video observations at Grand Popo, Benin, analysed using recently developed methods, were employed to estimate the main nearshore parameters: wave height, period and direction, surface elevation, bathymetry

and topography, as well as shoreline change. These estimates were compared to field observations collected during the 10-day Grand Popo 2014 experiment and showed reasonable agreement. This shows the ability of low-cost video imagery in continuously and quantitatively monitoring a large number of key coastal variables over long durations, pending substantial errors that need to be further quantified, and ultimately reduced. In particular, the measurement of sea level brings new

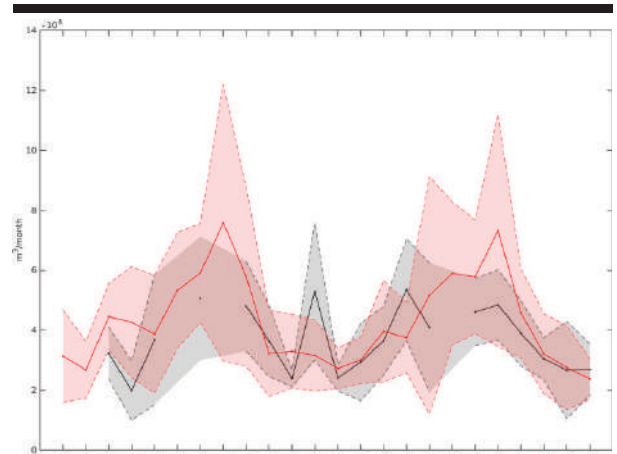


Figure 4. Monthly video estimates of Longshore Sediment Transport estimated using the Kaczmarek *et al.* (2005) formula, computed from (red) ERA-Interim re-analyses (using Larson *et al.*, (2010) for wave propagation to the shore) and (black) video estimates. Shaded zones stand for day-to-day dispersion (standard deviation).

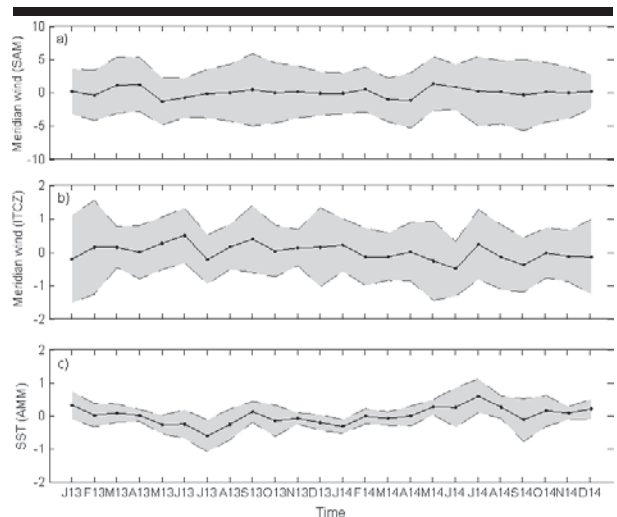


Figure 5. Monthly video estimates of proxies for regionally climatic modes : (a) meridian wind in the South Atlantic (SAM), and (b) meridian wind (ITCZ) and (c) Surface Sea Temperature (AMM) in the Bight of Benin computed from daily Era-Interim re-analyses. Shaded zones stand for day-to-day dispersion.

perspectives in the assessment of tidal harmonics in remote or hazardous areas where the deployment of buoys encounter difficulties. Also, it has to be pointed out that, in contrast with tidal gauges or spatial altimetry, this technique provides the actual shoreline elevation, which includes all regional and coastal components of sea level (including wave-induced setup and run-up), a key aspect in assessing coastal vulnerability.

All studied variables show substantial variability at the monthly scale, wave energy peaking in the southern hemisphere winter when waves are larger in the South Atlantic Ocean. Interestingly, shoreline and elevation behavior seem to be strongly linked. In this storm-free area, elevation preferentially controls shoreline response at the short-term scale while waves dominate monthly shoreline evolution.

#### ACKNOWLEDGMENTS

The Grand Popo experiment was supported by French INSU/CNRS EC2CO-LEFE/IRD, UNESCO co-chair ICPMA/IPB. We are indebted to the naval services of Benin at Grand Popo for their logistic support during the field experiment and for allowing the installation of the permanent video system on their semaphore. This research has received support from French grants through ANR (COASTVAR: ANR-14-ASTR-0019). We acknowledge use of the ECMWF ERA Interim dataset ([www.ECMWF.Int/research/Era](http://www.ECMWF.Int/research/Era)). We would like to express our gratitude to IRD/JEAI-RELIFOME (Institut de Recherche pour le Développement-Jeune Equipe Associée à l'IRD) for its financial support.

#### LITERATURE CITED

- Aarninkhof, S., 2003. Nearshore Bathymetry derived from Video Imagery. *Delft University of Technology PhD Thesis*
- Almar, R.; Cienfuegos, R.; Catalán, P.A.; Michallet, H.; Castelle, B.; Bonneton, P., and Marieu, V. 2012. A new breaking wave height direct estimator from video imagery, *Coastal Engineering*, 61, 42-48
- Almar, R.; Ranasinghe, R.; Senechal, N.; Bonneton, P.; Roelvink, D.; Bryan, K.; Marieu, V., and Parisot, J.P., 2012. Video based detection of shorelines at complex meso- macrotidal beaches, *Journal of Coastal Research*. COAS\_49646, 28(5), 1040-1048
- Almar, R. ; Du Penhoat, Y. ; Honkonnou, N. ; Castelle, B. ; Laibi, R. ; Anthony, E. ; Senechal N.; Degbe, G.; Chuchla, R. ; Sohoun, Z., and Dorel, M., 2014. The Grand Popo experiment, Benin, *Journal of Coastal Research*, SI 70, 651-656, ISSN 0749-0208
- Almar, R.; Kestenare, E.; Reyns, J.; Jouanno, J.; Anthony, E.J.; Laibi, R.; Hemer, M.; Du Penhoat, Y., and Ranasinghe, R., 2015. Response of the Bight of Benin (Gulf of Guinea, West Africa) coastline to anthropogenic and natural forcing, Part1: Wave climate variability and impacts on the longshore sediment transport, *Continental Shelf Research*, 110, 48-59
- Almar, R.; Almeida, P.; Blenkinsopp, C., and Catalan, P., 2016. *Journal of Coastal Research*, Special Issue, No. 75
- Catalan, P. and Haller, M., 2008. Remote sensing of breaking wave phase speeds with application to non-linear depth inversions, *Coastal Engineering*, 55, 93-111
- Davidson, M.; Splinter, K., and Turner, I., 2013a. A simple equilibrium model for predicting shoreline change. *Coastal Engineering*, 73, 191-202.
- Dossou, K.M.R and Glehouenou-Dossou, B., 2007. The vulnerability to climate change of Cotonou (Benin), *Environment and Urbanization*, 19(1), 65:79
- Holman, R. and Haller, M., 2013. Remote sensing of the nearshore. *Annual Review of Marine Science*, 113, 5-95
- Kaczmarek, L.M.; Ostrowski, R.; Pruszek, Z., and Rozynski, G., 2005. Selected problems of sediment transport and morphodynamics of a multi-bar nearshore zone. *Estuarine, Coastal and Shelf Science*, 62, 415-425
- Laibi, R.; Anthony, E.; Almar, R.; Castelle, B., and Senechal, N., 2014. alongshore drift cell development on the human-impacted Bight of Benin sand barrier coast, West Africa. In Proceedings 13th International Coastal Symposium (Durban, South Africa), *Journal of Coastal Research*, SI 70, 78-83
- Larson, M.; Hoan, L.X., and Hanson, H. 2010. A direct formula to compute wave properties at incipient breaking, *Journal of Waterway, Port, Coastal and Ocean Engineering*, 136(2), 119-122
- Melet, A.; Almar, A., and Messignac, B., 2015. What dominates sea level at the coast: a case study for Cotonou, *Ocean Dynamics* (in revision)
- Sterl, A. and Caires, S., 2005. Climatology, variability and extrema of ocean waves- the web-based KNMI/ERA-40 Wave Atlas. *Int. J. Climatol.* 25, 963-977
- Stockdon H.F. and Holman R.A. 2000, Estimation of Wave Phase Speed and Nearshore Bathymetry from Video Imagery, *Journal of Geophysical Research*. 105(C9), pp 22,015-22,033
- Wright, L.D. and Short, A.D., 1984. Morphodynamic variability of surf zones and beaches: A synthesis. *Marine Geology*, 56, 93-118
- Yates, M.L.; Guza, R.T. and O'Reilly W.C., 2009. Equilibrium shoreline response: Observations and modeling. *Journal of Geophysical Research*, 114

# Appendix II : Development of a West and Central Africa regional video camera network to monitor coastal response to multi-scale ocean forcing

In: Troels Aagaard, Rolf Deigaard, David Fuhrman (eds), Proceedings of Coastal Dynamics 2017, 12-16 June 2017 Helsingor, Denmark, pp. 1540-1550

## DEVELOPMENT OF A WEST AND CENTRAL AFRICA REGIONAL VIDEO CAMERA NETWORK TO MONITOR COASTAL RESPONSE TO MULTISCALE OCEAN FORCING

Gregoire Abessolo Ondo<sup>1,2</sup>, Rafael Almar<sup>2</sup>, Bruno Castelle<sup>3</sup>, Magnus Larson<sup>4</sup>, Minette Tomedi Eyango<sup>1,5</sup>, Frédéric Bonou<sup>6,7</sup>, Yves Du Penhoat<sup>2,6,7</sup>, Ibrahima Camara<sup>8</sup>, Moussa Sall<sup>9</sup>, Raphaël Onguéné<sup>10</sup>, Gael Alory<sup>2,6,7</sup>

### Abstract

Incident wave conditions and morphological beach response in the region of West and Central Africa are investigated using data collected with a regional network of permanent video cameras systems. Daily beach profiles were computed combining video shoreline detection at different tide levels and bathymetric estimate from wave celerity at three specific sites: Grand Popo (Benin), Mbour (Senegal) and Kribi (Cameroon). Results show that the low tide terrace of the intermediate-reflective beach of Grand Popo affects shoreline response at the event and seasonal time scales by modulating wave energy at the beach face. Based on this preliminary study and in the framework of a sustainable video station deployment, this paper highlights the potential of a video station network to address waves and coastal response on the time scales from hours to decade(s) in tropical coastal environments where data are lacking.

**Key words:** shoreline, bathymetry, morphodynamics, regional climate, remote sensing, wave forcing

### 1. Introduction

Coastal vulnerability, defined as the susceptibility of a coastal area to be impacted by either inundation or erosion, affects the majority of world coastlines and results in the destruction of property and infrastructure (Gianluigi *et al.*, 2014, Tano *et al.*, 2016). Understanding this coastal vulnerability remains a scientific challenge (Stive, 2004). Climate change drives sea-level rise and changes in storminess that will increase this vulnerability in coastal areas (Stive *et al.*, 2002). Damage and losses associated with erosion and flooding also sometimes reflect absent or inadequate coastal management strategies due to a lack of understanding of coastal processes (Hoggart *et al.*, 2014, Nabil *et al.*, 2014). This is particularly true in developing countries where rampant anthropization increases coastal risks to people. Numerous studies show the significant impact of storms (Masselink *et al.*, 2015, Castelle *et al.*, 2015, ) and surge events (Quinn, 2014) on coastal areas, and the link between high frequency (short-term events, <30 days) and longer term (inter-annual) evolution has been investigated through equilibrium shoreline models (Splinter *et al.*, 2014, Hanson *et al.*, 2010). In developing countries, the sparse or the lack of available data sets and

---

<sup>1</sup> Laboratoire de Ressources Halieutiques (LRH), EDSFA, University of Douala, Cameroon. [gregsolo55@yahoo.fr](mailto:gregsolo55@yahoo.fr)

<sup>2</sup> LEGOS (CNRS/CNES/IRD/Université de Toulouse), Toulouse, France [rafael.almar@ird.fr](mailto:rafael.almar@ird.fr) [gael.alory@legos.obs-mip.fr](mailto:gael.alory@legos.obs-mip.fr) [yves.du-penhoat@ird.fr](mailto:yves.du-penhoat@ird.fr)

<sup>3</sup> EPOC (Université de Bordeaux/CNRS) Talence, France [b.castelle@epoc.u-bordeaux1.fr](mailto:b.castelle@epoc.u-bordeaux1.fr)

<sup>4</sup> Department Of Water Resources Engineering (DWRE), Lund University, Sweden [magnus.larson@tvrl.lth.se](mailto:magnus.larson@tvrl.lth.se)

<sup>5</sup> ISH Yabassi, University of Douala, Cameroon, [tomeditabi@yahoo.fr](mailto:tomeditabi@yahoo.fr)

<sup>6</sup> International Chair in Mathematical Physics and Applications/ Unesco Chair, University of Abomey-Calavi, Cotonou Benin, [fredericbonou@yahoo.fr](mailto:fredericbonou@yahoo.fr)

<sup>7</sup> Institut de Recherches Halieutiques et Océanologiques du Bénin (IRHOB), Centre Béninois de la Recherche Scientifique et Technique, 03 BP 1665 Cotonou, Benin

<sup>8</sup> LPAO-SF/ESP, Université Cheikh Anta Diop, Sénégal [ibrahima1.camara@ucad.edu.sn](mailto:ibrahima1.camara@ucad.edu.sn)

<sup>9</sup> Centre de Suivi Ecologique (CSE), MOLOA, Sénégal, [sall@cse.sn](mailto:sall@cse.sn)

<sup>10</sup> Institut Universitaire de Technologie (IUT) de Douala, University of Douala, Cameroon [ziongra@yahoo.fr](mailto:ziongra@yahoo.fr)

suitable modeling tools, result on a multi-scale coastal evolution poorly known (Almar *et al.*, 2014). And it is even more pertinent in tropical coasts, characterized by a strong inter-annual variability and generally moderate average energy with energetic extreme events. In West and Central African regions in the Gulf of Guinea, coasts are exposed to the influence of energetic swells from the South Atlantic (southern hemisphere sub: 30:35°S, and extra-tropics: 45:60°S), modulated by the Southern Annular Mode (SAM) and locally generated short-crested waves, influenced by equatorial fluctuations of the local Inter-Tropical Convergence Zone (ITCZ) (Almar *et al.*, 2015, Laibi *et al.*, 2014). Shimura *et al.* (2013) showed that the North Atlantic Oscillation (NAO), with maximum wave energy during austral summer period, is not the dominant mode for waves on the Sénégal coast (in the western part of West African region), also affected by South Atlantic dynamic. Beaches of this region are commonly microtidal, low-tide terraced with moderate energetic swell  $H_S \sim 1-1.5$  m. Miles *et al.* (2004) showed that the terrace/steep beach exhibit characteristics of dissipative/reflective sites. During low tide, large wave dissipation occurs along the full extension of the terrace, contrasting with high tide where waves dissipate most of their energy at the lower beach face. The low tide terrace protects the beach by dissipating wave energy further offshore and has therefore an impact on shoreline cross-shore response. This study suggested that shoreline evolution is influenced simultaneously by wave height in the breaking zone, water depth, and terrace width. Available literature concerning the evolution of the width of the terrace is still scarce. Understanding the dynamics of specific tropical Low Tide Terrace beaches is therefore of strong scientific interest that we address thereafter.

The wide range of scales of variability of coastal systems poses severe challenges to conventional in-situ instruments, which are limited with regard to data collection in both space and time. Instead, remote sensing approaches can provide high-frequency and high-resolution proxy information on beach changes on spatially extensive areas (Holmann and Stanley, 2007). Video imagery offers an attractive low-cost alternative for continuous long-term monitoring, particularly suited for developing countries. Video nearshore monitoring was largely developed during the last decades and now offers a wide coverage of many nearshore variables such as shoreline (Boak *et al.*, 2005, Almar *et al.*, 2012a, Osorio *et al.*, 2012), intertidal beach morphology (Uunk *et al.*, 2010, Osorio *et al.*, 2012), breaking wave height (Almar *et al.*, 2012b), wave celerity (Almar *et al.*, 2008), bathymetry (Almar *et al.*, 2011, Birrien *et al.*, 2013, Sembiring *et al.*, 2014, Bergsma *et al.*, 2016), and recently nearshore currents (Almar *et al.*, 2016a). Overall, Abessolo *et al.* (2016) suggested that video stations are efficient tools to monitor coastal processes at high frequency (minutes to hours) over the long term (years to decades), in complement to other conventional approaches, in the Gulf of Guinea. The potential of using such video systems was shown with a comparison between video and field measurements. A reasonable agreement was found for the significant wave height  $H_s$ , peak period  $T_p$ , direction, and beach profile, within the error range of existing methods (0.3-0.7 m reported in Plant and Kingston, 2007). The development of video systems along the coasts of Central and West Africa offers the possibility to describe regional oceanic forcing and coastal response at different pilot sites.

In this work, we investigate wave dynamics and beach response in the tropical sub-region of Central and West Africa using low-cost video stations and recent advances in processing video data. An analysis of the evolution of daily wave characteristics, shoreline positions, and bathymetric profiles is presented. This study includes a validation of intertidal and bathymetric beach profiles from video with field measurements followed by an analysis of 3.5 years of evolution of the terrace width at the Grand Popo site.

## **2. Methods**

### **2.1. Video systems and data**

This study focuses on the West and Central Africa region. Data used in this paper were collected continuously at 3 field sites with long-term low-cost video stations. Video stations consist of a camera collecting images at high frequency (2 Hz) and an on-site computer processing the raw images and storing three types of secondary images every 15 minutes: snapshot, cross-shore time stacks, and 15-min time-averaged images. Video stations are installed at (see Figure 1):

- Grand Popo (GPP), Benin, since February 2013, using a VIVOTEK IP 7361 camera (1600 x 728 pixels). This site is an intermediate-reflective, micro-tidal (from 0.3 to 1.8 m for neap and spring tidal ranges, respectively), wave-dominated (annual mean from ERAInterim  $H_S \sim 1.4$  m,  $T_p \sim 9.4$  s,

S-SW,  $RTR \sim 1$ ), medium grain-sized  $D_{50} = 0.6$  mm, alongshore uniform, low-tide terrace beach. This site is far enough from the influence of major towns, industrial areas, and harbours (Cotonou, 80 km and Lome, 60 km, respectively, in the down- and updrift directions). Some groyne fields were constructed 20 km updrift during 2015 with limited influence on Grand Popo.

- Mbour (MBR), Sénégal, since December 2014, using a VIVOTEK IP 7361 camera (1176 x 720 pixels). This site is micro-tidal (from 0.3 to 2 m for neap and spring tidal ranges, respectively), wave-dominated (annual mean from ERAInterim  $H_S \sim 1.5$  m,  $T_P \sim 9.2$  s, NW-SW,  $RTR \sim 1$ ), medium grain-sized  $D_{50} = 0.4$  mm, located 80 km south of Dakar, 5 km from the seaside Sally resort.
- Kribi (KRB), Cameroon, since May 2015, using a VIVOTEK IP 7160 camera (1600 x 1200 pixels). This site is an intermediate-reflective, micro-tidal (from 0.4 to 1.8 m for neap and spring tidal ranges, respectively), wave-dominated (annual mean from ERAInterim  $H_S \sim 0.9$  m,  $T_P \sim 11$  s, SW,  $RTR \sim 1$ ), medium grain-sized  $D_{50} = 0.5$  mm, alongshore winding, rocky beach. This site is located in an urban area with high anthropogenic influence. A new deep water port has been constructed about 25 km upstream.

The ERAInterim hindcast data set of global meteorological variables (Sterl and Caires, 2005), generated by the ECMWF Wave Atmospheric Model WAM (The Wamdi Group, 1988), are used in this study.

On each study site, several ground control points were taken with GPS or DGPS (centimeter precision), including camera location. Geo-referencing and rectification of distortion (due to camera lens) of secondary images was accomplished using the direct linear transformation method (Holland *et al.*, 1997) applied to control points.

A 10-day field experiment was conducted at Grand Popo, Benin from 10 March to 19 March, 2014 (Abessolo *et al.*, 2016, Almar *et al.*, 2016b). Measurements included both sea and beach morphological surveys with Differential GPS and bathymetric sonar, while offshore forcing (waves and tide) was characterized using an Acoustic Doppler Current Profiler (ADCP) moored in 10-m depth.

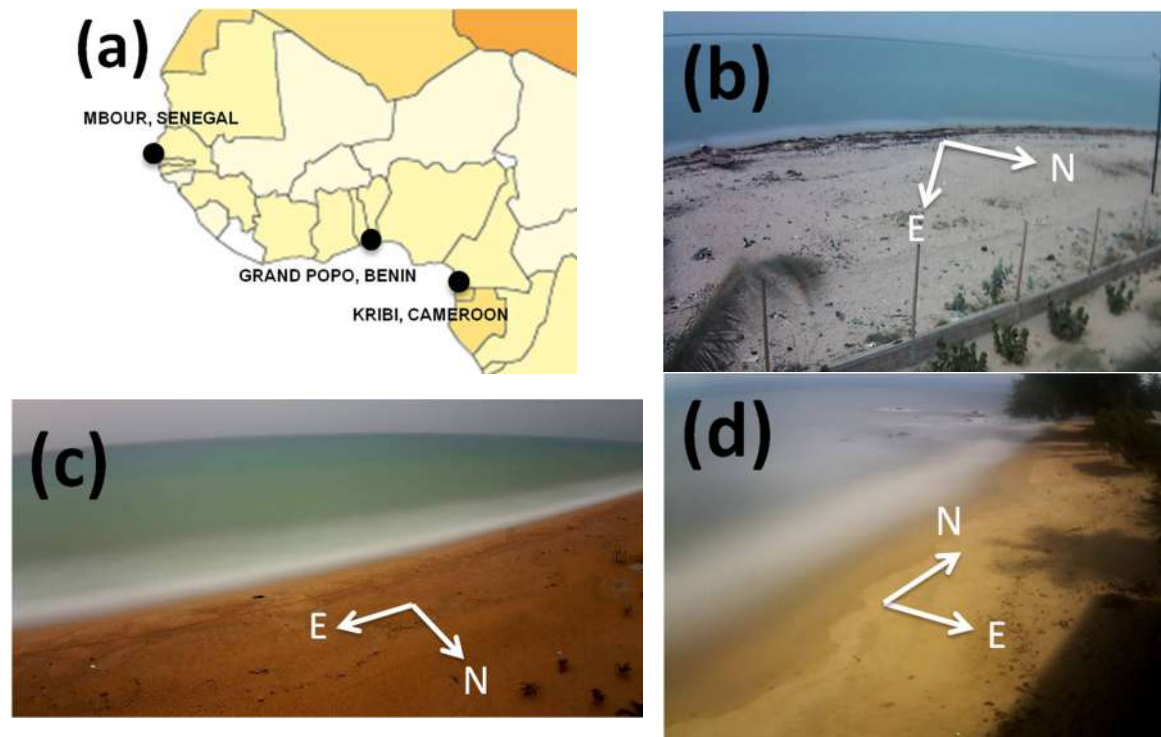


Figure 1. Video station locations in West and Central Africa (a) and 15-min video averaged images at Mbour (b), Grand Popo (c), and Kribi (d)

## 2.2. Wave characteristics from video images

Three wave characteristics are extracted in this study:  $H_S$ , mean period ( $T_m$ ), and direction ( $Dir$ ). The  $H_S$  video estimations are obtained from the cross-shore time stacks images using the method relying on the abrupt change of wave optical characteristics at the breakpoint (Almar et al., 2012). Wave breakpoints are detected from the pixel intensity threshold. The pixel intensity peak, which appears at the wave crest, is calculated by the standard deviation of pixel intensity of each time series. This allows for tracking the change of intensity and for identifying the specific points with a sudden pixel intensity rise. The wave height can therefore be estimated as  $H_S = (L_0 - cor) \tan(\beta)$  with the correction parameter  $cor = L_0 / (\tan(\alpha_i) \tan(\beta))$ ,  $L_0$  being the width of the crest,  $\alpha_i$  the incident wave angle to the shore, and  $\beta$  the camera view angle.

$T_m$  is computed from the offshore pixel intensity time series following the mean zero-crossing method detailed in Almar et al. (2008). Wave direction is estimated from the instantaneous and 15-minute averaged images. The technique consists of removing the averaged image from the instantaneous image (remove the background that does not move) and to highlight the wave crests (that move), then rectifying on a regular grid, and recovering the angle of the crest of the waves by the Radon transform (Almar et al., 2013).

Video  $H_S$  and  $T_m$  data are regressed using field offshore forcing measurements (collected during the Grand Popo field measurements of March 2014 with an ADCP) for the case of Grand Popo site, or ERA-Interim hindcast data, generated by the ECMWF Wave Atmospheric Model WAM (The Wamdi Group, 1988) in the Atlantic Ocean, for the cases of Kribi, Cameroon and Mbour, Sénégal. These hindcast data were propagated from deep water to the breakpoint using Larson et al. (2010) formula.

## 2.3. Automated shoreline delineation

The approach adopted in this study is the MSV (Minimum Shoreline Variability) method (Almar et al., 2012). The MSV method determines the shoreline location on time-averaged video images by combining two intrinsic shoreline properties: the color difference between water and sand and the presence of swash, not necessarily breaking. Beach pixels usually exhibit high red-channel ( $R$ ) values and low green-blue-channel ( $G-B$ ) values (i.e., high  $R/G-B$  ratios), whereas water pixels exhibit intense green-blue-channel values and low red-channel values (i.e., low  $R/G-B$  ratios). The  $R/G-B$  ratios are thus computed for all pixels within the region of interest. The local minimum, i.e., the transition zone between lower and higher  $R/G-B$  peaks associated with water and beach, respectively, is taken as a first estimate of the shoreline. Based on the physical fact that swash is always present at the shoreline, regardless of the complexity of the topography and the local occurrence of breaking, the shoreline is detected using the swash signature. Several contour lengths  $L$  are computed for different  $R/G-B$  values around the local minimum identified.  $L$  depends on the width of the region of interest and its variation  $\Delta L$  is typically on the order of 1 to 30% of  $L$ . The local minimum of  $\Delta L/L$  for varying  $R/G-B$  is used to infer the associated value of  $R/G-B_{shoreline}$  and thus the contour position ( $x, y$ ), while assuming that two close contours of  $R/G-B$  values at the shoreline have similar shapes. The identified shoreline on time-averaged images is converted to real-world coordinates using a rectification matrix obtained from the direct linear transformation method (Holland et al., 1997).

Determination of the intertidal beach profile involved the delineation of the shoreline at different tidal levels (Aarninkhof et al., 2003) and interpolation between low and high tides day by day. Sea level for the study period 2013-2016 was extracted from WXTide32 model, version 4.7. To reduce the longshore detection error, shoreline video positions were averaged alongshore.

## 2.4. Celerity detection and automated bathymetric inversion

First, time-stack images were pre-treated to clean up the wave intensity signal. A pass-band filter between 0.05 and 0.5 Hz was used to remove low-frequency (changing in light due to clouds) and high-frequency components (wind-waves or a rapid adjustment of the camera "auto-iris"). Then, the signal was normalized by dividing the intensity wave signal with the local intensity maximum (Almar et al., 2008).

Second, the wave spectrum on a time stack image was evaluated and the main components were extracted. For each spectral component  $f_i$ , the associated celerity  $C_{ij}$  for a position  $j$  on the cross-shore stack was estimated using the method presented by Almar et al. (2008) and Birrien et al. (2013), based on time-

and space-domain correlation. An arbitrary time lag  $\Delta t=3$  seconds was fixed. For each position  $j$ , a time-domain cross-correlation  $R$  was computed with the neighboring position  $k$  from 1 to  $n$ , using the previously fixed  $\Delta t$ . The index with the maximum correlation gave an estimate of the time-integrated distance  $\Delta x$  made by waves during  $\Delta t$ . Thus, we get a local estimate of the celerity as  $C_{ij}=\Delta x/\Delta t$ , corresponding to the spectral component  $f_i$ . By combining the celerities  $C_{ij}$ , an accurate estimate of the celerity was obtained. This was repeated for each of the positions  $i$ .

The bathymetric inversion scheme was based on the linear dispersion relation using video estimates of periods and celerities. This yielded estimates of the depth  $D_{ij}$  corresponding to the celerity  $C_{ij}$  for the spectral component  $f_i$  at a position  $j$  on the cross-shore stack. The local estimation of the depth  $D_j$  at the position  $j$  of the cross-shore stack was given by weighted averages of  $D_{ij}$ . The video depth estimates were regressed using field bathymetric surveys collected during the Grand Popo field measurements of March 2014 for the case of Grand Popo, Benin.

### 3. Results

#### 3.1. Wave characteristics and shoreline variability

Figure 2 shows the monthly evolution of wave characteristics and shoreline position from video imaging for our study sites. At Grand Popo (GPP), Benin, 3.5-year processed data (February 2013 to May 2016) shows a well-observed variability of  $H_S$  and shoreline position (black dots), negatively correlated 73 %. High values of  $H_S$  (1.6 m), corresponding to the most eroded beach state, are obtained for the June-July-August period (JJA), including high energetic S-SW swells from the South Atlantic (average  $T_m$  of 10.2 s and wave incidence of  $19^\circ$  with respect to shore normal) and wind waves generated locally. An observed trend of decreasing  $H_S$  is captured ( $\sim -0.1$  m for the study period) as well as for wave direction (trend  $\sim -3^\circ$ ), see Abessolo et al., (2017).

At Kribi, Cameroon, 1-year processed data (May 2015 to May 2016) shows a maximum monthly  $H_S$  value of 1 m, obtained for the JJA period. Wave forcing estimates correspond to high energetic swell from the South Atlantic with an average monthly  $T_m$  of 9.5 s and a shore normal direction  $6^\circ$ . Swell waves thus arrive with an incidence almost normal to the coast and the shoreline location seems to be positively correlated to  $H_S$ . Both  $H_S$  and shoreline position show a lower monthly variability comparing to Grand Popo.

At Mbour, Senegal, 11 months (December 2014 to October 2015) of video data were processed. A maximum monthly  $H_S$  value of 1.6 m was obtained in February with an average  $T_m$  of 9.5 s, and a shore normal wave direction of  $24^\circ$ , corresponding to high energetic swells generated from the north Atlantic during austral summer period, that is, December-January-February (DJF). The  $H_S$  and shoreline position are positively correlated (60 %). Compared to Grand Popo and Kribi sites, wave direction and shoreline variability are more important. We can observe a change in wave direction between February and May.

#### 3.2. Bathymetric profile evolution at Grand Popo beach, Benin

A validation of video-derived intertidal and bathymetric profiles is presented in Figure 3 for a 10-day field experiment conducted at Grand Popo, Benin from 10 March to 19 March, 2014. In Figure 3a, the principle of video intertidal beach reconstruction is illustrated, by interpolating shoreline location at different tide levels. These intertidal profiles were averaged over the validation period (Figure 3d, the blue line). The celerity extraction is illustrated in Figure 3b with the time-domain cross-correlation matrix  $R$ , previously averaged over the 10-day experiment, where a significant maximum correlation ( $>25\%$ ) is observed for a cross-shore area between 75 and 175 meters from the location of the camera. The neighboring pixels (Interval in Figure 3b) of maximum correlation give the corresponding time-integrated distance  $\Delta x$  made by the waves during  $\Delta t=3$  s. The associated celerity of this maximum correlation is shown in Figure 3c. A root-mean-square error (RMSE) of 0.1 meters is obtained, implying a well estimated terrace shape with the video; see Figure 3d (red line). This video bathymetric estimation was smoothed over 20 meters for the cross-shore stack. The low-tide terrace is detected for a depth  $\sim 1$  meter. The width of the terrace at Grand Popo, Benin can be considered as proportional to the distance  $\sim$  between the shoreline location and the 1-meter depth contour.

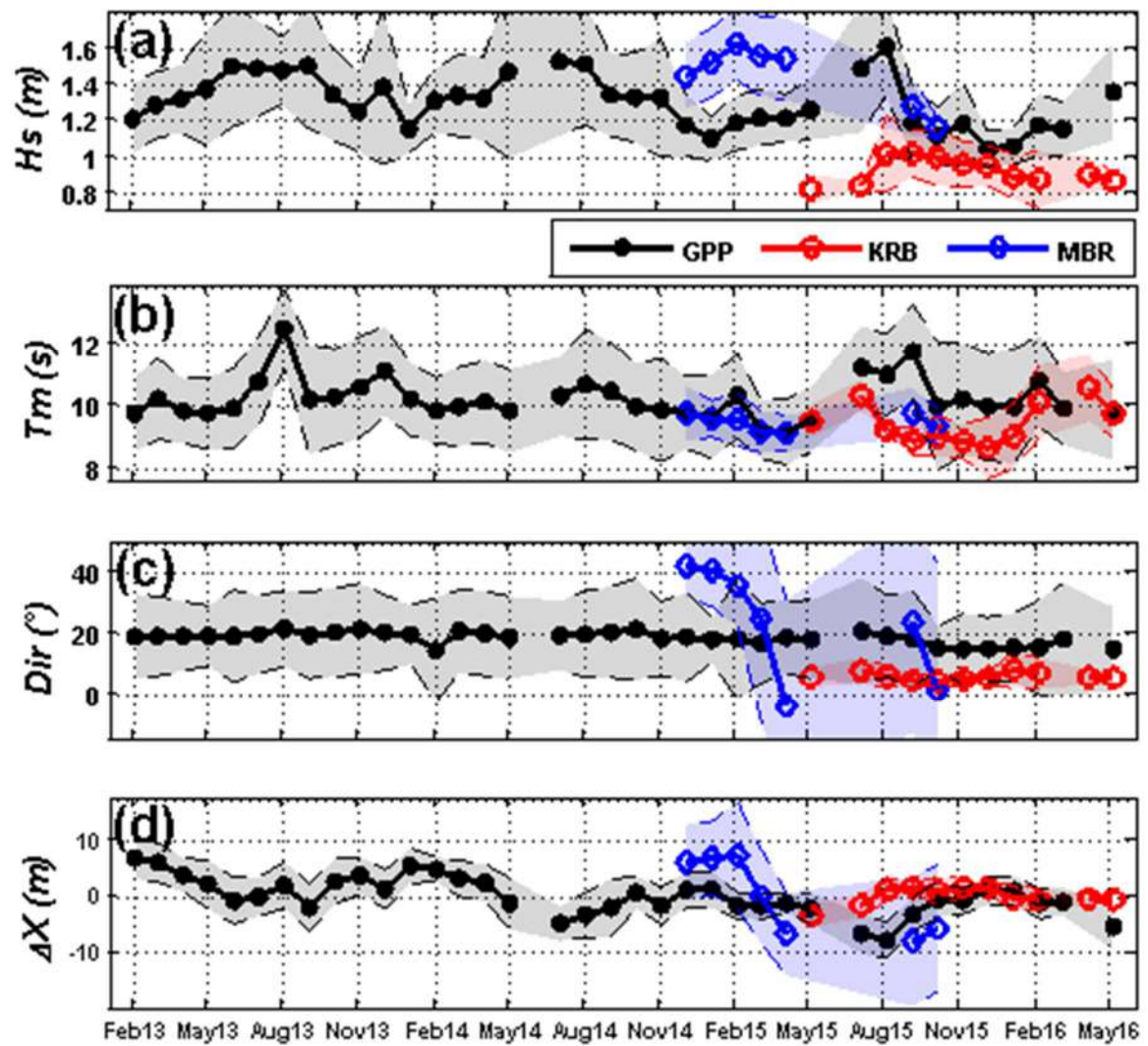


Figure 2. Monthly averaged video estimates (a)  $H_s$ , (b)  $T_m$ , (c) shore normal wave's direction and (d) shoreline variation around the average location, for the three study sites Grand Popo (GPP) in black dots, Kribi (KRB) in red circles and Mbour (MBR) in blue diamond-shaped. Shaded zones (black, blue and red) stand for day-to-day dispersion (standard deviation). Austral winter periods are in shaded yellow zones.

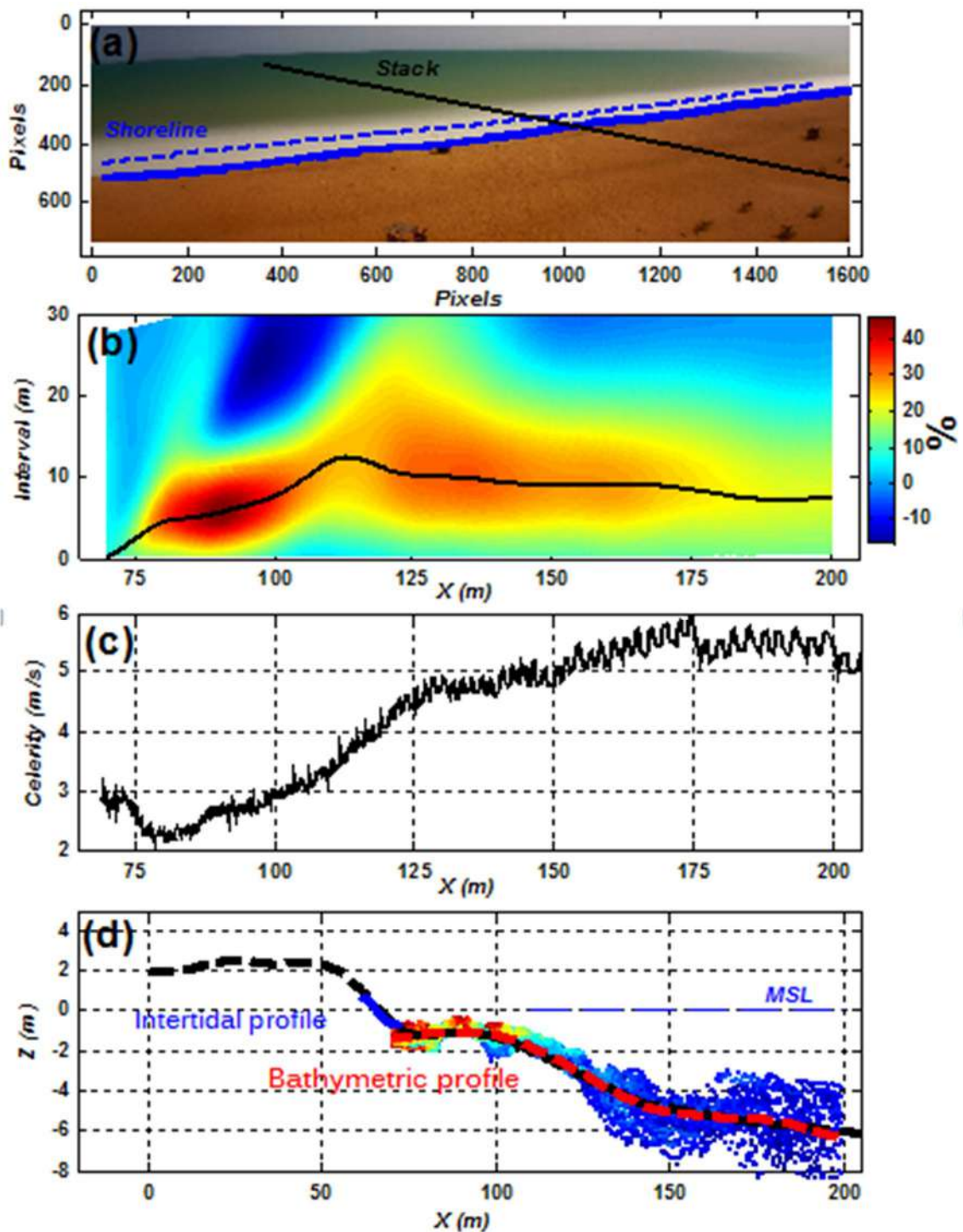


Figure 3. Validation of intertidal and bathymetric video profiles for the period of 10 to 19 March, 2014 at Grand Popo, Benin: (a) Shoreline detection on time-averaged images. Blue line is shoreline location for the presented image (high tide) and blue dashed line the shoreline location at low tide. Black line stands for the cross-shore stack for celerity detection (b) Matrix  $R$  of the correlation coefficients for each pixel  $X$  over the cross-shore stack from the beach to offshore.  $Interval$  represents the distance  $\Delta x$  (pixels) corresponding to the time lag  $\Delta t=3$  seconds. The black line stands for the maximum correlation for the position  $X$ . (c) Video celerity estimation on the cross-shore stack (d) Comparison of video intertidal (blue) and bathymetric profiles (red) with data density colored and Grand Popo 2014 DGPS and bathymetric sonar (black). MSL stands for mean sea level.

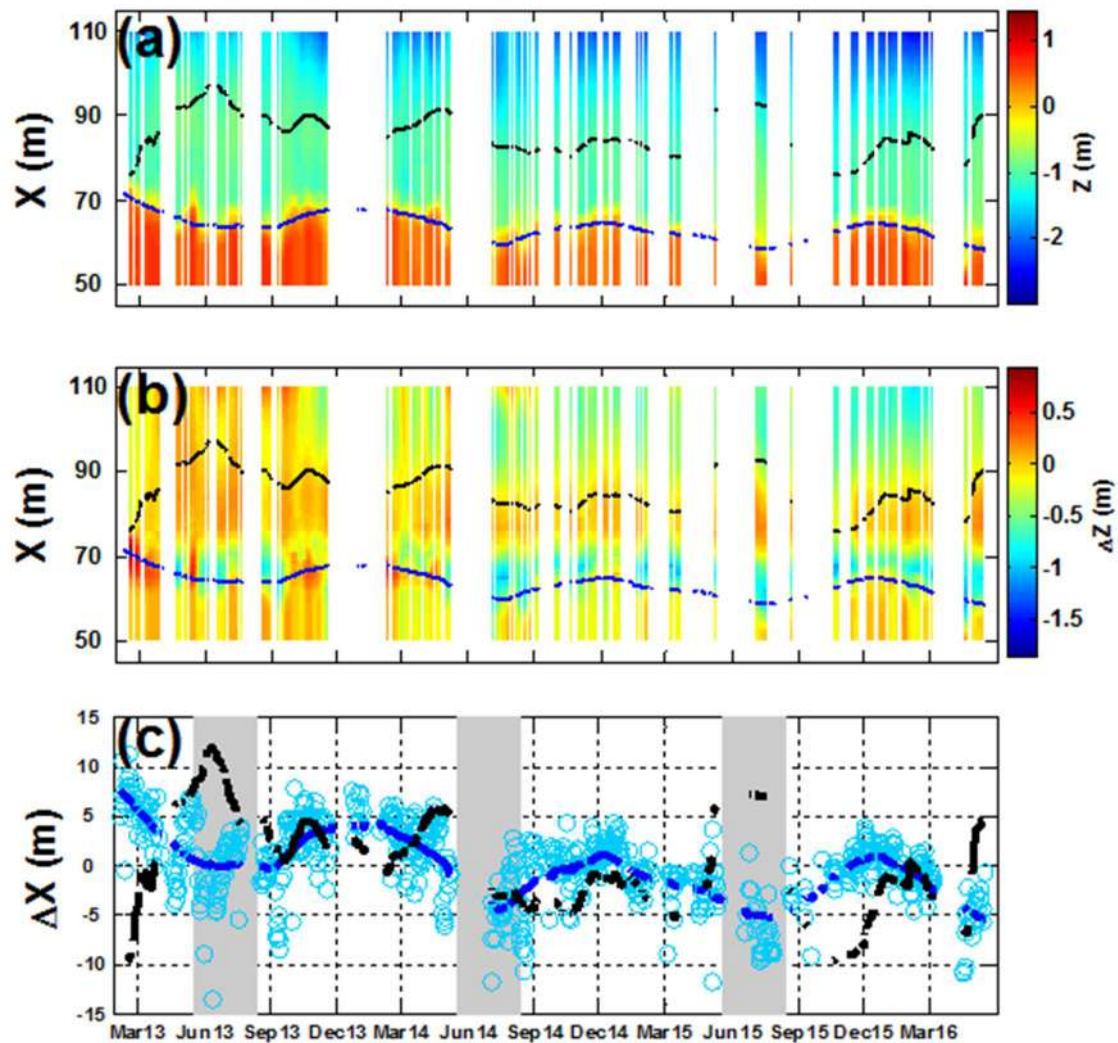


Figure 4. Video-derived profile evolution at Grand Popo, Benin: (a) Daily video intertidal and bathymetric profile evolution with regard to the position of the video camera. The black line stands for the end of the terrace (depth equal to 1 meter) and the blue line stands for the shoreline location. These lines were smoothed over 30 days. (b) Perturbation of daily beach profiles. This perturbation is computed by removing the initial beach profile from each daily profile. (c) Evolution of daily position of the end of the terrace (black line) and daily shoreline location (blue line) with austral winter period in grey. For each variable, data  $\Delta X$  are obtained by removing the average position. Solid lines are smoothed over 30 days. Blue circles are daily shoreline location.

The video system installed at Grand Popo beach collects time-averaged and time stack images every 15 minutes. Daily intertidal video profiles are computed with shoreline detection on time-averaged images and daily bathymetric profiles are obtained by averaging 15-min bathymetric profiles, computed from each time stack image. Using the validation presented on Figure 3, the maximum of time-domain cross-correlation matrix  $R$  better than 25 % is observed for cross-shore area between 75 and 175 meters from the location of the camera. Grand Popo terrace is located between 75 and 100 meters, as observed during field measurements. An overall profile of the beach, combining intertidal and bathymetric profiles, is reconstructed for a cross-shore distance of 60 meters, corresponding to the area between 50 and 110 meters from camera location (see Figures 4). Beyond the influence of waves, offshore bathymetry (depth below 3 meters) is considered as unmoved. Daily profiles were smoothed over 15 consecutive days.

In Figure 4a, the location of the shoreline and the end of the terrace (depth equal to 1 meter) show substantial event and inter-annual variability. Grand Popo beach presents an average distance from shoreline to end of terrace (depth equal to 1 meter below MSL) of 18 m, with minimum 15 m and maximum 22 m. The terrace is located at 65-100 m from the camera location. Figure 4b shows the perturbation of the beach profile, computed by removing the initial profile from each daily beach profile. Two erosive perturbations can be observed regarding the location of the shoreline and the end of the terrace, respectively, ~60 m and ~100 m from camera location. These perturbations are also observed in Figure 4c on the inter-annual scale with, respectively -0.3 m/year for shoreline position and -0.2 m/year for the position of the end of the terrace, for the study period 2013 to 2016. By removing respective trends, a negative correlation of 41 % is obtained at the monthly scale. During the erosive phase June-July-August (JJA) the width of the terrace seems to increase, whereas it decreases during accretive phase December-January-February (DJF).

Looking in Figures 2 and 4, the terrace width is small during the austral summer period (December-January-February) when wave energy is low, while it is large during the winter period (June-July-August) when wave energy is high. The erosive shoreline phase therefore corresponds to an accretive terrace phase and the accretive shoreline phase corresponds to an erosive terrace phase.

#### **4. Conclusion**

Regarding the regional wave climate in West and Central Africa, important morphological beach changes occur with high wave energy conditions, corresponding to  $H_S$  values. The region is under the influence of both north and south Atlantic climate dynamics and local generated wind-waves, leading to such different responses in the coastal environments as observed in this study. Kribi beach is less affected by energetic swells, coming from the South Atlantic, modulated by SAM (average  $H_S \sim 0.9$  m), but terrace width seems to be similar to Grand Popo. Seasonal shoreline variation is the smallest compared to Grand Popo and Mbour. The Mbour site presents a typical impact of both north and south Atlantic forcing, with important changes in the wave direction. However, this needs to be confirmed by field measurements. Grand Popo site is characterized by a typical  $H_S$ -terrace width configuration, leading to a particular variability in shoreline position. The regional network installed in West and central Africa is therefore important for monitoring both hydrodynamic and near-shore morphological process.

The temporal correlations between three parameters derived from video image analysis were investigated at Grand Popo, Benin with the following result:  $H_S$  and shoreline position was negatively correlated and the shoreline position was also negatively correlated with the position of the end of the terrace, therefore to the terrace width as well. When high energetic wave conditions occurs (June-July-August period for Grand Popo), the wave energy combined with the sea level are sufficient to induce beach-face erosion and the retreat of the shoreline. An increase of the terrace width is observed, probably due to eroded sediment (from the beach face) that is trapped between the incident waves and the swash zone. This leads to a wider dissipative surf zone. When incident wave energy decreases, dissipation occurs along the extension of the terrace. The shoreline moves offshore due to onshore transport sediments from the terrace, resulting in a decreasing of terrace width. During austral winter (June-July-August), the shoreline retreat is even more significant at high tide when the beach face is most affected. These observations indicate the effect of terrace on event and seasonal scales in a typical intermediate to reflective beach as Grand Popo.

#### **Acknowledgements**

This publication was made possible through support provided by the IRD. We would like to express our gratitude to JEAI-RELIFOME (Jeune Equipe Associée à l'IRD) for its financial and technical supports in maintaining the video systems. The Grand Popo experiment was supported by French INSU/CNRS EC2CO-LEFE/IRD, UNESCO co-chair ICMPA (UNESCO co-chair ) of Université d'Abomey Calavi, Benin. We are indebted to the "Forces Navales" of Benin at Grand Popo and the "Hôtel Palm Beach" at Kribi for their logistic support during field experiments and for allowing the installation of permanent video systems in their premises. Thanks are due to Elodie Kestenare for processing ERA-Interim data. We acknowledge use of the ECMWF ERA Interim dataset ([www.ECMWF.Int/research/Era](http://www.ECMWF.Int/research/Era)).

## References

- Abessolo Ondo, G., Almar, R., Kestenare, E., Bahini, A., Houngue, G. H., Jouanno, J., Du Penhoat, Y., Castelle, B., Melet, A., Meyssignac, B., Anthony, E. J., Laibi, R., Alory, G., Ranasingue, R., 2016. Potential of Video Cameras in Assessing Event and Seasonal Coastline Behaviour: Grand Popo, Benin (Gulf of Guinea). *Journal of Coastal Research*, SI 75: 442-446.
- Abessolo Ondo, G., Bonou, F., Tomety, F. S., Du Penhoat, Yves, Perret, C., Degbe, C. G. E., Almar, R., 2017. Event to seasonal and inter-annual coastal evolution at Grand Popo, Benin. *Water*, (submitted).
- Almar, R., Senechal, N., Bonneton, P., Roelvink, J. A., 2008. Wave celerity from video imaging: validation with in-situ Pre-ECORS data. *Proc. I. C. C. E.* 1 (5), 661–673.
- Almar, R., Cienfuegos, R., Catalán, P. A., Birrien, F., Castelle, B. and Michallet, H., 2011. Nearshore bathymetric inversion from video using a fully non-linear Boussinesq wave model. *Journal of Coastal Research*, SI 64: 20 – 24.
- Almar, R., Ranasinghe, R., Catalan, P. A., Senechal, N., Bonneton, P., Roelvink, D., Bryan, K. R., Marieu, V., and Parisot J. P., 2012a. Video-based detection of shorelines at complex meso-macro tidal beaches. *Journal of Coastal Research*, 28(5): 1040-1048.
- Almar, R., Cienfuegos, R., Catalan, P. A., Michallet, H., Castelle, B., Bonneton, P., and Marieu, V., 2012b. A new breaking wave height direct estimation from video. *Coastal Engineering*, 61: 42-48.
- Almar, R., Bonneton, P., Michallet, H., Cienfuegos, R., Ruessink, G. and Tissier, M., 2013. On the use of the radon transform in studying nearshore wave dynamics. *Coastal Dynamics 2013*, 73-82.
- Almar, R., Honkonnou, N., Anthony, E. J., Castelle, B., Senechal, N., Laibi, R., Mensah-Senoo, T., Degbe, G., Quenum, M., Dorel, M., Chuchla, R., Lefebvre, J. P., Du Penhoat, Y., Laryea, W. S., Zodehougan, G., Sohoun, Z., Addo, K. A., Ibaceta, R., Kestenare, E., 2014. The Grand Popo beach 2013 experiment, Benin, West Africa: from short timescale processes to their integrated impact over long-term coastal evolution. *Journal of Coastal Research*, SI 70, 651-656.
- Almar, R., Kestenare, E., Reyns, J., Jouanno, J., Anthony, E.J., Laibi, R., Hemer, M., Du Penhoat, Y., Ranasinghe, R., 2015. Response of the Bight of Benin (Gulf of Guinea, West Africa) coastline to anthropogenic and natural forcing, Part1: Wave climate variability and impacts on the longshore sediment transport. *Continental Shelf Research*, Vol 110, 48-59.
- Almar, R., Larnier, S., Castelle, B., Scott, T., Floch, F., 2016a. On the use of the Radon transform to estimate longshore currents from video imagery. *Coastal Engineering*, 114: 301–308.
- Almar, R., Almeida, P., Blenkinsopp, C., and Catalan, P., 2016b. Surf-swash interactions on a low-tide terraced beach. *Proceedings of the 14th International Coastal Symposium* (Sydney, Australia). *Journal of Coastal Research*, Special Issue, 75, 348-352.
- Angnuureng, D. B., Almar, R., Addo, K. A., Castelle, B., Senechal, N., Laryea, S. W., Wiafe, G., 2016. Video Observation of Waves and Shoreline Change on the Microtidal James Town Beach in Ghana. *Journal of Coastal Research*, SI 75: 1022-1026.
- Aarninkhof, S.G. J.; Turner, I.L.; Dronkers, D.T.; Caljouw, M. and Nipius, L., 2003. A video-base technique for mapping intertidal beach bathymetry. *Coastal Engineering*, 49 (4), 275–289
- Ba, A. and Senechal, N., 2013. Extreme winter storm versus Summer storm: morphological impact on a sandy beach. *Journal of Coastal Research*, SI 65: 648-653.
- Bergsma, E.W.J., Conley, D.C., Davidson, M.A. and O'Hare, T.J., 2016. Video-based nearshore bathymetry estimation in macro-tidal environments. *Marine Geology*, 374: 31–41.
- Birrien, F., Castelle, B., Marieu, V., Dubarbier, B., 2013. On a data-model assimilation method to inverse wave-dominated beach bathymetry using heterogeneous video-derived observations. *Ocean Engineering*, 73: 126–138.
- Boak, E. H., Turner, I. L., 2005. Shoreline Definition and Detection: A Review. *Journal of Coastal Research*, 21(4): 688-703.
- Castelle, B., Marieu, V., Bujan, S., Splinter, K. D., Robinet, A., Sénéchal, N., Ferreira, S., 2015. Impact of the winter 2013–2014 series of severe Western Europe storms on a double-barred sandy coast: Beach and dune erosion and megacusp embayments. *Geomorphology*, 238, 135–148.
- Di Paola, G., Aucelli, P. P. C., Benassai, G., Rodriguez, G., 2014. Coastal vulnerability to wave storms of Sele littoral plain (southern Italy). *Nat Hazards*, 71:1795–1819.
- Hanson, H., Larson, M., Kraus, N. C., 2010. Calculation of beach change under interacting cross-shore and longshore processes. *Coastal Engineering* 57, 610–619. doi:10.1016/j.coastaleng.2010.02.002
- Hoggart, S.P.G., Hanley, M.E., Parker, D.J., Simmonds, D.J., Bilton, D.T., Filipova-Marinova, M., Franklin, E.L., Kotsev, I., Penning-Rowsell, E.C., Rundle, S.D., Trifonova, E., Vergiev, S., White, A.C., Thompsona, R.C., 2014. The consequences of doing nothing: The effects of seawater flooding on coastal zones. *Coastal Engineering*, 87: 169–182.

- Holland, K. T., Holman, R.A. and Lippmann, T.C., 1997. Practical use of video imagery in near-shore oceanographic field studies. *IEEE J. Oceanic Engineering*, 22(1): 81-92.
- Holman, R.A. and Stanley, J., 2007. The history and technical capabilities of Argus. *Coastal Engineering*, 54: 477–491.
- Laibi, R., Anthony, E., Almar, R., Castelle, B., Senechal, N., Kestenare, E., 2014. Longshore drift cell development on the human-impacted Bight of Benin sand barrier coast, West Africa. *Journal Of Coastal Research*, SI 70, 78-83.
- Larson, M., Hoan, L. X., Hanson, H., 2010. Direct formula to compute wave height and angle at incipient breaking. *Journal of Waterway, Port, Coastal and Ocean Engineering*, 136/2, 119-122.
- Masselink, G., Scott, T., Russel, P., Davidson, M. A., Conley, D. C., 2015. The extreme 2013/2014 winter storms: hydrodynamic forcing and coastal response along the southwest coast of England. *Earth Surface Processes and Landforms*.
- Osorio, A.F., Medina, R., Gonzalez, M., 2012. An algorithm for the measurement of shoreline and intertidal beach profiles using video imagery: PSDM. *Computers and Geosciences*, 46: 196–207.
- Plant, N.G., Aarninkhof, S.G.J., Turner, I.L., and Kington, K.S., 2007. The performance of shoreline detection models applied to video imagery. *Journal of Coastal Research*, 23(3), 658–670
- Postacchini, M. and Brocchini, M., 2014. A wave-by-wave analysis for the evaluation of the breaking-wave celerity. *Applied Ocean Research*, 46: 15–27.
- Quinn, N., Lewis, M., Wadey, M. P. and Haigh, I. D., 2014. Assessing the temporal variability in extreme storm-tide time series for coastal flood risk assessment. *Journal of Geophysical Research: Oceans*, 119: 4983–4998, doi:10.1002/2014JC010197.
- Sembiring, L., Dongeren, A., Winter, G., Ormond, M., Briere, C. and Roelvink, D., Nearshore bathymetry from video and the application to rip current predictions for the Dutch Coast. *Proceedings 13th International Coastal Symposium (Durban, South Africa)*, *Journal of Coastal Research*, Special Issue No. 70: 354-359, ISSN 0749-0208.
- Senechal, N., Coco, G., Castelle, B. and Marieu, V., 2015. Storm impact on the seasonal shoreline dynamics of a meso- to macrotidal open sandy beach (Biscarosse, France). *Geomorphology*, 228: 448–461.
- Shimura, T., Mori, N. and Mase, H., 2013. Ocean Waves and Teleconnection Patterns in the Northern Hemisphere. *Journal Of Climate*, 26, 8654-8670. DOI: 10.1175/JCLI-D-12-00397.1
- Splinter, K. D., Turner, I. L., Davidson, M. A., Barnard, P., Castelle, B. and Oltman-Shay, J., 2014, A generalized equilibrium model for predicting daily to inter-annual shoreline response. *Journal Of Geophysical Research, Earth Surf.*, 119, 1936–1958, doi:10.1002/2014JF003106.
- Sterl, A., Caires, S., 2005. Climatology, variability and extrema of ocean waves– the web-based KNMI/ERA-40 Wave Atlas. *International Journal Climatology* 25, 963–977.
- Stive, M. J. F., Aarninkhof, S. G. J., Hamm, L., Hanson, H., Larson, M., Wijnberg, K. M., Nicholls, R. J., Capobianco, M., 2002. Variability of shore and shoreline evolution. *Coastal Engineering* 47, 211-235..
- Stive, M., 2004. How important is global warming for coastal erosion? *Climate Change*, 64, 27–39.
- Tano, R.A., Aman, A., Kouadio, K. Y., Toualy, E., Ali, K.E. and Assamoi, P., 2016. Assessment of the Ivorian Coastal Vulnerability. *Journal Of Coastal Research*, 32, 6, 1495–1503.
- The Wamdi Group, 1988. The WAM model- a third generation ocean wave prediction model. *Journal of Physical Oceanography*, 18, 1775–1810.
- Touili, N., Baztan, J., Vanderlinden, J. P., Kane I. O., Diaz-Simal, P., Pietrantoni, L., 2014. Public perception of engineering-based coastal flooding and erosion risk mitigation options: Lessons from three European coastal settings. *Coastal Engineering*, 87: 205–209.
- Uunk, L., Wijnberg, K.M., Morelissen, R., 2010. Automated mapping of the intertidal beach bathymetry from video images. *Coastal Engineering*, 57: 461–469.

# Appendix III : Réponse d'une plage à terrasse face aux variations intra-saisonniers régionales du niveau de la mer

XVèmes Journées Nationales Génie Côtier – Génie Civil La Rochelle, 29 au  
31 mai 2018, DOI:10.5150/jngcgc.2018.016, Editions Paralia CFL, disponible  
en ligne – <http://www.paralia.fr> – available online



## Réponse d'une plage à terrasse face aux variations intra-saisonniers régionales du niveau de la mer

Grégoire ABESSOLO ONDOA<sup>1,2</sup>, Rafael ALMAR<sup>1</sup>, Bruno CASTELLE<sup>3</sup>,  
Magnus LARSON<sup>4</sup>, Julien JOUANNO<sup>1</sup>

1. LEGOS, OMP, UMR 5566 (CNES-CNRS-IRD-Université de Toulouse)  
14 Avenue Edouard Belin, Toulouse, France.  
*gregsolo55@yahoo.fr ; rafael.almar@ird.fr ; julien.jouanno@legos.obs-mip.fr*
2. Laboratoire d'Ecosystèmes et de Ressources Halieutiques, Université de Douala  
BP 2701, Douala, Cameroun.
3. EPOC, OASU, UMR 5805 (CNRS - Université de Bordeaux)  
Allée Geoffroy Saint-Hilaire – CS 50023 – 33615, Pessac Cedex, France.  
*bruno.castelle@u-bordeaux.fr*
4. Department of Water Resources Engineering (DWRE), Lund University  
John Ericssons väg 1, P.O. Box 118, S-221 00 Lund, Sweden.  
*magnus.larson@tvrl.lth.se*

### Résumé :

Les vagues et la marée constituent les deux principaux forçages utilisés dans la littérature pour comprendre la dynamique des plages à terrasse. Dans ce travail, l'influence des oscillations de niveau d'eau sur la réponse morphologique d'une plage à terrasse face aux événements de vagues est étudiée pour la première fois. Pour cela, les profils intertidaux et bathymétriques ont été extraits à partir de trois années et demie de données acquises par un système vidéo installé sur la plage à terrasse de Grand Popo au Bénin. Les variations intra-saisonniers régionales de niveau d'eau ont été extraites des données altimétriques de niveau de la mer en utilisant un filtre 21-91 jours. Les résultats montrent que l'impact des événements de vagues sur la morphologie de plage dépend de la hauteur d'eau sur la terrasse, donc des fluctuations intra-saisonniers de niveau, pouvant être associées aux ondes océaniques de Kelvin.

### Mots-clés :

Profil intertidal, Bathymétrie, Sédiments, Marée, Vagues, Niveau d'eau océanique, Acquisition vidéo, Altimétrie, Morphologie.

## Thème 2 – Dynamique sédimentaire

### 1. Introduction

La synthèse sur la variabilité morpho-dynamique des plages (WRIGTH & SHORT, 1984) permet de classer les plages sableuses en six états caractérisés par des morphologies différentes: dissipatif, intermédiaire à barre sableuse longitudinale uniforme, intermédiaire à barre en croissant, intermédiaire à barres sableuses transverses, intermédiaire à terrasse et réfléchif. Cette classification est utilisée pour décrire les différents états d'une plage en réponse au forçage hydrodynamique. Les plages à terrasse représentent un cas très particulier où on peut observer les trois différents régimes hydrodynamiques (réflectif, intermédiaire et dissipatif) à différents niveaux de marée le long du profil (MILES & RUSSEL, 2004). Sur le site de Nha Trang au Vietnam, ALMEIDA *et al.* (2017) ont observé que des vagues énergétiques couplées à un niveau haut de marée conduisent à une érosion du haut de plage, tandis qu'une accumulation de sédiments au bas de plage est observée pour des vagues moins énergétiques couplées à un niveau bas de marée. La marée est donc un facteur clé de la variabilité morphologique des plages à terrasse.

Contrairement aux levés classiques par DGPS, les systèmes d'acquisition vidéo formés d'une ou plusieurs caméras permettent de dériver à haute fréquence et de façon quasi-continue l'évolution de la morphologie de la plage sur des échelles temporelles relativement longues (interannuel à décennal). Les techniques d'acquisition vidéo ont été largement développées et permettent aujourd'hui d'acquérir un ensemble de paramètres morphologiques et hydrodynamiques du littoral. En utilisant 3 années et demi de données vidéo, ABESSOLO *et al.*, (2016) ont observé que, sur la plage à terrasse de Grand Popo, Bénin (Golfe de Guinée), la marée module l'évolution du trait de côte avec une contribution relative de 79 % par rapport aux vagues (hauteur significative  $H_s$ ) à l'échelle journalière tandis qu'à l'échelle mensuelle, le trait de côte est modulé par les vagues (contribution relative de 72 % par rapport à la marée). Dans l'Atlantique tropical, DING *et al.*, (2009) ont étudié la variabilité du niveau d'eau océanique en utilisant des données altimétriques. Celle-ci est dominée par un cycle saisonnier caractérisé par des composantes annuelle et semi-annuelle. En utilisant un filtre passe-bande 21 - 91 jours, POLO *et al.* (2008) ont extrait des propagations horizontales de variation de niveau d'eau dont les caractéristiques sont similaires à celles des ondes de Kelvin, se propageant de l'équateur en suivant la côte dans le Golfe de Guinée ( $\sim 2$  m/s). Alors que l'effet des ondes de Kelvin sur les upwellings côtiers de cette région a déjà été démontré (POLO *et al.*, 2008), ces oscillations d'ondes de Kelvin, couplées à un forçage local (vent, pression, etc.) sur une plage à terrasse pourraient modifier la hauteur d'eau  $h_b$  dans la zone de déferlement, et donc l'impact des vagues sur la morphologie du littoral. Notamment, une augmentation de  $h_b$  entrainerait une augmentation de l'énergie des vagues proche du bord et donc une augmentation de l'intensité des processus hydro-sédimentaires dans la zone du jet de

rive. La fluctuation du niveau d'eau serait donc une composante active du forçage océanique.

Dans ce travail, alors que les vagues et la marée sont classiquement les deux seuls forçages étudiés pour appréhender la dynamique des plages à terrasse, nous proposons d'évaluer l'influence des oscillations de niveau d'eau sur la morphologie intertidale et bathymétrique d'une plage à terrasse dans un environnement à forte variabilité saisonnière de niveau d'eau (Golfe de Guinée). Cette influence est évaluée en étudiant l'impact des événements extrêmes de  $H_s$  sur la réponse morphologique de plage, à partir de trois années et demie de données vidéo (Février 2013 à Juin 2016), durant des anomalies positives et négatives de niveau d'eau.

## **2. Matériel et méthodes**

### 2.1 Site d'étude

La plage de Grand Popo (6,2°N – 1,7°E) au Bénin se trouve dans la Baie du Bénin du Golfe de Guinée (figures 1.a et 1.b) et est soumise à l'action de la houle provenant de l'hémisphère Sud (45°-60°) et du vent généré localement dans la zone tropicale (5°N – 15°S). Les valeurs moyennes annuelles sont  $H_s \sim 1,4$  m,  $T_p \sim 9,2$  s, avec une orientation S-SO et un marnage relatif  $RTR \sim 1$  conformément aux données ERA-Interim (ALMAR *et al.*, 2014). Cette plage est du type intermédiaire à réfléchif avec une terrasse à marée basse uniforme le long de la côte et un haut de plage réfléchif avec une pente  $\sim 0,15$ . Ce site est micro-tidal : 0.3 à 1.8 m de marnage respectivement en mortes et vives eaux. POLO *et al.* (2008) ont montré la propagation d'ondes océaniques côtières intra-saisonnières qui remontent la côte de l'équateur jusqu'à 10°N – 15°N, via le Golfe de Guinée, avec des amplitudes crête à crête  $\sim 10$  cm sur les côtes d'Afrique de l'Ouest. Cette côte est aussi caractérisée par une forte saisonnalité de l'anomalie du niveau d'eau océanique (DING *et al.*, 2009), en réponse à des modes de bassin forcé par le vent et impliquant propagation et réflexion d'ondes de Kelvin et de Rossby saisonnières.

### 2.2 Données morphologiques vidéo

En Février 2013, un système vidéo a été installé au sommet de la tour d'un bâtiment de la Marine Béninoise à Grand Popo (ALMAR *et al.*, 2014). Les lignes d'eau sont extraites des images moyennées en utilisant la méthode "Minimum Shoreline Variability" (ALMAR *et al.*, 2012). Les profils intertidaux journaliers sont obtenus en interpolant les positions moyennées des lignes d'eau à plusieurs niveaux de marée. Les données de marée ont été extraites du modèle FES2014 (LYARD *et al.*, 2016). Les profils bathymétriques ont été obtenus en appliquant la méthode d'inter-corrélation spatio-temporelle et d'inversion bathymétrique décrite dans ABESSOLO *et al.* (2017). Les profils vidéo obtenus en combinant les profils intertidaux et bathymétriques, ont été filtrés (moyenne glissante sur 30 jours) afin d'éliminer le bruit. La comparaison des

## Thème 2 – Dynamique sédimentaire

profils vidéo aux relevés de terrain (figure 1.c) montre que l'erreur quadratique moyenne (RMSE) est de 0,1 m sur la terrasse et croit jusqu'à 2 m au-delà (ABESSOLO *et al.*, 2017). L'erreur temporelle associée à ces profils reste cependant difficile à quantifier. L'enjeu est la définition d'un critère de sélection des images adéquates pour la minimisation de cette erreur.

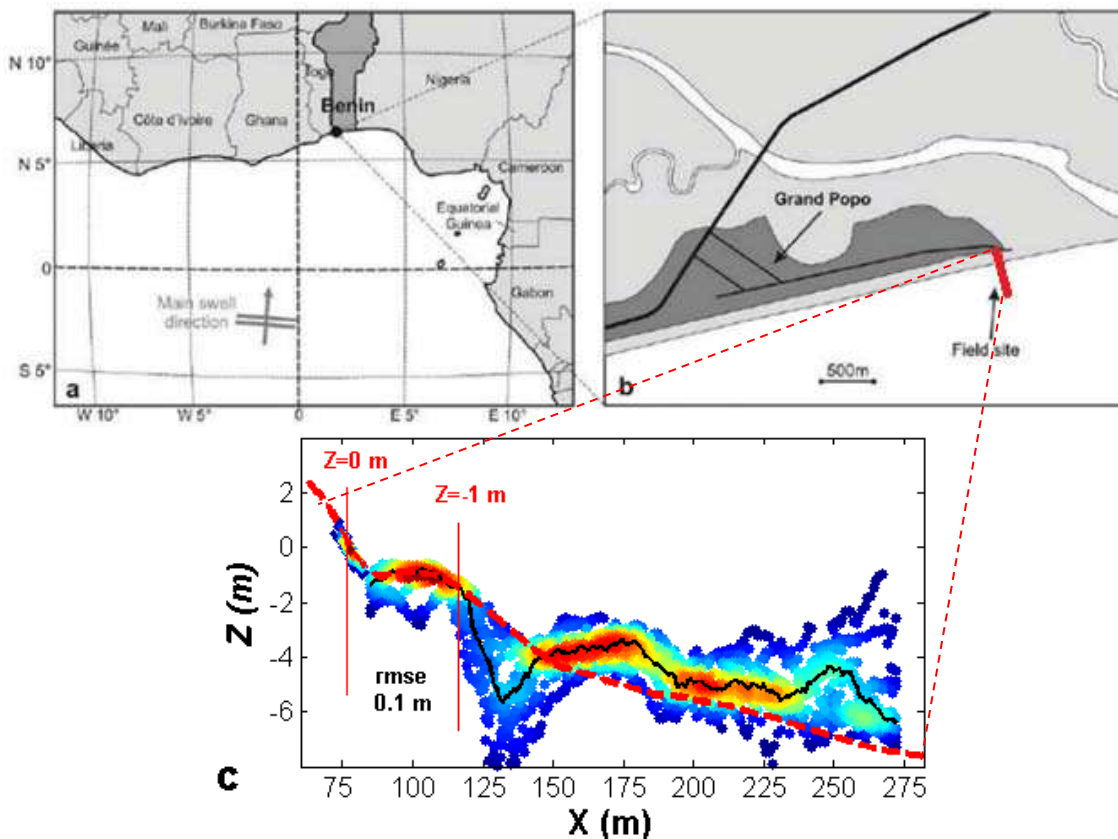


Figure 1 : (a) et (b) Site d'étude. (c) Profil de plage (trait rouge interrompue) obtenue durant la campagne Grand Popo 2014 et profil vidéo moyenné (trait noir). Les profils vidéo instantanés obtenus durant la campagne de mesure sont en densité de couleur. X et Z représentent respectivement la position par rapport à la caméra et la hauteur.

### 2.3 Données altimétriques de niveau d'eau

Les données journalières d'anomalie de niveau d'eau ont été extraites des produits "SSALTO/DUACS multimission gridded and delayed-time products", à  $1/4^\circ$  au large de la côte de Grand Popo, suffisamment loin pour minimiser les valeurs manquantes et suffisamment près pour que le signal soit cohérent avec le niveau d'eau à la côte. Les variations intra-saisonnières d'anomalie du niveau de la mer ( $SLA_i$ ) sont obtenues en utilisant un filtre passe-bande 21–91 jours (POLO *et al.*, 2008). Dans cette étude, on ne fera pas de discrimination entre les variations de niveau d'eau correspondantes aux ondes de Kelvin, celles dues à un forçage local (vent) ou celles dues à une activité

tourbillonnaire méso-échelle. Le quantile 70% a été utilisé pour la détection des évènements de niveau d'eau positifs et négatifs.

#### 2.4 Données hydrodynamiques

Les données de vagues ont été extraites de février 2013 à juin 2016 des produits de ré-analyses ERAInterim (1979 à nos jours) au point 6.25°N, 1.75°E. Celles-ci ont été ramenées empiriquement au point de déferlement (LARSON *et al.*, 2010). Le quantile 95% est généralement utilisé pour la détection des évènements extrêmes de  $H_s$  (ANGNUURENG *et al.*, 2017). En appliquant ce seuil ( $H_{s0} = 1,85$  m), les évènements extrêmes sur la plage de Grand Popo ( $H_s > H_{s0}$ ) ont une durée moyenne de 1,6 jour (ABESSOLO *et al.*, 2017). Cependant, dans notre étude, les données morphologiques vidéo et altimétriques de niveau d'eau sont journalières. Afin d'avoir une durée moyenne d'évènements de  $H_s$  de l'ordre de quelques jours, un seuil de détection a été fixé au quantile 70 %. Seuls les évènements d'une durée supérieure à deux jours, survenant durant un évènement de niveau d'eau positif, respectivement négatif, ont été moyennés pour obtenir un évènement d'ensemble, à comparer à la variation d'ensemble de la morphologie (analyse d'ensemble : ANGNUURENG *et al.*, 2017) durant des niveaux d'eau haut et bas. Le potentiel des vagues ( $H_s$ ) sur la morphologie (Y) a été estimé par  $\Delta H_s / \Delta Y$ .

### 3. Résultats

#### 3.1 Evolution du profil vidéo intertidal et bathymétrique

Les positions de ligne d'eau et de fin de la terrasse (profondeur à 1 m) journalières montrent une variabilité saisonnière (figures 2.c et 2.d). La terrasse étant considérée comme la partie du profil entre la ligne d'eau et la profondeur à 1 m, la largeur de la terrasse est respectivement maximale et minimale en Juillet-Aout et Janvier-Février. La figure 2.e montre les variations relatives au profil initial. On y observe une tendance érosive :  $\sim -1$  m/an pour la fin de la terrasse et  $\sim -0.3$  m/an pour la ligne d'eau. Une corrélation  $r \sim -0,74$  est obtenue pour des séries temporelles de ligne d'eau et de fin de terrasse, dans lesquelles les tendances respectives ont été retirées.

#### 3.2 Détection des évènements de niveau d'eau et de $H_s$ associés

Les figures 2.a et 2.b montrent les séries temporelles de  $H_s$  et de fluctuations intra-saisonnières de niveau d'eau. La durée moyenne des évènements détectés de  $H_s$  est de 3,8 jours pour un seuil de 1,58 m. Seuls les évènements de  $H_s$  correspondants à des oscillations significatives (quantile 70 % de niveau haut et bas) de  $SLA$  ont été pris en compte. On dénombre 19 évènements de  $H_s$  durant des oscillations positives (anomalie  $\sim + 3$  cm) et 20 durant des oscillations négatives (anomalie  $\sim - 3$  cm). A cause des

## Thème 2 – Dynamique sédimentaire

données vidéo manquantes, seuls 11 et 10 évènements de  $H_s$  respectivement ont été considérés.

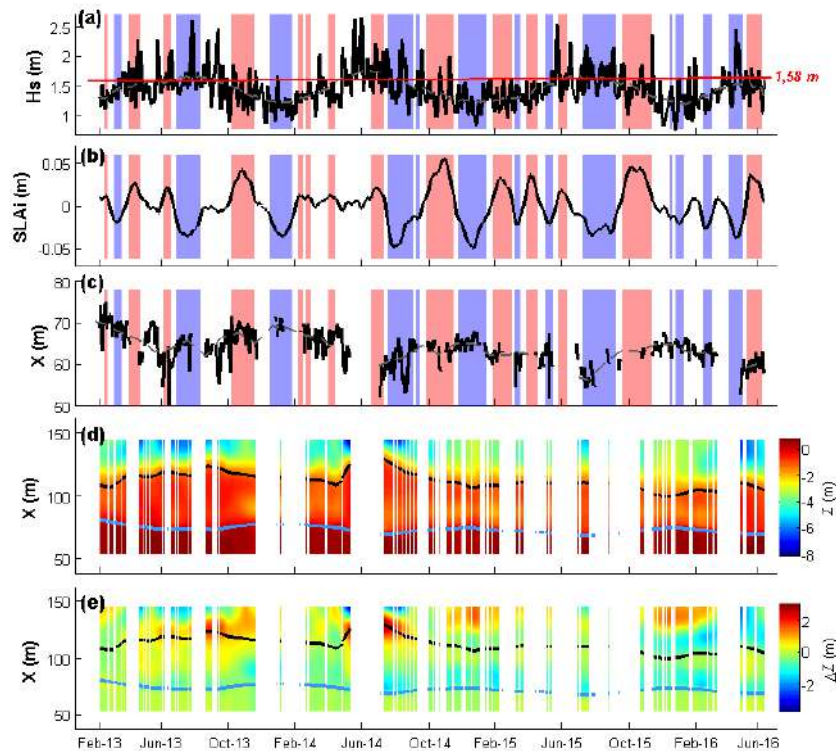


Figure 2. Séries temporelles de (a)  $H_s$  (ligne rouge : seuil de détection à 1,58 m), (b) variations intra-saisonniers du niveau de la mer au large, (c) ligne d'eau, (d) profils vidéo journaliers de plage et (e) perturbations calculées en retirant de chaque profil journalier le profil initial. Les bandes rouges et bleues correspondent respectivement aux variations intra-saisonniers positives et négatives du niveau d'eau (quantile 70 %). Les lignes bleue et noire représentent la ligne d'eau et la position à 1 mètre de profondeur, lissées avec une moyenne mobile sur 30 jours.

Les variations intra-saisonniers ( $\sim 10$  cm) devraient être plus fortes au bord du talus continental et notamment à la côte, avec un plateau très étroit dans le Golfe de Guinée ( $\sim 30$  km). La compréhension de la propagation de l'anomalie de niveau d'eau du large vers la côte reste cependant un enjeu scientifique (MELET *et al.*, 2016).

Le tableau 1 montre que la ligne d'eau et les évènements de  $H_s$  sont négativement corrélés durant des oscillations positives et positivement corrélés durant des oscillations négatives (tableau 1). Sur la figure 3, pour un niveau d'eau haut  $SLA_i > 0$ , on observe pour une variation événementielle  $\Delta H_s \sim 0,3m$  une érosion du haut de plage  $\Delta Y_0 \sim -3m$  et un engraissement de la terrasse  $\Delta Y_{-1} \sim +2m$ . Pour un niveau d'eau bas  $SLA_i < 0$ , une variation événementielle  $\Delta H_s \sim 0,3m$  conduit à un engraissement du haut de plage  $\Delta Y_0 \sim +5m$  et un recul de la fin de terrasse à 1 mètre de profondeur  $\Delta Y_{-1} \sim -5m$ . La terrasse

présente des variations avec un engraissement de la terrasse et du bas de plage lorsque  $H_s$  diminue pour des oscillations positives ou lorsque  $H_s$  croît durant des oscillations négatives. Lorsque  $H_s$  croît durant des oscillations positives, on note une forte érosion du haut de plage avec une accumulation de sédiments à la fin de la terrasse tandis tout le profil change très peu pour  $H_s$  et  $SLA_i$  faibles.

La figure 3 montre aussi que les évènements détectés de  $H_s$  sont plus intenses lorsque le niveau d'eau est bas, alors qu'ils sont moins intenses lorsque le niveau d'eau est haut.

*Tableau 1. Corrélation entre  $H_s$  et morphologie durant des oscillations de niveau d'eau ( $SLA_i$ ) positives et négatives.*

<i>Corrélation</i>	<i>H<sub>s</sub></i>	
	<i>SLA<sub>i</sub> &gt; 0</i>	<i>SLA<sub>i</sub> &lt; 0</i>
<i>Ligne d'eau Y<sub>0</sub></i>	<i>- 0.80</i>	<i>0.59</i>
<i>1 m – profondeur Y<sub>-1</sub></i>	<i>0.76</i>	<i>0.40</i>

Pour des niveaux haut et bas de  $SLA_i$ , le potentiel d'action des vagues sur la morphologie  $\Delta H_s/\Delta Y$  vaut respectivement -0,15 et 0,08, soit une forte dissipation des vagues sur la terrasse lorsque le niveau d'eau est bas. Sur la terrasse, l'action des vagues dépend quasiment du niveau d'eau :  $SLA$  et marée. La quantification de l'erreur temporelle associée au profil vidéo reste nécessaire pour valider ces observations.

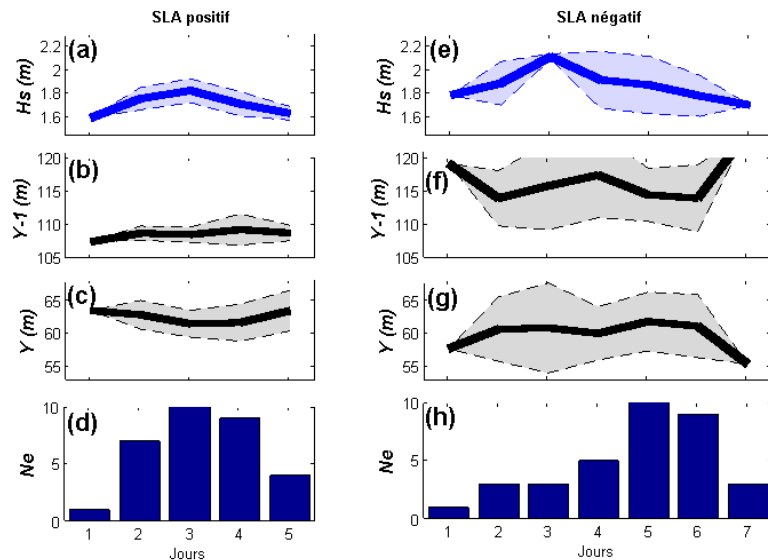


*Figure 3. Analyse d'ensemble respectivement pour des oscillations positives et négatives de variations intra-saisonniers de niveau d'eau : (a)-(e) : Evènements de  $H_s$ , (b)-(f) : Ligne d'eau  $Y$  (m), (c)-(g) : Position à 1 mètre de profondeur, (d)-(h) : Nombre d'évènements détectés  $Ne$ .*

## Thème 2 – Dynamique sédimentaire

Les résultats de cette étude montrent qu'une variation de quelques centimètres de la hauteur d'eau sur la terrasse pendant quelques jours peut modifier l'impact des vagues sur la morphologie de la plage.

### 4. Conclusions

Dans ce travail, l'influence des fluctuations intra-saisonnières de la mer sur l'évolution de la morphologie d'une plage à terrasse durant des événements de  $H_s$  a été étudiée. 21 événements de  $H_s$  (quantile 70% :  $H_s > 1,58$  m) ont été identifiés, dont 11 et 10 respectivement pour des oscillations positives (anomalie  $\sim + 3$  cm) et négatives (anomalie  $\sim - 3$  cm) de niveau d'eau. Les résultats obtenus montrent que la hauteur d'eau sur la terrasse est un facteur clé de la dynamique d'une plage à terrasse : (i) lorsque  $H_s$  croît durant des oscillations positives, le haut de plage s'érode tandis que les sédiments se déposent sur le bas de la terrasse, (ii) lorsque  $H_s$  croît durant les oscillations négatives ou lorsque  $H_s$  décroît durant les oscillations positives, les sédiments se déposent en bas de plage, (iii) lorsque  $H_s$  décroît pendant des oscillations négatives, la morphologie varie très peu. Cette étude suggère que sur ce type de littoral, en plus des conditions de vagues et de marée, les fluctuations de niveau d'eau, doivent être prises en compte pour diagnostiquer les évolutions morphologiques.

### 5. Références bibliographiques

- ABESSOLO O. G., ALMAR R., CASTELLE B., LARSON M., TOMEDI EYANGO, M. BONOU F., DU PENHOAT Y., CAMARA I., SALL M., ONGUENE R., ALORY G. (2017). *Development of a West and Central Africa regional video camera network to monitor coastal response to multiscale ocean forcing*. Proceedings of Coastal Dynamics, 11 – 16 June 2017, Helsingør, Danemark, pp 1540-1550.
- ABESSOLO O. G., ALMAR R., KESTENARE E., BAHINI A., HOUNGUE G.-H., JOUANNO J., DU PENHOAT Y., CASTELLE B., MELET A., MEYSSIGNAC B., ANTHONY E. J., LAIBI R., ALORY G., RANASINGHE W. M. R. J. B. R. (2016). *Potential of video cameras in assessing event and seasonal coastline behaviour: Grand Popo, Benin (Gulf of Guinea)*. J. Coast. Res. pp 442–446. <https://doi.org/10.2112/SI75-089.1>
- ALMAR R., HONKONNOU N., ANTHONY E. J., CASTELLE B., SENECHAL N., LAIBI R., MENSAH-SENOO T., DEGBE G., QUENUM M., DOREL M., CHUCHLA R., LEFEBVRE J.-P., DU PENHOAT Y., LARYEA W. S., ZODEHOUGAN G., SOHOU Z., ADDO K. A., IBACETA R., KESTENARE E. (2014). *The Grand Popo beach 2013 experiment, Benin, West Africa: from short timescale processes to their integrated impact over long-term coastal evolution*. Journal of Coastal Research, SI 70, pp 651-656. <https://doi.org/10.2112/SI70-110.1>
- ALMAR R., RANASINGHE R., CATALAN P. A., SENECHAL N., BONNETON P., ROELVINK D., BRYAN K. R., MARIEU V., PARISOT J. P. (2012). *Video-based*

*XV<sup>èmes</sup> Journées Nationales Génie Côtier – Génie Civil*  
*La Rochelle, 29 au 31 mai 2018*

- detection of shorelines at complex meso-macro tidal beaches.* Journal of Coastal Research, Vol. 28(5), pp 1040-1048. <https://doi.org/10.2112/JCOASTRES-D-10-00149.1>
- ALMEIDA L. P., ALMAR R., BLENKINSOPP C., MARTINS K., BENSILA R., DALY C. (2017). *Swash dynamics of a sandy beach with low tide terrace.* Proceedings of Coastal Dynamics, 11 – 16 June 2017, Helsingør, Danemark, pp 258-267.
- ANGNUURENG D. B., ALMAR R., SENECHAL N., CASTELLE B., ADDO K. A., MARIEU V., RANASINGHE R. (2017). *Shoreline resilience to individual storms and storm clusters on a meso-macrotidal barred beach.* Geomorphology, Vol. 290, pp 265-276. <https://doi.org/10.1016/j.geomorph.2017.04.007>
- DING H., KEENLYSIDE N. S., LATIF M., (2009). *Seasonal cycle in the upper equatorial Atlantic Ocean.* Journal of Geophysical Research, Vol. 114, c09016, <https://doi.org/10.1029/2009jc005418>
- LARSON M., HOAN L.X., HANSON H. (2010). *Direct formula to compute wave height and angle at incipient breaking.* J. Waterw. Port Coast. Ocean Eng, 136, pp 119-122. [https://doi.org/10.1061/\(ASCE\)WW.1943-5460.0000030](https://doi.org/10.1061/(ASCE)WW.1943-5460.0000030)
- LYARD F. H., CARRERE L., CANCELET M., BOY J. P., GEGOUT P., LEMOINE J. M. (2016). *The FES2014 tidal atlas, accuracy assessment for satellite altimetry and other geophysical applications.* Journal of Geophysical Research, Vol. 18, EGU2016-17693.
- MELET A., ALMAR R., MEYSSIGNAC B. (2016). *What dominates sea level at the coast: a case study for the Gulf of Guinea.* Ocean Dynamics, Vol. 66, pp 623–636. <https://doi.org/10.1007/s10236-016-0942-2>
- MILES J., RUSSEL P. (2004). *Dynamics of a reflective beach with low tide terrace.* Continental Shelf Research, Vol. 24(11), pp 1219-1247. <https://doi.org/10.1016/j.csr.2004.03.004>
- POLO I., LAZAR A., RODRIGUEZ-FONSECA B., ARNAULT S. (2008). *Oceanic Kelvin waves and tropical Atlantic intraseasonal variability: 1. Kelvin wave characterization.* J. Geophys. Res., Vol. 113, C07009. <https://doi.org/10.1029/2007JC004495>
- WRIGHT L.D., SHORT A.D. (1984). *Morphodynamic variability of surf zones and beaches: a synthesis.* Marine Geology, Vol. 56, pp 93-118. [https://doi.org/10.1016/0025-3227\(84\)90008-2](https://doi.org/10.1016/0025-3227(84)90008-2)

## *Thème 2 – Dynamique sédimentaire*



# Appendix IV : Modeling regional coastal evolution in the Bight of Benin, Gulf of Guinea, West Africa

In: Ping Wang, Julie D. Rosati, and Mathieu Vallee (eds), Proceedings of the 9th International Conference International Conference on Coastal Sediments 2019, Tampa/St. Petersburg, Florida, USA, 27 – 31 May 2019, <https://doi.org/10.1142/11391>, May 2019

## MODELING REGIONAL COASTAL EVOLUTION IN THE BIGHT OF BENIN, GULF OF GUINEA, WEST AFRICA

ONDOA GREGOIRE ABESSOLO<sup>1,2</sup>, MAGNUS LARSON<sup>3</sup>, RAFAEL ALMAR<sup>1</sup>,  
BRUNO CASTELLE<sup>4</sup>, EDWARD J. ANTHONY<sup>5</sup>, JOHAN REYNS<sup>6,7</sup>

1. LEGOS, OMP, UMR 5566 (CNRS/CNES/IRD/Université de Toulouse), 14 Avenue Edouard Belin, 31400, Toulouse, France. [gregsolo55@yahoo.fr](mailto:gregsolo55@yahoo.fr), [rafael.almar@ird.fr](mailto:rafael.almar@ird.fr).
2. Institute of Fisheries and Aquatic Sciences at Yabassi, University of Douala, BP 2701, Douala, Cameroun.
3. Department of Water Resources Engineering, Lund University, Box 118, S-221 00, Lund, Sweden. [magnus.larson@ivrl.lth.se](mailto:magnus.larson@ivrl.lth.se).
4. EPOC, OASU, UMR 5805 (CNRS - Université de Bordeaux), Allée Geoffroy Saint-Hilaire – CS 50023 – 33615, Pessac Cedex, France. [bruno.castelle@u-bordeaux.fr](mailto:bruno.castelle@u-bordeaux.fr).
5. Aix Marseille Univ., CNRS, IRD, INRA, Coll France, CEREGE, Aix-en-Provence, France. [anthony@cerege.fr](mailto:anthony@cerege.fr).
6. Department of Water Engineering, IHE-Delft, P.O. Box 3015, 2610 DA Delft, The Netherlands. [J.Reyns@unesco-ihe.org](mailto:J.Reyns@unesco-ihe.org).
7. Marine and Coastal Systems, Deltares, Delft, The Netherlands.

**Abstract:** The Bight of Benin coast is marked by the presence of three deepwater harbours which have affected the stability of the shoreline. In addition, several studies pointed out the overall diminution of sand supply due to the dams on Volta river channel and climate change effects. The combination of all these factors leads to a mixture of natural and artificial components affecting the coastline evolution in regional and long term scales. Here, we modeled the shoreline in the Bight of Benin, using the CASCADE model. The results show that the overall shape is well maintained and shoreline changes pretty well reconstructed. But, unresolved detailed information did not allowed to consider cross-shore sediment exchange and local deviations can be observed. However, the CASCADE model can be used to investigate regional and long term solutions for decisions-makers in the concerned countries.

### Introduction

In coastal management, a major issue is to understand the processes causing the variability of the coasts at different time scales. The damages and losses observed during extreme events and flooding are often a result of inadequate coastal management strategies. The long-term and large-scale adjustments of the shoreline to changes in wave climate, sea level rise, and sediment supply at open coasts can result into intensive erosion, threatening coastal societies, economical values, and valuable nature ecosystems (Ranasinghe 2016, Doody et al. 2004). Facing the increasingly intensive occupation of the coastal areas, it is of significant value to be able to predict the impact of such factors at several different time and space scales (French and Burningham 2009), leading to a

need of managing the coastal area regionally and not locally. The regional modeling that spans decades to centuries can be used to address the full consequences and interactions of engineering activities, as well as the wide-scale influence of natural processes and features (Larson, Rosati, and Kraus 2002).

In the Bight of Benin, West Africa, Gulf of Guinea, recent studies (Anthony et al. 2019, Giardino et al. 2018, Dada et al. 2015, Almar et al. 2015) have focused on understanding the observed disturbance of the shoreline stability over the last few decades. Three main observations have been made: (i) this wave-dominated coast is particularly exposed to erosion and flooding due to wave climate and sea level rise (Giardino et al. 2018; Almar et al. 2015); (ii) the stability of this coast has been strongly affected by the breakwaters at several deep-water harbors (Lome, Cotonou, and Lagos) and groins (Anthony et al. 2019; Giardino et al. 2018; Laibi et al. 2014); (iii) existing river dams and decrease in rainfall reduced the sediment supply from the Volta and Niger rivers (Anthony et al. 2019; Giardino et al. 2018). The prediction of the spatial and temporal responses of this coastal system is therefore important to decisions-makers in the concerned countries, which are low-income countries with 70% of the population in the coastal zone.

Several models have been developed for this purpose, encompassing in their description hundreds of kilometers of the coast (Larson, Kraus and Hanson 2002; Jiménez and Sánchez-Arcilla 2004; Hanson et al. 2008; Hoan et al. 2011; Ranasinghe et al. 2013). However, these models have typically simplified the representation of the cross-shore sediment exchange, employing sources and sinks with schematized values in time and space (Larson, Kraus and Hanson 2002). To improve the predictive capability of these models, longshore and cross-shore processes have been combined in a more rigorous manner, using physics-based formulations (Robinet et al. 2017; Vitousek et al. 2017). However, further simplifications are required as simulations are performed for large areas over long time periods (Larson et al. 2016). The regional coastal evolution model, known as CASCADE (Larson, Kraus and Hanson 2002) can be applied to stretches of coastline covering hundreds of kilometers, encompassing several barrier islands separated by inlets, including such phenomena as inlet creation, ebb- and flood-tidal shoal development, bypassing bars between beaches and inlets, channel dredging, regional trends in the shape of the coast, relative change in sea level, wind-blown sand, storms, periodic beach nourishment, and shore-protection structures such as groins and seawalls. Moreover, in the most recent development of the model, complex cross-shore material exchange can be included (Larson et al. 2016). These exchanges include dune erosion, wind-blown sand, overwash, berm erosion, and longshore bar development based on simplified physics-based relationships.

The overall objective of this work is to implement and develop the CASCADE model in the Bight of Benin, taking into account the main factors of shoreline variability of the area, to provide information for engineers, planners, and managers working on the decadal to century scale. First, background material and data were compiled for the study site with the purpose of calibrating the model. Second, the impact of the main harbors was considered and sediment transfer modeled. In a final step, the modelled shoreline at the end of the simulation was compared with the measured shoreline.

### **The Bight of Benin coast**

The Bight of Benin (Fig. 1) in the Gulf of Guinea, West Africa, is the embayment located between the Volta River delta in the west (Ghana) and the Niger River delta (Nigeria) in the east, exhibiting a mildly embayed sand barrier system (Anthony et al. 2019). The Volta River delta and the Niger River delta are among the three largest deltas in West Africa. The total length of the considered coastline is about 400 km, ranging between 1° to 5°E in longitude, and 5 to 7°N latitude.

The coast is a microtidal open-environment, facing the South Atlantic Ocean and exposed to a dominant long swell-wave component that travels far from mid- to high latitudes 45–60° in the South Atlantic and to the wind-sea component locally generated in the tropical band, 6°N to 15°S (Almar et al. 2015). This wave climate (mean values:  $H_s = 1.36$  m;  $T_p = 9.4$  s) drives an easterly longshore sediment transport ranging between 0 up to 1.2 million m<sup>3</sup>/year, depending on the location, according to Allersma and Tilmans (1993), Anthony and Blivi (1999) and Almar et al. (2015). Anthony and Blivi, (1999) identified the Volta River as the single most important fluvial sediment source for much of the sand barrier system of the Bight of Benin, with minor additional inputs (Anthony et al. 1996) from the Mono River in Benin. However, the Volta river discharge has been markedly reduced due to the decrease in rainfall over the Sahel since 1975 (Oguntunde et al., 2006), as well as the construction of the Akosombo dam between 1961 and 1965, approximately 100 km upstream from the sea (Anthony et al. 2019) and another smaller dam at Kpong, 24 km downstream of the Akosombo dam, constructed between 1977 and 1982. Three deepwater harbours have been constructed at the main cities on the bight coast: Lagos (1957), Cotonou (1962), and Lomé (1967). Recently, several groins have been built along the coast. An example is given by the field of nine groins of 100 m lengths and 20 m width over a distance of 3.5 km, constructed near the city of Aného (Togo) between 2012 and 2014.

The continental shelf is narrow, with widths of 15 to 33 km (Anthony et al. 2019; Giardino et al. 2018). Tides are semi-diurnal with a tidal range of

approximately 0.3 m and 1.8 m for neap and spring tides, respectively, whereas sea level rise is about +3.3 mm/year. The sediment size is medium-to-coarse sand, from 0.4 to 1 mm, with a median grain size  $D_{50} = 0.6$  mm.

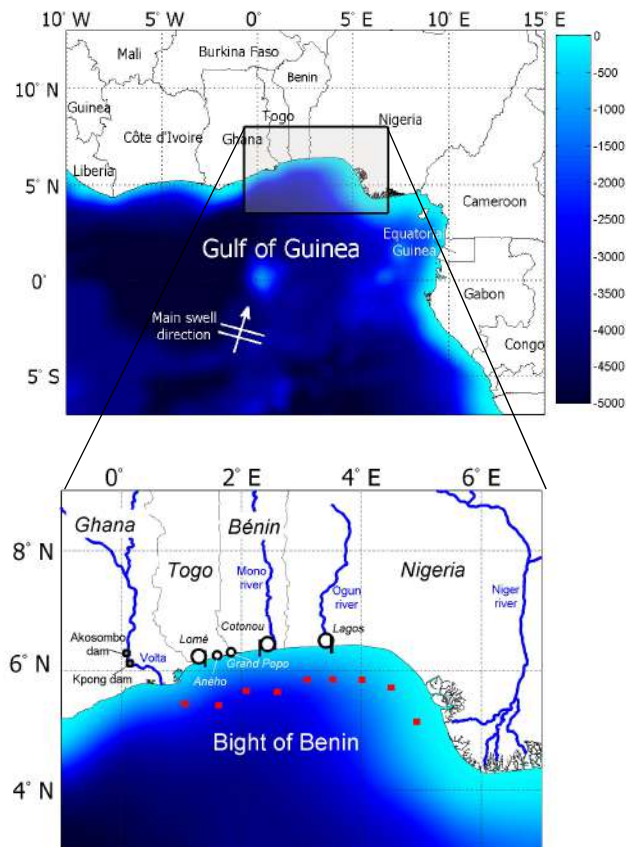


Fig. 1. The Bight of Benin in the Gulf of Guinea, with the tree main harbors at Lomé, Cotonou and Lagos. Red points stand for stations where wave characteristics were extracted.

**Methods**

***Observed Regional Shoreline and Wave data (1990-2015)***

Shoreline evolution in the Bight of Benin was determined using the LANDSAT 4-8 satellite images. Three images for each of the years 1990, 2000, 2005, 2010, and 2015 were chosen and downloaded from the USGS data portal Earth Explorer to offer large individual coverage as well as robust and accurate

determinations of shoreline change rates (accuracy 30 x 30 m). Rates of changes in shoreline position were digitized using the ArcMap extension module Digital Shoreline Analysis System (DSAS), version 4.3, coupled with ArcGIS®10. Details can be found in Anthony et al. 2019.

Hindcasted time series of waves, part of the ERA-Interim dataset (Sterl and Caires 2005), were extracted at seven different stations (see Fig. 1b) along the coast over the 1990-2015 period.

### ***Mathematical Modeling of Coastline Evolution: CASCADE***

The CASCADE model simulates coastal evolution at the regional scale covering 100s of km and several decades. A typical coastal setting to which CASCADE may be applied is barrier islands separated by inlets with and without jetties, where the sediment is transferred around the inlets through the ebb-shoal complex (Larson et al. 2002). Sediment sources and sinks that vary in time and space are included in the model as well as a wide range of cross-shore processes, including dune erosion, overwash, wind-blown sand, bar-berm material exchange, erosion during storms and sea level rise. Focus was on reproducing the evolution around the main harbors in the area including Lagos, Cotonou, and Lomé.

## **Results**

### ***Model setup and implementation***

CASCADE was implemented for a stretch of coastline along the Bight of Benin extending from a location just east of the Volta River to a location just west of Niger River. The modeled stretch is 374 km long, including the cities of Lome (Togo), Cotonou (Benin), and Lagos (Nigeria), which all have major harbors with structures that severely influence the sediment transport, causing downdrift erosion on a large scale (Anthony et al. 2019, Laibi et al. 2014). In addition, some of these harbors border lagoons or river mouths that further complicate the sediment transport and coastal evolution. However, in the present, initial phase of modeling, no effort was made to reproduce shoals and bars that might be present around the harbors, but they were described through a shore-perpendicular structures that block the sediment transport. After more information has been collected on the detailed morphology and its evolution around the harbors, it will be possible to add modeling of the shoals and bars, which will improve the description of the coastal evolution and lead to better resolution of the governing processes in these areas.

As a starting point in the modeling of this complex region, the boundaries of the modeling area were placed some distance away from the river deltas where historically (i.e., during the time period of observation, 1990-2015) no shoreline change was observed. This implies that a boundary condition corresponding to no longshore transport gradient can be employed, allowing sediment to be freely transported in and out over a boundary. Although such a boundary condition may work for the time period of study, simulations over longer periods, when significant changes to the system occur, may not reproduce the expected behavior. For example, major changes in the river sediment discharge that have occurred will in general not be described by the model with this type of boundary condition. A more extensive model approach should include the Volta and Niger River Deltas and the sediment discharge from major tributaries in the deltas.

The calculation grid employed a length step of 1000 m with a time step of 6 hr; the latter corresponded to the time resolution of the wave input. The positive x-axis is directed from east to west, implying that an observer standing on the beach facing the ocean consider transport to the right to be positive (westward). In total seven offshore wave stations were used as input with linear interpolation between the stations when wave conditions were assigned along the grid (input waves varied spatially). The typical water depth at the stations is 40 m, being more or less deep water. Since very limited information was available on the profile characteristics along the grid, the cross-shore sediment exchange routines were not activated, but the profile shape was kept constant. A median grain size of 0.5 mm was used throughout the grid; this was also due to lack of detailed information on the alongshore variation.

The simulations were performed with standard values in the model and comparison with the observed changes between 2000 and 2015 were performed. The shoreline from 1990 was not included in the simulation since this shoreline indicated significant general accumulation along most of the grid up until year 2000. This accumulation was typically in the range of 100 to 200 m; no clear mechanism has been identified so far that explains this seaward of movement of the shoreline. Thus, it could not be described by the model.

### ***Simulation results***

The simulated shoreline evolution from 2000 to 2015 is displayed in Fig. 2 together with the measured shoreline at the end of the simulation. The calculated and observed shoreline change between 2000 and 2015 is also shown, since the scale of the bight makes it difficult to appreciate the detailed evolution of the shoreline. The influence of the tree harbors at Lome, Cotonou, and Lagos are easily identified with distinct areas of erosion and accumulation. Although qualitatively the shoreline response predicted by the model agrees with the

observations, marked deviations occur locally and the magnitudes differ. Particularly the shoreline response around Lagos is not well resolved and the observed magnitude of seaward shoreline advance is much larger than the modeled. It is expected that more detailed information about morphology around the harbors will improve the simulations and form a basis for systematic model calibration and validation. The simulations also demonstrated that the model can maintain the overall shape of the bight, which tends to be difficult in this type of long-term simulations where diffusive processes smooth out shoreline gradients.

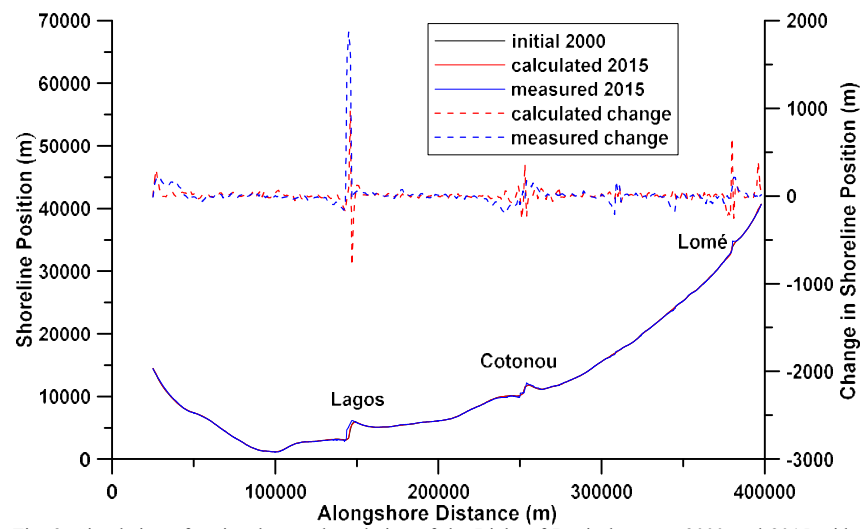


Fig. 2. Simulation of regional coastal evolution of the Bight of Benin between 2000 and 2015 with CASCADE. Calculated and measured shorelines at the end of the simulation period (2015) together with measured initial shoreline (2000). The calculated and measured shoreline change, from 2000 to 2015, is also displayed.

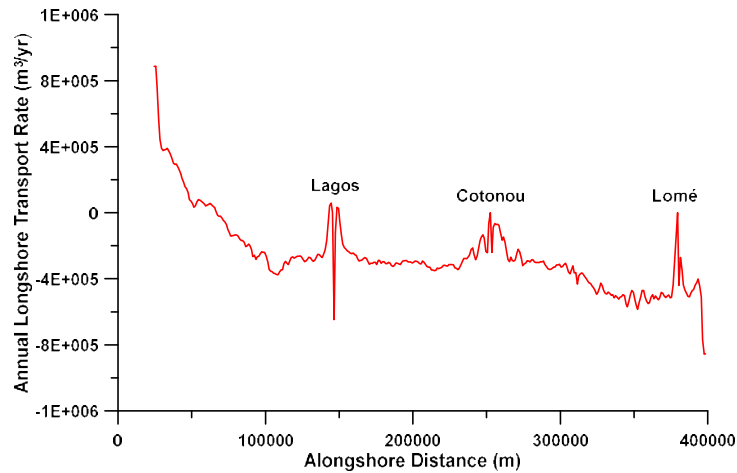


Fig. 3. Calculated annual net longshore transport rate based on the simulation between 2000 and 2015.

The derived mean annual transport rate along the bight is shown in Fig. 3 based on the simulation period 2000-2015. The large-scale transport pattern is predicted satisfactorily with the model calculation yielding local values in the expected range and in agreement with previous investigations (Almar *et al.* 2015). The net transport is to the east along most part of the bight, except for in the eastern part where the net transport is to the west (note that westward transport is taken positive, as previously explained).

### Conclusion

Several recent works observed show that, for the last thirty years, the shoreline in the Bight of Benin has been destabilized, because of the progressively diminishing sand supply from the Volta river downstream of the Akosombo dam, the presence of the three harbors and climate change. In this study, the main objective is to model the evolution of the coast in the Bight of Benin, Gulf of Guinea. The results of implementing the CASCADE model on the coast of the Bight of Benin shows that the overall shape of the bight coast is well maintained. However, local deviations are observed, particularly around Lagos harbor, as cross-shore sediment exchange routines were not activated. More detailed information about morphology and sediment supply around the harbors may improve the simulations. Moreover, it must be quite possible to derive the contributions of all the factors responsible of shoreline changes in the Bight of Benin, and therefore study what infrastructural solutions are adequate for this coast, in regional and long term scale.

## Acknowledgements

This publication was made possible through support provided by the IRD (French Institute of Research for Development).

## References

- Allersma, E., Tilmans, W.M.K., (1993). "Coastal conditions in West Africa – a review," *J. Ocean Coast. Manag.* 19, 199–240.
- Almar, R., Kestenare, E., Reyns, J., Jouanno, J., Anthony, E.J., Laibi, R., Hemer, M., Du Penhoat, Y., Ranasinghe, R., (2015). "Response of the Bight of Benin (Gulf of Guinea, West Africa) coastline to anthropogenic and natural forcing, Part1: Wave climate variability and impacts on the longshore sediment transport," *Continental Shelf Research*, 110, 48-59.
- Anthony, E.J., Almar, R., Besset, Reyns, J., Laibi, R., Ranasinghe, R., Abessolo Ondo, G., Vacchi, M., (2019). "Response of the Bight of Benin (Gulf of Guinea, West Africa) coastline to anthropogenic and natural forcing, Part 2: Sources and patterns of sediment supply, sediment cells, and recent shoreline variations," *Continental Shelf Research*, 173 (2019) 93–103.
- Anthony, E.J., Blivi, A.B., (1999). "Morphosedimentary evolution of a delta-sourced, driftaligned sand barrier-lagoon complex, western Bight of Benin," *Marine Geology* 158, 161–176.
- Anthony, E.J., Lang, J., Oyédé, L.M., (1996). "Sedimentation in a tropical, microtidal, wave-dominated coastal-plain estuary," *Sedimentology* 43, 665-675.
- Doody, P., Ferreira, M., Lombardo, S., Lucius, I., Misdorp, R., Niesing, H., Salman, A., Smallegange, M., (2004). "Living with Coastal Erosion in Europe: Sediment and Space for Sustainability: Results from the EUROSION Study," European Commission, Luxembourg, p. 38.
- French, J.R. and Burningham, H., (2009). "Coastal geomorphology: trends and challenges," *Prog. Phys. Geogr.* 33, 117-129.
- Giardino, A., Schrijvershof, R., Nederhoff, C.M., de Vroeg, H., Brière, C., Tonnon, P.-K., Caires, S., Walstra, D.J., Sosa, J., van Verseveld, W., Schellekens, J., Sloff, C.J., (2018). "A quantitative assessment of human interventions and climate change on the West African sediment budget,"

*Ocean Coastal Management*, 156, 249-265.

- Hanson, H., Larson, M., Kraus, N.C., (2010). "Long-term beach response to groin shortening, Westhampton Beach, Long Island, New York," *Proceedings of the 31st International Coastal Engineering Conference*, World Scientific.
- Hoan, L.X., Hanson, H., Larson, M., (2011). "A mathematical model of spit growth and barrier elongation," *Estuar. Coast. Shelf Sci.* 93 (4), 468–477.
- Jiménez, J., Sánchez-Arcilla, A., (2004). "A long-term (decadal scale) evolution model for microtidal barrier systems," *Coastal Engineering* 51 (8–9), 749–764.
- Laibi, R., Anthony, E., Almar, R., Castelle, B., Senechal, N., Kestenare, E., (2014). "Longshore drift cell development on the human-impacted Bight of Benin sand barrier coast, West Africa," *Journal of Coastal Research*, 70, 78–83.
- Larson, M., Palalane, J., Fredriksson, C., Hanson, H., (2016). "Simulating cross-shore material exchange at decadal scale. Theory and model component validation," *Coastal Engineering*, 116, 57-66.
- Larson, M. and Kraus, N.C., (2003). "Modeling regional sediment transport and coastal evolution along the Delmarva Peninsula". *Proceedings Coastal Sediments '03*, ASCE (on CD).
- Larson, M., Kraus, N.C., and Hanson, H. 2002. Simulation of regional longshore sediment transport and coastal evolution – The Cascade model. Proc. 28th Coastal Eng Conf., World Scientific Press.
- Larson, M., Rosati, J.D., and Kraus, N.C., (2002). "Overview of regional coastal processes and controls," Coastal and Hydraulics Engineering Technical Note CHETN XIV-4, U.S. Army Engineer Research and Development Center, Vicksburg, MS.  
<http://chl.wes.army.mil/library/publications/chetn/pdf/chetn-xiv4.pdf>.
- Oguntunde, P.G., Friesen, J., van de Giesen, N., Savenije, H.H.G., (2006). "Hydroclimatology of the Volta River Basin in West Africa: Trends and variability from 1901 to 2002," *Physics and Chemistry of the Earth*, 31, 1180–1188.

- Palalane J., Fredriksson C., Marinho B., Larson M., Hanson H., Coelho C. (2016). "Simulating cross-shore material exchange at decadal scale. Model application," *Coastal Engineering* 116, 26–41.
- Ranasinghe, R., (2016). "Assessing climate change impacts on open sandy coasts: a review," *Earth-Sci. Rev.*, 160, 320–332.
- Ranasinghe, R., Duong, T., Uhlenbrook, S., Roelvink, D., Stive, M. (2013). "Climate change impact assessment for inlet-interrupted coastlines," *Nat. Clim. Chang.*, 3, 83–87.
- Robinet, A. (2017). "Modélisation de l'évolution long-terme du trait de côte le long des littoraux sableux dominés par l'action des vagues," PhD thesis, Bordeaux.
- Sterl, A. and Caires, S. (2005). "Climatology, variability and extrema of ocean waves- the web-based KNMI/ERA-40 Wave Atlas," *Int. J. Climatol.*, 25, 963–977.
- Vitousek, S., Barnard, P.L., Limber, P, Li Erikson and Cole, B. (2017). "A model integrating longshore and cross-shore processes for predicting long-term shoreline response to climate change: CoSMoS-COAST," *Journal of Geophysical Research*, doi: 10.1002/2016JF004065.

# Appendix V : A deep learning approach for estimation of the nearshore bathymetry

In : Malvárez, G. et Navas, F. (eds.), Proceedings from the International Coastal Symposium (ICS) 2020 (Seville, Espagne). Journal of Coastal Research, 2020, Special issue no 95, p. 1011-1015. Coconut Creek (Floride),  
ISSN 0749-020

# A deep learning approach for estimation of the nearshore bathymetry

Rachid Benshila<sup>†</sup>, Grégoire Thoumyre<sup>†</sup>, Mahmoud Al Najar<sup>†</sup>, Grégoire Abessolo<sup>†</sup>, Rafael Almar<sup>†</sup>, Erwin Bergsma<sup>†</sup>, Guillaume Hugonnard<sup>§</sup>, Laurent Labracherie<sup>§\*</sup>, Benjamin Lavie<sup>§</sup>, Tom Ragonneau<sup>§</sup>, Ehouarn Simon<sup>§</sup>, Bastien Vieuble<sup>§</sup> and Dennis Wilson<sup>‡</sup>

<sup>†</sup>Laboratoire d'Etudes en Géophysique et Océanographie Spatiales  
Université Paul Sabatier  
Toulouse, France

<sup>§</sup>Institut National Polytechnique de Toulouse  
Toulouse, France

<sup>‡</sup>Institut Supérieur de l'Aéronautique et de l'Espace  
Toulouse, France

<sup>§\*</sup>ALTRAN  
Toulouse, France

www.cerf-jcr.org



www.JCRonline.org

## ABSTRACT

Benshila, R. ; Thoumyre, G. ; Al Najar, M. ; Abessolo, G. ; Almar, R. ; Bergsma, E. ; Hugonnard, G. ; Labracherie, L. ; Lavie, B. ; Ragonneau, T. ; Simon, E. ; Vieuble, B., and Wilson D. , 2020. A deep learning approach for estimation of the nearshore bathymetry. In : Malvarez, G. et Navas, F. (eds.), *Proceedings from the International Coastal Symposium (ICS) 2020* (Seville, Espagne). *Journal of Coastal Research*, numéro spécial no 95, p. 11-15. Coconut Creek (Floride), ISSN 0749-020

Bathymetry is an important factor in determining wave and current transformation in coastal and surface areas but is often poorly understood. However, its knowledge is crucial for hydro-morphodynamic forecasting and monitoring. Available for a long time only via in-situ measurement, the advent of video and satellite imagery has allowed the emergence of inversion methods from surface observations. With the advent of methods and architectures adapted to big data, a treatment via a deep learning approach seems now promising. This article provides a first overview of such possibilities with synthetic cases and its potential application on a real case.

**ADDITIONAL INDEX WORDS:** *Bathymetry, deep Learning, Big Data, morphodynamics*

## INTRODUCTION

With 40% of the world's population living within 100 km of a coast, the ability to understand, monitor and predict the evolution of the coastal topography is crucial. However, the lack of high-frequency bathymetric datasets remains a recurrent problem in coastal studies. Regular topographic surveys are required not only for the validation of hydro-sedimentary models but also for long-term forecasting. But these surveys via in-situ measurements are expensive and complex to deploy.

Video imagery techniques and methods (Holman and Stanley, 2007), which are cheaper and easier to implement, are an alternative to the massive and occasional deployment of measuring instruments in a highly variable coastal environment. Recent methodological advances (Almar et al, 2011) thus allow a complete estimation of the coastal system based on video observations and make it possible to evaluate the full hydrodynamics (wave height, period, speed, direction, currents). These quantities are bathymetric proxies that characterize the underlying beach morphology and allow its reconstruction. Recently, new opportunities have been opened up by transposing these video imagery techniques to satellite images (SPOT in Poupardin et al., 2016 ; Pléiades in Almar et al., 2019 ; and Sentinel-2 in Bergsma et al., 2019), allowing the treatment of wider areas (but with a lower acquisition frequency).

- they are based on Airy's linear theory and therefore do not give a clear picture of the evolution of the surf zone
- from a perspective of global application, they are not well adapted to large volumes of data, and processing time becomes prohibitive

Machine learning methods could be an alternative to remove these locks. To our knowledge, they are only rarely used in the coastal domain (see Goldstein et al 2018 for a review). From a methodological point of view, these problems seem well adapted to deep learning. Deep learning has so far shown impressive capabilities in image processing tasks, particularly in object classification, but it has only recently been applied to regression tasks from satellite images (Basu et al., 2015). The estimation of coastal systems using video or satellite imagery is therefore a specific application of deep learning methods, for which the development of new learning architectures and techniques may be necessary. The possibility of simulating different coastal scenarios is also possible in our case, by generating large datasets using numerical simulators, which are then used for training artificial neural networks. This paper investigates those capabilities. It is structured as follow: the general concept of deep learning is summarized briefly, before the presentation of the specifics used in this study. The results on academic test cases are presented before discussing their validity and potential application on real data.

## METHODS

### Background

John McCarthy, when introducing the term of artificial intelligence, defines it as "the science and engineering of making intelligent machines ". Actually, artificial intelligence is a generic term that encompasses all types of fields of study and

DOI: 10.2112/SI95-0XX.1 received Day Month Year; accepted in revision Day Month Year.

\*Corresponding author: rachid.benshila@legos.obs-mip.fr

©Coastal Education and Research Foundation, Inc. 2020

However, these direct bathymetric inversion methods still suffer from several limitations:

techniques that aim to enable man-made machines to perform tasks that would normally require human intelligence. It has many different forms and methods. Artificial neural networks are one of these forms: algorithms that draw inspiration from and are inspired by the human brain. They are intended to allow machines to perform tasks without being explicitly programmed. To do this, they find digital models in large amounts of data contained in vectors, into which all real-world data must be translated, whether images, texts, sounds or time series. Their use is multiple: regression, classification or data mining. In the case of bathymetric inversion, this is a regression problem. From a large number of input/output pairs (here bathymetry/wave height), the neural network must be able to build a prediction function.

### Video data

The goal of this study is to develop and train a neural network able to evaluate the bathymetry with video images as input. The type of data to deal with are typically timestacks derived from video at 2Hz, with an extension of 1Km off-shore, and averaged alongshore, see Fig. 1.

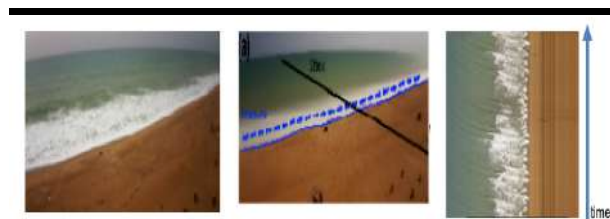


Figure 1. raw image (left), transect averaging (center), final time evolution (right)

### Data generation

For bathymetric estimation there are not enough observed data available to perform the learning phase. Synthetic data emulating video images are used. Two-dimensional x-z bathymetries are considered.

The training dataset are therefore created using two separate tools. First, a random bathymetric profile generator is used. The process of creating a bathymetric profile can be summarized as follows:

- specification of a random slope from a predefined distance, so that the maximum depth (2 km offshore) is between about 40 m and 100 m.
- addition of random sand bars with random parameters for height and width.
- check, and correct if necessary, that no offshore bumps are above sea level.

Around 2000 different random bathymetries are created. The bathymetries obtained are then used to perform simulations with the Boussinesq model FUNWAVE-TVD (Shi et al, 2012). The model is forced offshore with a Jonswap spectrum with random parameters. Each bathymetry is used with 10 different sets of random waves parameters. The whole process leads to 20,000 different simulations, each 10 minutes long (after spin-up). A

post-processing step is then needed to emulate video images from the water elevation computed by the model by cropping and normalizing them.

### Estimator part I: auto-encoder

The final dataset consists of two parts. On one hand the time-stacks of water elevation and on the other hand the corresponding field (pseudo-) truth, the bathymetry. First, the whole set of time-stacks needs to be processed to keep only the most relevant part of information. This first processing is based on a decomposition in two parts, an encoder and a decoder, that gathered are close to identity function. The first part, the encoder, reduce the dimension of the image, keeping the important features of the data (removing de facto this way the noise), see Fig. 2. Then the second part, the decoder, try to reconstruct as close as possible the original data from the encoded one. The idea of using a symmetric model decomposed in two parts, is to train both parts together, the auto-encoder, to use then the encoder part to pre-process data, reducing the input dimension and keeping only main features, before training a more complex neural network.

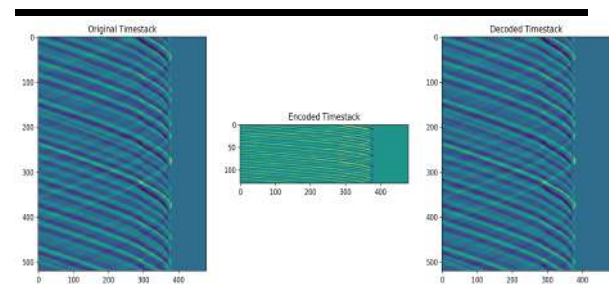


Figure 2. Auto-encoder: raw timestack (left), encoded (center), decoded (right)

This auto-encoder takes as input images covering a 480m transverse transect as explained above, for 600s, and returns a small reduced image on the time axis.

Using the trained encoder, a new data set with coded time intervals is created.

### Estimator part II: CNN

For the learning phase itself, the encoded dataset (associated to the corresponding bathymetries this time) feeds a convolutional network (hereafter CNN). Indeed, neural networks were originally composed of layers of neurons whose final output were used to build a decision function based on a vector of data. They are therefore ill-suited to images, whose transformation would result in a loss of two-dimensional information. The CNNs introduced by LeCun (1998) allow direct action on image matrices. The use of a CNN allows to reduce the complexity of the network and the number of free (trainable) parameters and avoid the use of a fully connected network where each neuron would be connected to all others, whose cost would be prohibitive. With a CNN, the final network

has also the appreciable property to be invariant for translation: a pattern can be detected regardless its position. To do so, pooling layers can be added. Fig. 3 shows the final CNN developed. This CNN is composed of 5 parts. First forth are identical parts: two bi-dimensional convolutions, one max-pooling and a dropout layer:

- the kernel of convolution is changed at each layer
- the max pooling layer act as subsampling layer: a group of values is gathered into its maximum.
- the dropout layer is a layer that takes out temporally a quarter of the training dataset

The combination of the weights of the trained encoder and CNN forms the bathymetric estimator (Fig. 4).

The best structure was found empirically, testing which combinations was best to predict the bathymetry. The conv2D layers use more and more (3, 3) kernels which improved the accuracy of the model, and same goes for (2,2) max-pooling. Then the dropout layers avoid the over-fitting of the network. Finally, the last part composed of a flattening layer to have the 1D shape of the expected output and 2 dense layers that lead to the final output. In term of practical implementation, *Keras* and *Tensorflow*, two python libraries, are used to create the neural networks. These libraries offer a very wide range of possibilities for building neural networks, from the number of layers already implemented to the possibility of adding your own functions/layers. This allow to create a robust architecture that can be adapted to any neural network model for this bathymetric regression problem. Training is performed on GPU.

**Post-processing**

Once the evaluation is done, a post-processing of the bathymetric estimate can be performed to smooth the result. The smoothing algorithm chosen is Savitzky-Golay (Savitzky, 1964), a digital filter that increase the accuracy of the data without distorting the signal trend.

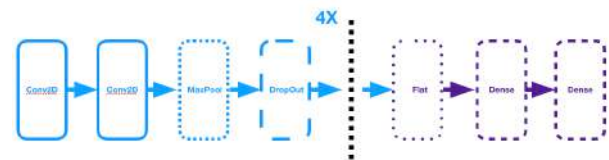


Figure 3. CNN detail

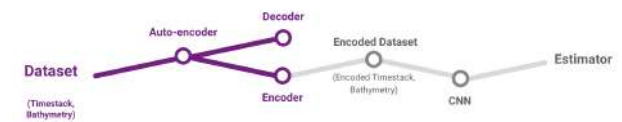


Figure 4. Global view for the full estimator

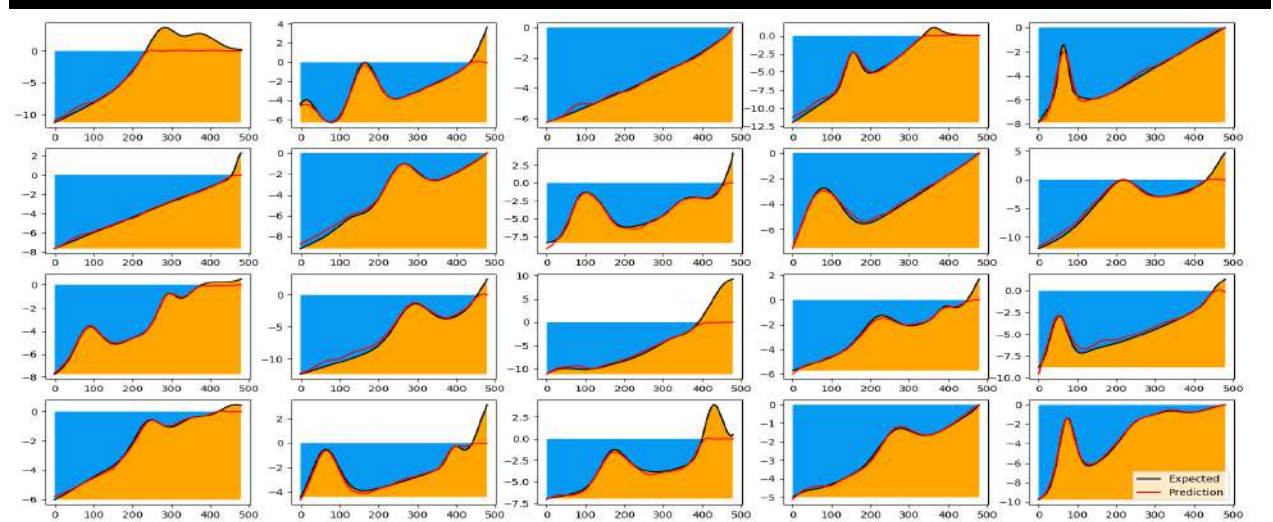


Figure 5. Estimation (in red) for various bathymetries

**RESULTS**

Once the network trained, tests are performed using synthetic time stacks (still generated with FUNWAVE-TVD) as an input, on various bathymetries. Bathymetric inversion from the elevation time stack, using the auto encoder and then the CNN, gives the results shown in Fig. 5.

The predicted bathymetry (in red) matches very well to the ground truth (in black), 87% of cases per thousand have an average vertical error of less than 20 cm. All bathymetry over the water is set to zero because there is no information about it in the time stack and only the underwater part is relevant for this study.

Note that in addition to all the parameters mentioned above to create both the neural networks and the dataset, number of

hyper-parameters needed to be tuned to get these results. First of all, all random parameters to generate bathymetries and wave conditions to get the most extensive training dataset. Then, the size of the data set, the number of layers or the set of layers, the loss function. All were empirically determined by multiple experiments. At the end, the optimal size of the data set to form the networks is about 20,000 synthetic cases. The most optimal loss function is a simple root mean square error function that best shows the vertical disparities between prediction and ground truth. In addition, the results are quite similar with a training on noisy time stacks (Gaussian noise with  $\sigma = 30\text{cm}$ , not shown) since it is mainly de-noised by the encoder. Another

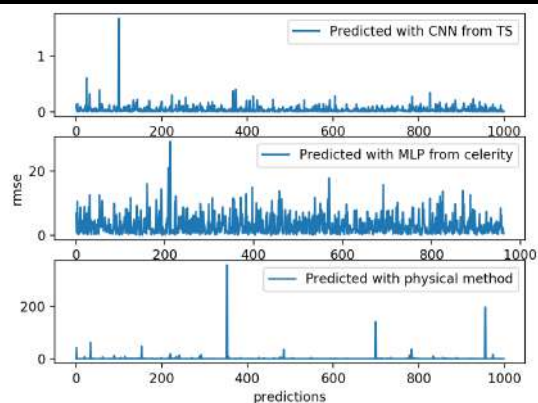


Figure 6. Root mean square error for the three different estimators

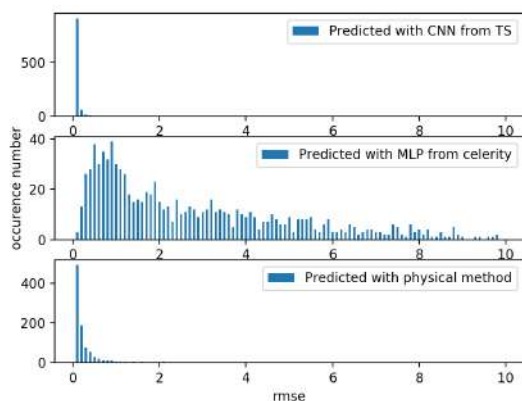


Figure 7. Occurrence of extreme errors

network (hereafter MLP, architecture of the network not showed) was also trained using celerity time stacks (still from synthetic data) instead of water elevation, to see if introducing more implicit physical information (inherently from the dispersion relationship) could improve the results. Comparison are performed between the first network (elevation based), the second one (celerity based) and a classical inversion method from celerity (Almar et al 2011). Results are presented Fig. 6 and 7. The CNN method is precise and reliable, the MLP is less precise but still reliable,

and the traditional method is not always reliable but precise when filtering out of the extreme cases. The difference between the two neural models is mainly explained that even if the information given to the MLP is the same data used for the standard bathymetry inversion method, there is less information in the celerity vector than in the elevation time stack itself.

## DISCUSSION

The results when dealing with a synthetic dataset show that deep learning is a promising method for bathymetric inversion. But what happens with real video images? A first attempt to use the former trained network is then performed, using real data from Grand Popo beach, in Benin, an intermediate Low Tide Terrace (LTT) to reflective beach, according to the classification proposed by Wright and Short (1984). Data acquisition is described in Abessolo et al, 2016.

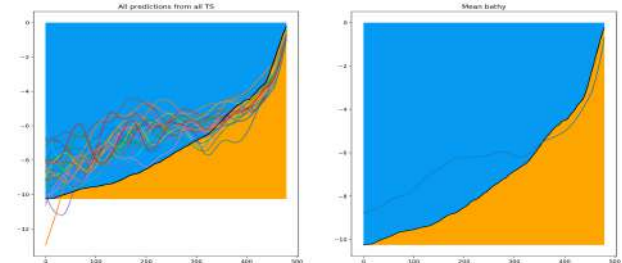


Figure 8. various bathymetry estimations (left) and mean (right)

The CNN is tested with different time stacks from different periods and wave conditions. Results Fig. 8 show that if the network succeeds to reconstruct the mean bathymetry when testing it with different times tacks, its accuracy is much lower than on synthetic dataset as summarized in Tab 1. One problem leading to this loss of accuracy is the extent of data covered by the training data set. The data set is created randomly, which can create a range of unrepresented cases. A solution to this problem could be to create a non-random data set, not fully exhaustive of course. This could be done by setting fixed values instead of ranges to create bathymetries and wave conditions. This would still lead to a huge data set (several hundred thousand data) that would require extensive training (and would certainly lead to excessive adaptation of the network).

Table 1. RMS for with synthetic data (2 left columns) and real (right)

Inversion Method	RMSE<0.2	RMSE>20	RMSE
CNN	87%	0%	2.4
MLP	6%	9%	7.3
Traditional	56%	11%	0.8

In the case of Grand Popo, the synthetic and actual data are not yet close enough, which explains the visible error in Fig. 8. The main difference comes from the white spots generated by wave breaking which is not really treated by the pre-treatment itself, but could be resolved using an optical model (Chickadel, 2003).

Another visible problem is the influence of wave reflection in synthetic cases, not in real dataset. This could be solved by processing the training dataset to extract and eliminate reflection prior to the training.

Other leads to follow could be to embed this approach into other methods. The bathymetric estimate from a trained neural network could be used as a first guess to emulate real observations and be integrated in an inversion system using data assimilation, such as the one developed by Wilson et al (2014). In this case, we may expect our bathymetry estimate from a wave time stacks to be more adapted to the assimilation scheme than the raw observations (Rodríguez-Fernandez, 2019).

Finally, the same kind of approach could be investigated to deal with satellite dataset. Such work is ongoing with a first example is shown Fig. 9. (Al Najar et al, in prep). However, methodological developments are needed to take into account the different properties of the data.

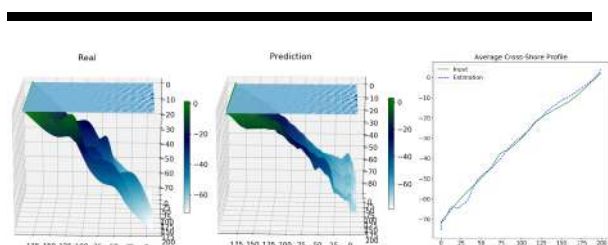


Figure 9. example of application to satellite data from Pleiades

## CONCLUSIONS

Deep learning algorithms are successfully applied to bathymetric reconstruction based on video images. Results on synthetic data achieve the same accuracy as more traditional methods and are more robust in the case of extreme errors. However, the improvement of results on real cases requires a better representation of the learning base. The potential is also high for application at a higher scale to satellite images.

## ACKNOWLEDGEMENTS

Computation have been performed at IDRIS supercomputing center under allocation A0050107298. Some were performed at CALMIP under project P19063. The authors also benefit from ENSEEIHT infrastructures.

## LITERATURE CITED

- Abessolo Ondo, G., and al, 2016. Potential of video cameras in assessing event and seasonal coastline behaviour: Grand Popo, Benin (Gulf of Guinea). *Journal of Coastal Research*, Special Issue 75, 442–446.
- Abdi, M.; and al, 2015. Tensorflow : Large-scale machine learning on heterogeneous systems. *Software available from tensorflow.org*.
- Almar, R.; Bergsma, E. W. , Maisongrande, P., and de Almeida, L.P.M, 2019. Wave- derived coastal bathymetry from satellite video imagery: A showcase with pleiades persistent mode. *Remote Sensing of Environment*, 231:111263, 2019.
- Almar, R.; Cienfuegos, R., Catalan, P., Birrien, F., Castelle, B., and Michallet, H., 2011. Nearshore bathymetric inversion from video using a fully non-linear Boussinesq wave model. *Journal of Coastal Research*. SI 64(1), 20-24.
- Almar, R. ; Michallet, H., Cienfuegos, R., Bonneton, P., Tissier, M. and G. Ruessink, 2014. On the use of the Radon Transform in studying nearshore wave dynamics. *Costal Engineering*.
- Al Najar, M. ; and Coauthors, 2019. Satellite Derived Bathymetry Using Deep Learning. *To be submitted to Coastal Morphodynamics*.
- Basu, S.; Ganguly, S., Mukhopadhyay, S., DiBiano, R., Karki, M. and Nemani, R., 2015. DeepSAT: a learning framework for satellite imagery. *Proceedings of the 23rd SIGSPATIAL international conference on advances in geographic information systems*
- Bergsma, E.W.J.; Almar, R., and Maisongrande, P., 2019. Radon-Augmented Sentinel-2 Satellite Imagery to Derive Wave-Patterns and Regional Bathymetry. *Remote Sensing*, vol. 11, p 1918.
- Chickadel, C.; Holman, R., Freilich, M., 2003. An optical technique for the measurement of longshore currents. *J. Geophys. Res.* 108. 10.1029/2003JC001774.
- Chollet, F.; and Coauthors, 2015. Keras. <https://keras.io>
- Holman, R.A; and Stanley, J., 2007. The history and technical capabilities of Argus. *Coastal Engineering*, vol 54
- Goldstein, E.; Coco, G., and Plant, N. G., 2018. A Review of Machine Learning Applications to Coastal Sediment Transport and Morphodynamics. *EarthArXiv*
- Le Cun, Y.; Boser, B., Denker, J.S., Henderson, D., Howard, R.E., Hubbard, W., and Jackel, L. D., 1998. Handwritten Digit Recognition with a Back-Propagation Network. *Proceedings of NIS*
- McCarthy, J., 2004. What is artificial intelligence? *Catholic University of America*
- Poupardin, A. ; Idier, D., de Michele, M., Raucoles, D. , 2016. Water Depth Inversion From a Single SPOT-5 Dataset. *IEEE Transactions on Geoscience and Remote Sensing*.
- Rodríguez-Fernández, N.; de Rosnay, P.; Albergel, C.; Richaume, P.; Aires, F.; Prigent, C.; Kerr, Y., 2019. SMOS Neural Network Soil Moisture Data Assimilation in a Land Surface Model and Atmospheric Impact. *Remote Sens.* 11, 1334.
- Savitzky A. ; and Golay, M.J.E. 1964. *Analytical Chemistry*, vol. 36, pp. 1627–1639.
- Shi, F., Kirby, J. T., Harris, J. C., Geiman, J. D., & Grilli, S. T., 2012. A high-order adaptive time-stepping TVD solver for Boussinesq modeling of breaking waves and coastal inundation. *Ocean Modelling*, 43–44, 36–51.
- Wilson, G.W. Özkan-Haller, ; H. T., Holman, R. A., Haller, M.C., Honegger, D. A. and Chickadel, C. C. , 2014. Surf zone bathymetry and circulation predictions via data assimilation of remote sensing observations. *JGR Oceans*.
- Wright, L.D.; and Short A.D, 1984. Morphodynamic variability of surf zones and beaches : A synthesis. *Marine Geology*, Vo 56, 93-118.

# **Appendix VI : Assessment of the Evolution of Cameroon Coastline: An Overview from 1986 to 2015**

**In: Almar, R.; Almeida, L.P.; Trung Viet, N., and Sall, M. (eds.), Tropical Coastal and Estuarine Dynamics. Journal of Coastal Research, 2018, Special Issue, No. 81, pp. 122–129. Coconut Creek (Florida), ISSN 0749-0208.**

## Assessment of the Evolution of Cameroon Coastline: An Overview from 1986 to 2015

Gregoire Abessolo Ondo<sup>†‡#\*</sup>, Raphael Onguéné<sup>§#</sup>, Minette Tomedi Eyango<sup>†±</sup>, Thomas Duhaut<sup>†</sup>, Crepin Mama<sup>##</sup>, Donatus B. Angnuureng<sup>&</sup>, and Rafael Almar<sup>‡</sup>



www.cerf-jcr.org

<sup>†</sup>LERH, EDSFA  
University of Douala  
Douala, Cameroon

<sup>‡</sup>LEGOS  
CNRS/IRD/CNES/UPS  
Toulouse, France

<sup>§</sup>IUT Douala  
University of Douala  
Douala, Cameroon

<sup>±</sup>ISH at Yabassi  
University of Douala  
Yabassi, Cameroon

<sup>†</sup>Laboratoire d'Aérodynamique  
CNRS/UPS  
Toulouse, France

<sup>&</sup>CCM  
University of Cape Coast  
Cape Coast, Ghana

<sup>#</sup>JEAI-RELIFOME  
University of Douala  
Douala, Cameroon



www.JCRonline.org

### ABSTRACT

Abessolo Ondo, G.; Onguéné, R.; Tomedi Eyango, M.; Duhaut, T.; Mama, C.; Angnuureng, B.D., and Almar, R., 2018. Assessment of the evolution of Cameroon coastline: An overview from 1986 to 2015. In: Almar, R.; Almeida, L.P.; Trung Viet, N., and Sall, M. (eds.), *Tropical Coastal and Estuarine Dynamics. Journal of Coastal Research*, Special Issue, No. 81, pp. 122–129. Coconut Creek (Florida), ISSN 0749-0208.

The coast of Cameroon is located at the bottom of the Gulf of Guinea with varied nearshore environments and oceanic forcing influenced by the presence of several islands. It is also the area of important river flows. Here, the global evolution of the Cameroonian coastline and hydrodynamic between 1986 and 2015 is investigated using satellite images and ECMWF EraInterim re-analysis wave data. Seven areas of important cross-shore changes have been identified with only one case of human-induced variation that corresponds to the construction of a new harbour at Kribi. This paper presents the results of using SYMPHONIE model with DOUALA26 configuration to assess the changes in Cameroon estuaries. The other areas are mainly located at the mouths of the rivers and at the entrance of Cameroon and Rio Del Rey estuaries. The results of the circulation model show that the convergence of Wouri, Dibamba river flows and littoral drift corresponds to the accumulation of sediments observed at "Souleyba", while the eroded area at "Cap Cameroun" corresponds to the estuary output current. This work provides an understanding of erosive or accretive coastal processes using barotropic currents modeling in estuaries.

**ADDITIONAL INDEX WORDS:** *Coastline, wave, nearshore currents, erosion, sand accumulation, river flows, altimetric observations, modelling oceanic circulation.*

### INTRODUCTION

Coastal areas are dynamic and complex multifactorial systems. A wide number of often conflicting human socio-economic activities occur in these areas. These include urbanisation, agriculture, tourism, recreation, industrial, port and shipping activities. The study of the vulnerability of the coastal environment is an important issue on global scale (Bosom and Jiménez, 2011; Tano *et al.*, 2016). The vulnerability is characterized by the susceptibility of a coastal area to the effects of either inundation or erosion (Gianluigi *et al.*, 2014) and depends on a large number of different nearshore processes. An increase in the occurrence and intensity of extreme events such as storms and heat waves associated with climate change and increasing anthropogenic pressure greatly increases the vulnerability of these already highly sensitive areas (Richards and Nicholls, 2009). The damages and losses observed during eroding and flooding events, reflect the absence or inadequate coastal management strategies or a lack of understanding about coastal processes (Hoggart *et al.*, 2014). In West Africa, several

studies have been carried out on the dynamics of coastal areas to assess its vulnerability (Almar *et al.*, 2014; Appeaning Addo *et al.*, 2008; Laibi *et al.*, 2014). The results have helped influence coastal policy formulation and promoted the development of sustainable management practices in coastal regions throughout the developed world. Almar *et al.* (2014) have demonstrated the importance of understanding at multi-scale (from one-time event to inter-annual) the causes of the dramatic erosion observed throughout the Bight of Benin. Studies have focused on the interaction between the strong littoral drift ( $\sim 500\,000\text{ m}^3\text{yr}^{-1}$ ) and human engineering works (Almar *et al.*, 2015; Laibi *et al.*, 2014). The impact of the sea level rise has been also evaluated (Melet, Almar, and Meyssignac, 2016). All these studies revealed the influence of climate change and storminess seasonality on the evolution of coastal areas. However, sustainable coastal management is rarely practiced in developing countries, one of the fundamental reasons for this being a general lack of reliable and accurate historic data on shoreline position.

In Central Africa, the available literature on the impacts of extreme events and sea level rise is still very scarce, because of the sparse or the lack of available data sets and suitable modeling tools. The Cameroon coast is a very dynamic and unique coastline as its formation includes several

DOI: 10.2112/SI81-016.1 received 30 September 2017; accepted in revision 15 January 2018.

\*Corresponding author: gregsolo55@yahoo.fr

©Coastal Education and Research Foundation, Inc. 2018

geomorphological processes (earthquakes, rivers, estuaries, rocks and sandy beaches). The high discharge of river flows and the presence of islands (Bioko, Sao-Tomé, Principe) influence the oceanic forcing circulation in the bottom of the Gulf of Guinea. Typically along the Cameroon coast characterized by several estuaries, the presence of mangrove forests mitigates the impact of sea level level changes (Onguéné, 2015). However, Cameroon estuary is exposed to the increase of salinity intrusion and changes in the sediment transport, which are probably linked to climate change. The Cameroon coast also have habours and marine protected areas (*e.g.*, Kribi Campo and Mouanko) which are susceptible to processes of coastal erosion. There are no or very limited complete evaluation of the coastline changes along the entire coastline of Cameroon. Assessing the evolution of the coastline different scales is particularly important for the management of human socio-economic activities of this coastline given its rich biodiversity.

To understand the nearshore dynamics of the estuarine region, modeling efforts have been carried out using the SYMPHONIE model (Marsaleix *et al.*, 2008, 2012; Marsaleix, Auclair, and Estournel, 2009), in a configuration covering the eastern part of the Gulf of Guinea (Onguene, 2015). It is a 3D coastal circulation model adapted at the regional scale for the salinity, temperature, density, sea surface height and currents. The model is taking into account the influence of mangroves and the wet-dry areas in the water flux circulation. The main difficulty of using this model is the validation of the outputs, due to the lack of in-situ measurements.

Larger part of the Cameroon coast remains uninvestigated. There is currently no field measured data or high frequency observations along many parts of the coast in Cameroon to be used to reveal the variability of the coastline. Despite, in this paper, we assess the global evolution (inter-annual scale) of Cameroon coastline from 1986 to 2015 based on four satellite images to identify the areas with significant changes. The main aim of this paper is to comprehend the general pattern of coastal evolution by giving a complete description of the site, shoreline changes and providing potential studies that could enhance the understanding of this coastline.

### STUDY SITE

The coast of Cameroon (Figure 1a) covers over 400 km, from Campo (border with Equatorial Guinea) to Abana (border with Nigeria). The coast is characterized by several river mouths: the Sanaga river (the country's longest watercourse), Nyong river, Kienké river, Lobe and Ntem rivers, and estuaries. In particular, Wouri estuary is one of the largest in the region. Giresse *et al.* (1996) defined four subsets of the coast (rectangles in Figure 1.b), a methodology that is adapted for the current study:

- Subset 1 (north part): Estuarine complex of Rio del Rey and Cross-River (from 4°30'N-8°30'E to 4°14'N-8°56'E). The Rio del Rey basin is an area that corresponds to a mangrove coast, composed of a group of islands and channels with about half of the area belonging to the intertidal zone. This complex area can be regarded as the southern extension of the vast Niger Delta. Onshore the oldest sediments of the Rio del Rey basin that crop out are the Mundek Formation (Ala and Selley, 1997). This consists of coarse pebbly cross-bedded fluvial sandstones that are broadly comparable to the Bima sandstone of Nigeria to the

west.

- Subset 2 (between Idenau and Limbé): This is a Volcanic rocky coastline (from 4°14'N-8°56'E to 3°58'N-9°17'E), defined primarily by the flows of Mount Cameroon. This area is characterised by small basaltic cliffs separated by small bays with pebble and sand beaches;

- Subset 3: Cameroon estuary (from 3°58'N-9°17'E to 3°34'N-9°38'E). This is a mangrove coast that borders the bay of Douala, a deep funnel of 30 km and width of 50 km, also called "Bouches du Cameroun". This bay lined with mangrove is the receptacle of the main rivers of the region: Mungo, Wouri, and Dibamba;

- Subset 4 (south part): Sandy coast (from 3°34'N-9°38'E to 2°20'N-9°48'E), running from the Sanaga mouth to Campo. From Campo to Londji, small segments of meager sandy beaches alternate with rocky headlands or flatlands (usually Precambrian). From Londji to the Sanaga mouth, the coast is composed of a set of sandy cords and restingas with parallel shelter lagoons behind.

The tidal range is about 1.8 m in Campo, 1.5 m in Kribi and 1.2 m in Petit-Batanga. It rises to 2 m in Douala estuary. In the Rio del Rey, which is a wide, open and shallow bay at the bottom of the Bay of Biafra, the tidal range reaches 2.4 and 3 m for neap and spring tides. These values were given by Giresse *et al.* (1996). The coast is exposed to long period swell waves that travel far from mid- to high latitudes (45–60°) in the South Atlantic and wind waves generated locally (Almar *et al.*, 2015). Significant heights of swell show a high variability with maximum in June-July-August and minimum in December-January-February.

## DATA AND METHODS

### Coastline Detection

Over a longer engineering time scale, such as 10-100 years, the position of the shoreline has the potential to vary by hundreds of meters or more. The definition of shoreline proxy to extract the shoreline is complex (Boak and Turner, 2005) as it depends on the kind of data and study area. In the case of this study, three indicators were used to identify the shoreline: landward edge of shore protection structure, seaward stable dune vegetation line and wet/dry line. Because, these are the most visible feature on the data used in this study and depending on the type of the coast (harbor, mangrove forest, sand beach).

Four historical images of two Landsat TM (Thematic Mapper), ETM+ (Enhanced Thematic Mapper Plus) and OLI (Operational Land Imager) are retrieved from Earth Explorer corresponding to Landsat 5, 7 and 8. All the images are in sun-synchronous polar orbit. The TM and OLI sensors are 700 km high with a repeatability of 16 days. These satellites have a swath of 185 km and a complete scene of 185 km / 185 km. It should be noted that there is difficulty of having clear images (without clouds) over the first half of the coast due to the presence of Mount Cameroon. After visual observation of various downloaded scenes, four (04) years were selected for this study: 1986, 1987, 2001 and 2015. The selected images do not cover the entire Cameroonian coast. It was therefore necessary to create mosaics with all the images available for each year in order to extract the coastlines. These image mosaics have been superimposed on Google Earth images to improve

detection.

The correction made in QGIS for superimposing the image vectors files is only possible for images that have been obtained with sensors of the same properties. The four coastlines extracted were orthorectified and projected in the UTM/WGS84 projection system. Digitization of the coastline was done manually to avoid detection errors. However, the accuracy is limited to the resolution of the images used (~ 30 meters) and

the digitization. The digitization error has been estimated equal to pixel resolution (~30 meters maximum). In order to study shoreline mobility, year-to-year coastline variation was measured on transects perpendicular to the coast, with reference to the 1986 coastline. The different variations between coastlines were then estimated and averaged in relation to the various forcing data.

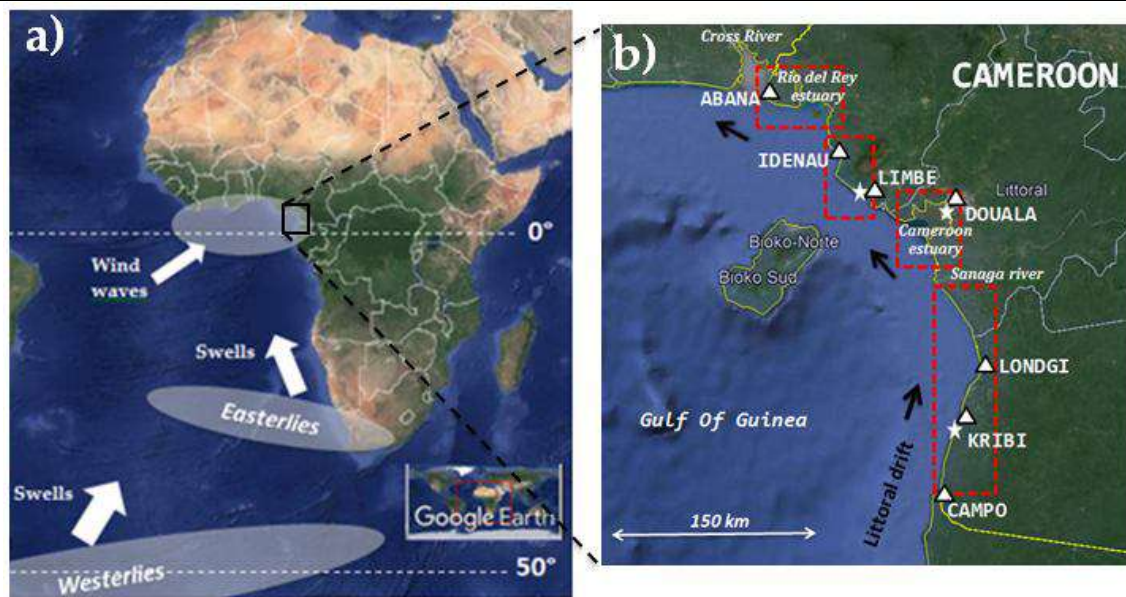


Figure 1. (a) Regional map with directions of swells and wind waves. (b) Cameroon coast: White triangles stand for main coastal cities, and white stars stand for harbors. Black arrows show the evolution of the littoral drift. Red dashed rectangles show the different subsections of the coast, according to Giresse *et al.* (1996).

### Oceanic Forcing

Wave parameters (significant height  $H_s$ , peak period  $T_p$  and direction) were derived from hindcast data, the ECMWF Wave Atmospheric Model (WAM) model (The Wamdi Group, 1988) in the Atlantic Ocean between 2001 and 2017. These wave data are part of the ERA-Interim dataset, which involves analysis of global meteorological variables (Dee *et al.*, 2011; Sterl and Caires, 2005). Wave data were extracted from the ECMWF data server on a  $0.125^\circ$ - $0.125^\circ$  grid, with a 6-hour temporal resolution. The ERA-Interim take into account an ocean wind-wave model coupled to atmospheric conditions. Though the wave data have been extensively validated against buoy and altimeter data (Sterl and Caires, 2005), high waves ( $H_s > 5$  m) and very low waves ( $H_s < 1$  m) tend, respectively, to be under- and over-estimated (Caires, Swail, and Wang, 2006). The scarcity of field data in the Gulf of Guinea affects the hindcast quality. The ERA-Interim outputs for the Cameroon coastline need to be treated with extreme caution. ERA-Interim waves are propagated to the shore using formula by Larson *et al.* (2010).

### Modelisation of Barotropic Currents

The Cameroon coast is the site of important river flows,

particularly at the Cameroon Estuary (CE), where four large rivers (Moungo, Wouri, Dibamba and Sanaga) have their mouth. To understand the circulation in CE, especially coastal currents, we used SYMPHONIE model (Marsaleix *et al.*, 2008, 2012; Marsaleix, Auclair, and Estournel, 2009). This is a 3D coastal circulation model adapted at the regional scale for the salinity, temperature, density, sea surface height and currents. These parameters are calculated along the horizontal polar grid and vertical in generalized sigma coordinate. The equations of the model are resolved by the finite difference method. In this paper, the SYMPHONIE configuration built by Onguene (2015) in the central Africa coast, called DOUALA26, is used. DOUALA26 has 300 meters of resolution near the polar point located on the to the CE at  $10.16^\circ$  E and  $4.35^\circ$  N. The horizontal polar grid has 418 points along radial axis, 514 along angular axis and vertically discretized in 20 levels. The daily atmospheric and oceanic forcing data in DOUALA26 are extracted from GLORYS MyOcean V2 reanalysis. To force DOUALA26, the seasonal rivers discharge extracted from Dai *et al.* (2009) and ORSTOM database were used. In addition to the parameters, mangrove grid built by Onguene (2015) is included in order to take into account drag coefficient due to trees in this

area. The drag coefficient is linearized in DOUALA26.

Tidal forcing terms were implemented following FES2012 atlas (Carrère *et al.*, 2012). The tidal harmonics (M2, S2, K2, N2, K1, O1, Q1, P1 and M4) are reanalysed in DOUALA26 grid in barotropic mode. Bathymetric data used in DOUALA26 is a combination of data from GEBCO in the continental shelf, digitalized CM93 navigation charts and bathymetry surveys done in 2013 in Cameroon estuary. The model has been run over 8 years, from 2002 to 2009. The temporal resolution is 5 minutes and barotropic current are obtain by averaging the 20 verticals levels during the period of simulation.

**RESULTS**

**Identified Eroding or Accreting Areas**

Figure 2 shows seven different areas (label from 1 to 7) within the four sections of the coast where significant erosion or accretion (more than 100 m cross-shore) over the last 30 years is detected. Only one case of human-induced variation was detected upstream of the Lobé water falls and corresponds to the construction of Kribi harbor in 2014 (black circle 7 in Figure 2a). The identified sites 1, 2, 3, 4, 5 and 6, respectively: Rio Del Rey estuary (subsection 1), North part of entrance of Cameroon estuary: “Cap Cameroon”, and South part of entrance of Cameroon estuary: “Souleyba” (subsection 3), Sanaga river mouth, Nyong river mouth and Lokoudje river mouth (subsection 4). The shoreline changes of subsection 2, between Mene river and the Northern entrance of the Cameroon estuary, was observed to be stable with all shoreline changes within the error range of 60 m. Significant shoreline variations are observed at river mouths and estuaries (Figures 2b and 2c), with the coastline of 1986 taken as a reference. The associated errors are estimated at ± 60 meters.

**Coastline Variation with Waves**

Figure 3 shows that the entire coast of Cameroon is subject to uniform peaks of wave events and their intensities are stronger in the southern part of the coast. The results reveal three types of sites along the whole coastline: Those with an accumulation (1, 3, 4, 6), those marked by erosion (2 and 5) and the stable subsection 2 (Idenau to Limbe). From North (1) to South (6), the variation of the waves becomes large. This outcome is not consistent with the different calculated erosive or accretion trends, suggesting the potential influence of other parameters. It remains difficult to explain the shoreline variations observed with ocean forcing because of the few temporal resolution.

However, the trends for waves (-0.001m/year) and whole shoreline (+0.54m/year) between the period of 1986 and 2015 suggest that as wave impact continue to decrease, the overall Cameroonian coast accumulates sediment and the significant parameter that may be used to explain the variability of the coastline is the sedimentary discharge of rivers and estuaries.

**Coastline Variation at Rivers Mouths**

Sanaga, Nyong and Lokoudje rivers have significant annual flows, respectively  $6.2 * 10^{10} \text{ m}^3/\text{year}$ ,  $1.4 * 10^{10} \text{ m}^3/\text{year}$  and  $1.2 * 10^{10} \text{ m}^3/\text{year}$ . The specific erosion of the entire Sanaga Basin is 44 tonnes/km<sup>2</sup>/year and results in an annual influx of 6 million tonnes of future sediment to the ocean (Giresse *et al.*, 1996). Sediment dynamics at the river mouths depend on the

interaction between river flows and ocean forcing. Changes in the coastline at these areas have been described to be more dependant on the time of acquisition of image, because the position of the sandbar depends on seasonal variability of rivers runoff (Onguéné, 2015).

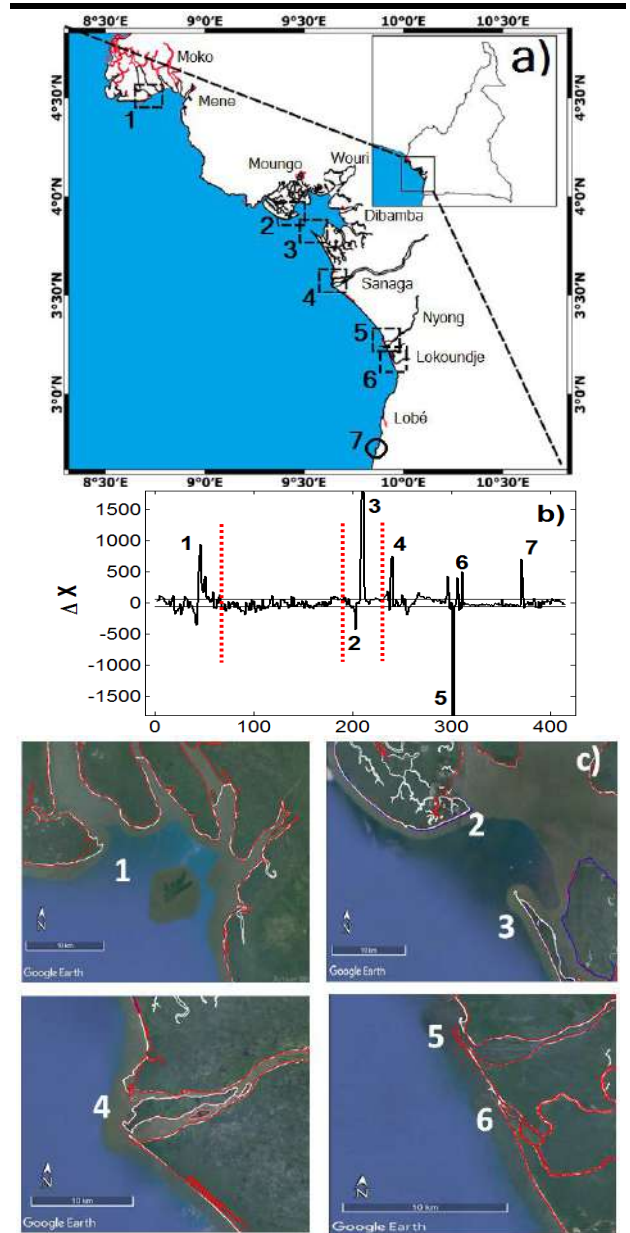


Figure 2. (a) The areas represented by black dotted rectangles (1 to 6) stand for significant variations (more than 100 meters) due to natural forcing. Area 7 (black circle) corresponds to the construction of Kribi harbor. (b) Cross-shore variation (ΔX) of shoreline from 1986 to 2015 (in meters). Error range is shown with the two horizontal lines. X-axis gives the transect number. Distance between two transects is 1 km. Red vertical dashed

lines give the four subsections of the coast. (c) Superposition of coastlines of 1987 (blue), 2001 (red) and 2015 (white). Google Earth images corresponding to the eroded or accumulated areas (1 to 6).

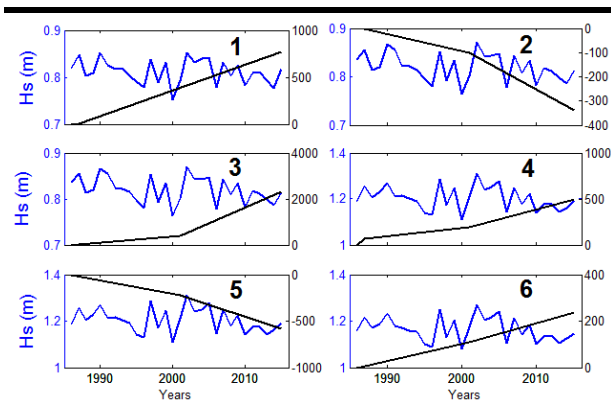


Figure 3. Evolution of annual median variations in significant wave heights (blue) and variations in coastline positions (black) for the different identified sites (1 to 6). Coastline variations were obtained by calculating the difference between the coastline position for a given year and the 1986 coastline. All variations are expressed in meters.

At seasonal scale, the high flows of rivers coincide with maximum significant wave heights  $H_s$ , while the low flows correspond with small swells. The sediments brought by the stream will be displaced more or less significantly depending on the season in the direction of the littoral drift. At event scale, the tide control the morphological evolution of the coast. These event and seasonal interactions between flows, tide and waves, coupled with the long-term impact of sea level rise (Figure 4), with a trend of 3.4 mm/year, could explain this strong variability of coastline position at rivers mouths over the study period. In this study, it is postulated that the sediment deposition is related to the size of the rivers. This preliminary results suggest that bigger rivers seem to have more sediment and hence accumulation (Figure 3, panels 4 and 6) than smaller rivers (Figure 3, panel 5).

#### Coastline Variation in Estuaries

In the estuarine complex of Rio del Rey and Cross-River, there is an accumulation of sediments (+8,2 m/year): The area of an island has doubled since 2001. In the Cameroon estuary, significant shoreline position changes are observed at the entrance to the estuary. The area of "Cap Cameroun" (Figure 2b, labelled 2) has experienced a coastal retreat of more than 300 meters during 30 years while the area of "Malimba" has experienced a significant accumulation of sediments, +82 m/year on the sand bar (Figure 2, labelled 3). The Cameroon estuary is characterized by the discharges of the Wouri, Moungo and Dibamba rivers. Upstream of the coastal drift (~ 30 km), Sanaga river discharges also affect the dynamics in the Cameroon estuary.

These estuaries are therefore the seat of a complex dynamic that takes into account the contribution of rivers and the influence of waves (shoreline drift). The understanding of the variation of the coastline in front of the estuaries requires oceanic forcing, atmospheric and discharges in sediments of the rivers. The simulation results presented in Figure 4 show barotropic circulation in the Cameroon estuary at an averaged spatial resolution of the order of 400 meters.

The circulation has been averaged monthly to obtain residual current velocities over a simulation period of 8 years (2002 to 2009). The influence of coastal drift on coastal currents is well observed especially in January when the rivers run off contribution is low. Sanaga river flows (Figure 4, labelled A) are brought back to the entrance of the estuary (Figure 4, labelled 3) where they encounter Dibamba (Figure 4, labelled B) and Wouri (Figure 4, labelled C) rivers discharges. The results show that current outflows from the estuary and runs along the coast of "Cap Cameroon" (Figure 4, labelled 2) with maximum intensities during the rainy season (June, July, August). The Sanaga river discharge plays the key role of sediment transport in the Cameroon estuary. In the rain season (July), the attenuation of barotropic current can be explained by the opposition of the coastal drift and river flow and the influence extended over 40 km of Sanaga mouth. Dynamics in April and October is similar. These months correspond respectively to the beginning and end of the long rain season in the region. The velocities of the observed currents remain very proportional to the discharge rates of the rivers. Figure 4 shows that the model output displays strong surface currents during the middle half of the year (April to September) compared to the other half of the year.

It is noted that the rivers Sanaga, Wouri and Dibamba have a strong flow in July and a low flow in January, in agreement with the rainfall of the region. The accumulation of sediments observed at the southern entrance of the estuary (Figure 2, labelled 3) coincides fairly well with the zone of convergence of the currents at this point (Figure 4, labelled 3). There is a strong supply of sediments on both sides by the river discharges (Wouri and Dibamba) and coastal currents. At the northern entrance (Figure 4, labelled 2), a high erosion is observed where the estuary output current remains low closed to the coast. However, there is the presence of a strong current leaving the estuary 4 km offshore. The resolution of the model around 400 meters at this location does not fully explain the strong erosion observed. The model gives a fairly clear idea of the sediment dynamics in the Douala estuary and the impact of river discharges in the area at seasonal scale, but the lack of high resolution bathymetric data set at this location is probably limiting the reality of the rivers outflows. Despite this outcome from the model, this barotropic current outputs of this model is yet to be validated in the Cameroon estuary because of the lack of field data.

#### DISCUSSION

This study remains an overview and requires an extension to various temporal scales. Generally, the coastline of Cameroon is characterized by erosion and accretion at different magnitudes. Subsection 2 has been observed to be stable with not erosion or accretion while the other sections experience either erosion or

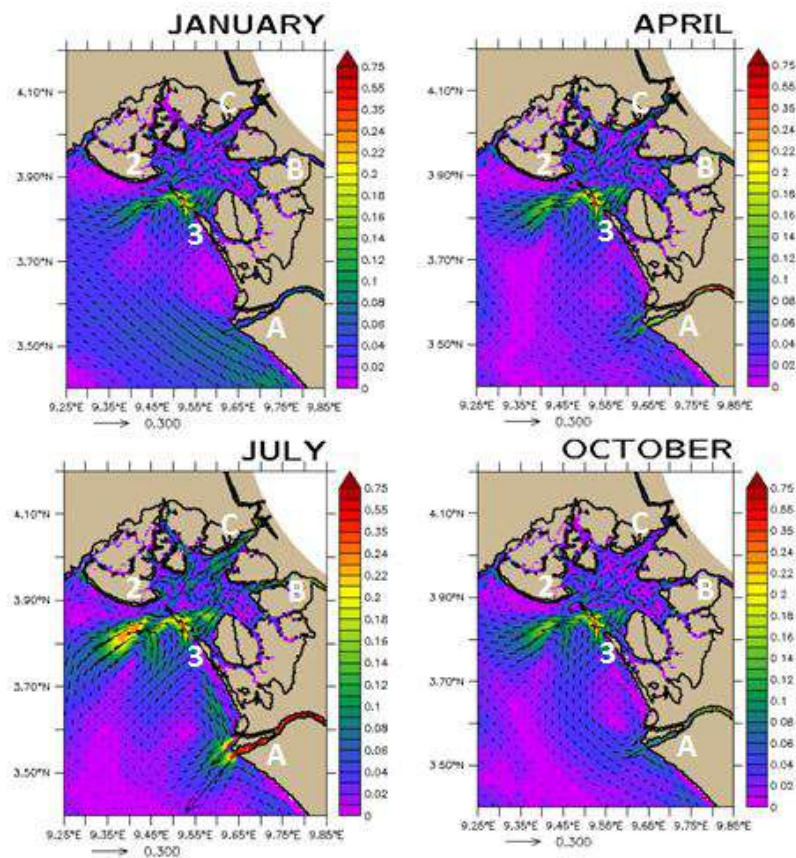


Figure 4. Monthly averaged barotropic currents over 2002-2009 period in Cameroon estuary with SYMPHONIE model, DOUALA26 configuration. The colorbar gives the amplitude of velocity in m/s.

accretion (Figure 3).

The model outputs show residual current velocities obtained by averaging barotropic currents. Bathymetry data, ocean and atmospheric forcing data with good spatial resolution are key for a realistic model. The OGCM used to run the model 25 km of spatial resolution is very well adapted for the open ocean part of our grid, but this result can be limited near the coast and estuaries. Validation of SYMPHONIE model with its DOUALA26 configuration remains a priority.

Besides, processes at the event scale and effects of sea level rise have not been taken into account in the model. Large eventual river flows could significantly modify the circulation in the Wouri estuary and affect unidentified areas, given the fact that the influence of several parameters are not investigated. The erosion observed on site 2 identified could not be explained with SYMPHONIE circulation model which shows very weak coastal currents concomitant with strong erosion, unlike the accumulation observed at the southern entrance to the Cameroon estuary, which coincides with the convergence of residual currents. The processes responsible for the erosion observed at "Cap Cameroun" (Figure 4, labelled 2) could correspond to

phenomena linked to the coupling of sea level rise and oceanic forcing. However, the lack of high-frequency (day-month) morphological data of the coastline doesn't make it possible to investigate this issue.

The resolution of the Landsat images (~ 30 meters) remains a difficulty in the precision of the coastline positions. Although this study was carried out with sites of erosion or sediment accumulation corresponding to a variation of more than 100 meters, it is clear that the small-scale processes, which are often very significant, have not been taken into account.

This study focuses on river mouths and estuaries, where significant variations can occur due to the inflow of river sediments.

## CONCLUSION

This study is a global approach to understand the evolution of Cameroon coastline from 1986 to 2015. We detected areas of significant cross-shore variation (more than 100 meters) with Landsat images of 1986, 1987, 2001 and 2015. These variations could be classified according to two types of sites: those located at the mouth of a river and those located in an estuary, where

there is a convergence of several discharges of rivers. Using oceanic forcing and river flows, we evaluated the barotropic currents using the SYMPHONIE model with the DOUALA26 configuration in the Cameroon estuary. The model results show that the convergence of rivers flows current create an accumulation area. This convergence of barotropic currents leads to an emergent stream of the estuary, which could be in correlation with the erosive zone of the estuary. The mouths of the rivers remain very dynamic places due to sediment discharges. In all, the Cameroon coastline is stable (accretion trend of +0.54 m/yr) over a 400 km scale. This work provides an understanding of erosive or accretive coastal processes using barotropic currents modeling in estuaries.

#### ACKNOWLEDGMENTS

We would like to express our gratitude to IRD/JEAI-RELIFOME (Institut de Recherche pour le Développement- Jeune Equipe Associée à l'IRD) for its financial support. This research has received support from French grants through ANR (COASTVAR: ANR-14-ASTR-0019). We acknowledge use of the ECMWF ERA Interim dataset ([www.ecmwf.int/research/era](http://www.ecmwf.int/research/era)). We acknowledge use of Landsat images downloaded from the website [earthexplorer.usgs.gov](http://earthexplorer.usgs.gov). Thanks are due to Pharell Willy Sone Essoh and Junior Iroume for their help in processing Landsat images.

#### LITERATURE CITED

- Abessolo Ondoa, G.; Almar, R.; Kestenare, E.; Bahini, A.; Houngue, G.H.; Jouanno, J.; Du Penhoat, Y.; Castelle, B.; Melet, A.; Meyssignac, B.; Anthony, E.J.; Laibi, R.; Alory, G., and Ranasingue, R., 2016. Potential of video cameras in assessing event and seasonal coastline behaviour: Grand Popo, Benin (Gulf of Guinea). *In: Vila-Concejo, A.; Bruce, E.; Kennedy, D.M., and McCarroll, R.J. (eds.), Proceedings of the 14th International Coastal Symposium* (Sydney, Australia). *Journal of Coastal Research*, Special Issue No. 75, pp. 442-446.
- Ala, M.A. and Selley, R.C., 1997. The West African coastal basins. *In: Selley, R.C. (ed.), African Basins. Sedimentary Basins of the World, Volume 3*. Amsterdam; New York: Elsevier Science, pp. 173-186.
- Almar, R.; Honkonnou, N.; Anthony, E.J.; Castelle, B.; Senechal, N.; Laibi, R.; Mensah-Senoo, T.; Degbe, G.; Quenum, M.; Dorel, M.; Chuchla, R.; Lefebvre, J. P.; Du Penhoat, Y.; Laryea, W. S.; Zodehougan, G.; Sohoun, Z.; Addo, K.A.; Ibaceta, R., and Kestenare, E., 2014. The Grand Popo beach 2013 experiment, Benin, West Africa: From short timescale processes to their integrated impact over long-term coastal evolution. *In: Green, A.N. and Cooper, J.A.G. (eds), Proceedings 13<sup>th</sup> International Coastal Symposium* (Durban, South Africa). *Journal of Coastal Research*, Special Issue No. 70, pp. 651-656.
- Almar, R.; Kestenare, E.; Reynolds, J.; Jouanno, J.; Anthony, E.J.; Laibi, R.; Hemer, M.; Du Penhoat, Y., and Ranasinghe, R., 2015. Response of the Bight of Benin (Gulf of Guinea, West Africa) coastline to anthropogenic and natural forcing, Part1: Wave climate variability and impacts on the longshore sediment transport. *Continental Shelf Research*, 110, 48-59.
- Appeaning Addo, K.; Walkden, M., and Mills, J.P., 2008. Detection, measurement and prediction of shoreline recession in Accra, Ghana. *ISPRS Journal of Photogrammetry and Remote Sensing*, 63(5), 543-558.
- Boak, E.H. and Turner, I.L., 2005. Shoreline definition and detection: A review. *Journal of Coastal Research*, 21(4), 688-703.
- Bosom, E. and Jiménez, J.A., 2011. Probabilistic coastal vulnerability assessment to storms at regional scale - application to Catalan beaches (NW Mediterranean). *Natural Hazards and Earth System Science*, 11, 475-484.
- Caires, S.; Swail, V.R., and Wang, X.L., 2006. Projection and analysis of extreme wave climate. *Journal of Climate*, 19(21), 5581-5605.
- Carrère, L.; Lyard, F.; Cancet, M.; Guillot, A., and Roblou, L., 2012. FES2012: A new global tidal model taking advantage of nearly 20 years of altimetry. *In: Ouwehand, L. (ed.), Proceedings of "20 Years of Progress in Radar Altimetry"* (Venice, Italy).
- Dee, D.P.; Uppala, S.M.; Simmons, A.J.; Berrisford, P.; Poli, P.; Kobayashi, S.; Andrae, U.; Balmaseda, M.A.; Balsamo, G.; Bauer, P.; Bechtold, P.; Beljaars, A.; Van De Berg, L.; Bidlot, J.R.; Bormann, N.; Delsol, C.; Dragani, R.; Fuentes, M.; Geer, A.J.; Haimberger, L.; Healy, S.; Hersbach, H.; Hólm, E.V.; Isaksen, I.; Kållberg, P.W.; Köhler, M.; Matricardi, M.; McNally, A.; Monge-Sanz, B.M.; Morcrette, J.J.; Peubey, C.; De Rosnay, P.; Tavolato, C.; Thépaut, J.N., and Vitart, F., 2011. The ERA-Interim reanalysis: Configuration and performance of the data assimilation system. *Quarterly Journal of the Royal Meteorological Society*, 137(656), 553-597.
- Dai, A.; Qian, T.; Trenberth, T., and Milliman, J., 2009. Changes in continental freshwater discharge from 1948 to 2004. *Journal of Climate*, 22, 2773-2792.
- Dolan, R.; Hayden, B.P.; May, P., and May, S.K., 1980. The reliability of shoreline change measurements from aerial photographs. *Shore and Beach*, 48(4), 22-29.
- Gianluigi, D.P.; Aucelli, P.P.C.; Benassai, G., and Rodriguez, G., 2014. Coastal vulnerability to wave storms of Sele littoral plain (southern Italy). *Natural Hazards*, 71, 1795-1819.
- Giresse, P.; Megope, F.J.; Nguetchoua, G., and Aloisi, J.C., 1996. *Carte Sédimentologique du Plateau Continental du Cameroun*. Paris, France: ORSTOM, *Collection Notice Explicative N° 111*, 12p.
- Hoggart, S.P.G.; Hanley, M.E.; Parker, D.J.; Simmonds, D.J.; Bilton, D.T.; Filipova-Marinova, M.; Franklin, E.L.; Kotsev, I.; Penning-Rowsell, E.C.; Rundle, S.D.; Trifonova, E.; Vergiev, S.; White, A.C., and Thompsona, R.C., 2014. The consequences of doing nothing: The effects of seawater flooding on coastal zones. *Coastal Engineering*, 87, 169-182.
- Laibi, R.; Anthony, E.; Almar, R.; Castelle, B., and Senechal, N., 2014. Alongshore drift cell development on the human-impacted Bight of Benin sand barrier coast, West Africa. *In: Green, A.N. and Cooper (eds), Proceedings 13<sup>th</sup> International Coastal Symposium* (Durban, South Africa). *Journal of Coastal Research*, Special Issue No. 70, pp. 78-83.
- Larson, M.; Hoan, L.X., and Hanson, H. 2010. A direct formula to compute wave properties at incipient breaking. *Journal of Waterway, Port, Coastal and Ocean Engineering*, 136(2),

- 119-122.
- Marsaleix, P.; Auclair, F.; Floor, J.W.; Herrmann, M.; Estournel, C.; Pairaud, I., and Ulses, C., 2008. Energy conservation issues in sigma-coordinate free-surface ocean models. *Ocean Modelling*, 20, 61-89.
- Marsaleix, P.; Auclair, F., and Estournel, C., 2009. Low-order pressure gradient schemes in sigma coordinate models: The seamount test revisited. *Ocean Modelling*, 30, 169-177.
- Marsaleix, P.; Auclair, F.; Duhaut, T.; Estournel, C.; Nguyen, C., and Ulses, C., 2012. Alternatives to the Robert-Asselin filter. *Ocean Modelling*, 41, 53-66.
- Melet, A.; Almar, R., and Meyssignac, B., 2016. What dominates sea level at the coast: A case study for the Gulf of Guinea. *Ocean Dynamics*, 66, 623-636.
- Onguene, R., 2015. Modélisation Multi-Echelles de la Circulation Océanique en Afrique Centrale, de la Plaine Abyssale à l'Estuaire du Cameroun. Toulouse, France: University of Toulouse III Paul Sabatier, Ph.D. dissertation, 216p.
- Richards, J. and Nicholls, R.J., 2009. *Impacts of Climate Change in Coastal Systems in Europe. PESETA Coastal Systems study*. Luxembourg: European Commission, Joint Research Center. *JRC Scientific and Technical Reports, JRC 55390, EUR 24130 EN*.
- Sterl, A. and Caires, S., 2005. Climatology, variability and extrema of ocean waves- the web-based KNMI/ERA-40 wave atlas. *International Journal of Climatology*, 25, 963-977.
- Tano, R.A.; Aman, A.; Kouadio, K.Y.; Toualy, E.; Ali, K.E., and Assamoi, P., 2016. Assessment of the Ivorian Coastal Vulnerability. *Journal of Coastal Research*, 32(6), 1495-1503.
- The Wamdi Group, 1988. The WAM model-a third generation ocean wave prediction model. *Journal of Physical Oceanography*, 18, 1775-1810.



**TITLE : RESPONSE OF SANDY BEACHES IN WEST AFRICA, GULF OF GUINEA, TO MULTI-SCALE FORCING**

---

**ABSTRACT :**

This thesis presents a multi-scale investigation of the role of waves, sea level and human settlements to understand long-term coastal evolution of the 400-km long sandy Bight of Benin coast (Gulf of Guinea, West Africa). Coastal morphology and its ocean drivers are monitored using local shore-based video camera and regional satellite remote sensing. New video developpements show the potential of video camera in sensing daily beach profile, waves and sea level at the coast. The results reveal the dominant influence of waves on shoreline variability at the event (daily) and seasonal scales, whereas at the intraseasonal and interannual scales, the shoreline is dominantly modulated by sea level changes. Over longer periods (decades), anthropogenic influence, such as deep water harbours and the reduction of sediment river (such as Volta and Niger) discharge due to dams significantly alter sediment transport, creating several erosion zones. These observations over the long term are satisfactorily reproduced by the implemented shoreline model, specially in the vicinity of the harbors, and allows to estimate, for example, the amount of sediment nourishment necessary to limit erosion downstream of Lagos harbor. Beside their fundamental interest, these results put strong basis to improve regional coastal policies.

---

**KEYWORDS:** Bight of Benin, waves, sea level, sediment transport, nearshore, shoreline, beach profile, long term shoreline modeling

**AUTEUR** : ABESOLO ONDOA Grégoire

**TITRE** : RÉPONSE DES PLAGES SABLEUSES D'AFRIQUE DE L'OUEST, GOLFE DE GUINÉE, FACE AU FORÇAGE MULTI-ÉCHELLE

**DIRECTEURS DE THÈSE** : ALMAR Rafael et LARSON Magnus

**LIEU ET DATE DE SOUTENANCE** : SALLE PYRENÉES, OBSERVATOIRE MIDI-PYRENÉES, TOULOUSE, FRANCE, LE 11 JUIN 2020 A 14 HEURES

---

## **RÉSUMÉ**

Cette thèse présente une étude multi-échelle du rôle des vagues, du niveau de la mer et des infrastructures humaines pour comprendre l'évolution à long terme des 400 km de côte sableuse dans la Baie du Bénin (Golfe de Guinée, Afrique de l'Ouest). La morphologie côtière et les forçages océaniques sont mesurés au niveau local par un système d'observation vidéo et au niveau régional par télédétection satellite. De nouvelles améliorations des techniques vidéo montrent le potentiel des systèmes vidéo dans l'estimation journalière du profil de la plage, des vagues et du niveau de la mer à la côte. Les résultats révèlent l'influence dominante des vagues sur la variabilité côtière aux échelles événementielle (journalière) et saisonnière, tandis qu'aux échelles intrasaisonnière et interannuelle, le trait de côte est modulé de manière dominante par les changements du niveau de la mer. Sur des périodes plus longues (décennies), les influences anthropiques, telles que les ports en eau profonde et la réduction des flux sédimentaires fluviaux (à l'exemple de la Volta et le Niger) due aux barrages, modifient considérablement le transport sédimentaire, conduisant à l'apparition de plusieurs zones d'érosion. Ces observations à long terme sont reproduites de manière satisfaisante par le modèle de trait de côte mis en œuvre, en particulier à proximité des ports, et permettent d'estimer, par exemple, la quantité de sédiments nécessaire pour limiter l'érosion en aval du port de Lagos. Outre leur intérêt fondamental, ces résultats constituent un cadre solide pour l'amélioration des politiques côtières dans la région.

---

**MOTS CLÉS** : Baie du Bénin, vagues, niveau de la mer, transport sédimentaire, littoral, trait de côte, profil de plage, modélisation d'évolution long terme du trait de côte

---

**ÉCOLE DOCTORALE** : SDU2E - Sciences de l'Univers, de l'Environnement et de l'Espace

**SPÉCIALITÉ** : Océan, Atmosphère, Climat

---

**UNITÉ DE RECHERCHE** : LEGOS (Laboratoire d'Études en Géophysique et Océanographie Spatiale) – UMR 5566 – Observatoire Midi-Pyrénées, 14 Avenue Édouard Belin, 31400, Toulouse, France